Quantifying Relative Surface Level Brain Motion in Postmortem Human Subjects Using High-Frequency B-Mode Ultrasound

Dissertation

Presented in Partial Fulfillment of the Requirements for the Degree Doctor of Philosophy in the Graduate School of The Ohio State University

By

Angela Clara Tesny

Graduate Program in Mechanical Engineering

The Ohio State University

2022

Dissertation Committee

Yun-Seok Kang, Advisor

John H. Bolte IV

Alan Litsky

Rebecca Dupaix

Abstract

Motor vehicle crashes are a leading cause of bleeding head injury, especially in the elderly population. Acute subdural hematomas (ASDH) are particularly lethal. The increased frequency of ASDH with age has been attributed to the rupture of bridging veins, necessitating a better understanding of the relationship between rotational kinematics and bridging vein failure. As bridging veins run from the surface of the cortex through the meninges and into the dural sinuses, any relative motion between the brain and the skull may result in the shearing of the bridging veins, resulting in ASDH. The increased atrophy in the elderly population compared to their younger counterparts results in an initial strain on the bridging veins, suggesting one of the reasons why the elderly population is more susceptible to ASDH from bridging vein failure.

Previous studies have quantified whole brain motion under a variety of dynamic loading conditions. Further, finite element (FE) models of the brain have been utilized to supplement the investigation of the brain's susceptibility to injury; however, the experimental brain data currently used to validate these models are lacking surface-level validation data. The objective of this dissertation is to provide experimental brain displacement data at the surface of the brain to contribute to further validation of FE models and aid in the investigation of the relationship between head kinematics and brain displacement that could result in an ASDH in the elderly.

Surface-level brain displacements were quantified in this dissertation work using high-frequency, Brightness-mode (B-mode) ultrasound due to its advantages of noninvasiveness and high resolution. However, the use of ultrasound to quantify displacement while the probe is

rotating under high rates has not yet been validated. As an initial objective of this dissertation work, the ultrasound was validated under the same conditions that it was utilized for quantifying brain displacement in postmortem human subjects (PMHS). A custom validation fixture was fabricated to replicate brain motion under rotation in a PMHS. Rather than tracking human tissue samples, a three-dimensional (3D) phantom was created. Displacement of the 3D printed tracking phantom was compared to displacement obtained from a linear potentiometer. On average, the difference between the measurement systems was 0.05 mm, or a 1.5% difference. Combined with an NRMSD value of 1.26, these results indicate that the accuracy of the ultrasound as a measurement system is not influenced by high-rate rotation, and thus can be utilized to quantify brain displacement in PMHS.

Displacements between surface-level brain tissues and the skull were quantified using high-frequency, B-mode ultrasound in five PMHS. Each subject underwent pre-test magnetic resonance (MR) imaging and brain parenchymal fraction (BPF) was calculated. Brain temperature of each subject was monitored and controlled throughout both preparation and testing, as lower temperatures have been shown to reduce the effects of postmortem degradation. The head of each subject was removed at the C6-C7 vertebral level, and artificial cerebrospinal fluid (aCSF) was reintroduced via the subarachnoid space. A small window was opened through the skull for the ultrasound to image the underlying tissue at 3 cm posterior to the bregma and 3 cm lateral to the centerline. The head was secured in a cage that ensured uniform rotation in the sagittal plane in an anterior-posterior direction. A custom rotation fixture delivered repeatable pulses over a wide range of input kinematics. Each subject's brain was brought to physiological intracranial pressure before each rotation test. All rotation tests across all five subjects were complete within 56 hours postmortem. The moment of inertia (MOI) of each subject was

calculated post-test. Tissue tracking video sequences collected by B-mode ultrasound were analyzed using a commercial video tracking software. Peak brain displacements were quantified at the surface of the cortex, 1 mm deep into the cortex, and 2 mm deep into the cortex.

This dissertation provides over 300 displacement curves from five subjects varying in age, sex, and anthropometry that can be used to improve and validate human body models. Subject-specific parameters such as the postmortem time at which the rotation test was conducted, BPF, and MOI were all significant predictors of peak brain displacement. These data provided in this dissertation provide another step towards understanding subdural hematoma injury risk based on kinematic input.

Dedication

To my mom,
who in the fifth grade told my teacher to stop giving me “A+ supers” because I was getting complacent. You taught me I can always work harder and to never stop learning and improving, so this is for you.

And to Nicki, Jeremy, Leah, Noah, Chloe, Elliot, Eliza, Bear, and Luna
Even on the days I didn’t think I would make it; you all knew I would.

Acknowledgements

This year marks my 22nd year of school, and by far the most important thing I've learned was taught to me by my high-school basketball coach, Chris Hassinger; "life's about relationships." This has led me to treasure every person that has come into my life, no matter how brief. Though I feel I should acknowledge every professor, teammate, fellow classmate, coach, mentor, and friend that has helped me get to where I am today, the page limit simply won't allow it. So, if you're reading this, thank you from the bottom of my heart.

Firstly, and perhaps most importantly, I would like to acknowledge my advisor, Dr. Yun Seok Kang. Not only did he offer me a tremendous amount of technical guidance and support that made me a better researcher and engineer, his friendship and patience has made me a much better person. I absolutely could not have done this without you and cannot thank you enough for sticking with me through multiple 24+ hour testing shifts (sorry HJ and Ian), deciphering my nonsense, answering my calls no matter the time, and your endless, unwavering support. When I committed to OSU with you as my advisor, you sent me an email that said "I promise I will do my best to make you successful. I will work with you and stand right next you till you become Dr Tesny. Nothing will be easy, but you can do it. Now you are my family." We did it, and I am so proud to be your first PhD student.

To the rest of my committee, Dr. John Bolte IV, Dr. Alan Litsky, and Dr. Rebecca Dupaix, thank you so much for your guidance during these past few years and encouraging me to critically evaluate my work. Each of you have challenged me and provided much-appreciated feedback that improved my dissertation work.

This work would not have been possible without the support of the subdural project team; Alex Bendig, Heather Rhule, Kevin Moorhouse, Colton Thomas, and Ann Mallory. The contributions each of you made to this work was above-and-beyond, and for that I will always be grateful. I must also thank my other colleagues from TRC and NHTSA VRTC that somehow got roped into the overnight testing shifts; Laura Watkins, Scott Bazzle, Rakshit Ramachandra, Michelle Murach, and Brian Suntay. And a big thank you to Jim Clevinger for his insights and contributions to this project over the past few years. Additionally, thank you to Brett Bryan from the Ohio State University Wexner Medical Center for performing the MRIs during this dissertation work and helping us get these scans completed as quickly as possible.

Thank you to all my colleagues (who became more like family) at the Injury Biomechanics Research Center. I must acknowledge Dr. Angela Harden, Dr. Mandy Agnew, and Dr. Randee Hunter; three incredible women and researchers who have been amazing examples of the success you can achieve when you're truly passionate about the work you're doing. It has been an honor to be a part of #TeamTibia, #TeamRib, and #TeamUlna. I'd also like to acknowledge the model gang, Vikram Pradhan and Tim DeWitt, who committed some pretty late nights and early mornings to help me with subdural testing. It has been a pleasure mentoring our new engineering grad students; Mara Dunning Van Meter, Rosalie Connell, and Angelo Marcallini, as well as a multitude of undergraduate students that have spent time assisting in the IBRC. Thanks to each of you for reminding me why I love what we do. I'd like to especially thank Gretchen Baker not only for your MATLAB help and talking things through with me, but also for simply understanding. I could not have gotten through this without you. Finally, for being my constant sounding boards, holding me accountable to achieve the highest level of

success, and being there for me through it all, thank you to my lab mates and best friends Zac Haverfield and Carla Goldsmith.

Lastly, thank you to my friends and family for your endless love and support. To Rachel Letts and George, you were there for me during the most challenging parts of my life. I cannot thank you enough for every piece of advice, every laugh, every walk to Stauf's, and the comfort of watching TV together after a long day. To Akshara Sreedhar, Molly Tillis, and Nicole Fye, thank you for always having my back and listening to me ramble about my project, whether it was in the lab or on zoom. I am so grateful our time at the IBRC bonded us as lifelong friends. To Dr. Sarah Boylan, Lindsey Hall, and Holly Wendell, thank you for knowing the real me and loving me anyways. I would be way less sane if I didn't have you in my life. To my Aunt Kelly, thank you so much for letting me be your roommate both at the start and end of my PhD journey. And to my grandma Carol who texted me every day without fail over the past 5 years, I love you.

Vita

2013……. Medina High School

2017……..……. B.S.M.E.,
Ohio Northern University

2020……...……...……..…….. M.S.,
Mechanical Engineering, The Ohio State University

2017-2022...…….. Graduate Research Associate,
The Ohio State University

Publications

Tesny, A., Mallory, A., Thomas, C., Rhule, H., Morehouse, K., Kang, Y.S. (in progress). Validation of high-speed, high-frequency, B-mode ultrasound under high-rate, rotational motion.

Tesny, A., Mallory, A., Thomas, C., Rhule, H., Morehouse, K., Kang, Y.S. (in progress). Measurement of brain-skull relative motion using B-mode ultrasound under rotational motion.

Kang, Y.S., Millis, W., Thomas, C., Stricklin, J., Willis, A., Pradhan, V., **Tesny, A**., Kwon, H.J., Ramachandra, R., and Morehouse, K. (2021). Head-to-T1 Relative Rotation of the BioRID-II, Hybrid III, and Post Mortem Human Subjects with Increased Backsets in Moderate-Speed Rear Impacts. *Proceedings of the 2021 International IRCOBI Conference on the Biomechanics of Injury.*

Wang, J, Z., Loeber, B., **Tesny, A**., Hu, G., and Kang, Y.S. (2021). Neck biofidelity comparison of THOR-AC, THOR, and Hybrid III 50th dummies. *Proceedings of the 2021 International IRCOBI Conference on the Biomechanics of Injury.*

Tesny, A., Mallory, A., Thomas, C., Rhule, H., Morehouse, K., Kang, Y.S. (2019). Quantifying Relative Brain Motion in a Post Mortem Human Subject. *The Ohio State University Injury Biomechanics Research Symposium.* [Not Peer Reviewed]

Field of Study
Major Field: Mechanical Engineering
Minor Field: Bioethics

Table of Contents

List of Tables

List of Figures

Chapter 1: Background and Significance

1.1 Background and Significance for Acute Subdural Hematoma

It has been well established that motor vehicle crashes (MVC) are a leading cause of head injury (Vollmer et al., 1991; Mosenthal et al., 2002; Hukkelhoven et al., 2003; Urban et al., 2012; Taylor et al., 2017). In MVCs, the percentage of elderly occupants that die or suffer long-term disability compared to younger occupants is significantly higher given similar crash severities (Pentland et al., 1986, Roozenbeek et al., 2013). The United States population of those aged 65 and over has been growing rapidly since 2010, specifically by over a third over the last decade (United States Census Bureau, 2021). Increases in the elderly population pose significant challenges for automotive safety and countermeasure design as patient age is a strong predictor of morbidity and mortality (Coronado et al., 2005; Stitzel et al., 2008; Mallory et al., 2010).

Due to the increased vulnerability in the elderly population, older occupants are more likely than their younger counterparts to sustain bleeding head injuries during MVCs (Gennarelli et al., 1972; Sawuchi and Abe, 2008; Mallory, 2010; Fountain et al., 2017). Acute subdural hematomas (ASDH), along with diffuse axonal injury (DAI), account for more head injury deaths than all other lesions combined (Gennarelli et al., 1982). Despite medical advances, morbidity and mortality rates from ASDH remain high with mortality rates cited over 50% (Sawuchi and Abe, 2008; Taussky et al., 2008). Previous analysis of MVC databases has suggested that the increased frequency of ASDH with age is primarily related to the rupture of bridging veins and suggests a clear association between increasing age and increased mortality,

especially in the case of individuals over the age of 65 (Grossman et al., 2002; Bergeron et al., 2004; Coronado et al., 2005; Stitzel et al., 2008; Mallory et al., 2011; Daugherty et al., 2017). Loss of brain parenchyma due to neurodegeneration is known as brain atrophy and has been shown to occur in aging adults even in the absence of neurodegenerative diseases (Vågberg et al., 2017). Age-related decrease in brain volume results in enlargement of the subdural space, leading to an initial strain on the bridging veins, contributing to increased instances of ASDH occurring in the elderly population. The increased frequency of ASDH with age combined with poor outcomes necessitates a better understanding of injury tolerance to ASDH associated with bridging vein bleeds in the older population.

1.2 Relevant Anatomy

Between the brain and skull are three cranial meninges, the membranous coverings of the brain and spinal cord that provide a supportive framework for the cerebral and cranial vasculature and protect the cranial nervous system from damage. The outermost layer is the dura mater, a tough, thick, double-layered membrane which includes an external periosteal layer and an internal meningeal layer (Moore et al., 2013). The dural venous sinuses are located between the two layers of the dura mater and are responsible for the venous drainage of the cranium and empty into the internal jugular veins. The dura folds inwards to form four dural reflections: the falx cerebri which separates the right and left hemispheres, the tentorium cerebelli which separates the occipital lobes from the cerebellum, the falx cerebelli which separates the left and right cerebellar hemispheres, and the diaphragma sellae which cover the hypophysial fossa of the sphenoid bone (Moore et al., 2013).

The middle layer of the meninges is the arachnoid. Beneath it lies the subarachnoid space, which contains the cerebrospinal fluid (CSF), which acts to cushion the brain. Small portions of the arachnoid called arachnoid granulations project into the dura, allowing CSF to re-enter the circulation via the dural venous sinuses. Beneath the subarachnoid space lies the pia mater which is very thin and tightly adhered to the surface of the brain and spinal cord (Moore et al., 2013).

The central nervous system consists of the cerebrum, cerebellum, brainstem, and spinal cord. The brain has a particularly high oxygen demand, representing the one fifth of the body's total oxygen consumption (Jain et al., 2017).

1.2.1. Arterial System

There are two paired arteries responsible for the blood supply to the brain: the vertebral arteries and the internal carotid arteries. Within the cranial vault, terminal branches of these arteries form an anastomosis called the circle of Willis.

The internal carotid arteries originate at the bifurcation of the left and right common carotid arteries at the level of the fourth cervical vertebrae. They enter the brain via the carotid canal of the temporal bone and do not supply any branches to the face or neck. After passing anteriorly through the cavernous sinus, each internal carotid branches into the ophthalmic artery, which supplies the structures of the orbit, the posterior communicating artery, the anterior choroidal artery, and the anterior cerebral artery. The internal carotids continue as the middle cerebral artery, which supplies blood to the lateral portions of the cerebrum (Moore et al., 2013).

The left and right vertebral arteries branch from the subclavian arteries medial to the anterior scalene muscle, ascending the posterior aspect of the neck through the holes in the

transverse processes or the cervical vertebrae. The vertebral arteries enter the cranial cavity through the foramen magnum which branches into the meningeal branch which supplies the falx cerebelli, the anterior and posterior spinal arteries, and the posterior inferior cerebellar artery. The vertebral arteries then converge to form the basilar artery, which later terminates by bifurcating into the posterior cerebral arteries (Moore et al., 2013).

1.2.2 Venous System

The venous drainage of the central nervous system is complex and uniquely does not follow the arterial supply. The cerebrum, cerebellum, and brainstem are drained by numerous veins that empty into the dural venous sinuses, which lie between the periosteal and meningeal layers of the dura. All the dural venous sinuses, 11 in total, ultimately drain into the internal jugular vein. The straight, superior, and inferior sagittal sinuses are contained in the falx cerebri and converge at the confluence of sinuses overlying the internal occipital protuberance. From the confluence, the transverse sinus continues bilaterally and curves into the sigmoid sinus to meet the opening of the internal jugular vein. The cavernous sinus lies on either side of the sella turcica, and from here blood returns to the internal jugular vein through the superior or inferior petrosal sinuses (Moore et al., 2013).

1.2.2.1 Bridging Vein Anatomy

Bridging veins (BV) drain venous blood from the cerebral cortex into the dural sinuses by crossing through the dura mater. Despite their importance, especially in head injury biomechanics, not much is known concerning their histology, morphology, and mechanical behavior because apart from a complex morphology, BV also exhibit complex mechanical

behavior as they exhibit non-linear, viscoelastic behavior (Famaey et al., 2015). Due largely to human variation, the number of bridging veins and direction of inflow into the SSS shows high variability but can generally be categorized in one of five ways: antegrade (along the flow direction of the SSS, perpendicular, retrograde (opposed to the flow direction of the SSS), hairpin shaped (changing direction shortly before entering the sinus, or lacunae (enlarged venous spaces) (Famaey et al., 2015; Yamashima et al., 1984; Brockmann et al., 2011). Additionally, the entrances of the bridging veins along the SSS are not evenly distributed. To give a more general description of BV location based on anatomical landmarks, Han and colleagues (2006) divided the SSS into four segments from anterior to posterior according to a percentage of the length of the falx, where the first two segments have an average length of about 5 cm and the last two segments measured about 7 cm. Nearly all of the bridging veins that entered segment 3 (an area roughly 0.7 cm posterior to the bregma and 3 cm anterior to the lambda) of the SSS occurred at an angle opposed to the direction of blood flow, indicating that veins in this area are more susceptible to injury under anterior-posterior rotation (Han et al., 2006).

The properties of bridging veins including the length, outer diameter (OD), and wall thickness (WT) have been studied extensively under a variety of test setups (Table 1). The average outer diameter of a bridging vein is between 0.5 and 5.3 mm, which can vary significantly along the length of the vein.

Table 1: Comparison of SSS-BV geometric parameters, from (Famaey et al., 2015)

Author	Length (mm)	OD (mm)	WT (mm)
Yamashima et al. (1984)	10.0-20.0	1.0-3.0	Subdural: 0.01±0.60 Subarachnoid: 0.05±0.20
Oka et al. (1985)	0-70.0	0.5-5.3	-
Lee et al. (1989)	6.4±4.0	1.4±0.6	0.05±0.02
Sampei et al. (1996)	-	0.5-4.0	-
Ehrlich et al. (2003)	-	1.4-3.1	-
Monson et al. (2005)	-	1.8±0.4	0.12±0.02
Delye et al. (2006)	Male: 22.1±7.6 Female: 18.0±6.0	Male: 2.7±0.9 Female: 2.7±1.1	Male: 0.03±0.01 Female: 0.04±0.02
Vignes et al. (2007)	-	0.5-4.0	-
Han et al. (2007)	-	Cadavers: 2.5±1.1 DSA: 3.4±0.8	- -
Monea et al. (2014)	-	3.4±1.2	0.04±0.02
OD= Outer Diameter, WT= Wall Thickness, DSA= Digital Subtraction Angiography			

1.3 Literature Review on ASDH from Bridging Vein Rupture

Acute subdural hematomas are characterized by large volumes of clotted blood between the dura and the arachnoid. Maxeiner (1998) proposed that two-thirds of the ASDH are caused by large contusions to the brain tissue. Next to head contusion and laceration of the cerebral veins and arteries, a rupture of the bridging veins is one of the main causes of ASDH, accounting for one-third of all the cases (Gennarelli and Thibault, 1982; Depreitere et al., 2006).

Bridging veins cross from the surface of the brain cortex through the arachnoid and dura mater into the dural sinuses (Figure 1), so any relative motion between these tissue layers may result in bridging vein failure. The falx protects from lateral displacement but there is no protection against anterior-posterior movement (Yamashima et al., 1984). Subdural hematomas associated with bridging vein damage are believed to result from stretching the veins to failure

with a motion of the brain relative to the skull during head rotation (Holbourn, 1943; Gennarelli et al., 1982).

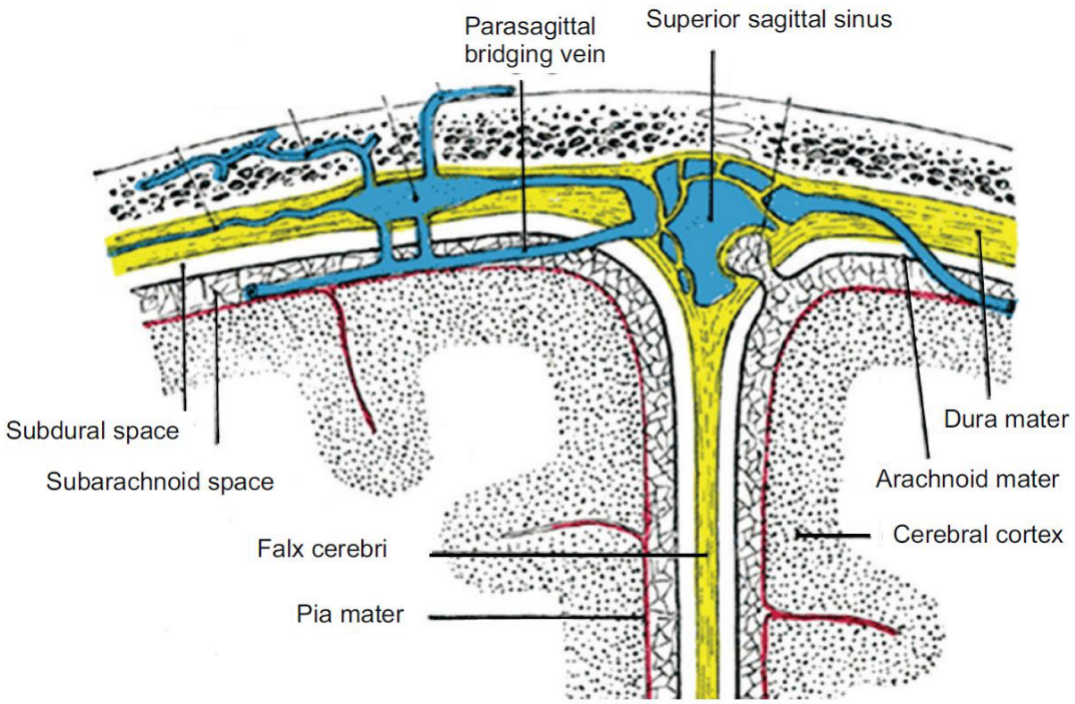

Figure 1: Coronal section through skull, meninges, and brain

Adapted from Gray, 20th Ed. (2000)

In a database review of both NASS/CDS (National Automotive Sampling System/ Crashworthiness Data System) and CIREN (Crash Injury Research and Engineering Network), Mallory and colleagues (2011) noted an age-related increase in the prevalence of ASDH sustained from bridging vein failure, especially in the case of frontal impacts. The combination of increased initial stretch of the bridging veins resulting from increased atrophy with age along

with the increased stiffness of those vessels in the aging population results in additional increased risk in the elderly (Löwenhielm, 1974; Stitzel et al., 2008; Famaey et al., 2013; Monea et al., 2014; Zhou et al., 2020).

1.3.1 Bridging Vein Tolerance from Isolated Testing

Bridging veins exhibit complex mechanical behavior as they behave non-linearly, are viscoelastic, and are prone to damage (Famaey et al., 2013). Efforts to characterize bridging vein geometry and other characteristics indicate various inflow directions to the superior sagittal sinus (Han et al., 2007; Brockmann et al., 2011). Because of this, the relative motion of the brain with respect to the skull will result in tensile and shear loading of at least some bridging veins, which may result in possible tearing. Using the failure properties of bridging veins in the literature, the probability of bridging vein failure given a level of rotational kinematics can be determined. A summary of bridging vein failure properties from the literature is summarized in Table 2.

Table 2: Comparison of bridging vein mechanical properties reported in the literature (from Famaey et al., 2015)

	σ_u (MPa)	ε_u (%)	σ_y (MPa)	ε_y (%)	E (MPa)
Lee et al. (1989)	3.33 ± 1.52	53.0 ± 19.5	--	--	--
Monson et al. (2005)	1.32 ± 0.62	50 ± 19.0	1.15 ± 0.47	29 ± 9.0	6.43 ± 3.44
Delye et al. (2006)	4.99 ± 2.55	25 ± 8.0	4.13 ± 2.14	18 ± 7.0	30.69 ± 19.40
Monea et al. (2014)	4.19 + 2.37	29.82 ± 13.3	1.73 ± 1.37	12.85 ± 13.6	25.72 ± 15.86

Ultimate stress and strain values are indicative of the actual failure limit; reported values of ultimate stress range between 1.32-4.99 MPa while values of ultimate strain range between 25-53% (Lee and Haut, 1989; Monson et al., 2005; Delye et al., 2006; Monea et al., 2014).

1.3.2 Bridging Vein Tolerance from Other Testing

Along with the complex geometry of bridging veins, the mechanical behavior is equally complex. Tolerance to bridging vein failure through impact has been proposed either through experimental impacts or finite element (FE) simulations. Löwenhielm (1974) found a maximum tolerable posterior-anterior rotational acceleration of 4,500 rad/s^2 through head-on collision experiments with whole cadavers, where pulse durations lasted between 15 to 44 ms (Löwenhielm, 1974). Deprietere and colleagues (2006) expanded the criterion, stating a maximum tolerable posterior-anterior rotational acceleration of 10,000 rad/s^2 for pulse durations shorter than 10 ms found through cadaveric experiments in which human heads were impacted by a pendulum (Deprietere et al., 2006). Additionally, tolerances have been proposed based on FE model simulations. Kleiven and colleagues (2002) found a maximum posterior-anterior rotational acceleration of 34,000 rad/s^2 at a 5 ms pulse duration by combining results of their three-dimensional (3D) FE head impact simulations with the tensile failure tests on bridging veins run by Lee and Haut (1989). Huang and colleagues (1999) found a posterior-anterior rotational acceleration limit of 71,200 rad/s^2 at a 3.5 ms pulse duration by combining the results of their 3D finite element head impact simulations with the same tensile failure tests from Lee and Haut (1989). Of note, tolerance level clearly decreases for longer pulse durations. However, large differences in the testing approach could account for the variability in results seen in these studies. The severe morbidity and mortality rate associated with ASDH originating from bridging vein failure necessitates thorough investigation of the bridging veins, a logical first step

in developing tolerance criteria for ASDH. However, experimental observations lack repeatability and are potentially highly affected by factors such as vessel collection, test setup, and postmortem factors and FE model simulations rely on the validation from these experimental tests and still lack the proper representation of the bridging veins.

1.4 Literature Review on Experimental Studies

1.4.1 Recreating Acute Subdural Hematoma

Both in vivo animal studies (Ommaya et al., 1968; Gennarelli and Thibault, 1982) and PMHS impact studies (Löwenhielm, 1974; Deprietere et al., 2005; Deprietere et al., 2006) have reported the relationship between gross head kinematics and the risk of ASDH under anterior-posterior rotation. Ommaya and colleagues (1968) produced subdural hematoma in rhesus monkeys by simulating a rear impact, postulating that brain injury in humans would be in the order of 6,000-7,000 rad/sec^2. In a subsequent review of this work, it was reported that subdural hematoma was produced with rotation at 8.73 rad/sec and 10,000 rad/sec^2 for a 5-6 ms duration (Ommaya et al., 2002). Gennarelli and Thibault (1982) also produced subdural hematomas in rhesus monkeys by applying anterior-posterior accelerations in a 60-degree arc with pulse durations varying between 5 and 25 ms, which produced visible bridging vein damage. Figure 2 shows the rotational acceleration inputs that resulted in ASDH, concussion, and diffuse axonal injury (DAI).

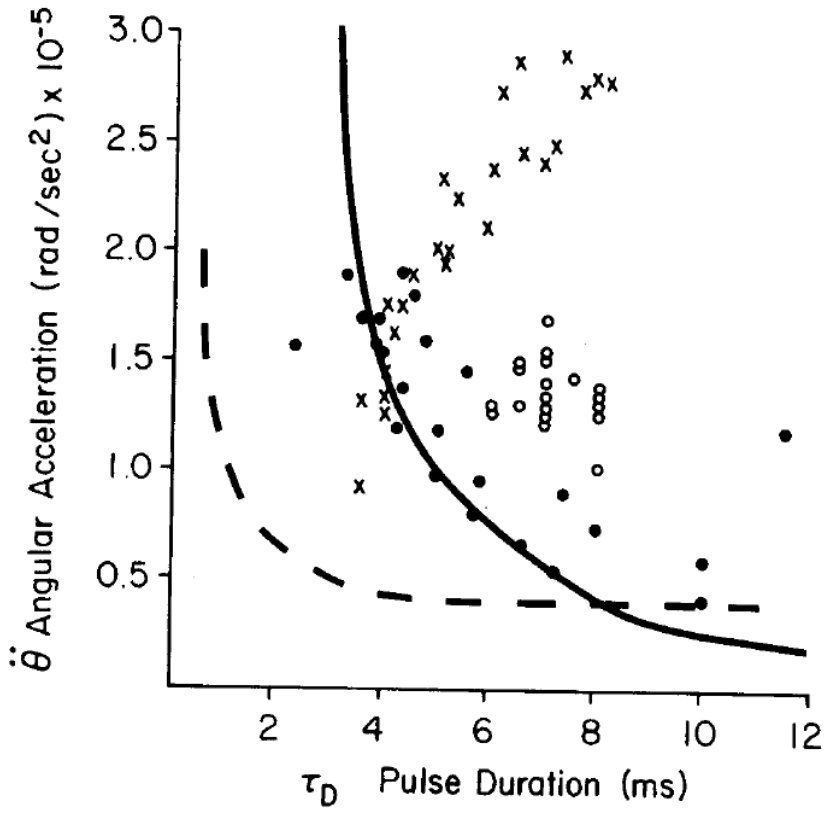

Figure 2: Angular acceleration and pulse duration induced head injury from Gennarelli and Thibault (1982). Instances of subdural hematoma are designated by the crosses, concussion by the closed circles, and DAI by the open circles

There is a distinction between the three major injury types given certain values of rotational acceleration and pulse duration. At pulse durations less than 5 ms and below 175 krad/sec^2, there was evidence of both subdural hematomas and cerebral concussion. As the pulse duration increased but rotational acceleration was held constant, ASDH did not occur. ASDH was more likely to occur at shorter pulse durations. Further scaling of these results estimated human injury limits of 12,500 rad/sec^2 (Newmann, 1998).

Additional efforts have investigated the recreation of ASDH in PMHS. Löwenhielm (1974) performed a series of head-on collision experiments with whole cadavers and concluded a maximum tolerable rotational acceleration of 4,500 rad/sec^2 for pulse durations between 15-44 ms (Figure 3).

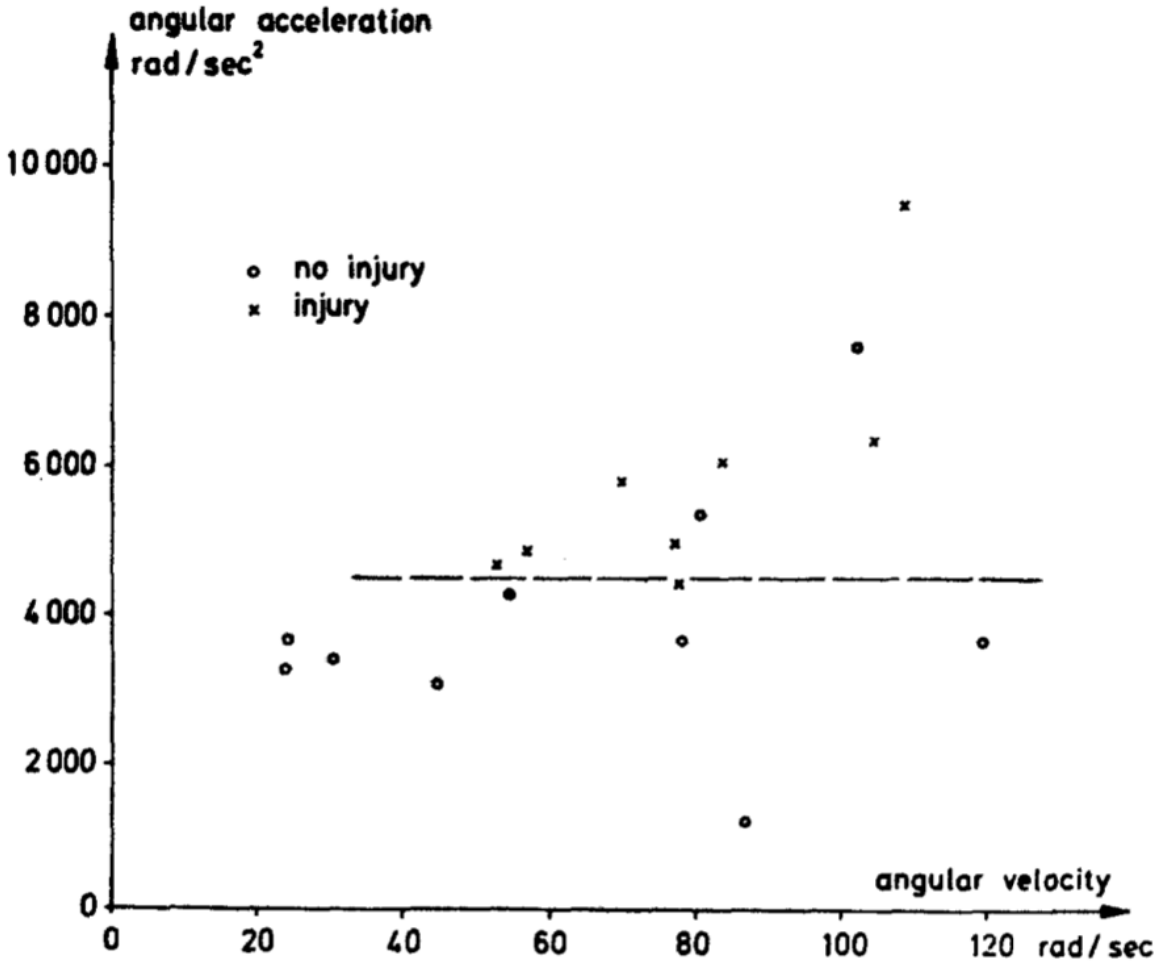

Figure 3: Maximum angular acceleration versus change in angular velocity from Löwenhielm (1974)

For pulse durations shorter than 10 ms, Deprietere and colleagues (2005, 2006) stated a maximum tolerable rotational acceleration of 10,000 rad/sec^2 based on experiments in which human cadaver heads were impacted by a pendulum.

Discrepancies in proposed tolerances to bridging vein failure are likely due to differences in experimental methodologies as well as the type of subject used (animal versus PMHS). Additionally, there are several confounding variables, including variables not accounted for in these studies, such as the postmortem time at which testing occurred and the brain parenchymal fraction (BPF) of the PMHS used. These studies published proposed tolerances to bridging vein failure by recreating injury; however, brain motion at the periphery was not quantified. Therefore, to better understand the relationship between input kinematics and superficial brain motion relative to the skull, additional investigation is required.

1.4.2 Quantifying Brain Motion

A larger subset of brain research has been focused on quantifying whole-brain motion. Documented research on relative motion between the brain and skull started as early as 1944 with studies looking at the direct, qualitative motion of the brain through transparent caps that replaced parts, or all, of the skull and dura in rhesus monkeys (Sheldon et al., 1944; Pudenz and Sheldon, 1946; Gosch et al., 1970). More recently, Ibrahim and colleagues (2010) reported in situ strain measurements of brain deformation during rapid, nonimpact head rotation in piglets, though data at the brain-skull interface were not included. Moreover, direct observational studies of motion at the surface of animal brains removed the boundary condition of the meningeal layers, and the literature remains unclear how the motion of an animal brain correlates to the brain motion seen in humans.

Radiographic studies of brain motion have utilized x-rays to track radiopaque makers and intravascular contrast fluid using both animal surrogates and PMHS. Hodgson and colleagues (1996) used intravascular contrast fluid and lead targets to track brain motion in anesthetized dogs subjected to impact. Results of this study suggest a shearing response of the brain, and the targets returned to their original positions suggesting that the brain underwent elastic deformation during this loading scenario. Additional radiographic studies of animal brains have revealed motion of surface-level brain vessels in addition to cortex displacements in the order of 2-3 mm (Sass et al., 1971; Shatsky et al. 1974).

Other researchers have utilized x-ray of lead markers in a series of impacts to study the motion of the brains of PMHS. Stalnaker and colleagues (1977) found that vascular and cerebrospinal repressurization greatly increased the coupling between the brain and skull, providing a more rigid response of the head. In addition, Nusholtz and colleagues (1984) introduced neutral density radiopaque gel into the brain tissue and ventricles. High-speed x-ray revealed only an internal distortion of the cortex tissue. No differential motion between the brain and skull was found except for a case involving skull fracture, where the relative motion of the brain with respect to the skull was reported to be in the order of 6 mm. This adhesion of the brain to the skull was described as a "stick-slip" condition, allowing relative motion at the surface only when the local skull acceleration from fracture could initiate this relative brain motion.

Most notably, a comprehensive study using high-speed, biplanar x-ray to track neutral density targets implanted within the brain tissue by Hardy and colleagues (2001, 2007) quantified three-dimensional, whole-brain displacement during rapid deceleration in inverted, repressurized cadaver heads resulting in head linear accelerations ranging from 38 to 291g, rotational velocities from 4 to 30 rad/sec and rotational accelerations from 2,370 to 24,206

rad/sec^2. Though tracking targets were generally inserted deeper in the brain, there were reported results for a tracking target near the surface of the cortex that displaced between 9 to 11 mm relative to the skull, and a marker approximately 10 mm into the cortex that displaced 2 to 3 mm relative to the skull. This discrepancy resulted in the conclusion that relative motion at the cortex required further investigation. In an analysis of the results from Hardy and colleagues' (2001) tests, Zou and colleagues (2007) reiterated this conclusion, cautioning that the rigid body motion results are unable to predict brain motion at the boundary between the brain and skull. While radiographic studies of motion in trauma level loading have tracked motion near the surface of the brain, they have lacked the resolution to differentiate motion of the meningeal layers from deformation deeper in the cortex.

As an alternative to high-speed radiography, Alshareef and colleagues (2018, 2020) proposed a novel methodology of implementing sonomicrometry crystals into the brain cortex to quantify deformation in response to various dynamic rotational pulses. PMHS were subjected to rotations in a single plane at either 20 or 40 rad/sec at pulse durations of either 30 or 60 ms. In the most severe case (40 rad/sec, 30 ms duration), the average peak displacements were in the order of 4 to 5 mm, while the maximum peak displacement was approximately 13 mm. While this study tracked motion deeper in the brain, the results closer to the surface of the brain were limited, and motion between the surface of the brain and the meningeal layers or dura was not quantified.

Advancements in magnetic resonance (MR) imaging have offered the opportunity to non-invasively measure brain motion in healthy volunteers. Brain motion ranging from less than 0.3 to 5 mm during normal pulsatile cardiac cycles has been reported, where the magnitude varied by brain region and was relatively small near the surface of the cortex (Poncelet et al., 1992; Maier

et al., 1994; Zhong et al., 2009). MR imaging has also captured brain motion relative to the base of the skull during flexion, with results yielding between 1 and 3 mm (Ji et al., 2004). Most notably, a series of MR studies have documented quantitative values for large displacements deep in the cortex with smaller relative motion near the surface of the cortex during mild head deceleration of 2-3 g in healthy volunteers (Bayly et al., 2005). Points along tag lines on the images were tracked and strain was estimated to be between 0.02-0.05. Subsequent work included angular acceleration, demonstrating that the brain "slides" relative to the skull, with the tangential motion of the brain surface being constrained by the skull and larger displacements were observed deeper in the cortex (Feng et al., 2010). Though volunteer studies of response to low severity impacts have come closer to tracking motion near the surface of the brain than postmortem studies, MR imaging is limited near the skull. It cannot capture motion right at the surface of the brain or between individual meningeal layers, and volunteer studies cannot predict response to trauma-level severity.

As indicated previously, testing with PMHS is one method used to study the mechanisms of traumatic brain injury resulting from motor vehicle crashes. However, a major limitation that affects brain research is the rate at which brain tissue degrades postmortem, as the properties of brain tissue are known to change after death. Stalnaker and colleagues (1977) described noticeable brain tissue degradation in whole-body tests, with excessive brain motion noted after periods longer than 4 days. Results from studies of isolated brain tissue have varied, with some studies showing stiffening up to 10 hours after sample collection (Rang et al., 2001; Garo et al., 2007; Hrapko et al., 2008). Other studies have shown either little difference in postmortem stiffness (Metz et al., 1970; Shen et al., 2006), documented reduced tissue stiffness at 3-4 hours postmortem up to 3 days postmortem (Bentil and Dupaix, 2013; Nicolle et al., 2004), or

softening over longer postmortem delays from 6 hours to 16 days (Darvish and Crandall, 2001). The results of these studies are conflicting, which may be attributed to the differences in test techniques, preparation methods, storage temperatures, and the use of either animal models or PMHS. However, it can be concluded that brain tissue stiffens in the hours immediately after death and then softens as postmortem time increases.

Additional studies have indicated that in as little as 12 hours, brain tissue at room temperature becomes unreliable for both mechanical and material property testing (Rashid et al., 2013). However, it has also been reported that cooler storage temperatures can slow the postmortem degradation of brain tissue (McElhaney et al., 1973; Puymirat et al., 1979; Darvish and Crandall, 2001; Ferrer et al., 2007; Zhang et al., 2010) and specifically reduce the drop in stiffness that occurs in the hours and days after death (Hrapko et al., 2008; Rashid et al., 2013). Rashid and colleagues (2013) performed tests in which porcine brain tissue samples were stored at three different preservation temperatures: ice cold (6°C), room temperature (22°C), and body temperature (37°C). The samples were tested in shear within 5 hours postmortem, and it was concluded that a 4-5°C preservation temperature was needed to minimize the differences between in vitro and in vivo porcine brain samples. It was also concluded that varying the tissue temperature between room temperature and body temperature did not contribute to the tissue response under compression, given that the tissue had been preserved at ice-cold temperature before testing. This same conclusion was drawn by Puymirat and colleagues (1979) after studying the influence of storage at deep cold temperatures. It was concluded that enzyme deterioration slowed at 4°C, and at this temperature with minimum postmortem delay, brain tissue can be used for reliable biomechanical measurements until 48 hours postmortem. Peters and colleagues (1997) conducted dynamic stress relaxation measurements on brain tissue

samples at five different temperatures between 7 and 37°C and determined that in the range studied, the time/temperature superposition principle is applicable to brain tissue. While this information is useful, there are still gaps regarding how whole-brain degradation is affected by the temperature at which it is stored and tested.

1.4.3 Modeling Studies

Finite element (FE) models are powerful tools that can be used to evaluate injury risk. Capturing the anatomical complexity of the brain in a model is proving essential in estimating injury tolerance and given the prevalence of head injuries in MVC, it is crucial that the complex geometry and mechanical properties of the brain are captured in these models. Obviously, depending on the geometry and material definition in the models, different models will yield different results. Notable FE head models that include bridging veins are the Shugar (1977) model modified by Huang (1999), the simulated injury monitor (SIMon) head model (Takhounts et al., 2008), the KTH FE head model (Kleiven et al., 2002), the Wayne State University Brain Injury Model (WSUBIM) (Zhou et al., 1995), and the global/local head model (Zoghi-Moghadam et al., 2009).

Some of these models have specifically investigated ASDH that occur because of the tearing of bridging veins. The Shugar model adopted by Huang (1999) used an indirect approach to approximate the measure of bridging vein deformation. The interface between the brain and skull was tied and CSF was not modeled, so the distance between a node in the brain and a node on the skull was used to approximate BV strain.

The KTH model created by Kleiven and colleagues (2002) contains 11 pairs of parasagittal BVs that were modeled according to the anatomical description given by Oka and

colleagues (1985). Zhou and colleagues (2019) utilized three versions of the KTH model with varying brain sizes and concluded that brain atrophy leads to increased cortical relative motion and increased strain on the bridging veins resulting in a higher risk of ASDH in the elderly. This model simulated the brain-skull interface by representing the cerebrospinal fluid (CSF) as arbitrary Lagrangian-Eulerian (ALE) multi-material fluid elements. Though the most common approach is to model the CSF as a soft solid material with low shear modulus (Madhukar et al., 2019), subsequent work by Zhou and colleagues (2020) concluded that CSF should be modeled as ALE elements with a sliding interface against the brain for models to be able to accurately predict ASDH risk.

Zoghi-Moghadam and colleagues (2009) proposed the global/local head modeling approach specifically to study bridging vein rupture in more detail. A global solid model was constructed based on the FE head model proposed by Horgan and Gilchrist (2003) and calculates the stresses and strains in the brain. A global fluid model of the CSF and subarachnoid space, in which the skull and brain are given rigid boundaries, is used to calculate the change in fluid pressure of the CSF. The outputs of the global models were then used to create a more detailed local solid model which outputs the strain of the bridging veins.

Validation of these numerical models against experimental data is a crucial step in ensuring the model is producing accurate results. Historically, FE models of the head are validated using intracranial pressure (ICP) data and/or brain displacement data. Nahum and colleagues (1977) recorded intracranial pressure history data during linear impacts to seated cadavers, and this pressure history is utilized in verifying results obtained from numerical models. Experiments that have provided validation data for many numerical models include Hardy and colleagues' (2007) neutral density target testing, Alshareef and colleagues' (2020)

sonomicrometry testing, and/or displacement data from tagged MRI experiments (Bayly et al., 2010; Feng et al., 2010).

1.5 Existing Head Injury Metrics

In general, the development of injury criteria for the brain has been correlated to injuries to the skull. Early work by Gurdjian and colleagues (1995) concluded that linear acceleration is a good predictor of brain injury, though notably 80% of those injury cases were accompanied by linear skull fractures. Plotting the effective linear acceleration of the head versus the impact duration of these results yielded the Wayne State Tolerance Curve (Lissner et al., 1960) (Figure 4).

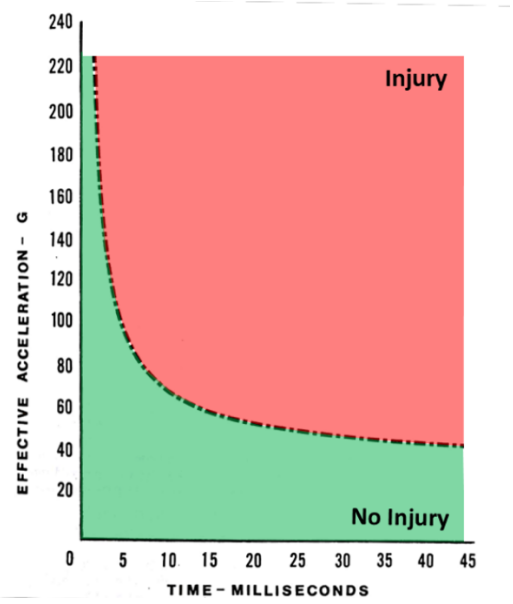

Figure 4:Wayne State Tolerance Curve

The most used criterion is the Head Injury Criterion (HIC), which was developed from the Wayne State Tolerance Curve, is based on the translational acceleration of the head and disregards rotational acceleration, impact force, and directional dependency. The calculation of HIC is given by Equation [1]:

$$HIC = \left\{(t_2 - t_1)\left[\frac{1}{(t_2-t_1}\int_{t_1}^{t_2} a(t)dt\right]^{2.5}\right\}_{max} \quad [1]$$

where a(t) is the resultant translational head acceleration and t_1 and t_2 are the initial and final times of the interval selected to maximize the HIC value. The National Highway Traffic Safety Administration (NHTSA) has incorporated HIC in regulation for motor vehicles to account for head injuries sustained by crash occupants during vehicle impacts. Under automotive standards, a 15 ms pulse is used, and a HIC_{15} value of 700 is the threshold limit for the 50th percentile male (Eppinger et al., 1999). However, HIC does not take the rotational motion of the head into consideration and was developed specifically for skull fractures; thus, multiple brain injury formulations that include rotational kinematics have been proposed to quantify brain injury risk.

In as early as 1943, it was proposed that the rotational motion of the head leads to closed head brain injuries (Holbourn, 1943). More specifically, Gennarelli and colleagues (1972) concluded that purely translational motion could not induce ASDH. Proposed as an extension to HIC, Newman and colleagues (1998) proposed the Head Injury Power (HIP) criterion, which calculates the sum of the mechanical energy per unit of time along each degree of freedom of the head. The calculation of HIP is given by Equation [2]:

$$HIP = ma_x \int a_x dt + ma_y \int a_y dt + ma_z \int a_z dt + I_{xx}\alpha_x \int \alpha_x dt + I_{yy}\alpha_y \int \alpha_y dt + I_{zz}\alpha_z \int \alpha_z dt \quad [2]$$

Where m is the mass, a_i is the translational acceleration, α_i is the rotational acceleration, and I_{ii} is the moment of inertia.

Kleiven and colleagues (2002) proposed the Power Index (PI) and more specifically the PI for predicting ASDH, which adds directional sensitivity to the HIP by adding scaling coefficients and differentiating between positive and negative accelerations. The scaling factors were established by comparing the maximum strain values found in the bridging veins during FE simulations (Kleiven, 2003). Results from this study indicated how anterior-posterior rotations result in the greatest strain on the bridging veins, making this type of rotation the most relevant for investigating ASDH from bridging vein failure.

As a more general injury criterion for the application of automotive safety assessment, the Brain Injury Criterion (BrIC) was developed as a correlate to the cumulative strain density measurement (CDSM) and maximum principal strain (MPS) (Takhounts et al., 2013). The calculation of BrIC is given by Equation [3]:

$$BrIC = \sqrt{\left(\frac{\omega_x}{\omega_{xC}}\right)^2 + \left(\frac{\omega_y}{\omega_{yC}}\right)^2 + \left(\frac{\omega_z}{\omega_{zC}}\right)^2} \quad [3]$$

BrIC is calculated as the resultant of the three-component axes of head angular velocities which are weighted by critical values determined by simulations using the SIMon FE head model (Takhounts et al., 2013). Apart from the PI for predicting ASDH, the injury criteria described above are not able to capture the injury risk of sustaining ASDH.

1.6 Research Aims

The goal of this dissertation is to quantify superficial brain displacements relative to the skull under a variety of anterior-posterior rotational loading severities. Despite robust efforts on understanding whole-brain motion, there exists a large gap in the research concerning surface-level brain motion. Not only is characterizing relative brain motion between the surface of the cortex and the skull imperative for understanding ASDH, but these data are also necessary for the validation of human body models due to the lack of availability of such data. As mentioned above, there are significant limitations associated with recreating injury using PMHS. Instead, brain motion under anterior-posterior rotation will be compared against published tolerances of bridging vein failure. As a first step towards relating relative brain motion and probability of ASDH, surface-level brain motion must be collected under a variety of loading scenarios using a validated measurement technique. Therefore, the specific aims for this work are as follows:

- Validation of high-frequency brightness mode (B-mode) ultrasound that rotates with the head as a measurement technique for quantifying surface-level brain motion under high-rate, rotational motion
- To quantify surface-level relative brain motion between the cortex and skull under a variety of loading conditions to provide novel data for the further validation of human body models

Chapter 2: Epidemiology of Subdural Hematoma

Trauma is the most common cause of death for those under the age of 45, with traumatic brain injury (TBI) being the cause of approximately one-half of the deaths secondary to trauma (Wilson et al., 2014; Fountain et al., 2017; CDC 2021). Approximately 1,700,000 people sustain a traumatic brain injury each year, with motor vehicle crashes (MVC) being a leading cause of hospitalization from TBI (Faul et al., 2010; Urban et al., 2012; Taylor et al., 2017).

Patient age has been shown to be a strong predictor of morbidity and mortality following severe closed head injury, with 65 years determined as the threshold for increased vulnerability (Vollmer et al., 1991; Mosenthal et al., 2002; Coronado et al., 2005; Stitzel et al., 2008; Mallory et al, 2010). In MVCs, the percentage of elderly occupants that die or suffer long-term disability is significantly higher given similar crash severity (Pentland et al., 1986). Individuals over the age of 65 are the most likely age group of the population to be hospitalized for TBI from any cause (Coronado et al., 2005; Taylor et al., 2017). Of these individuals, falls and MVCs are the two leading causes of head injury (Guerrero et al., 2000; Jager et al., 2000; Coronado et al., 2005; Fletcher et al., 2007).

2.1 Acute Subdual Hematomas Among Motor Vehicle Crash Occupants

Intracranial bleeding is a common and serious consequence of traumatic brain injury, with acute subdural hematoma (ASDH) identified as being especially lethal among bleeding head injuries (Seelig et al., 1981, Marshall et al., 1991, Mallory, 2010; Fountain et al., 2017).

Historically, outcomes have been worse for patients diagnosed with ASDH with mortality rates that have been cited as high as 68% (Seelig et al., 1981; Gennarelli et al., 1982; Bullock et al., 2006; Sawuchi et al., 2008; Taussky et al., 2008; Fountain et al., 2017). As an individual ages, the dura and skull become more tightly coupled, resulting in an increased susceptibility to bleeding head injuries (Stizel et al., 2008). Additionally, due to age-related atrophy, the brain volume of older individuals decreases, resulting in increased subdural space around the brain leading to greater initial bridging vein stretch (Smith et al., 2007; Stitzel et al., 2008, Vågberg et al., 2017). Combined with increasing stiffness of vessels in the elderly and the increased susceptibility of injury, the elderly possesses an increased risk to bleeding head injuries under rotational loading.

Age-related increases in ASDH being more frequent in frontal impacts are consistent with the studies that indicated anterior-posterior motion as the loading mechanism for ASDH resulting from bridging vein failure (Ommaya et al., 1968; Löwenhielm 1974; Gennarelli et al., 1982; Depreitere et al., 2006). This is consistent with reports that older individuals are more prone to subdural hematoma by bridging vein failure due to the increased relative brain motion and bridging vein tension caused by atrophy in the aging brain (Yamashima et al., 1984; Meany 1991; Kleiven et al., 2002).

The severity of a subdural hematoma is quantified during brain imaging examination by volume or width, which has been indicated as the most significant prognostic quality (Seelig et al., 1981; Urban et al., 2102; Walcott et al., 2014). The associated pathology of ASDH includes cerebral edema and increased intracranial pressures, with severity of ASDH increasing with the presence of a midline shift (Wilberger et al., 1991; Chiewvit et al., 2010; Urban et al., 2012; Zafrullah Arfin et al., 2013). Previous studies have indicated age, Glascow Coma Scale (GCS),

Injury Severity Scale (ISS), and pupil index as independent prognostic factors (Mallory et al., 2010; Fountain et al., 2017). Multiple factors are considered when determining the severity of an injury including threat to life, permanent or temporary disability, tissue damage, treatment complexity, length of recovery, quality of life lost, and cost. The Abbreviated Injury Scale (AIS) is used to quantify injury severity ranging from minor (AIS 1) to maximal (AIS 6) (AAAM, 2015). The lowest ASDH AIS severity code is a 3, representing serious threat to life even for a very small subdural hematoma (<0.6 cm thick). The maximum AIS score recorded for ASDH is a 5, representing very critical threat to life for a large or bilateral hematoma (>1 cm thick) (Stitzel et al., 2008).

2.2 Analysis of Head Kinematics During Motor Vehicle Crashes

To provide real-world context for the selection of the rotational kinematics to be used during fresh subject testing (Chapter 4), a variety of experimental and real-world data sources were analyzed. The search criteria for each of these data sources was limited to looking at only frontal impacts, which is most relevant to the experimental setup of anterior-posterior rotation in the sagittal plane, which corresponds to the most common direction of brain rotation resulting in bridging vein failure according to the literature (Ommaya et al., 1968; Löwenhielm 1974; Gennarelli et al., 1982; Depreitere et al., 2006). A CIREN database review was conducted to understand typical scenarios where occupants are sustaining ASDH in real-world frontal crashes with airbag contact as well as harder contact surfaces. Then, to understand the typical range of angular kinematics of the head that occur during crash and sled tests in these kinds of crash scenarios, the National Highway Traffic Safety Administration (NHTSA) vehicle database was searched for frontal crash tests that had rotational head kinematic data available. Additionally, PMHS sled test data were investigated for additional head kinematic data from FMVSS208 crash

scenarios with head-airbag interaction. The final dataset for comparison included head kinematics from experimental studies in the literature. Studies that have recreated acute subdural hematoma have indicted some ranges where experimental evidence consistent with injuries have been documented.

The CIREN database review signified what kinds of head contacts are associated with subdural hematomas in real-world crash scenarios. Frontal impacts were broadly defined as the principal direction of force (PDOF) of 11 to 1, as well as cases where the PDOF was between 10 and 2 if the general area of damage was to the front of the vehicle. By that definition, of the 278 subdural hematoma cases, 101 occurred because of a frontal impact. Of those 101 tests, there were 5 instances in which the head contact point was unknown, 22 cases where the head contact was with the airbag, and 4 cases were defined as “non-contact” injuries. Of the remaining 74 subdural cases, the contact locations are shown in Figure 5, where the contact location is organized from most frequent to least frequent moving counterclockwise.

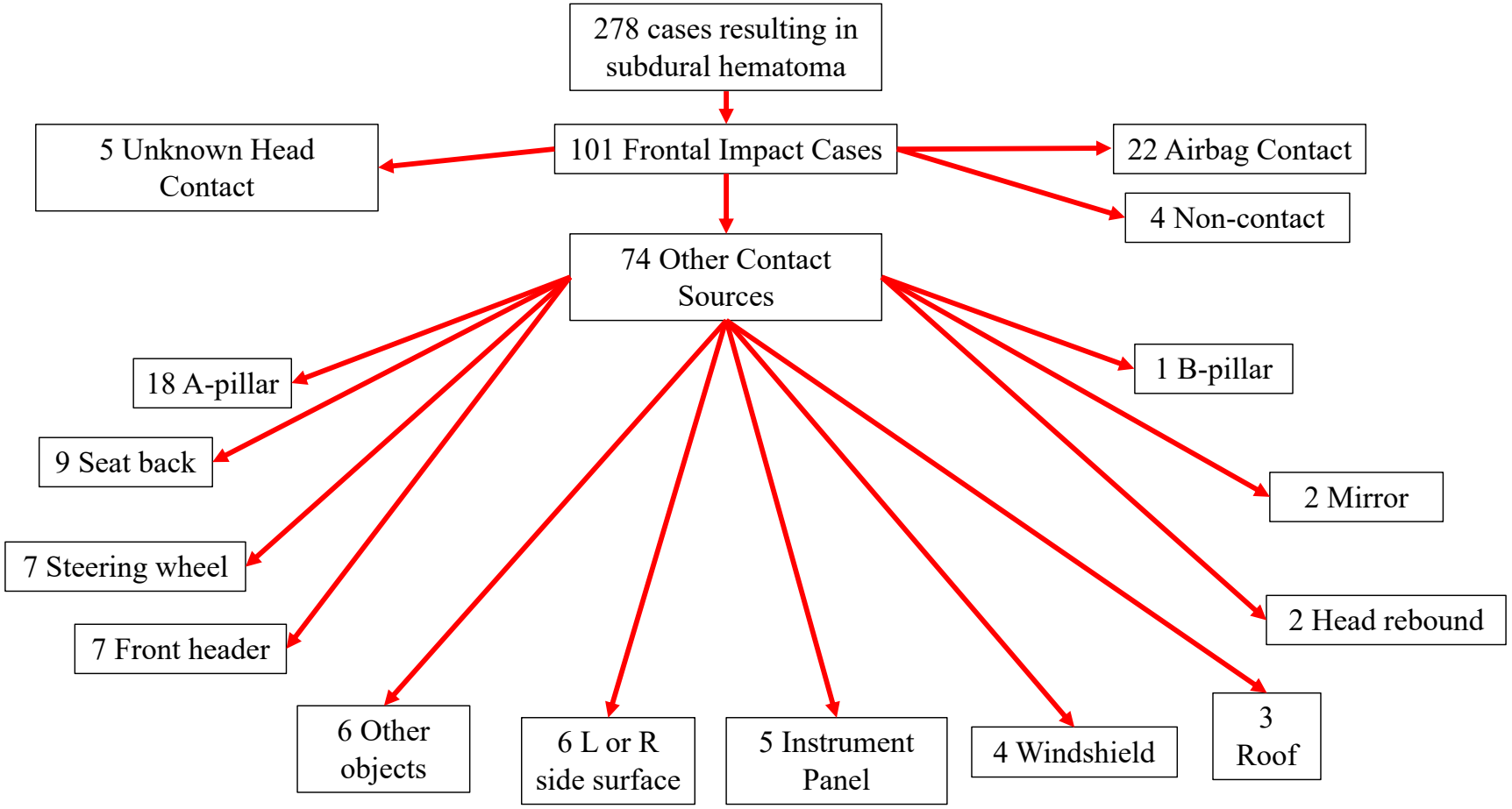

Figure 5: Head contact locations in the case of subdural hematoma from CIREN cases

The most frequently contacted surface was the A-pillar which occurred about 24% of the time in frontal crashes where a subdural hematoma occurred, consistent with reports in the literature (Urban et al., 2012). Also of note, 24% of subdural hematomas that occurred were airbag or non-contact injuries.

The NHTSA vehicle database search resulted in frontal crash tests with anthropomorphic test devices (ATD) head kinematic data that included nine-accelerometer arrays so that head angular acceleration could be accurately calculated. Three different types of tests were included: offset oblique, small overlap, and car-to-car crashes. In all instances, the THOR 50th percentile male, Hybrid III (HIII) 50th percentile male, and/or the HIII 5th percentile female ATDs were used, where one ATD was seated in the driver's seat, and one was seated in the front passenger's seat. The database provided information on what surfaces the head contacted in the vehicle which were separated into airbag, and non-airbag contact surfaces. The search criteria for the NHTSA database review are summarized in Figure 6.

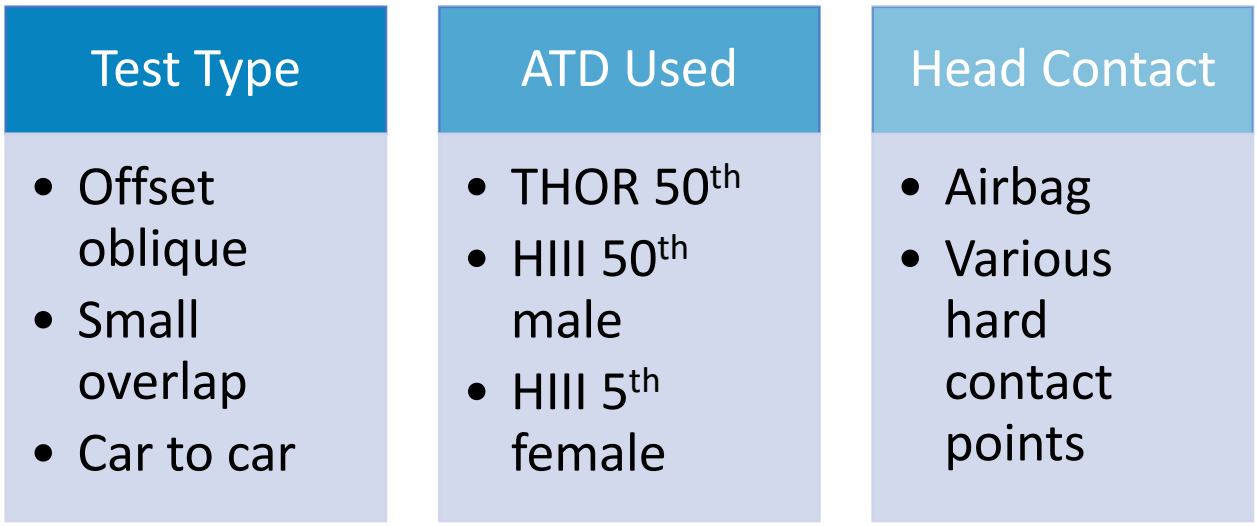

Figure 6: Summary of NHTSA database search criteria

The ATDs were instrumented with a nine-accelerometer array package, and rotational kinematic data about the y-axis was chosen for further analysis as it corresponds to what is measured during the fresh subject experimental tests; anterior-posterior rotation in the sagittal plane.

For the PMHS sled tests that were looked at to quantify additional head kinematic data from FMVSS 208 crash scenarios with head-airbag interaction, the original objective was to evaluate a modified restraint system designed for the elderly as compared to a current restraint system using elderly PMHS with ages ranging from 70 to 94 years (Kang et al., 2017). The experimental setup included a dual chamber driver air bag, adaptive seat belt, and knee air bags. Tests were conducted using ten 40th percentile PMHS aged 65 and up with a BMD below -1,

indicating osteopenia. Head kinematics were collected using six accelerometers and three angular rate sensors (Kang et al., 2015), resulting in six degrees of freedom head kinematics for each test (Figure 7).

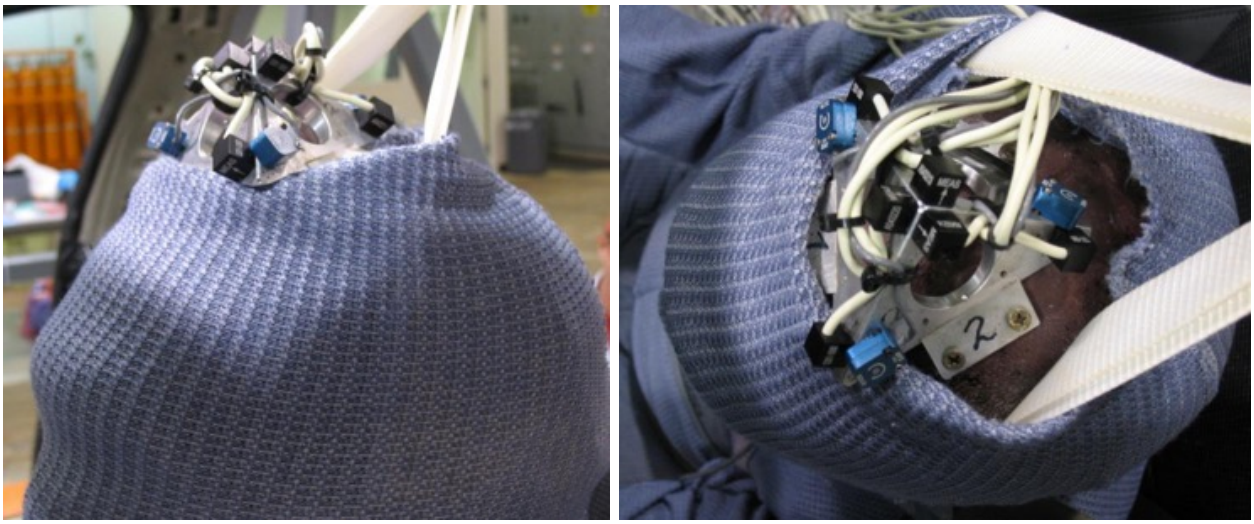

Figure 7: Tetrahedron for capturing 6 degrees-of-freedom head kinematics

Several experimental studies have proposed rotational severity thresholds for obtaining a subdural hematoma as described in Chapter 1.

2.3 Implications of Epidemiological Studies

Rotational acceleration, rotational velocity, and their corresponding time durations were collected from the NHTSA crash data, PMHS sled tests, and the experimental data from the

literature. The rotational acceleration data versus the time duration of the loading is shown in Figure 8, and the rotational velocity versus the time duration is shown in Figure 9.

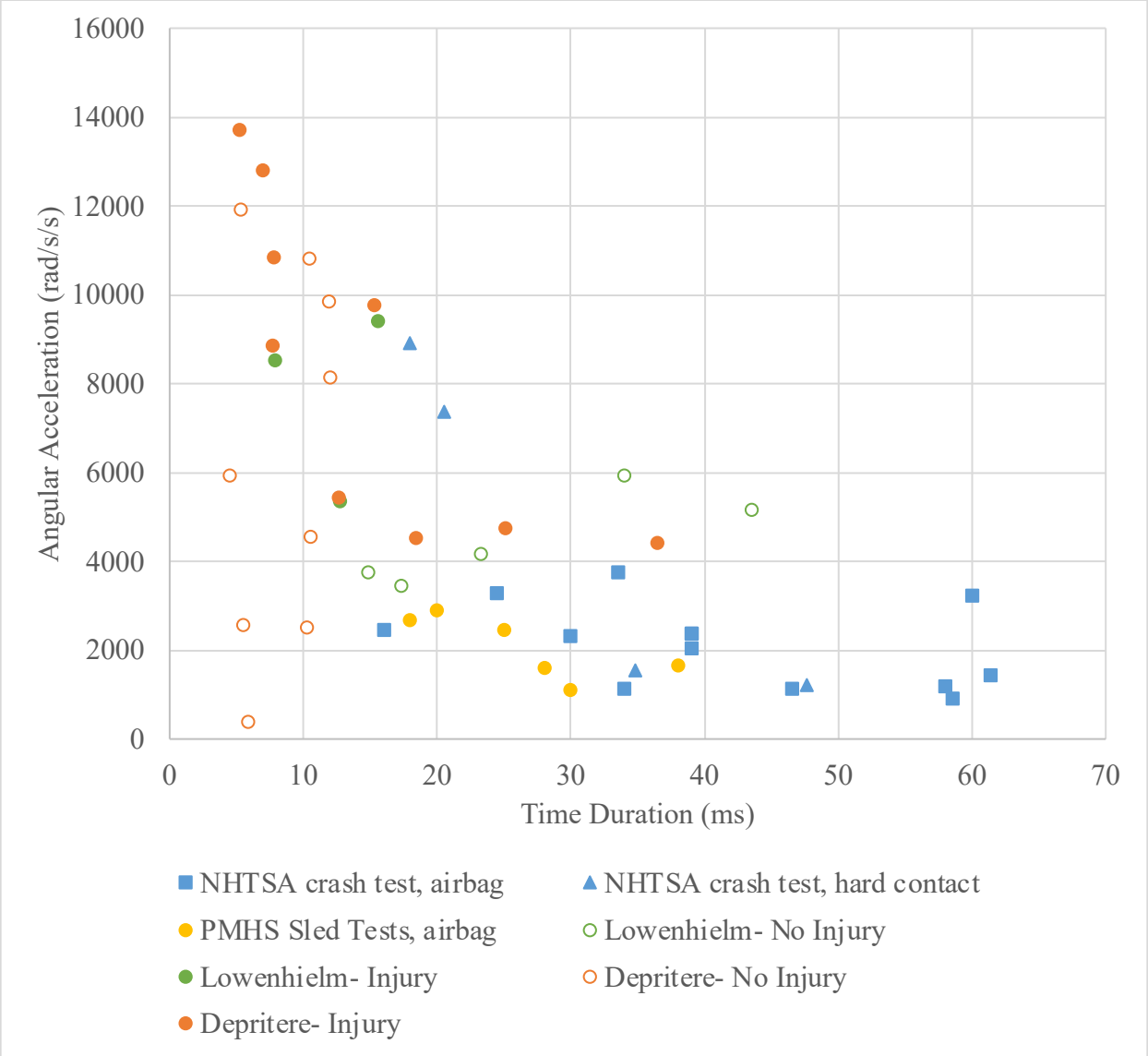

Figure 8: Comparison of rotational acceleration data from multiple data sources

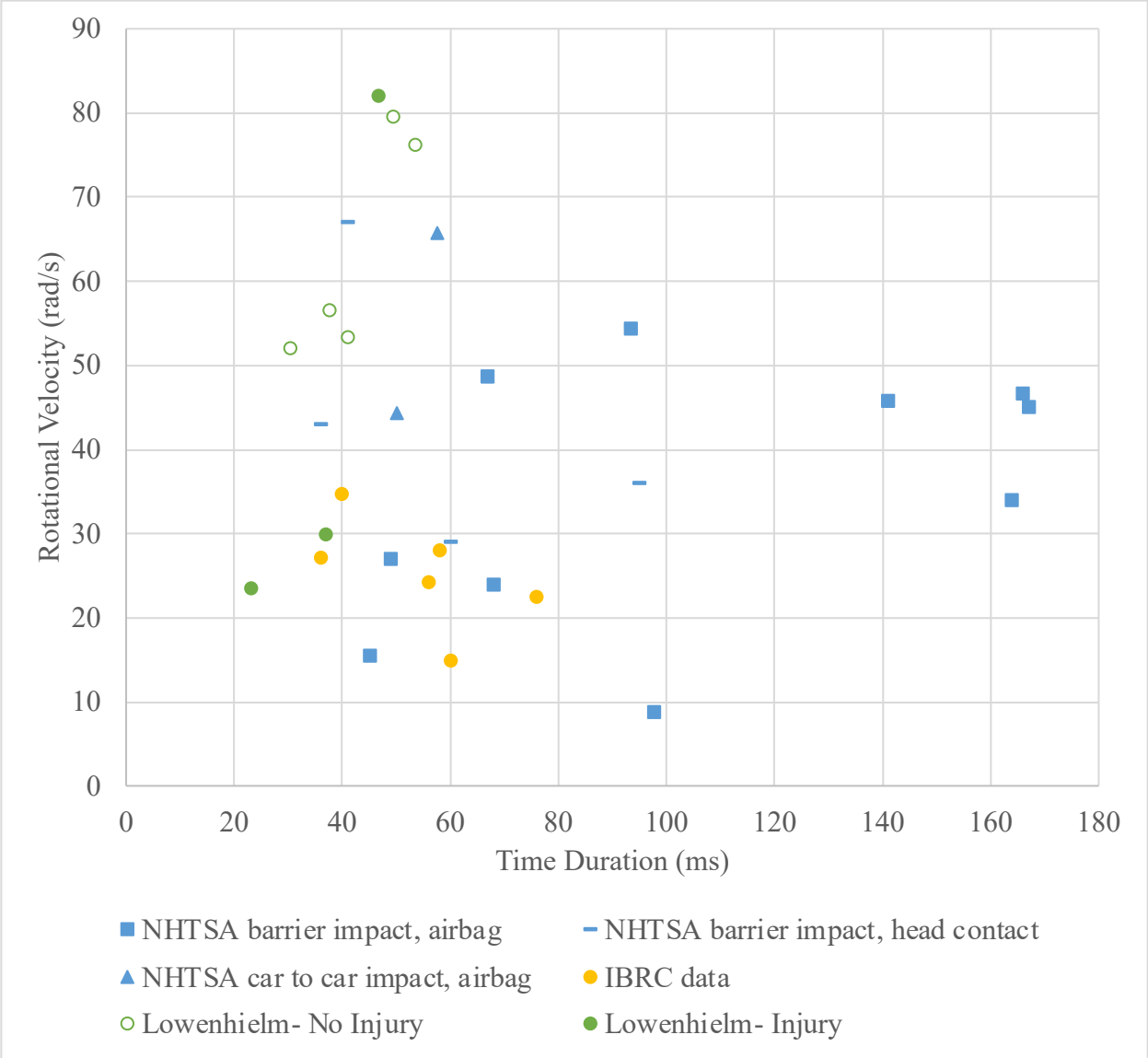

Figure 9: Comparison of rotational velocity data from multiple data sources

Visualization of scenarios where subdural hematomas have been shown to occur in combination with real-world pulses that are known to occur during motor vehicle crashes helped to inform test matrix decisions as described in Chapter 4: PMHS Testing to Quantify Relative Surface Level Brain Motion. Based on the analysis of the initial CIREN review cases, ideally test

conditions should include rotational kinematics consistent with airbag interactions as well as contacts to harder surfaces.

Chapter 3: Validation of the Ultrasound Measurement Technique

3.1 Validation Background and Significance

Ultrasound has been an increasingly popular tool used widely for diagnostic and therapeutic applications as it allows for the non-invasive visualization of tissue structures in real time. Due to its advantages of noninvasiveness and fine resolution, a unique application of ultrasound is for it to be used as a measurement device in injury biomechanics experimental testing. In general, the ability to quantify the internal organ response, such as the superficial motion of a postmortem human subject's brain during rotational loading, is limited by the scarcity of non-invasive imaging approaches with the ability to distinguish between tissue layers near the superficial brain. To obtain quantitative data at the surface of the brain requires the validation of an ultrasound probe as a lateral measurement system under trauma level loading.

Previous attempts to quantify human brain motion have included the insertion of accelerometers directly into the brain (Trosseille et al., 1992) and more recently the implementation of sonomicrometry crystals into the brain cortex to quantify deformation in response to dynamic rotational pulses (Alshareef et al., 2018, 2020). Radiographic studies have utilized x-rays to track radiopaque markers and intravascular contrast fluid in the postmortem human brain (Hodgson et al., 1966; Shatsky et al. 1974; Nusholtz et al., 1984; Hardy et al., 2007). These efforts have quantified deeper brain motion, but results of brain motion near the surface of the brain were limited and the measurement techniques utilized were invasive, which could be considered a limitation of those studies as motion near the surface of the brain was not

quantified. There have been additional efforts to utilize non-invasive measurement techniques to minimize the disruption of realistic boundary conditions. Advancements in magnetic resonance (MR) imaging have offered the opportunity to non-invasively measure brain motion in healthy volunteers. Most notably, a series of MR studies documented quantitative values for large displacements deep in the cortex with smaller relative motions near the surface of the cortex (Bayly et al., 2006; Feng et al., 2010). While volunteer studies of response to low severity impacts have come closer to tracking motion near the surface of the brain than postmortem studies, MR imaging is limited near the skull because it cannot capture motion right at the surface of the brain or between individual meningeal layers. Additionally, volunteer studies cannot predict response to trauma-level severity.

Specifically, ultrasound has been a proposed measurement technique to avoid the invasiveness of measurement systems such as x-ray and the implementation of sensors directly into the brain cortex. Non-invasive measurement techniques such as ultrafast ultrasound have been used to track the response of abdominal organs, though compression was only measured in the direction of impact (Beillas et al., 2013; Helfenstein-Didier et al., 2015; Le Ruyet and Beillas, 2015). The shear motion of superficial brain tissue and the meningeal layers has been tracked using two-dimensional, high frequency, brightness mode (B-mode) ultrasound (Mallory, 2014). High frequency, B-mode ultrasound can produce two-dimensional (2D) images at frame rates up to 1000 frames per second at axial resolutions up to 40 microns. At this resolution, B-mode ultrasound offers the potential to differentiate between the meningeal layers at the surface of the brain. The use of high frequency, B-mode ultrasound in a stationary, off-board orientation has been validated as a measurement technique to quantify superficial brain motion between 0.19 and 2.29 m/s (Mallory et al., 2018). However, as the stationary probe was mounted off-board, a

large section of the skull had to be removed to image the underlying tissue as the head rotated past the stationary probe. This limited data collection to only low-level severities due to bulging of the tissue and high relative velocities between the probe and the imaged tissue. Though high-frequency B-mode ultrasound was proven accurate in quantifying lateral tissue motion in an off-board, stationary condition, an ultrasound probe to measure tangential motion under the high velocity and dynamic loading scenarios during injury biomechanics testing have not yet been validated.

To overcome the limitation of tracking ability, several updates were made to the PMHS experimental plan outlined by Mallory (2014). The size of the window opening in the skull was substantially reduced, eliminating the limitation of excess tissue bulging. Additionally, the probe location was moved from an off-board, stationary position, to instead rotate with the head. The decreased relative velocity between the probe and underlying tissue being imaged resulted in the possibility of testing at higher speeds. However, the use of an ultrasound probe as a measurement device has not yet been validated under rotation. B-mode ultrasound generates two-dimensional (2D) images using the sound waves emitted from piezoelectric crystals in the ultrasound transducer. Mechanical vibrations in the piezoelectric crystals are converted into electrical signals, resulting in image formation as ultrasound waves pass through various mediums (Abu-Zidan et al., 2011). As these piezoelectric crystals are known to be sensitive to impulsive acceleration, the effects of rotating the ultrasound probe on the accuracy of displacement measures must be investigated. Therefore, the objective of this study was to evaluate the accuracy of displacements captured using a rotating ultrasound probe.

3.2 Validation Materials and Methods

A custom validation fixture was fabricated to replicate the test setup used to measure superficial brain motion in postmortem human subjects (PMHS). The validation fixture was installed in a custom rotation fixture to deliver repeatable high-rate, rotational pulses. An overall view of the rotation fixture is shown in Figure 14. A linear force from pressurizing the pneumatic ram is applied to the fixture's loading arm, which initiates a rotational acceleration of the cage about the fixture's axis.

When PMHS are tested in the rotation fixture, the subject's head will be secured in a cage using threaded locator bolts to ensure uniform rotation in an anterior-posterior direction. A small window opening will be cut to allow the ultrasound probe to image the underlying tissue. A superstructure will be installed to house the ultrasound probe, allowing the probe to rotate near the dura.

To validate the ultrasound probe measurements under rotation, the same experimental setup was used with the same ultrasound probe that will be used during PMHS testing (Figure 10). The design of the validation fixture allows for a phantom to move relative to the probe, replicating the motion of the superficial brain relative to the probe during PMHS testing.

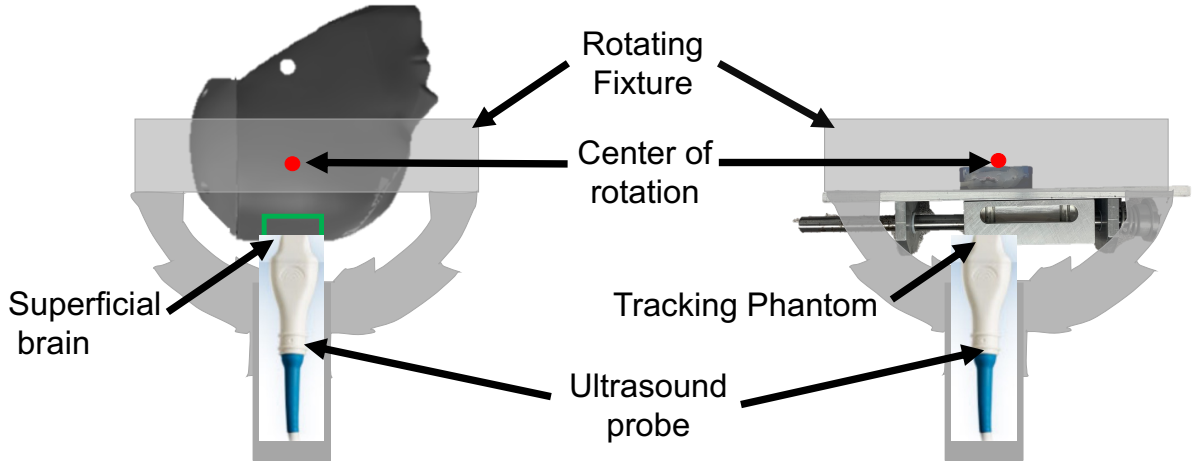

Figure 10: Design of the validation fixture, replicating the setup used for PMHS testing

The validation fixture (Figure 11) is comprised of a metal gel cup mounted to a shaft with a spring-loaded on the shaft to limit the amount of motion of the cup. The stiffness of the spring was varied to optimize the linear motion of the cup. The gel cup can slide freely along the direction of motion (Figure 11), while the base fixture functions as a constraint to keep the sliding motion in a single plane.

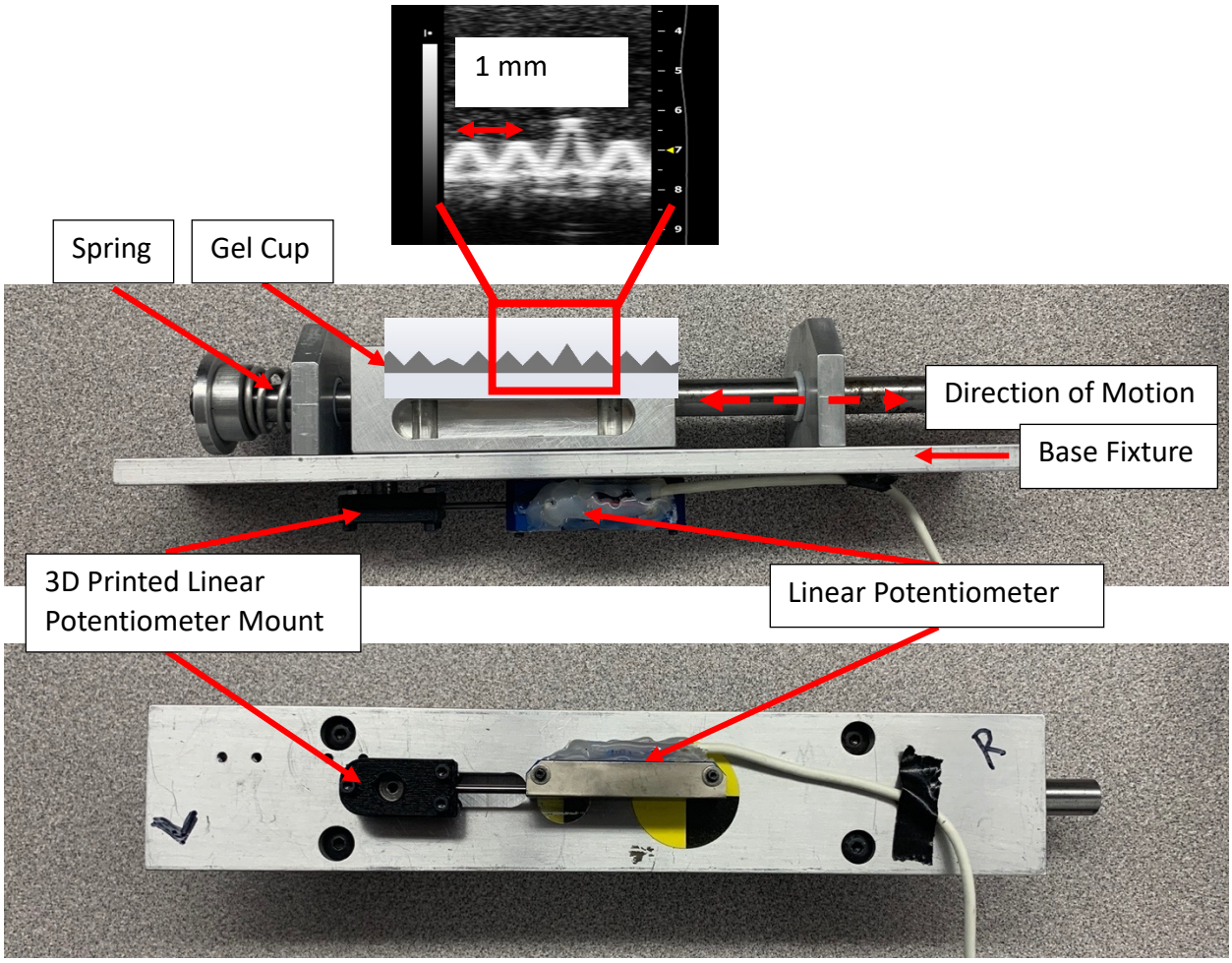

Figure 11: Validation fixture

Instead of tracking human tissue samples, a 3D printed phantom (Dremel DigiLab PLA, Robert Bosch Tool Co., Racine, WI) was created with peaks occurring at regular intervals of 1 mm that can be imaged by the ultrasound measurement system and easily tracked using a commercial tracking software (Figure 12). A 3D printed tracking phantom was utilized to minimize the error associated with tracking human tissue samples. Any misalignment between the image plane and plane of tissue motion can change the appearance of tissue features that can lead to errors in displacement (Mallory et al., 2018). To image the 3D printed tracking specimen

in the bottom of the metal cup, the gel cup was filled with a phantom made of a 10:1:1 mixture by volume of distilled water, gelatin powder (Knox, Treehouse Foods Inc., Camden, NJ), and confectioner's sugar (Domino Foods Inc., Baltimore, MD).

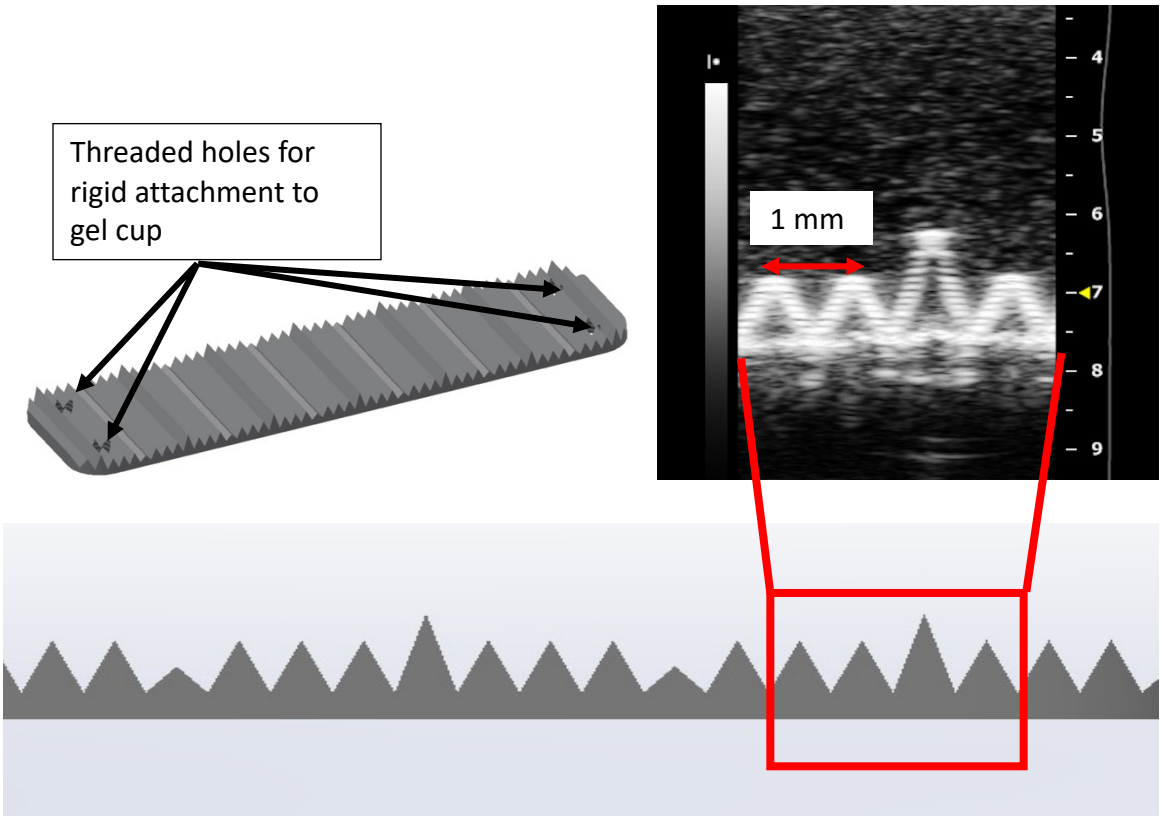

Figure 12: 3D printed piece for tracking (bottom) and corresponding ultrasound view (top right). Oblique view showing attachment points (top left)

The validation fixture was then installed in a cage on the rotation fixture (Figure 13). The ultrasound probe was installed in a superstructure which functions to ensure that the probe is installed perpendicularly to the gel cup and 3D printed tracking piece.

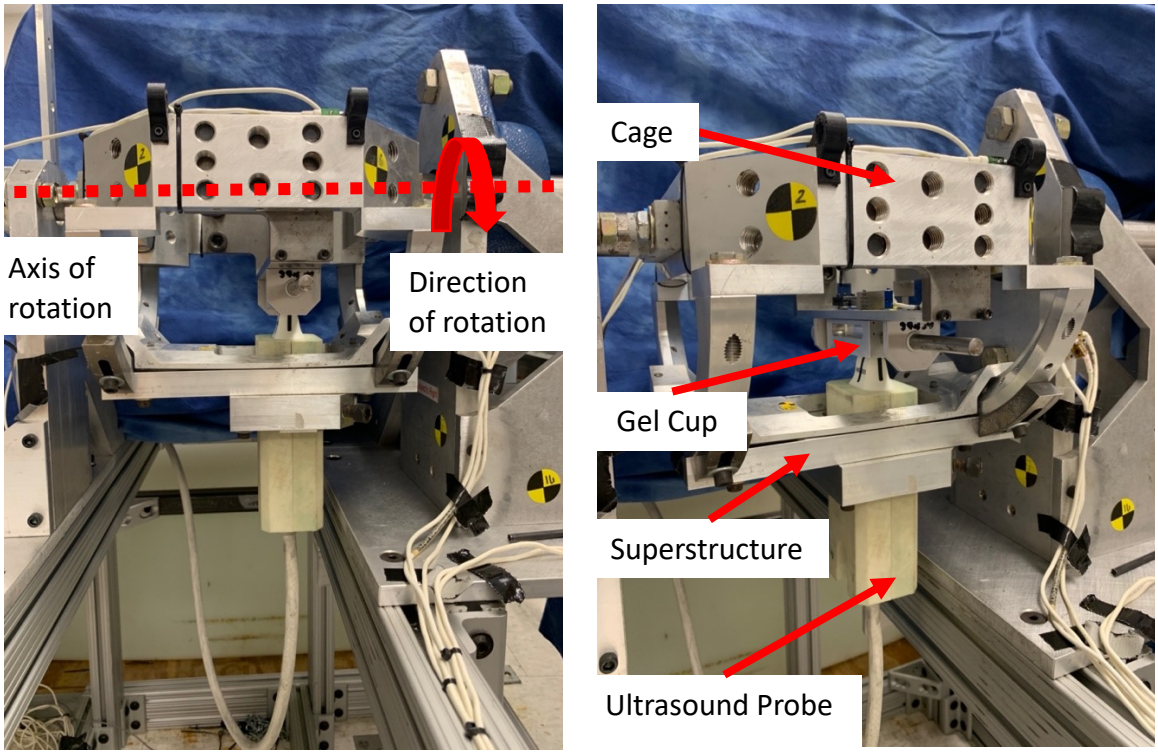

Figure 13: Frontal (left) and oblique view of validation fixture installed in rotation fixture (right)

The relative motion of the cup was measured using a fixture mounted linear potentiometer (Figure 11). The measurements obtained from the potentiometer will be compared to the measurements from the ultrasound to evaluate the accuracy of the probe's measurement capabilities under rotation.

The differences in peak displacement from the two measurement techniques were compared under three conditions: high velocity, low displacement tests; low velocity, high displacement tests; and high velocity, high displacement tests (Table 3).

Table 3: Validation test matrix

Test Description	Kinematic Ranges		Displacement Range (mm)
	Rotational Acceleration (rad/s/s)	Rotational Velocity (rad/s)	
High velocity, low displacement	1640-2995	21.3-33.4	1.0-4.0
Low velocity, high displacement	1267-2161	13.9-21.5	8.0-15.0
High velocity, high displacement	2504-3207	29.9-35.4	14.0-14.5

High-speed, high frequency motion images of the 3D printed phantom were collected using a VEVO 2100, brightness-mode (B-mode) ultrasound imaging system (VisualSonics Inc., Toronto, Ontario, Canada) with a 550S probe at a center frequency of 40 MHz. Images were collected at a frame rate of 693 frames per second at an image width of 4.08. Tissue tracking video sequences were collected by B-mode ultrasound and analyzed using a commercial motion tracking software (TEMA, Image Systems, Linköping, Sweden). A peak on the ultrasound image (Figure 12) was tracked semi-automatically, and the time history was compared to the time history obtained from the linear potentiometer.

The ultrasound probe was installed in a retrograde orientation, meaning that the tissue motion was in the opposite direction as the sweep of the ultrasound (Mallory et al., 2018). When images are collected in the retrograde orientation, points on the ultrasound image appear to be closer together than actuality due to the time it takes for the sweep of the ultrasound to finalize data collection. Therefore, the following correction was applied to correct the data during post processing (Equation 4):

$$t_{actual} = t_0 * FR * \left(\frac{x}{x_{width}}\right) \quad [4]$$

where $t_{actual:}$ corrected time

$t_{0:}$ uncorrected time,

FR: frame rate at which the data was collected,

x: x-position of the tracked point in the frame

x_{width}: width of the entire ultrasound image.

The shaft and both sides of the cage were instrumented with angular rate sensors (DTS ARS18K PRO, Diversified Technical Systems, Seal Beach, CA) to measure rotational velocity about the Y-axis. Reported angular velocities were from shaft angular rate sensor while the others were used as redundant measures. Uniaxial accelerometers (7624C-2K, Endevco, San Juan Capistrano, CA) were fixed to the anterior and posterior fixture for calculation of rotational acceleration about the axis of rotation. The instrumentation locations are shown in Figure 14.

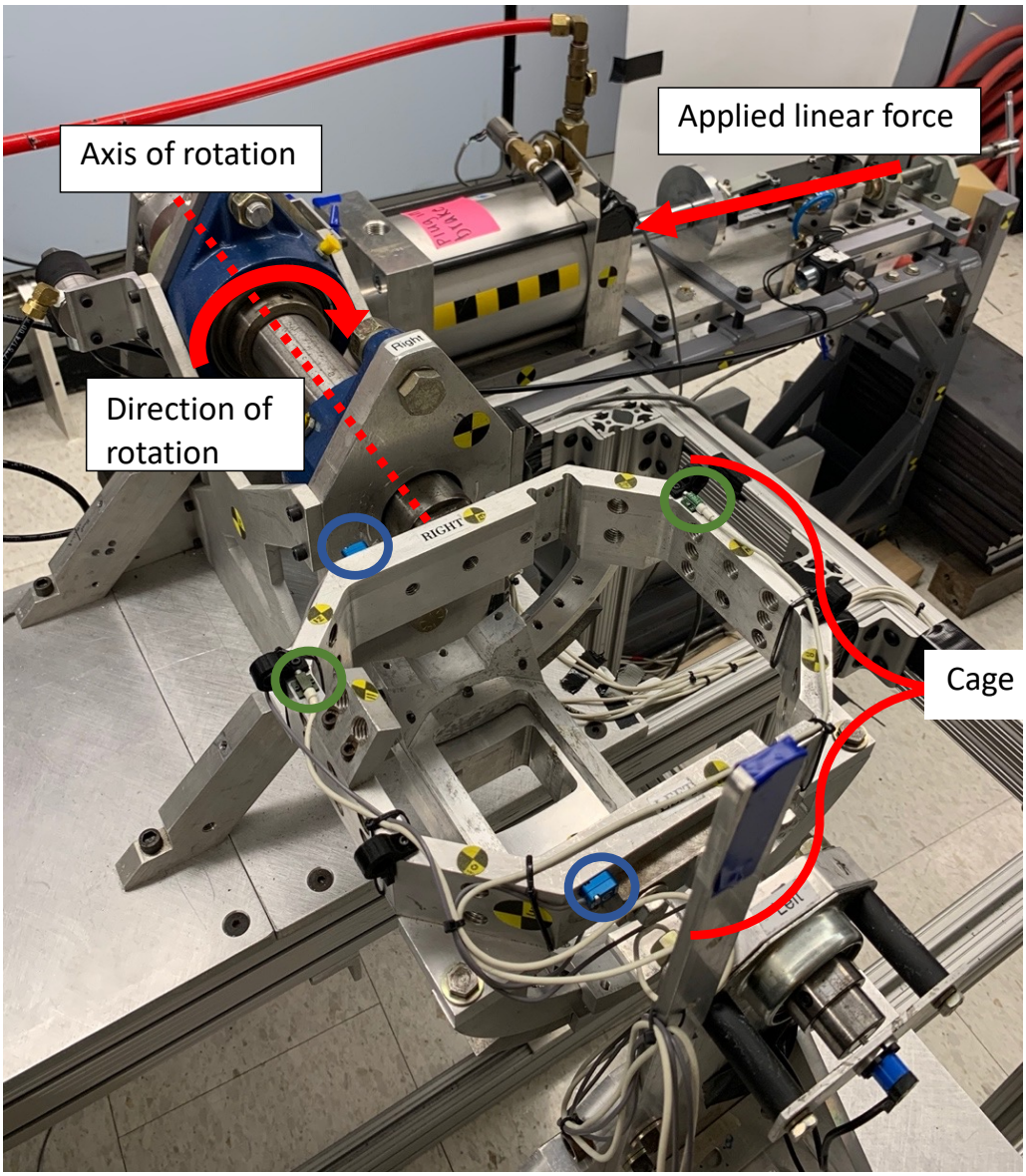

Figure 14: Overview of rotation fixture; accelerometer locations shown in green circles, angular rate sensor locations shown in blue circles

The linear potentiometer mounted to the validation fixture was specified by the manufacturer to have maximum linearity error of +/- 1.0% during calibration testing (Servo Instrument Co., Baraboo, WI).

Multiple tracked points were used to estimate the cumulative displacement of the tracking phantom. After each new tracked point was added, the time-displacement of the previously tracked points was curve-fit using a shape-preserving piecewise cubic interpolation (MATLAB, MathWorks, Natick, MA). An example of a single tracked point is shown in Figure 15.

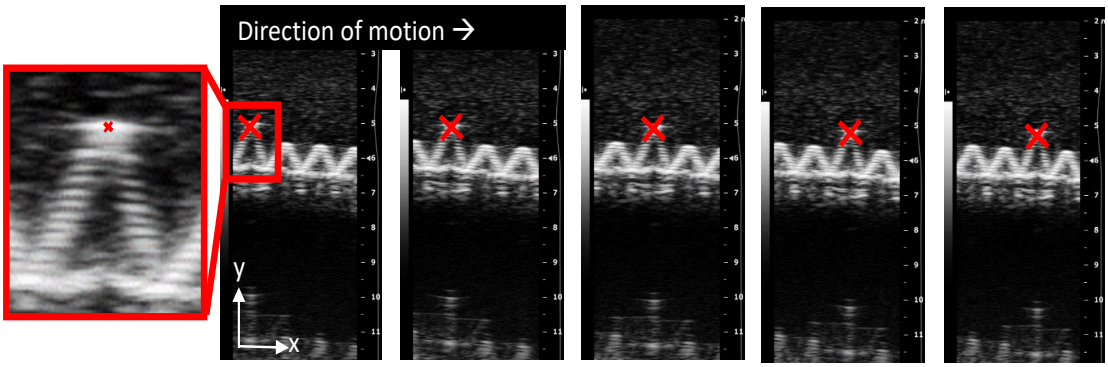

Figure 15: Sample tracked point location

Both the linear potentiometer and angular rate data were filtered using CFC180, and accelerometer data were filtered using CFC60 (SAE J211).

Two evaluations were conducted to investigate the agreement between the tracked ultrasound displacement results and the linear potentiometer results. The percent difference between the peak displacement measured from the linear potentiometer and the tracked ultrasound data were calculated to compare similarities in peak displacement. Additionally, the normalized root mean standard deviation (NRMSD) between the displacement curves up to the peak displacement was calculated as a measure of similarity between the two measurement systems along the time history up to peak displacement. The fixture data were collected at

20,000 Hz while the ultrasound data were calculated at 693 Hz, so to calculate NRMSD, a common time channel was created, and data were re-sampled using a linear interpolation function to obtain comparable data for the analysis.

3.3 Validation Results

Results from the 27 validation tests are summarized in Table 4.

Table 4: Validation test results

			Peak Displacement (mm)				
Test #	Rotational Acceleration (rad/s/s)	Rotational Velocity (rad/s)	Linear Pot	Ultrasound	Difference in peaks (mm) Pot-Ultrasound	% Difference in peaks	NRMSD
1	1798	22.9	1.25	1.30	-0.05	-3.98	3.23
2	1833	21.7	1.26	1.27	-0.01	-0.87	2.42
3	1828	21.3	1.22	1.23	-0.01	-1.01	1.74
4	2361	25.8	2.11	2.07	0.04	1.82	1.08
5	2218	25.6	1.98	1.95	0.03	1.42	0.69
6	2277	25.8	2.08	2.06	0.02	0.83	1.36
7	2743	29.2	3.01	2.95	0.06	1.87	0.31
8	2779	29.5	3.04	2.94	0.09	3.04	1.82
9	2768	29.7	3.08	2.95	0.13	4.19	1.57
10	3253	33.0	3.86	3.95	-0.10	-2.47	3.95
11	3288	33.4	3.92	3.97	-0.05	-1.34	1.57
12	3215	33.2	3.90	3.99	-0.10	-2.51	0.82
13	1510	13.9	8.28	8.47	-0.20	-2.35	0.84
14	1525	14.0	8.65	8.93	-0.28	-3.19	1.07
15	1490	14.1	8.60	8.60	0.00	0.00	1.31
16	1914	17.7	11.15	11.38	-0.23	-2.07	0.80
17	1948	17.6	11.13	11.35	-0.22	-2.05	0.55
18	2035	17.8	11.69	11.79	-0.10	-0.91	1.08
19	2501	21.4	14.24	14.28	-0.04	-0.30	0.64
20	2462	21.3	14.56	14.50	0.06	0.40	1.41
21	2513	21.5	14.56	14.58	-0.02	-0.19	1.13
22	3386	34.7	14.23	14.18	0.04	0.32	0.68
23	3558	34.4	14.26	14.30	-0.04	-0.32	0.76
24	3505	35.4	14.32	14.24	0.08	0.53	0.71
25	2888	30.4	13.95	14.05	-0.10	-0.75	0.78
26	2934	29.9	13.89	13.94	-0.05	-0.40	0.83
27	3211	30.3	13.95	14.05	-0.10	-0.75	0.78
				Minimum Value	-0.28	-3.98	0.31
				Maximum Value	0.13	4.19	3.95
				Average	-0.04	1.48	1.26
				Standard Deviation	0.10	1.18	0.82

The average difference in peaks across all tests was 0.04 mm with a standard deviation of 0.10 mm, corresponding to an average difference of 1.48% between the measurement techniques. A sample time-history plot of the displacement measured by the linear potentiometer compared to the displacement measured by the ultrasound is shown in Figure 16.

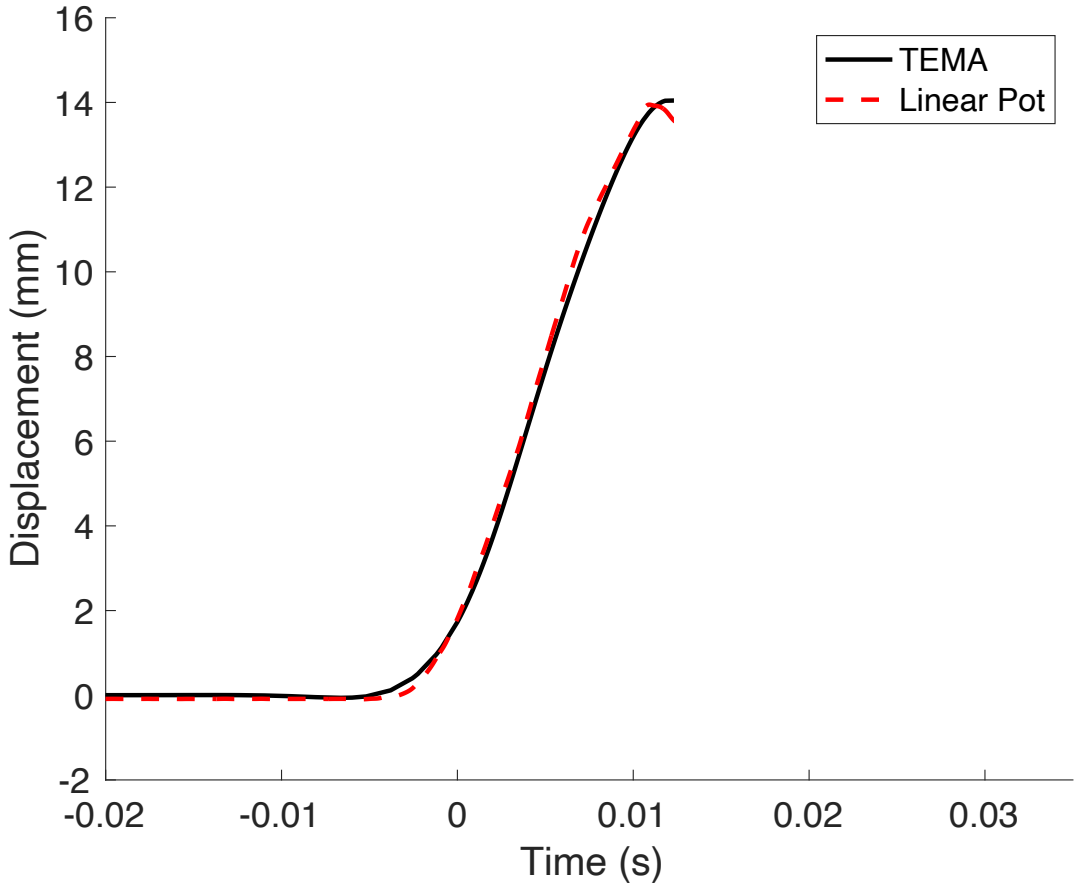

Figure 16: Time history plot of displacement comparing measurements from a linear potentiometer and ultrasound

The time-history plots for the remaining tests can be found in Appendix A.

3.4 Validation Discussion

The objective of this study was to validate the use of B-mode ultrasound under the high-rate, dynamic loading conditions that can be seen during injury biomechanics testing. Results show an average difference of about 1.5% between the linear potentiometer data and the tracked ultrasound data, suggesting that the ultrasound probe is a reliable measurement tool for quantifying lateral displacement, even when rotated at high rates. The average difference between measurement methods was about 0.04 mm for tests run with the ultrasound probe in the retrograde orientation. The average NRMSD value across all tests was 1.26, further exemplifying the accuracy of the ultrasound compared to the linear potentiometer.

There have been efforts to validate the accuracy of speckle tracking on B-mode ultrasound images in the case of tracking tendon motion (Korstanje et al., 2010). Though during this study, the ultrasound parameters were different and tissue velocity was much lower, at displacements between 1 and 14.5 mm the reported relative error (1.3±1.1%) was consisted with the relative errors reported in this study. The 1.5% difference recorded during this study is also consistent with the average differences obtained during a stationary validation trial (Mallory et al., 2018).

The displacement values obtained during this study are comparable to brain displacements recorded in the literature. A highspeed x-ray study of PMHS brain displacements under sagittal plane rotation by Hardy and colleagues reported displacements ranging between 0 and 8.11 mm (Hardy et al., 2007). A sonomicrometry study by Alshareef and colleagues reported displacements from sagittal plane rotation between 1.45 and 14.76 mm. (Alshareef et al., 2018,

2020), This suggests that B-mode ultrasound is an acceptable tool to capture high-speed tissue motion as seen in injury biomechanics testing.

The ultrasound images were tracked semi-automatically, offering the potential for bias from the person performing the tracking. To quantify this bias, the ultrasound data was re-tracked to quantify intra-observational error for each test in the series using the technical error of measurement (TEM) (Weinberg et al., 2005) [Equation 5]:

$$TEM = \sqrt{\frac{\sum D^2}{2N}} \quad [5]$$

where D: difference between two measurements

N: number of replicate tests

The average intra-observer error was only 0.003 mm for the entire dataset, indicating minimal bias from potential user error. Though intra-observational error was quantified and is consistent with other ultrasound validation studies (Mallory et al., 2018; Korstanje et al., 2010), inter-observational error was not quantified in this study.

An advantage of high-frequency B-mode ultrasound is the ability to capture tissue motion at relatively high sample rates compared to traditional ultrasound; however, this necessitates a narrow field of view across the width of the image. A narrow image width results in tracked points moving out of view if displacements are larger than the image width. Therefore, as tracked points moved out of the frame, additional points were tracked at the same depth.

It was hypothesized that rotating the ultrasound probe would influence its ability to accurately measure displacement because of how the piezoelectric crystals would be influenced by acceleration. From the distribution of errors seen in Table 4, speed did not make a discernable difference to the measurement of lateral motion. If the crystals in the ultrasound probe were susceptible to error under the influence of acceleration, larger errors would be expected at tests run at higher speeds. Qualitatively, image quality did not degrade at higher speeds.

The 1.5% error found between the tracked ultrasound data and the linear potentiometer displacement data combined with the noninvasiveness and ability to capture the high-rate motion of the ultrasound measurement system indicates that ultrasound is the optimal technique for quantifying surface-level brain motion at the speeds investigated during this study. While other studies that used imaging techniques such as implementing sensors directly into the brain and high-speed x-ray have been able to image brain tissue at injury level severities, the imaging methods were quite invasive, and they were unable to quantify motion close to the surface of the brain. Though ultrafast ultrasound is a non-invasive measurement option that can quantify more superficial tissue motion, previous studies were limited by only quantifying compressive tissue motion.

This study is not without limitations. Though the quantified intra-observational error was low indicating good repeatability, inter-observational error was not quantified. Additionally, the tracking phantom that was utilized in this study was rigid and may not properly reflect additional tracking errors associated with tracking biological samples. However, the purpose of this study was to investigate that any source of error was not attributed to rotating the probe, so a rigid phantom was desired. Furthermore, the kinematic severities and displacements investigated in this study were based on previous research studies and may not be applicable to future tests.

Future work should investigate ultrasound as a measurement technique under a wider range of kinematics and displacements.

3.5 Validation Conclusions

With an ultrasound probe rotating at velocities between 13.9 and 35.4 rad/s and accelerations between 1490 and 3558 rad/s^2, lateral displacement measurements of a phantom moving between 1 and 15 mm were accurate within 0.04 mm on average when compared to a linear potentiometer, demonstrating that high-frequency B-mode ultrasound can be used to effectively quantify lateral displacements even while the ultrasound probe is rotating at these severities.

Chapter 4: PMHS Testing to Quantify Relative Surface Level Brain Motion

4.1 Materials and Methods

The investigation of relative motion between the brain and the skull was conducted using high-frequency, B-mode ultrasound to capture brain tissue motion of postmortem human subjects (PMHS) under high-rate rotation. First, a fresh subject trial was completed for initial quantification of superficial brain motion and verification of methodology. An additional five subjects were tested for experimental brain displacement data.

4.1.1 Postmortem Human Subject Selection

PMHS used for testing were obtained through the Ohio State University's Anatomy Body Donor Program in accordance with all National Highway Traffic Safety Administration (NHTSA) and University guidelines on the use of anatomical donors. Acceptance constraints for the postmortem subjects were as follows:

- Subject access at no greater than 36 hours postmortem
- Head width at maximum no greater than 17 cm to accommodate test fixture dimensions
- No history of major head trauma or brain cancer
- Cause of death was not strangulation

Subject selection was not limited by height, weight, age, sex, or by history of neurological disease associated with brain atrophy including Alzheimer's disease, Parkinson's disease, or Multiple Sclerosis.

Rotation tests were completed using five postmortem human subjects. All tests were complete within 56 hours postmortem. Relevant subject information is summarized in Table 5. Subject characteristics such as anthropometry measurements and brain parenchymal fraction (BPF) are summarized in Table 6.

Table 5: Subject information

Subject #	Age (years)	Sex	Cause of Death	Subject Received (hours postmortem)	Testing Complete (hours postmortem)
01	77	Female	COPD	27.67	55.09
02	96	Female	Alzheimer's	25.17	42.80
03	96	Male	Alzheimer's	24.36	44.99
04	72	Male	Pancreatic cancer	12.00	30.70
05	79	Female	Cardiac arrest	15.83	34.13

Table 6: Subject characteristics

	Subject Measurement	Trial Subject	Subject 01	Subject 02	Subject 03	Subject 04	Subject 05	Average ± SD
Whole body	Stature (cm)	167.6	153.7	158.8	172.7	177.8	162.6	165.5 ± 9.0
	Mass (kg)	53.5	56.5	40.2	72.3	62.4	49.9	55.8 ± 10.9
Head/ Neck	Head/neck (kg)	4.10	4.00	3.32	4.57	3.65	3.81	3.91 ± 0.43
	Brain (kg)	--	1.21	1.00	1.15	1.06	1.22	1.13 ± 0.10
	BPF	--	0.619	0.556	0.490	0.751	0.662	0.616 ± 0.100
	MOI ($kg\text{-}m^2$)	--	0.0211	0.0165	0.0233	0.0274	0.0296	0.0236 ± 0.0052

4.1.2 MRI for Estimation of Atrophy

For each subject, BPF was quantified pre-test. Because measured BPF can vary based on the magnetic resonance (MR) scanner and processing technique, a consistent protocol was used. Previous work by Cook et al. (2017) worked to quantify atrophy in a large sample of healthy, older adults. Identical image collection and analysis procedures were used to account for and reduce any MR artifacts.

A clinical 3-Tesla MRI scanner (Ingenia 3.0T CX, Philips Healthcare, Andover, MA) was used to image the brain during the pre-test procedures. The acquired images were collected following ADNI protocols intended to minimize scanner-specific imaging artifacts (Jack et al., 2008). Statistical Parametric Mapping version SPM 12 (Wellcome Trust Centre for Neuroimaging, London), a voxel-based suite of MATLAB (MATLAB, MathWorks, Natick, MA) tools and procedures for interpretation of neuroimaging, was used to segment the brain into

the cerebrospinal fluid (CSF), white matter (WM), and gray matter (GM) components. Volumes of each segment were quantified, and BPF was calculated using Equation 6,

$$BPF = \frac{Total\ Brain\ Volume}{Intracranial\ Volume} \quad [6]$$

where total brain volume: the sum of GM and WM volumes and

intracranial volume: the sum of the GM, WM, and CSF volumes.

4.1.3 Temperature Monitoring and Control

4.1.3.1 Review of the Literature

One of the major limitations that affect brain research is the rate at which the brain tissue decays postmortem. Inconsistent test methodologies, including not accounting for or documenting postmortem time, make the comparison of previous work difficult due to the potentially significant differences in tissue state. One possible way to slow the effects of postmortem time is by controlling the temperature of the tissue (McElhaney et al., 1973; Puymirat et al., 1979; Darvish and Crandall, 2001; Ferrer et al., 2007; Zhang et al., 2010), however; there are large gaps in the literature regarding the optimal temperature at which to mechanically test brain tissue, though it has been indicated that in as little as 12 hours brain tissue at room temperature becomes unreliable for both mechanical and material property testing (Brands et al., 2000; Ferrer et al., 2007; Forte et al., 2017; Hrapko et al., 2008; Puymirat et al., 2006; Rashid et al, 2013). Rashid and colleagues (2013) performed experiments in which porcine

brain tissue samples were stored at three different temperatures: ice-cold (6°C), room temperature (22°C), and body temperature (37°C). The samples were tested in shear within 5 hours postmortem, and it was concluded that a storage temperature between 4-5°C was optimal for minimizing the difference between in vitro and in vivo porcine brain samples and that testing at higher temperatures did not make a significant difference if the preservation temperature was in the 4-5°C range. Puymirat and colleagues (2006) studied the influence of storage at deep cold temperatures and found that enzyme deterioration slowed at 4°C and that at 4°C with minimum postmortem delay, brains can be used for reliable biochemical measurements until 48 hours. However, there are still gaps in the research concerning how time and temperature affect whole-brain degradation. Therefore, it was targeted to keep brain tissue temperatures as close to 4°C as possible without freezing the tissue.

4.1.3.2 Temperature Trials for Method Development

It was important to monitor the temperature of the brain throughout testing, as it has been suggested that keeping the brain tissue cooler may lead to more accurate measurements, but freezing brain tissue has been shown to destroy mechanical properties (Ferrer et al, 2007). A significant objective of this study is to obtain measurements non-invasively. Therefore, a temperature trial was conducted to investigate if brain temperature could be measured without inserting temperature probes directly into the cortex of the brain. A temperature trial was conducted using a fresh-frozen PMHS. Temperature probes were inserted into the nose and ear, as well as probes in the epidural space, the subdural space, and 8 cm deep into the brain cortex. From Figure 17, it can be noted that the ear probe was an appropriate estimate for more superficial brain temperatures, and Figure 18 shows that the nose probe could be used as an estimate for deeper brain temperatures.

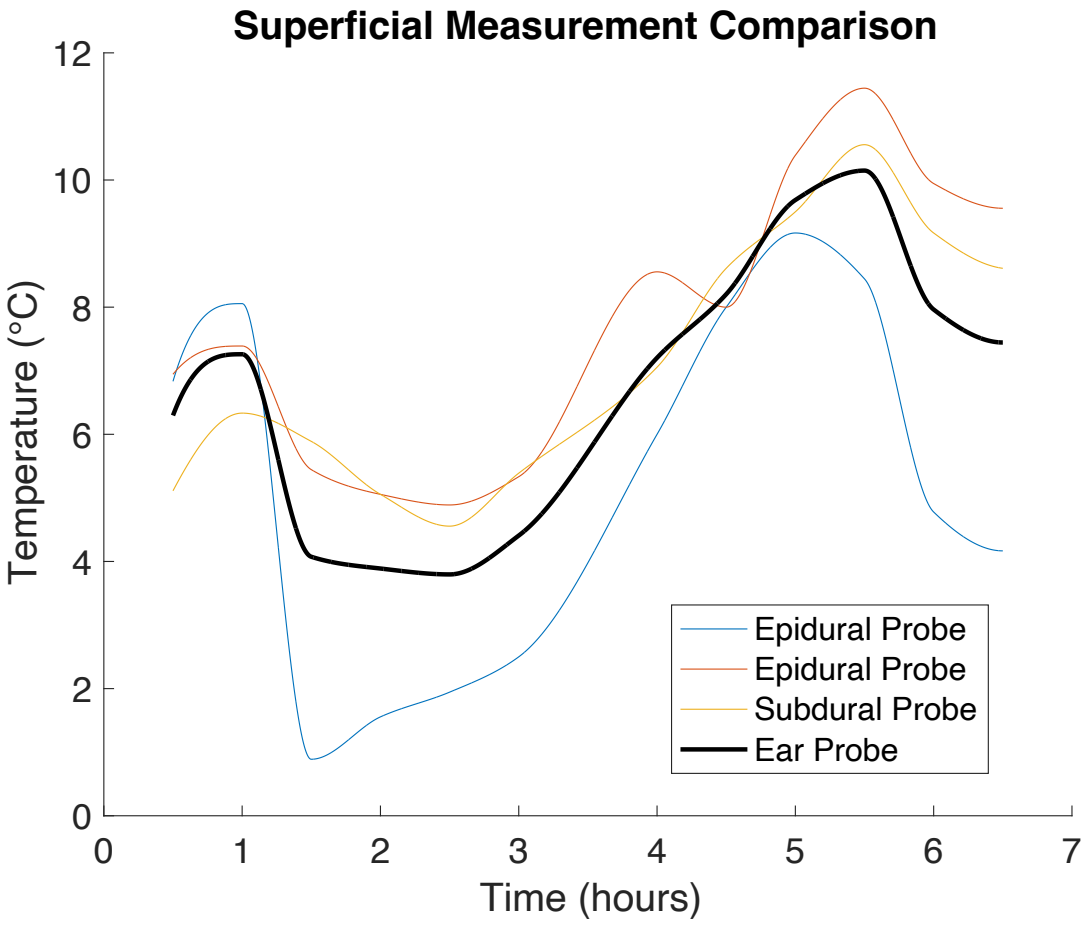

Figure 17: Superficial Brain Temperature Measurement Comparison

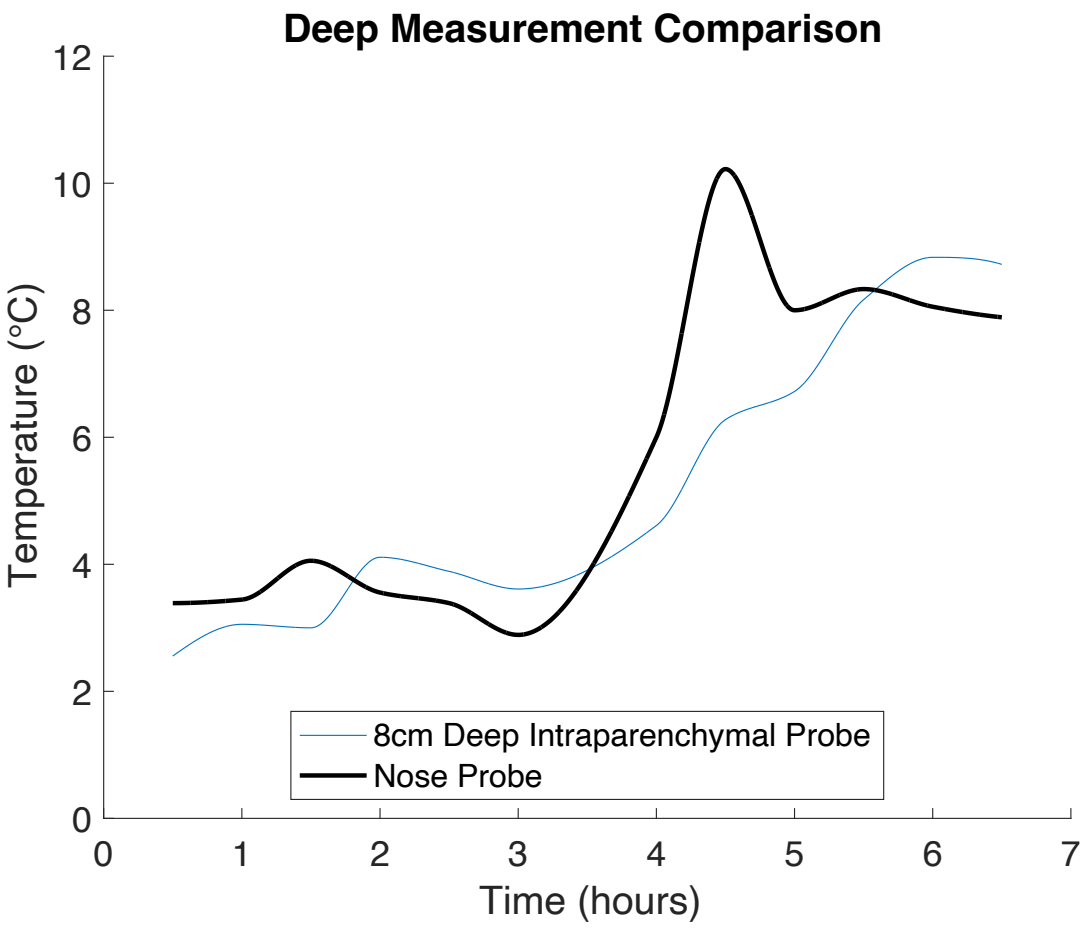

Figure 18: Deep Brain Temperature Measurement Comparison

The root mean standard deviation (RMSD) was calculated for both temperature measurement conditions. The temperature measurement from the ear probe was compared to the average curve of both epidural probe and subdural probe measurements, and the RMSD value was found to be 1.24. The RMSD value of the measurement from the nose probe compared to the measurement from the 8 cm deep intraparenchymal probe was found to be 1.40. These values indicate that a probe in the nose and a probe in the ear could be used to measure the temperature of the brain non-invasively.

To ensure that no part of the brain tissue would freeze, a lower limit of 4°C was chosen. Due to the literature being unclear on an upper-temperature threshold, there were efforts to keep the brain temperature as close to 4°C as possible throughout both subject preparation and rotation testing.

4.1.3.3 Application during PMHS Testing

Temperature monitoring and control began immediately after subject acquisition through the application of ice bags to the head and neck to begin cooling the brain tissue. Brain temperature was recorded throughout both subject preparation and rotation testing using a data logger with probes inserted in the ear and nose on the non-test side of the subject, and the room temperature was monitored from an additional probe (Figure 19).

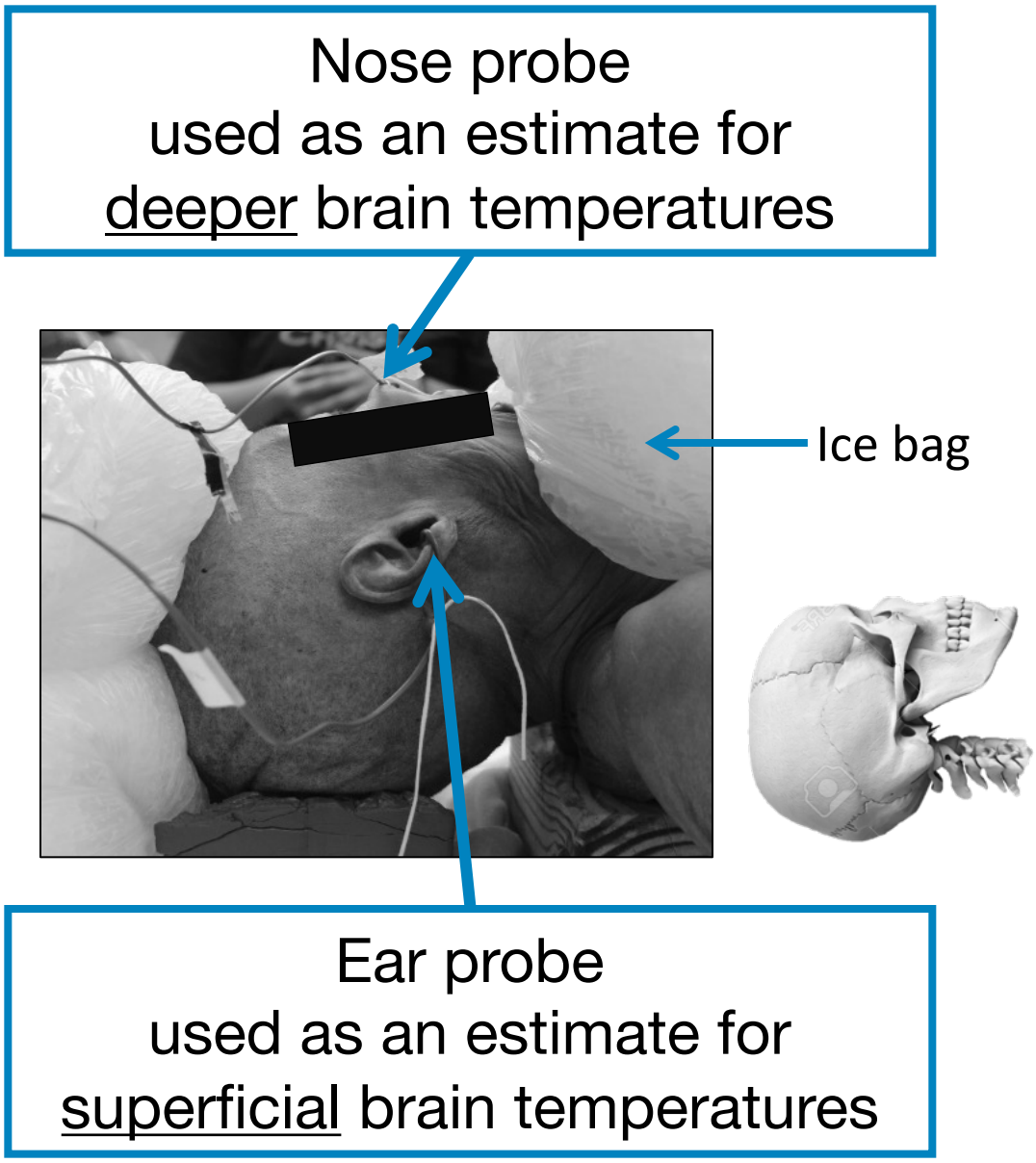

Figure 19: Temperature probe locations

An alarm on the temperature data logger was set to go off if temperatures reached 4°C to eliminate the possibility of freezing the brain tissue.

4.1.4 Separation of Head

Prior to the separation of the head and neck from the rest of the body, the external carotids were ligated to avoid pressurizing the subject's face (Figure 20).

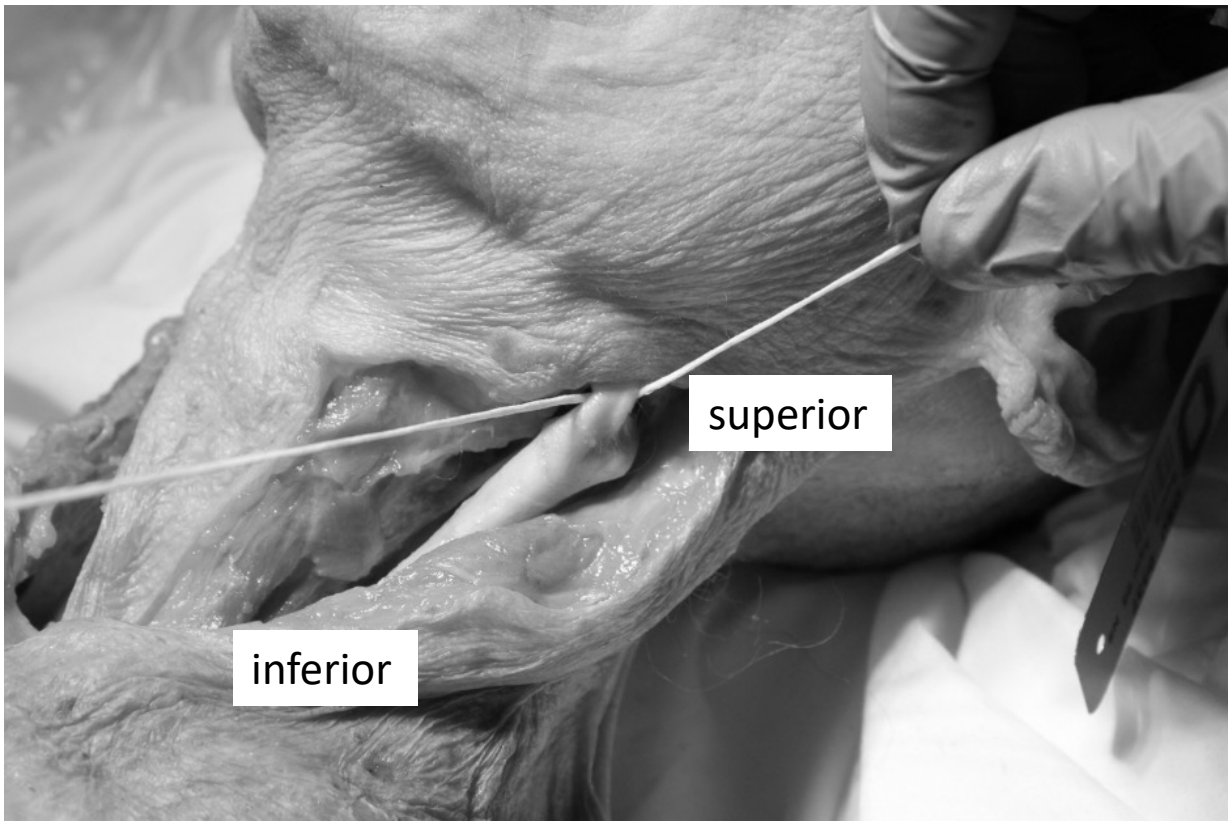

Figure 20: Ligation of the Left External Carotid

The internal jugulars, vertebral arteries, and internal carotid arteries were identified and later used for pressurizing the vascular system during rotation testing. The head and neck were then separated from the rest of the body by cutting through the C6-C7 vertebral level, severing the spinal cord last to minimize degradation of the cord.

4.1.5 Perfusion of Artificial Cerebrospinal Fluid

Immediately following the severing of the spinal cord, the space between the cervical vertebrae and the arachnoid was plugged with wax-covered yarn and Vaseline to limit the introduction of air or fluid into the space (Figure 21).

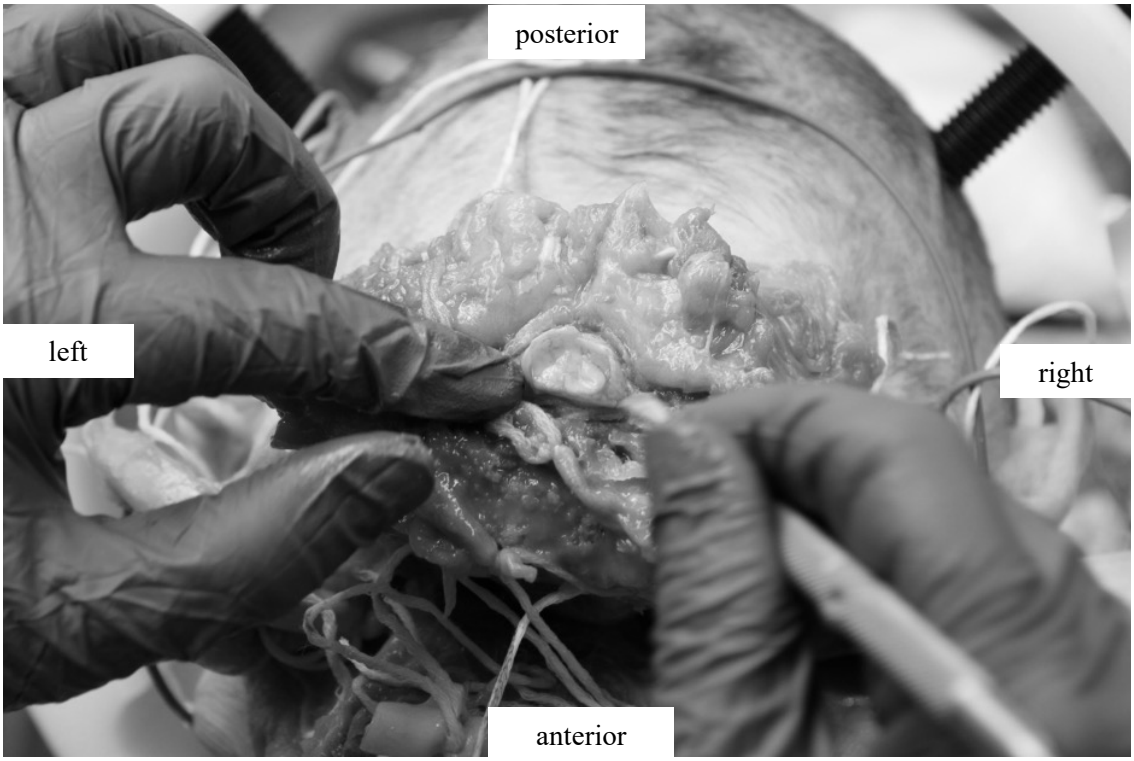

Figure 21: Sealing the space between the cervical vertebrae and arachnoid with wax-coated yarn

A Foley catheter sized 6F was inserted between the spinal cord and arachnoid (Figure 22) to perfuse the subarachnoid space with artificial cerebrospinal fluid (aCSF) prepared with

distilled water according to the recipe of Sugawara and colleagues (1996) plus sodium bicarbonate (Wetli et al., 2017) in an effort to re-introduce fluid into the cranial subarachnoid space while also slowing postmortem degradation. The aCSF with sodium bicarbonate will further be referred to as aCSF+. The aCSF+ is isotonic to physiological CSF; therefore, it was expected to minimize diffusion of the fluid into the brain, thus preventing unanticipated brain swelling.

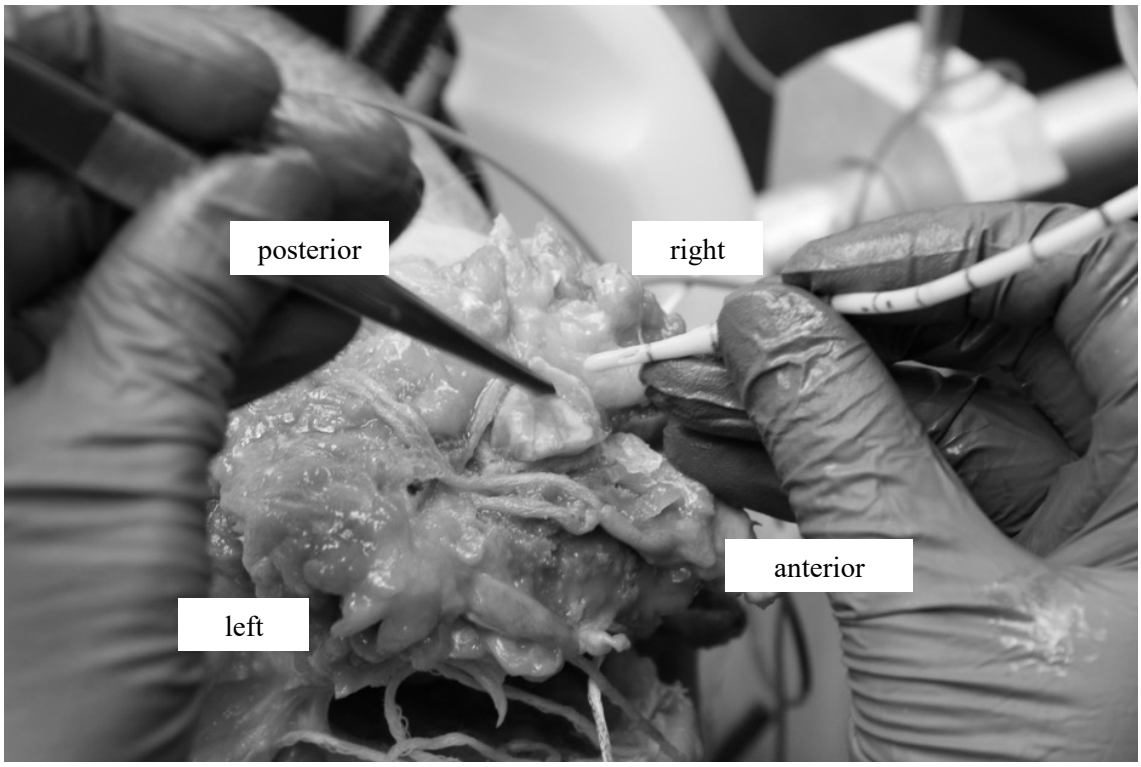

Figure 22: Insertion of the foley catheter into the subarachnoid space

The catheter was anchored in place at the transected surface of the neck using a custom anchoring fixture (Figure 23). The spinal bracing hardware was screwed into the body of the sixth cervical vertebrae and the catheter was glued to a support bracket that was threaded through

the bracing hardware to prevent the catheter from bending or being pulled out during the remaining subject preparation and rotation testing. Care was taken to ensure the flow of the catheter was not impeded during fixation.

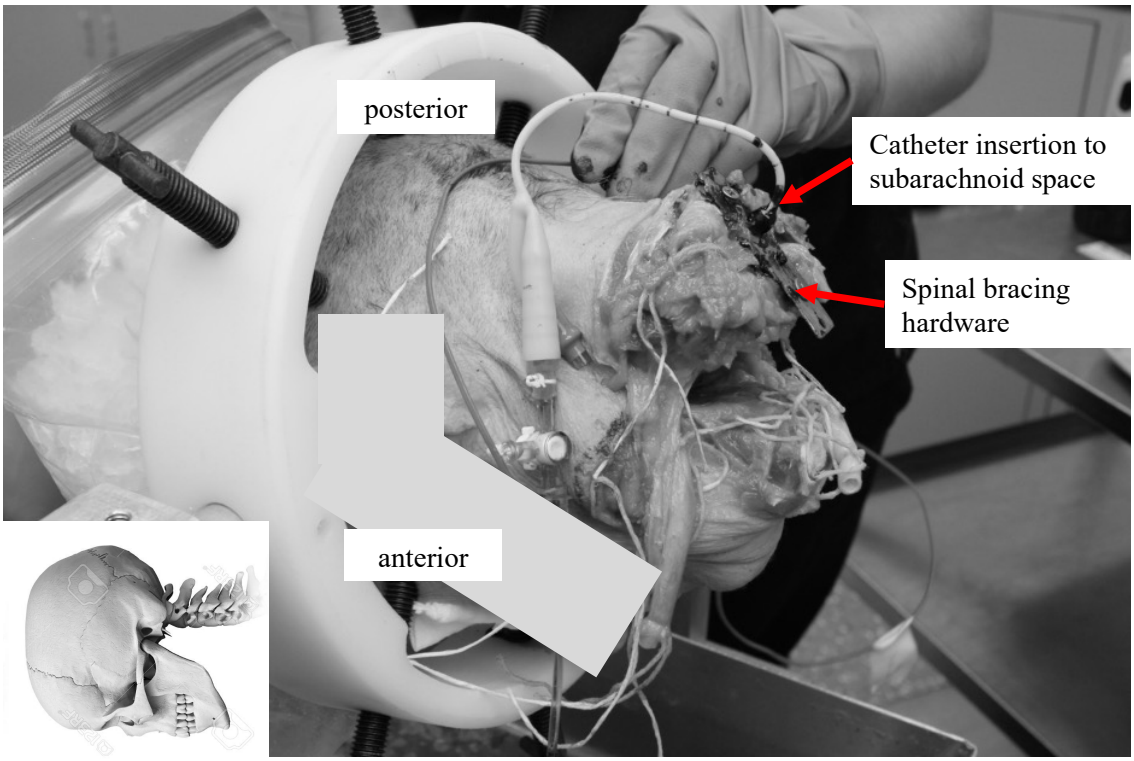

Figure 23: Custom spinal bracing hardware for anchoring aCSF+ catheter

The catheter was connected to a reservoir filled with aCSF+ with a fluid level approximately 30 cm above the level of the upper cervical spine. This height difference resulted in a nominal fluid pressure, allowing the aCSF+ to perfuse into the cranial subarachnoid space throughout both subject preparation and rotation testing. Green RIT dye (Quality Brands,

Stamford, Connecticut) was added to the aCSF+ to visualize the extent of subarachnoid perfusion during post-test dissection.

4.1.6 Opening of Cranial Viewing Window

To image the underlying dura, a window was opened through the cranial vault. The location for the primary ultrasound window was 3 cm posterior to the bregma and 3 cm lateral to the centerline. The opening was cut using a size 302 surgical craniotome (Model 6516-01-378-A176, Aesculap, Center Valley, PA), resulting in a window hole with a diameter of 8 mm. The window size was minimized to prevent the bulging of tissue out of the opening while also optimizing the view of the ultrasound (Figure 24).

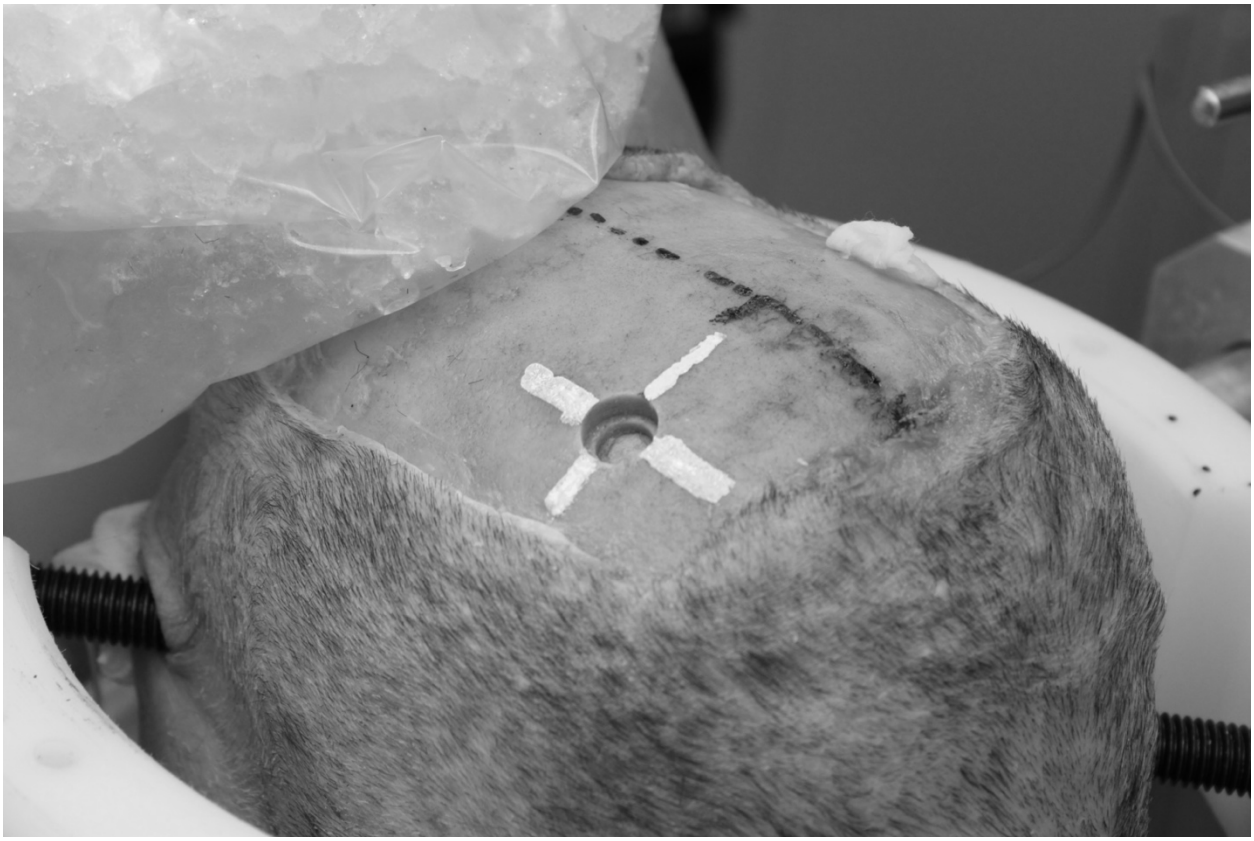

Figure 24: Skull opening (8 cm radius) for ultrasound viewing window

4.1.7 Head Positioning

The head was secured in a cage using threaded locator bolts to ensure uniform rotation in an anterior-posterior direction. It was positioned such that the dura underneath the ultrasound probe at the location of the transducer window was at an 8 cm radius of rotation from the rotation axis of the fixture. The center of rotation of the subject was found using the Head Alignment Tool (HAT), developed for increasing the efficiency of aligning each subject on its specific axis of rotation while maintaining the radial location where brain motion was measured (Figure 25). The laser of the HAT was aligned such that it ran along the center of the superior sagittal suture between the nasion and the posterior occiput while the ball pin sat in the hole created for the ultrasound viewing window. The location for the primary ultrasound window was 3 cm posterior to the bregma and 3 cm lateral to the centerline, as this was the location identified by the literature as a common site for bridging vein rupture (Han et al., 2006; Famaey et al., 2015). Center of rotation pins on the left and right were then inserted to confirm and mark the center of rotation.

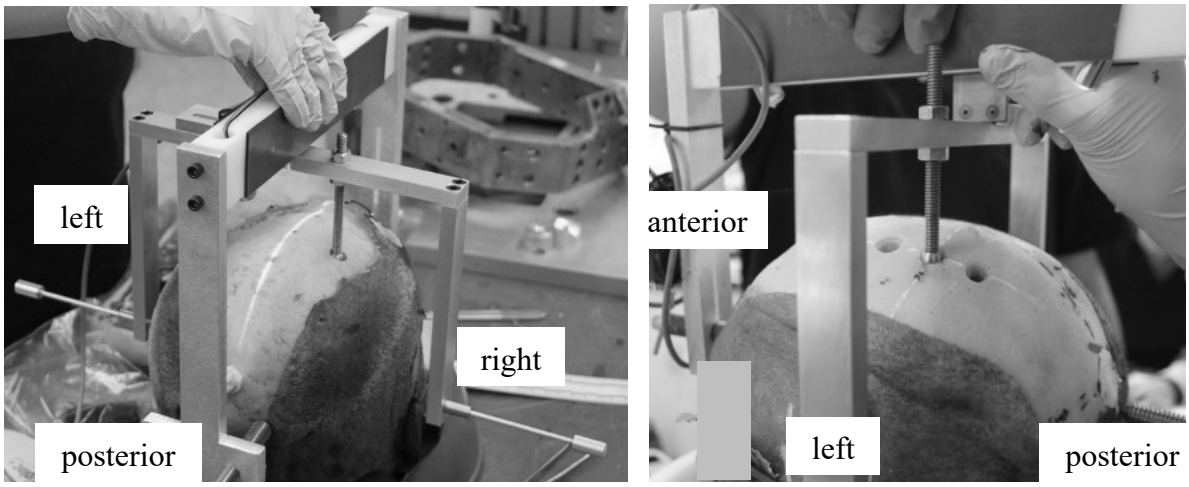

Figure 25: Head Alignment Tool (HAT)

To ensure that the ultrasound probe could be positioned close to the dura, the skull adjacent to the ultrasound viewing window was grinded down until only a thin layer of the skull remained around the periphery of the opening (Figure 26).

Figure 26: Window opening after grinding

The cage was then installed into a custom rotation fixture (Figure 27). With the cage installed in the rotation fixture, a superstructure was installed to house the ultrasound probe, allowing the ultrasound probe to rotate near the dura. A chin bar was also installed to increase stability during rotation (Figure 27).

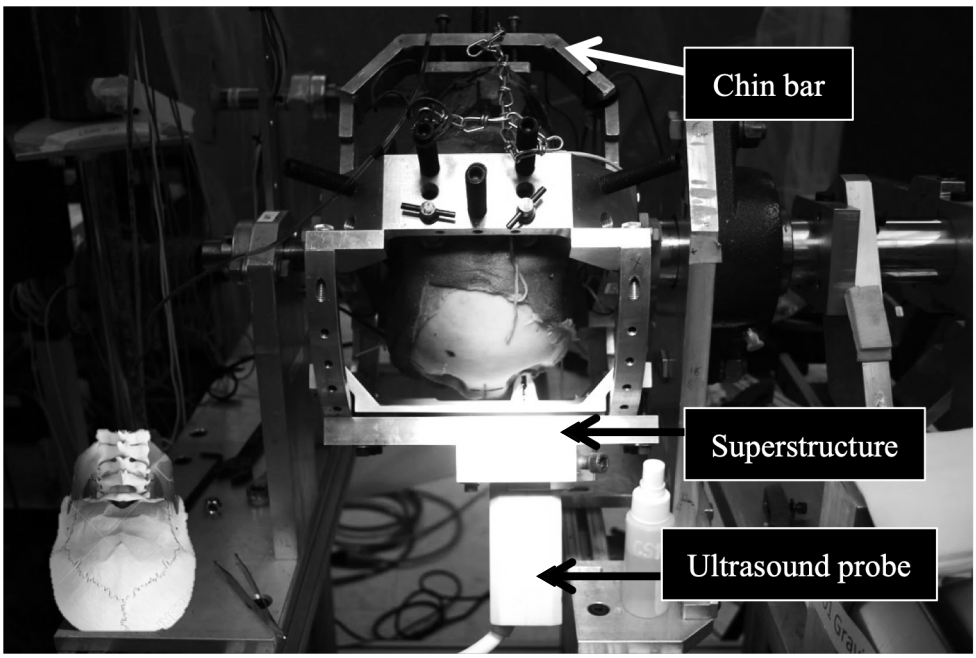

Figure 27: Head in cage installed in rotation fixture with chin bar at top, ultrasound probe mounted in superstructure at bottom

High-speed, high frequency, B-mode ultrasound images of the dura and underlying cortex were collected using a VEVO 2100 ultrasound imaging system (VisualSonics Inc., Toronto, Ontario, Canada) with a 550S probe with a center frequency of 40 MHz. Images were collected at 693 frames per second at an image width of 4.08 mm.

4.1.8 Flushing and Pressurization

The vasculature was flushed to clear the brain of potential clots and to introduce sodium bicarbonate to the vasculature to minimize the effects of postmortem degradation. The venous system was flushed via the internal jugular veins with yellow-dyed saline, and the arterial system was flushed via the internal carotid arteries with orange-dyed saline so that the extent of the fluid

perfusion could be examined during the post-test dissection. The arterial system was pressurized for testing using saline + sodium bicarbonate via the internal carotid arteries to bring the intracranial pressure (ICP) to within the physiological range of 5-15 mmHg (Raboel et al., 2012). A pressurization trial was conducted pre-test for each subject to determine the bag height and time of pressurization required to keep the brain in physiological ICP range during rotation testing. A pressure sensor (Millar, Houston, Texas, USA or Codman & Shurtleff Inc., Raynham, Massachusetts, USA) was inserted 5 cm deep intraparenchymally and secured with putty in the non-test side of the brain 3 cm posterior to the bregma and 3 cm lateral to the centerline to monitor and record ICP during rotation testing (Figure 28). During ICP evaluation, the head was inverted to the start position of rotation testing.

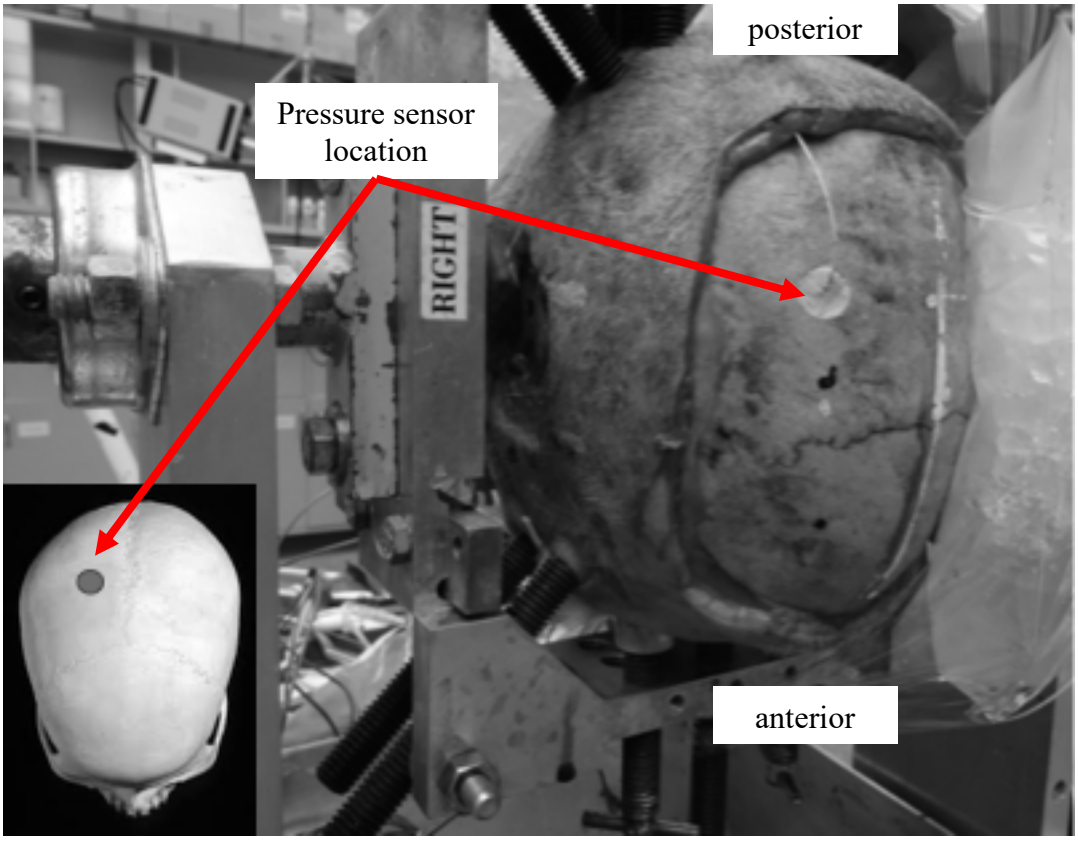

Figure 28: Placement of pressure sensor, skull in bottom left shows orientation and location of sensor placement

4.1.9 Sealing of Exposed Tissues

Neck tissue was trimmed as much as possible to the level of the C2/C3 vertebrae to minimize inertial effects during rotation testing. Tissues left after neck trimming, and scalp removal were sealed to prevent fluid leakage. All exposed tissues were sealed using gel cyanoacrylate (Loctite 426 Instant Adhesive, Loctite, Henkel Corporation, Düsseldorf, Germany).

4.1.10 Instrumentation

The rotation shaft and both sides of the cage were instrumented with angular rate sensors (DTS ARS18K PRO, Diversified Technical Systems, Seal Beach, CA) to measure rotational velocity about the Y-axis. Uniaxial accelerometers (7264C-2K, Endevco, San Juan Capistano, CA) were fixed to the anterior and posterior cage for calculation of rotational acceleration about the Y-axis during post-processing. As the head was rigidly attached to the cage, the kinematics of the cage and the kinematics of the head were assumed to be the same. A rotary potentiometer was installed on the fixture's rotation shaft to quantify the amount of head rotation for each test. Instrumentation locations on the fixture are shown in Figure 14.

4.1.11 Rotation Testing

4.1.11.1 Rotation Fixture

The cage was mounted on a steel shaft in the custom rotation fixture. Adjustability of the input pressure, moment arm length (Figure 29), and initial piston position (Figure 30) allows for specific tuning of the applied kinematic parameters for each test.

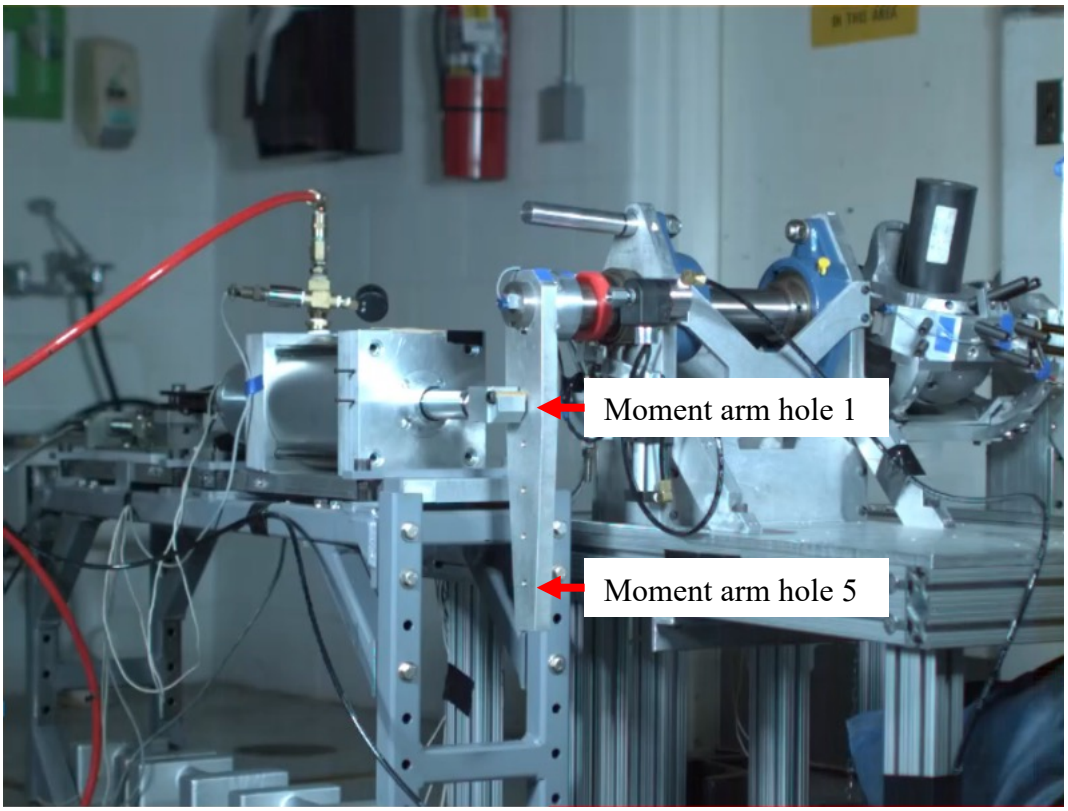

Figure 29: Adjustable moment arm length

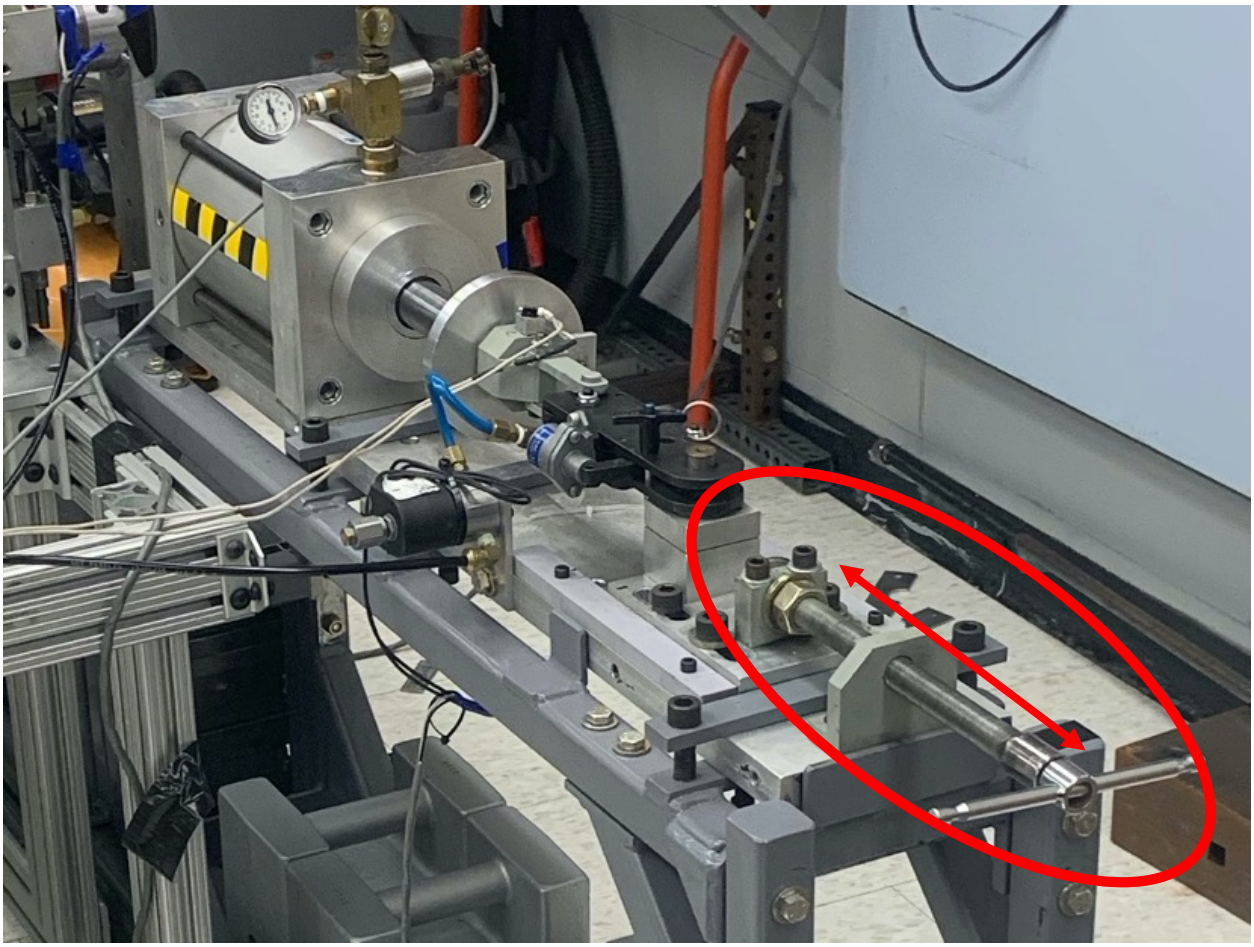

Figure 30: Adjustable initial piston positions

The brake (Figure 31) has a cam with a long lobe that rides along a microswitch arm, keeping the microswitch in the “off” position. As the moment arm is propelled forward by the pneumatic ram, the cam rotates away from the microswitch, moving into the “on” position. This triggers a solenoid allowing air into the pneumatic brake cylinder, pushing up on the moment arm. The moment arm tightens a strap brake on the rotation axle and gradually slows the head for a softer braking pulse.

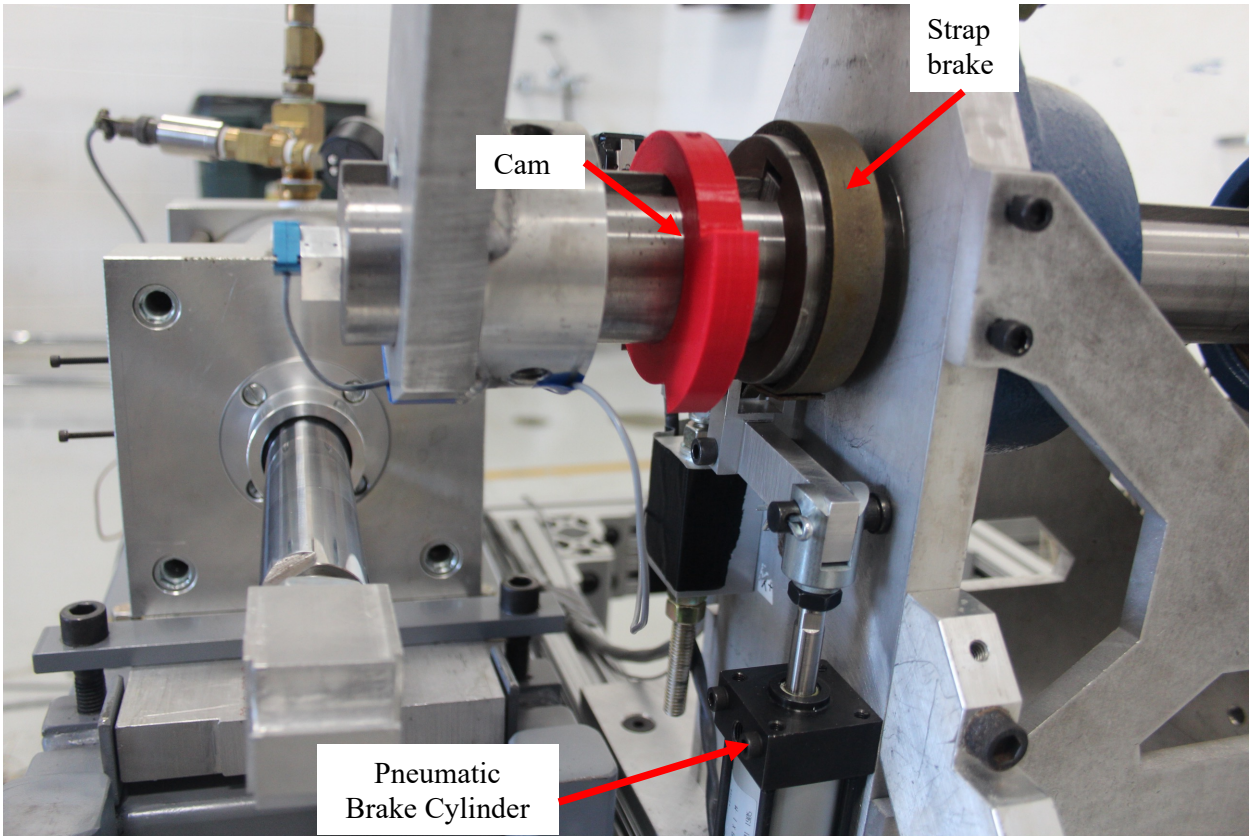

Figure 31: Braking system

A secondary function of the adjustable cam is the ability to regulate when the brake is engaged, therefore controlling the amount of time the head is in free flight. The brake was set to allow for a long enough period of free flight to capture peak brain displacement while also optimizing for the least severe brake pulse.

4.1.11.3 Test Matrix Development

The design of the rotation fixture allows for a greater ability to control the pulse as well as the ability to vary rotational acceleration and rotational velocity independently. Historically, experimental studies of acute subdural hematoma have focused on the effects of rotational acceleration, though physics and research on other head injuries would suggest that rotational velocity is more likely the dominant parameter. Therefore, the requirements of the initial test matrix for the first subject test were:

- To vary rotational acceleration and rotational velocity independently to inform which of these parameters has more effect on brain motion,
- To limit the severity of the tests to ensure the ultrasound brain motion could be tracked based on what could be tracked during the fresh subject trial, and
- To complete testing in a relatively short amount of time, since preliminary data from the fresh subject trial indicated that postmortem degradation could affect the motion of the brain.

The test setup was designed to minimize linear accelerations and off-axis rotations of the head for all loading severities. The test matrix for subjects 1-3 is shown in Table 7.

Table 7: Main test matrix for subjects 1-3

Test #	Description	Estimated Kinematic Input	
		Rotational Acceleration (rad/s/s)	Rotational Velocity (rad/s)
01	Baseline	800	8.50
02	Baseline	800	8.50
03	Baseline	800	8.50
04	Test 1	2040	18.7
05	Baseline	800	8.50
06	Test 2	2400	21.5
07	Baseline	800	8.50
08	Test 3	1750	24.1
09	Baseline	800	8.50
10	Test 4	2200	27.3
11	Baseline	800	8.50

Three lower-severity “baseline” tests were conducted at the start of rotation testing for analysis of kinematic and displacement repeatability. A baseline test was conducted in between each higher-severity test to assess whether any damage occurred in the brain tissue because of a higher severity test or from multiple rotation tests on a single subject. Four higher-severity tests in addition to the first three baselines and baselines in between compose the main test matrix for subjects 1-3. Following the main test matrix, which consists of the 11 tests in Table 7, additional testing was conducted to investigate the trackability of the ultrasound images collected at increasing rotational velocities and rotational accelerations. The post-test matrices for subjects 1-3 are found in Appendices B-D, respectively.

The test matrices for subjects 1-3 utilized the same kinematic inputs to investigate the influence of subject-specific characteristics on peak brain displacements. The main test matrices for subjects 4 (Table 8) and 5 (Table 9) prioritized tests with higher kinematics.

Table 8: Test matrix for subject 4

Test #	Description	Estimated Kinematic Input	
		Rotational Acceleration (rad/s/s)	Rotational Velocity (rad/s)
01	Baseline	800	8.50
02	Test 1	2750	21.1
03	Baseline	800	8.50
04	Test 2	3240	30.5
05	Baseline	800	8.50
06	Test 3	3750	26.4
07	Baseline	800	8.50
08	Test 4	4000	33.0
09	Baseline	800	8.50

Table 9: Test matrix for subject 5

Test #	Description	Estimated Kinematic Input	
		Rotational Acceleration (rad/s/s)	Rotational Velocity (rad/s)
01	Baseline	800	8.50
02	Baseline	800	8.50
03	Test 1	2800	22.2
04	Baseline	800	8.50
05	Test 2	3200	31.0
06	Baseline	800	8.50
07	Test 3	3700	27.1
08	Baseline	800	8.50
09	Test 4	4750	42.3
10	Baseline	800	8.50

4.1.12 Determination of Head CG and MOI

Moment of inertia (MOI) of the head and cage was estimated using pendulum rotation tests. MOI of the remaining rotating portions of the fixture, including the shaft and moment arm were calculated according to their geometric and material properties. The MOI was calculated using the equation for a simple pendulum [Equation 7]

$$T = 2\pi\sqrt{\frac{I}{mgR}} \quad for\ small\ \theta \tag{7}$$

where T is the calculated period, I is the moment of inertia, m is the mass, g is gravity, and R is the radius of gyration of the pendulum. Equation [7] only holds for small oscillation angles but can be corrected using the large angle correction formula in Equation [8].

$$T_{corrected} = \frac{T}{1+\frac{1}{16}\theta^2+\frac{11}{3072}\theta^4+\cdots} \tag{8}$$

The MOI for the oscillating system can be calculated by rearranging Equations [7] and [8] to get Equation [9].

$$I = mgR\left(\frac{T}{2\pi(1+\frac{1}{16}\theta^2+\frac{11}{3072}\theta^4+\cdots)}\right)^2 \quad [9]$$

The mass, m, of the head and cage was measured directly. To measure the radius of gyration, the head and cage were allowed to hang from two different positions on the cage such that the center of mass would locate itself below the center of the shaft (Figure 32).

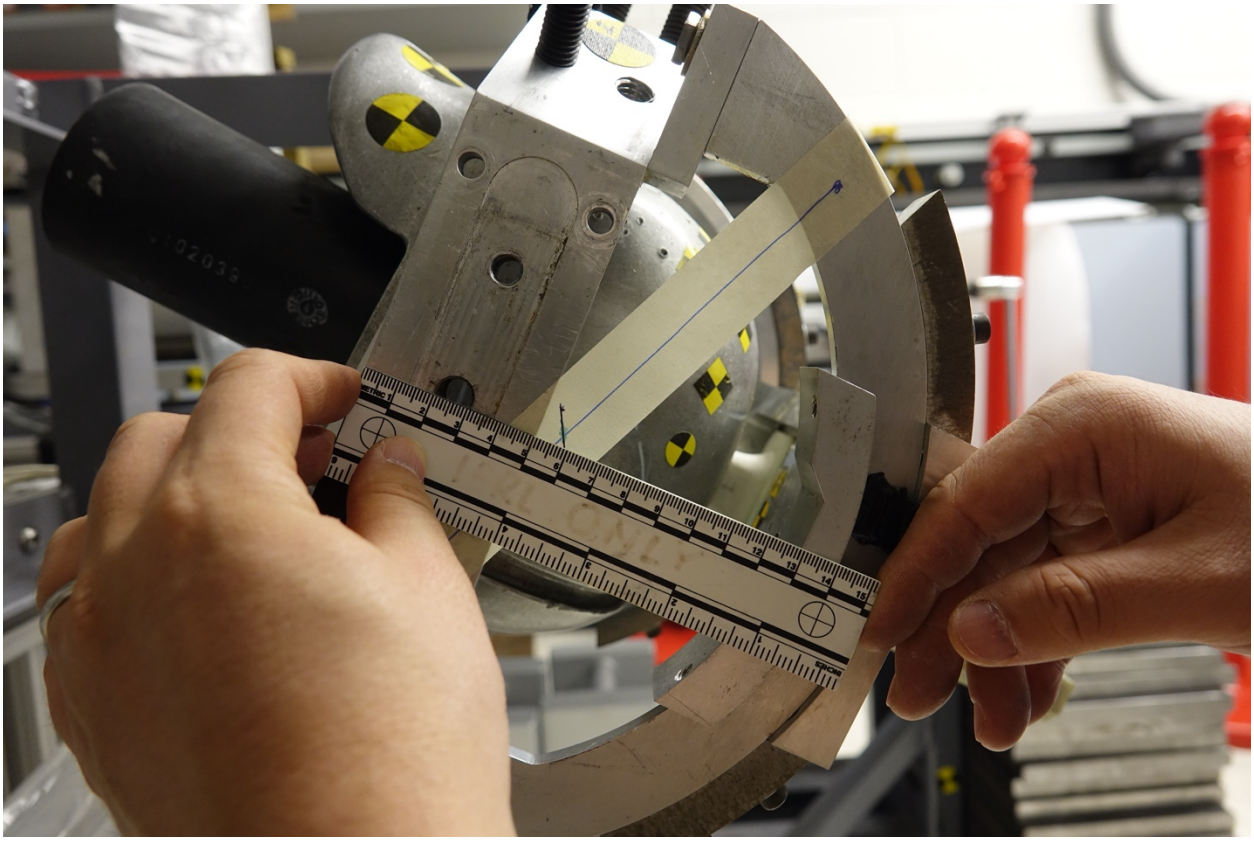

Figure 32: Intersection of the vertical lines through the center mounting hole of the cage indicates the system's center of gravity. The distance from the measured CG to the center mounting hole was used as the radius of gyration for the calculation of MOI

In each position, a vertically aligned laser was centered through the center of the shaft. The intersection point of the vertical lines drawn in each position was measured to the center mounting hole on the cage, representing the radius of gyration.

To measure the period, T, of the head and cage during the oscillation tests, the head was allowed to rotate freely in the posterior-anterior direction under the influence of gravity. The cage was instrumented with a rotary potentiometer that was used to determine the period. The large-angle correction was applied to each period, and the average period was used for the calculation of I. The MOI of the rotating portions of the fixture were subtracted from the total MOI to determine the isolated MOI of the head and cage system only, including the ultrasound probe and the components that secure the probe to the cage. Further, the MOI of the fixture's rotation shaft and moment arm were added in to determine the MOI of the entire rotating system. Also reported was the isolated MOI of the head itself.

4.1.13 Data Analysis

The primary measures in this study included the ultrasound images of the brain motion as well as the kinematics of the head and cage. Each of the test subjects was analyzed individually before subject-to-subject comparisons were made.

Kinematic data were measured using the sign convention according to SAE J211 (SAE, 2014). Data were recorded at 20 kHz using TDAS G5 software/hardware (Diversified Technical Systems, Seal Beach, CA). Rotational velocity and rotational acceleration data were processed by removing offsets prior to a motion and filtered at CFC 180 and CFC60, respectively, using a commercial data analysis software (MATLAB, MathWorks, Natick, MA). The rotational acceleration of the cage was found by calculating the difference between the front and rear cage

accelerometers and dividing by the distance between them. A rotary potentiometer was installed on the shaft of the cage to measure the angle through which the cage rotated.

Tissue tracking video sequences collected by B-mode ultrasound were analyzed using a commercial video tracking software (TEMA, Image System, Linköping, Sweden). The tracking of points on the cortex surface, 1 mm deep into the cortex, and 2 mm deep into the cortex were tracked semi-automatically, and the time histories were obtained. As image lines across the ultrasound image are collected sequentially, the use of the ultrasound probe under high-rate motion offers the potential for the collected images to be spatiotemporally distorted. Therefore, a spatiotemporal correction was applied to each of the tracked tests during post-processing (Mallory et al., 2018). The ultrasound probe was installed in such a way that it collected images in a retrograde orientation, meaning that the tissue motion was in the opposite direction as the sweep of the ultrasound. Figure 33 shows the orientation of the ultrasound probe in the way it was used during PMHS testing.

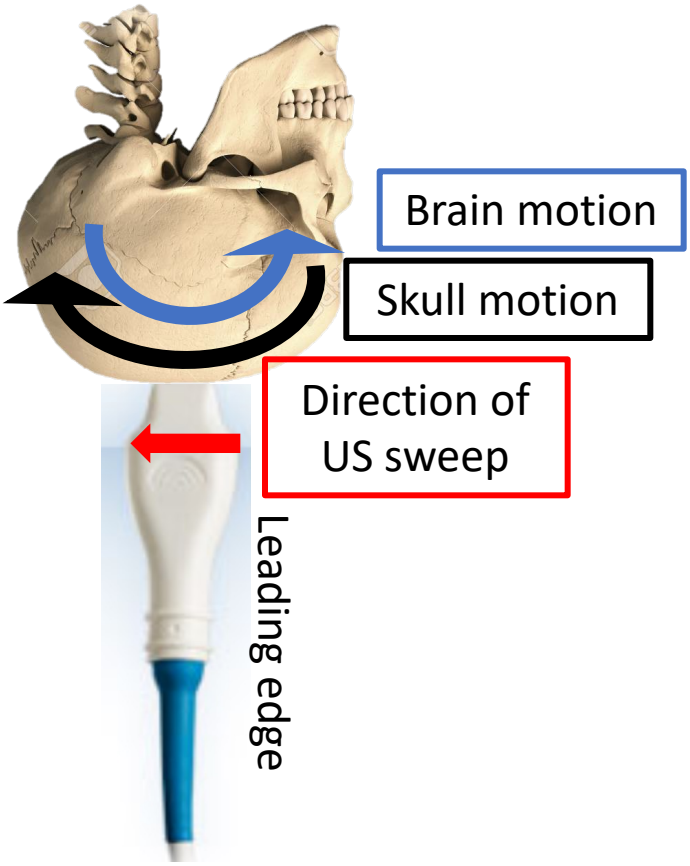

Figure 33: Retrograde orientation of ultrasound probe during PMHS testing

When images are collected in the retrograde orientation, points on the ultrasound image appear to be closer together than actuality due to the time it takes for the sweep of the ultrasound to finalize data collection. Therefore, the following correction was applied to correct the data during post-processing [Equation 10]

$$t_{actual} = t_0 * FR * \left(\frac{x}{x_{width}}\right) \quad [10]$$

where t_{actual} is the corrected time, t_0 is the uncorrected time, FR is the frame rate at which the data was collected, x is the x-position of the tracked point in the frame, and x_{width} is the width of the entire ultrasound image.

Multiple tracked points were used to estimate the cumulative displacement of the brain tissue. After each new tracked point was added, the time-displacement of the previously tracked points was curve-fit using a shape-preserving piecewise cubic interpolation in MATLAB. (MATLAB, MathWorks, Natick, MA).

4.2 PMHS Testing Results

4.2.1 Preliminary Fresh Subject Trial

A fresh PMHS subject trial was conducted for both verification of methods as well as the collection of preliminary data. It should be noted that the fresh subject trial did not include quantification of atrophy or pressurization of the brain during rotation testing as a pressurization trial was conducted post-test for method development. Preparation for rotation testing was completed within 47 hours of postmortem time, and the completion of rotation testing occurred within 58 hours of postmortem time. The breakdown of timing for each procedure is summarized in Table 10. Timing information was used as a benchmark for approximating time for future tests.

Table 10: Summary of test timing for fresh subject trial

Procedure	Time to Complete	Total Elapsed Postmortem Time
Pre-Procedure Preparation	1 hour 11 minutes	32 hours 11 minutes
Initial Body Preparation and Disarticulation	1 hour 54 minutes	34 hours 5 minutes
Subarachnoid Perfusion	17 minutes	34 hours 22 minutes
Flush with Preservatives	5 hours 3 minutes	39 hours 25 minutes
Positioning the Head	1 hour 44 minutes	41 hours 9 minutes
Window Preparation and Head Instrumentation	2 hours 43 minutes	43 hours 52 minutes
Setup in Rotation Fixture	2 hours 57 minutes	46 hours 49 minutes
Rotation Testing	11 hours 13 minutes	58 hours 2 minutes

During rotation testing, a total of 11 lower-severity tests were conducted as well as 9 higher-severity, pneumatic tests. Of these tests conducted, brain motion from only one higher-severity pneumatic test was able to be tracked and analyzed. Results from all trackable tests are summarized in Table 11.

For the lower-severity tests, the head was allowed to rotate in a posterior-anterior direction under the force of gravity from rest until contact with a padded stop, when it decelerates to a stop, i.e., accelerating in an anterior-posterior direction to match the loading of the higher-severity tests. For the added mass test, 480 grams of additional weight was added to the cage to slightly increase the severity of the deceleration using the gravity drop procedure.

Maximum displacement from each tracked location including the cortex surface, 1 mm deep in the cortex, and 2 mm deep in the cortex are recorded in Table 11. Since the dura was

firmly attached to the skull, it was assumed that any motion relative to the dura could be used to estimate motion relative to the skull.

Table 11: Fresh subject trial displacement results

Test Number	Test Type	Postmortem Time (hours)	Rotational velocity (rad/s)	Rotational acceleration (rad/s^2)	Max displacement relative to dura		
					Cortex surface (mm)	1 mm deep (mm)	2 mm deep (mm)
1	Baseline	50.30	2.18	117	0.01	0.06	0.07
2		50.52	2.11	121	0.02	0.05	0.07
3		50.67	2.06	117	0.01	0.05	0.06
4		50.88	2.08	120	0.01	0.01	0.02
5		51.55	2.13	118	0.02	0.06	0.08
6		52.45	2.01	117	0.03	0.09	0.09
7		52.63	2.15	131	0.01	0.10	0.12
8		52.77	2.04	122	0.03	0.08	0.09
9	Added mass	52.90	3.80	477	0.06	0.18	0.23
10	Baseline	53.12	2.09	112	0.02	0.08	0.08
11	Higher severity	53.86	26.2	3144	2.00	3.28	3.41
12	Baseline	54.13	2.13	135	0.02	0.11	0.14

The time history for the highest-trackable test is shown in Figure 34.

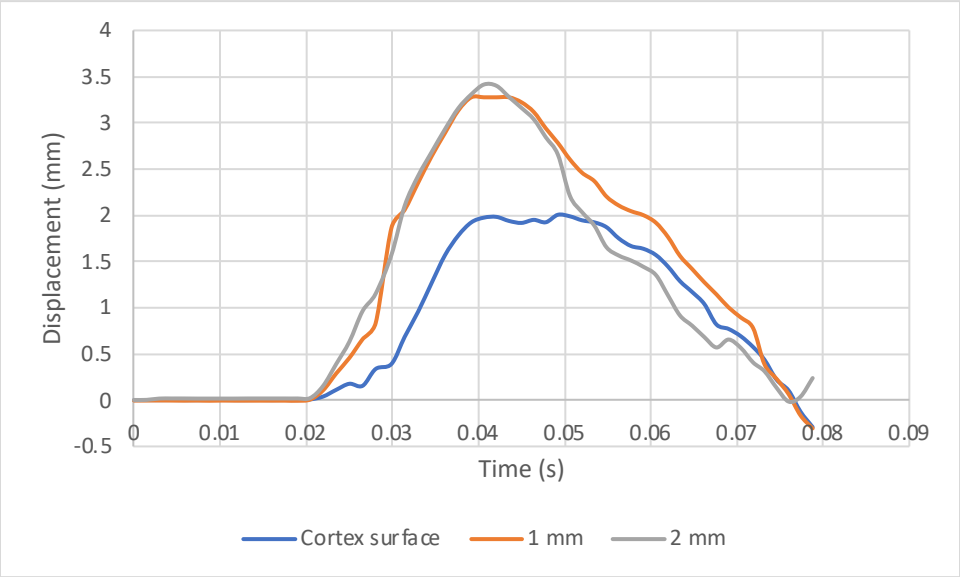

Figure 34: Fresh subject trial brain displacement time history for highest-severity test

4.2.2 Fresh Subject Tests

Rotation testing was completed using five postmortem human subjects. All testing was complete within 56 hours postmortem. When making subject-to-subject comparisons, it is important to recognize the potentially confounding variables that could result in differences in peak displacement results. Of note, differences in the anthropometry, MOI of the head and neck, BPF, and postmortem time at which rotation data were collected all have the potential to influence how much the brain moves relative to the skull.

The peak brain displacements for every trackable, non-damaged test were utilized in a multiple linear regression to determine the dependence of brain deformation on postmortem time, angular head kinematics, and MOI, BPF, and brain: head mass ratio of each subject. Analysis of the displacement results indicated that subjects 2 and 5 experienced a damaging test. A more detailed description of the evaluation of damaged tests is found in section 4.3 PMHS Testing Discussion. The model fits had an R^2 ranging from 0.797-0.821. Coefficient values are presented in Table 12.

Table 12: Multiple regression summary statistics for all trackable, non-damaged tests

	Analysis of Variance		Summary of Fit		Parameter Estimates						
					intercept	Postmortem time (hours)	Rotational Velocity (rad/s)	Rotational Acceleration (rad/s/s)	BPF	MOI	Brain: head mass
	F-ratio	df	Adjusted R^2	RMSE	Estimate (p-value)						
Cortex surface	<0.001*	56	0.821	1.514	14.71 (0.001*)	-0.0281 (0.311)	0.405 (<0.001*)	-0.00135 (0.002*)	-22.22 (<0.001*)	-272.5 (0.0028*)	23.08 (0.146)
1mm	<0.001*	63	0.797	1.757	12.86 (0.008*)	-0.0160 (0.537)	0.480 (<0.001*)	-0.0016 (0.001*)	-24.76 (<0.001*)	-232.1 (0.0247*)	29.07 (0.111)
2mm	<0.001*	63	0.799	1.664	12.31 (0.0075*)	-0.0199 (0.471)	0.434 (<0.001*)	-0.0014 (0.003*)	-23.4 (<0.001*)	-260.2 (0.0084*)	31.76 (0.067)
*Indicates statistical significance (p<0.05)											

The multiple regression analysis was statistically significant for all three locations tracked as evidenced by the F-ratio value for each test. The regressions showed a dependence of peak brain displacement on angular velocity, angular acceleration, BPF, and MOI. Significant relationships are shown graphically in Figure 35-Figure 38.

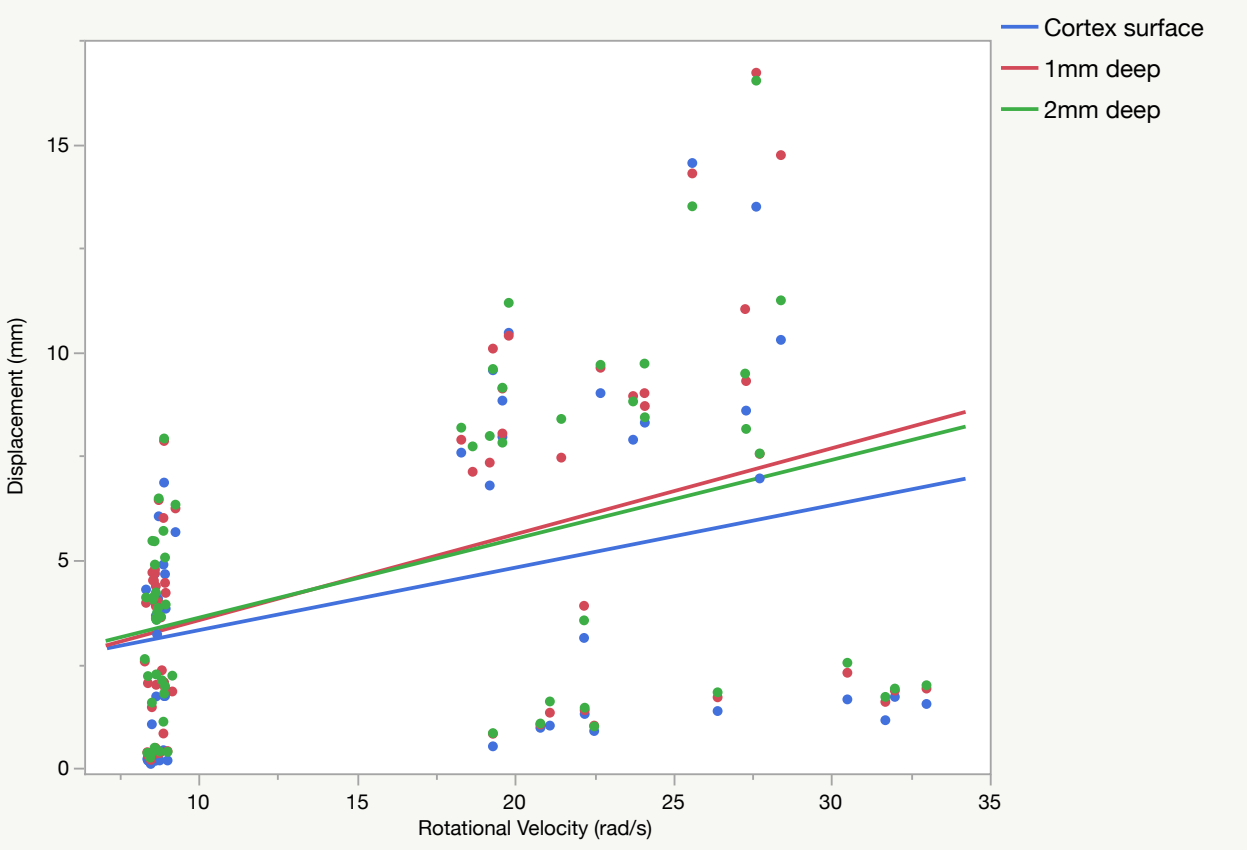

Figure 35: Peak brain displacement of all trackable, non-damaged tests versus rotational velocity

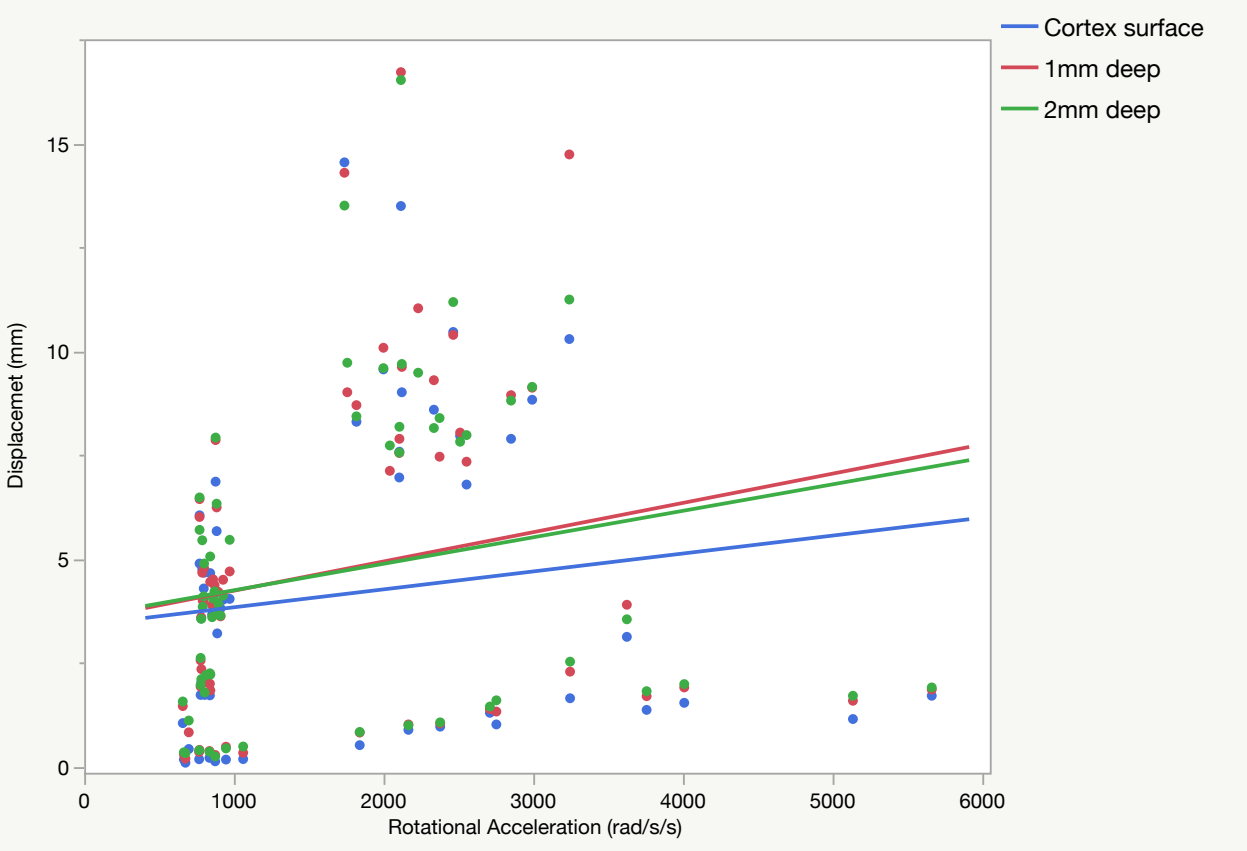

Figure 36: Peak brain displacement of all trackable, non-damaged tests versus rotational acceleration

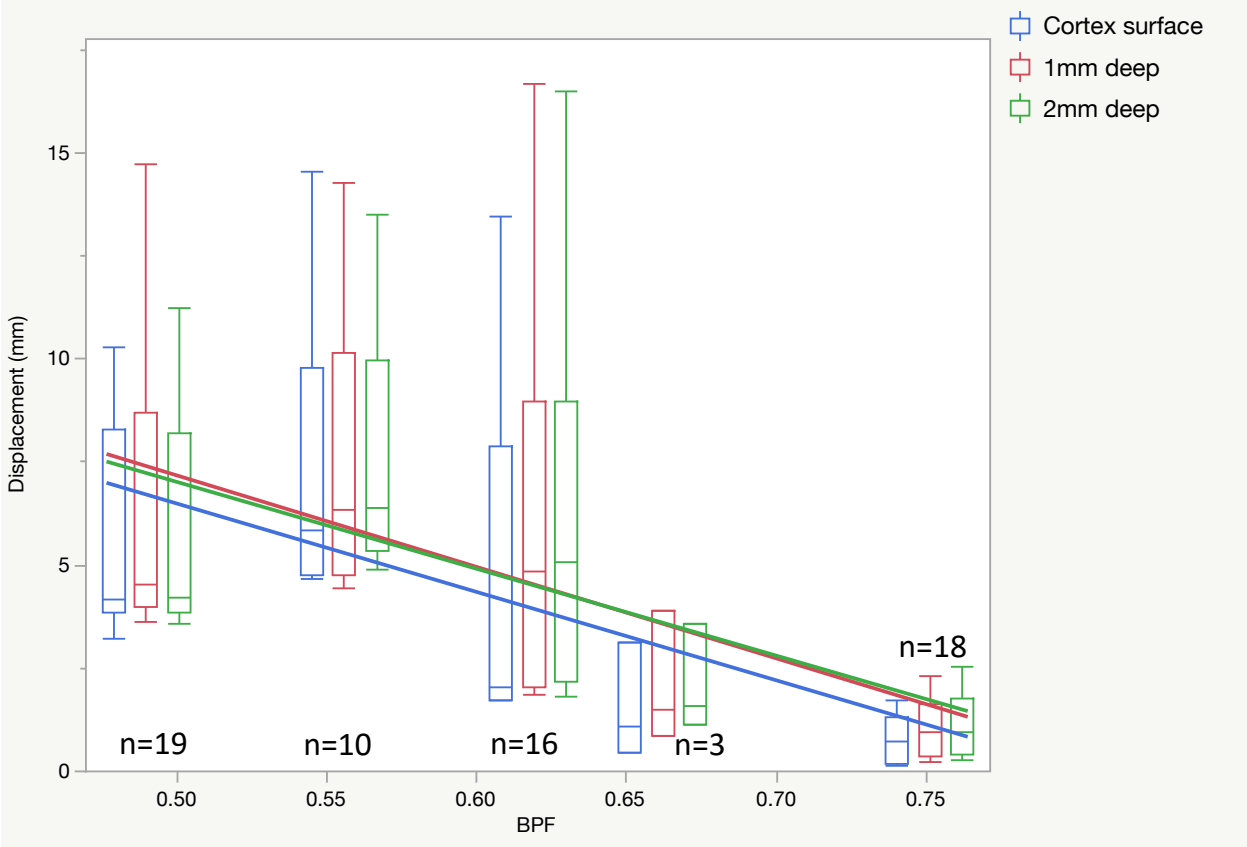

Figure 37: Boxplot of peak displacement of trackable, non-damaged tests versus BPF with trendlines of mean displacement

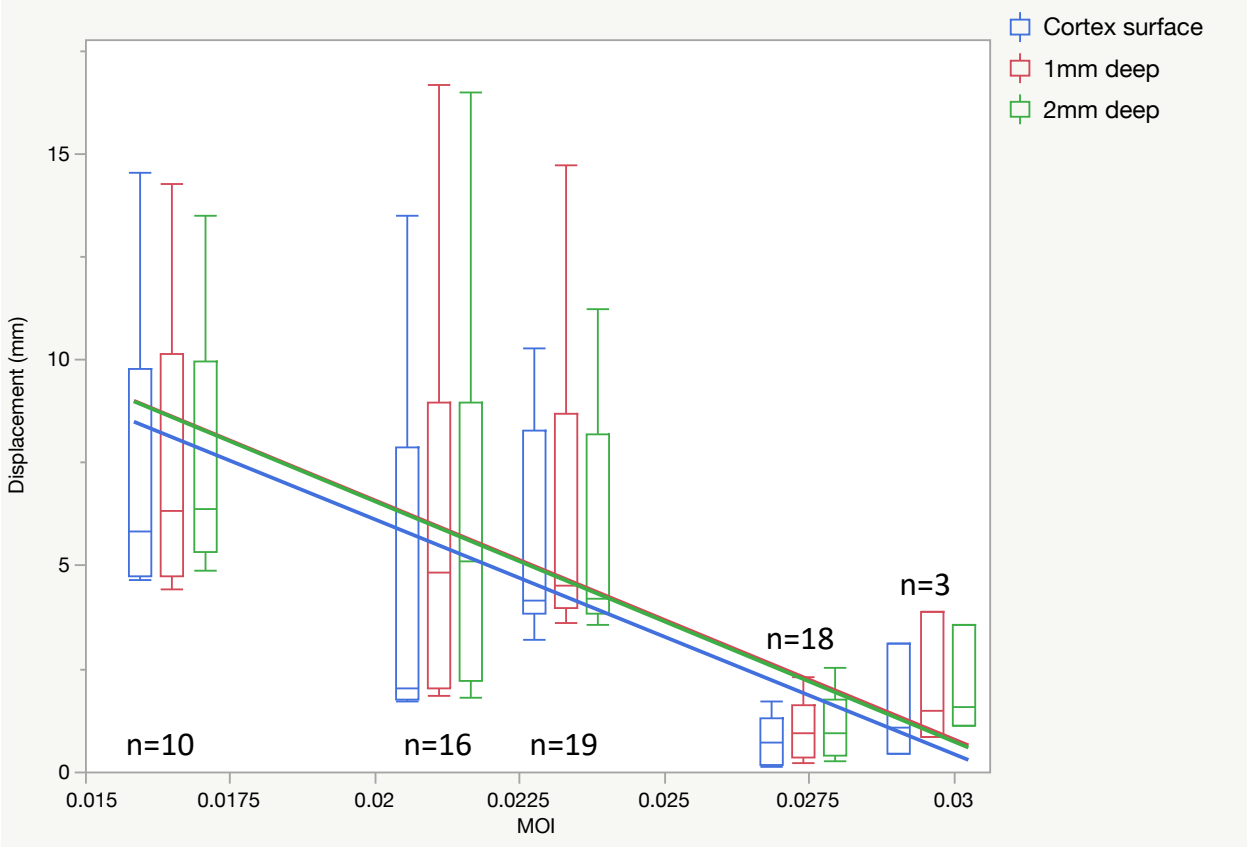

Figure 38: Boxplot of peak displacement of trackable, non-damaged tests versus MOI with trendlines of mean displacement at each tracked location

Results show an increase in brain displacement at all three tracked locations with increases in both rotational velocity and acceleration but decreases in brain displacement with increases in BPF and MOI.

Displacement results from tests with comparable kinematics across all 5 subjects were chosen for further comparison.

Comparison of baseline results

Though the target kinematics for the baseline tests were identical for each subject, due to differences in inertia, there were slight variations in the head kinematics when compared across all subjects. Time history plots of rotational acceleration and rotational velocities for all non-damaged baseline tests for all five subjects are shown in Figure 39.

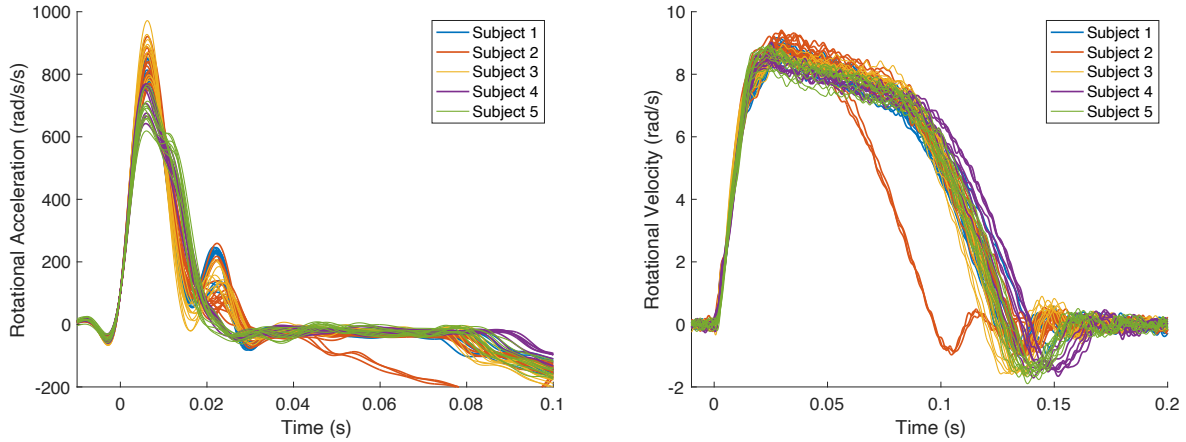

Figure 39: Comparison of baseline kinematics across all five subject tests

The %CV for rotational acceleration was <10% across baseline tests from all 5 subjects, while the %CV for rotational velocity was <5% across baseline tests from all 5 subjects, indicating good kinematic repeatability for the baseline tests. Of note, some tests from subject 2 (shown in orange in Figure 39) have shorter velocity duration compared to the rest of the velocity durations from all 5 subjects. This was due to adjustment of the brake to allow for testing at higher speeds during the post-test matrix.

The peak displacements for each tracked location per subject was quantified and is shown in a box plot in Figure 40.

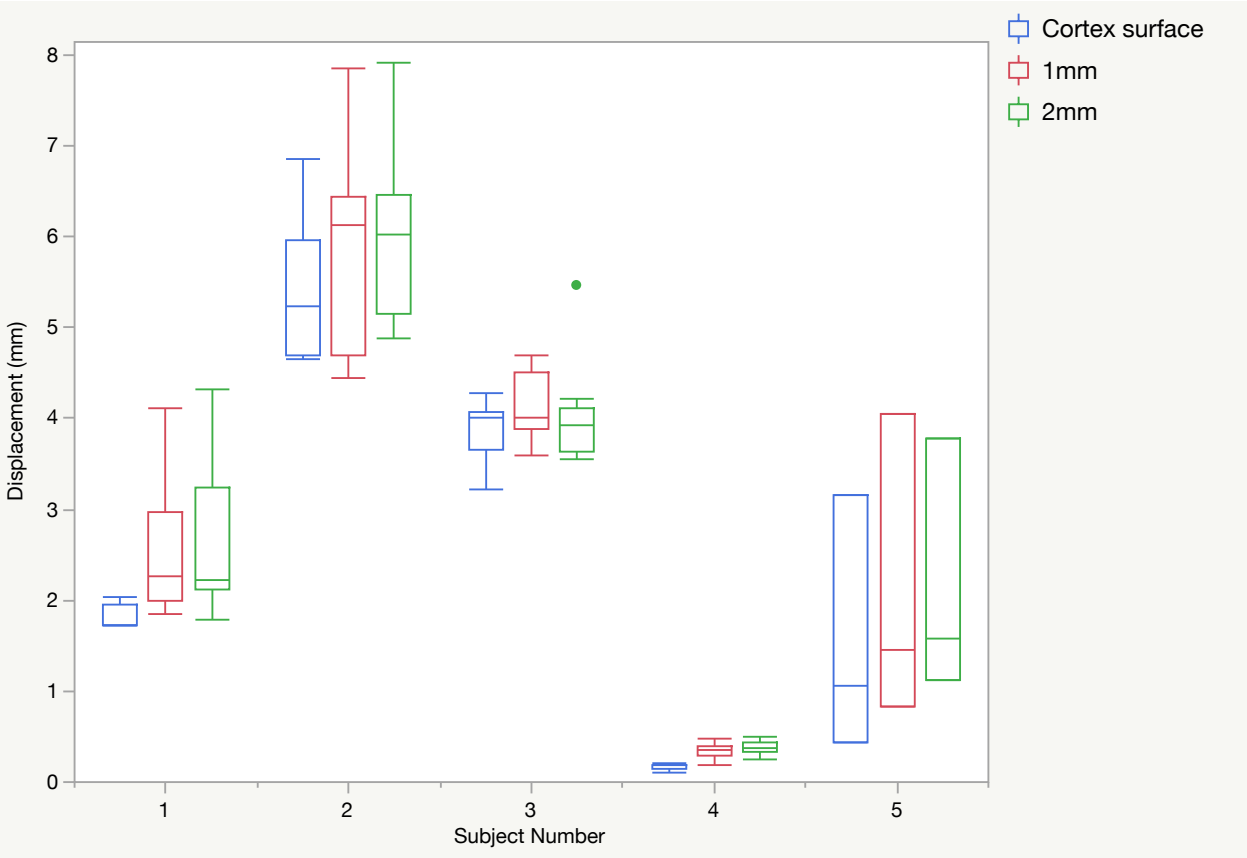

Figure 40: Boxplots of peak displacement for all trackable, non-damaged baselines tests by subject

The peak brain displacements for every trackable, non-damaged baseline test were utilized in a multiple linear regression to determine the dependence of brain deformation on postmortem time, angular head kinematics, and MOI, BPF, and brain: head mass ratio of each

subject. The model fits had an R^2 ranging from 0.888-0.933. Coefficient values are presented in Table 13 .

Table 13: Multiple regression summary statistics for all trackable, non-damaged baseline tests

	Analysis of Variance		Summary of Fit		Parameter Estimates						
					intercept	Postmortem time (hours)	Rotational Velocity (rad/s)	Rotational Acceleration (rad/s/s)	BPF	MOI	Brain: head mass
	F-ratio	df	Adjusted R^2	RMSE	Estimate (p-value)						
Cortex surface	<0.001*	32	0.933	0.541	17.64 (0.0015*)	-0.0566 (<0.001*)	-0.0834 (0.880)	0.0013 (0.331)	-13.83 (<0.001*)	-281.0 (<0.001*)	6.802 (0.422)
1mm	<0.001*	38	0.888	0.686	17.01 (0.0024*)	-0.0671 (<0.001*)	-0.0798 (0.882)	0.0020 (0.232)	-15.43 (<0.001*)	-281.8 (<0.001*)	12.77 (0.227)
2mm	<0.001*	38	0.898	0.661	17.05 (0.0016*)	-0.0713 (<0.001*)	-0.308 (0.554)	0.0026 (0.108)	-16.18 (<0.001*)	-283.9 (<0.001*)	20.37 (0.0499*)
*Indicates statistical significance (p<0.05)											

The multiple regression analysis was statistically significant for all three locations tracked as evidenced by the F-ratio value for each test. The regressions showed a dependence of peak brain displacement on postmortem time, BPF, and MOI.

Regardless of statistical significance, the peak displacements from the baseline tests were plotted against postmortem time for each individual subject. It is expected that due to increasing postmortem time and the accumulation of microdamage from multiple tests on a single subject there will be a linear increase in peak displacement as postmortem time increases. If a baseline peak displacement did not lie on the linear trendline, additional investigation was required to determine if a high-severity test caused damage to the brain tissue. Peak displacement versus postmortem time for subjects 1-5 are shown in Figure 41- Figure 45, respectively.

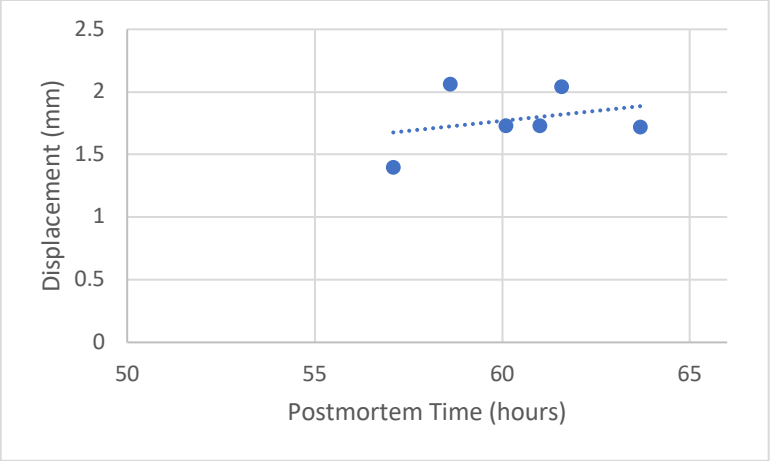

(a) cortex surface

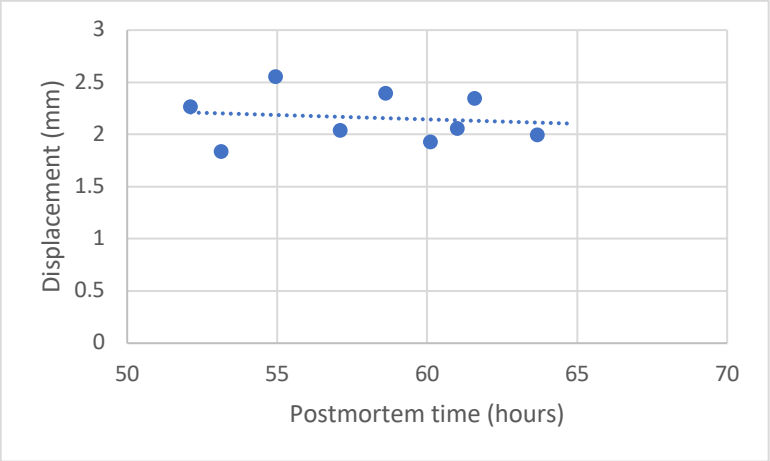

(b) 1 mm deep

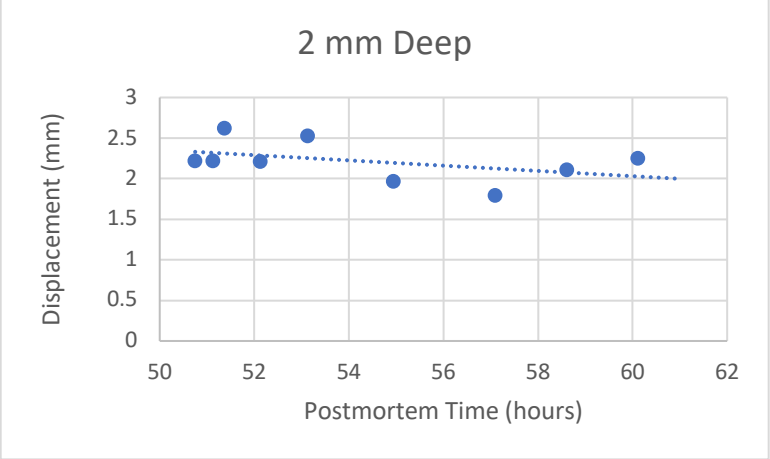

(c) 2 mm deep

Figure 41: Displacement of baseline tests measured at (a) the cortex surface, (b) 1mm deep in the cortex, and (c) 2 mm deep in the cortex versus postmortem time for subject 1

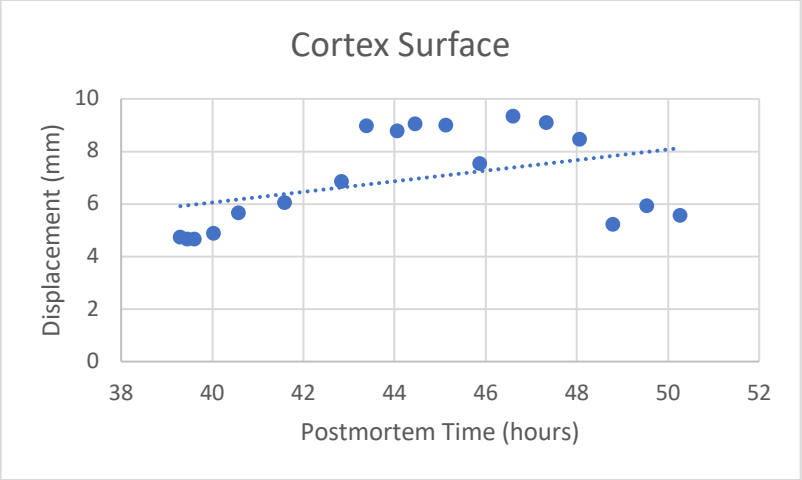

(a) cortex surface

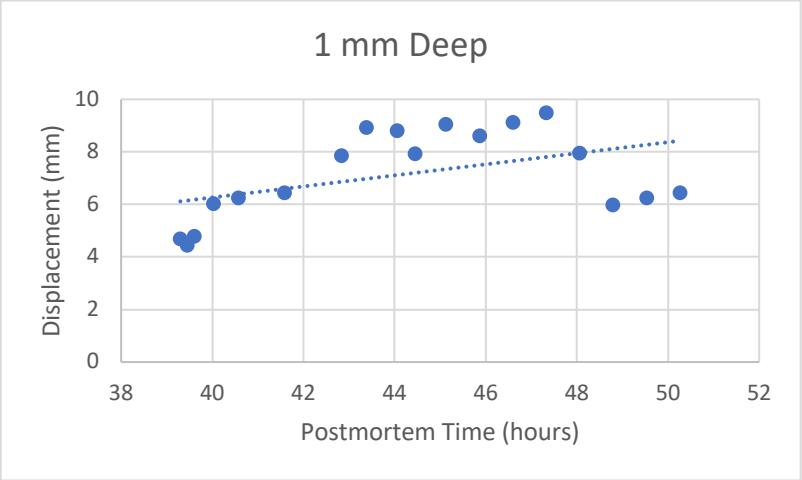

(b) 1 mm deep

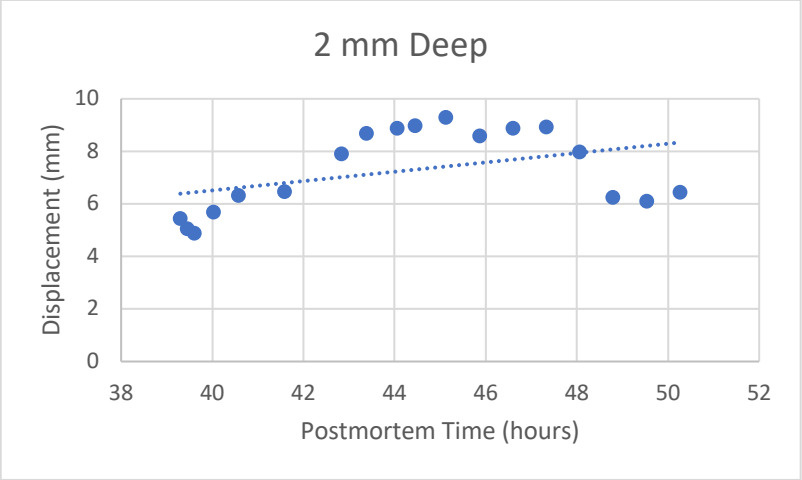

(c) 2 mm deep

Figure 42: Displacement of baseline tests measured at (a) the cortex surface, (b) 1mm deep in the cortex, and (c) 2 mm deep in the cortex versus postmortem time for subject 2

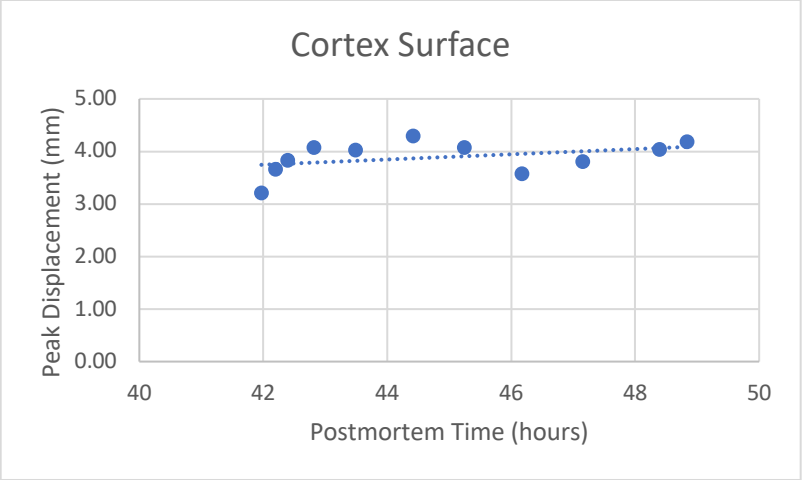

(a) cortex surface

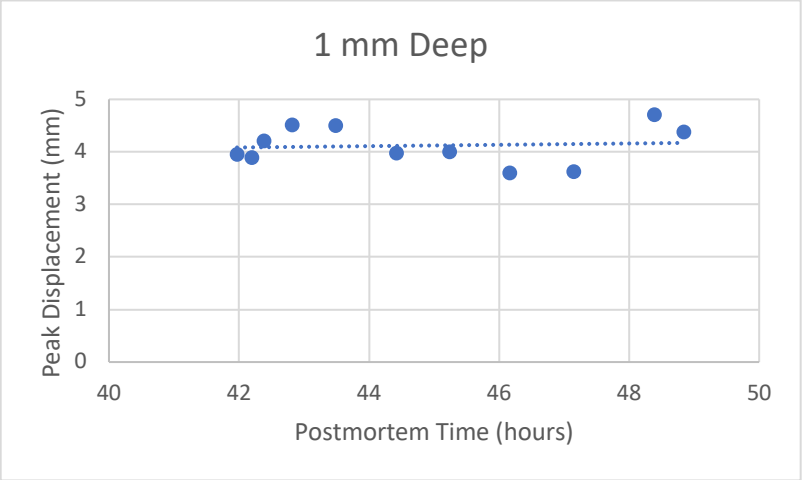

(b) 1 mm deep

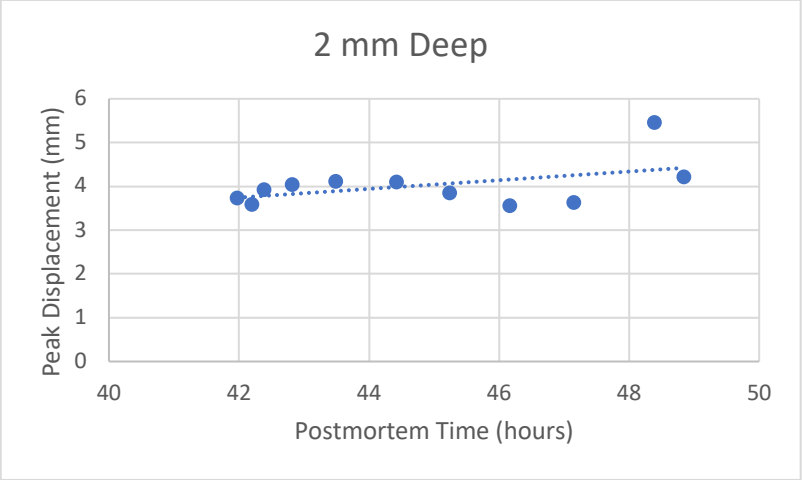

(c) 2 mm deep

Figure 43: Displacement of baseline tests measured at (a) the cortex surface, (b) 1mm deep in the cortex, and (c) 2 mm deep in the cortex versus postmortem time for subject 3

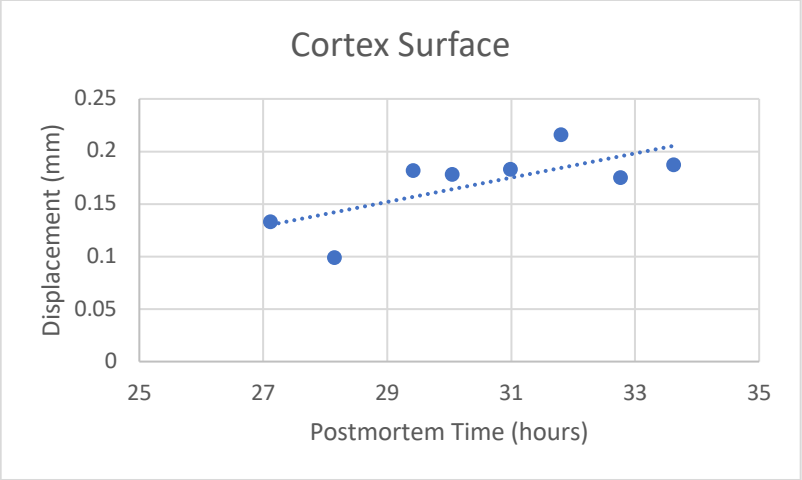

(a) cortex surface

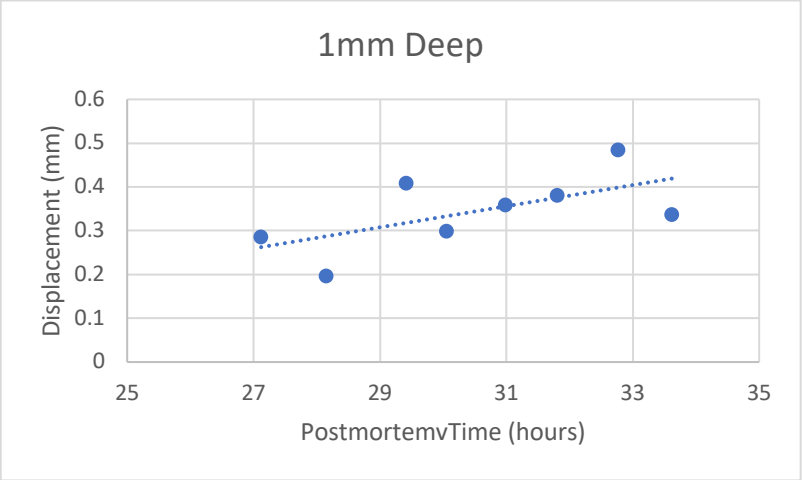

(b) 1 mm deep

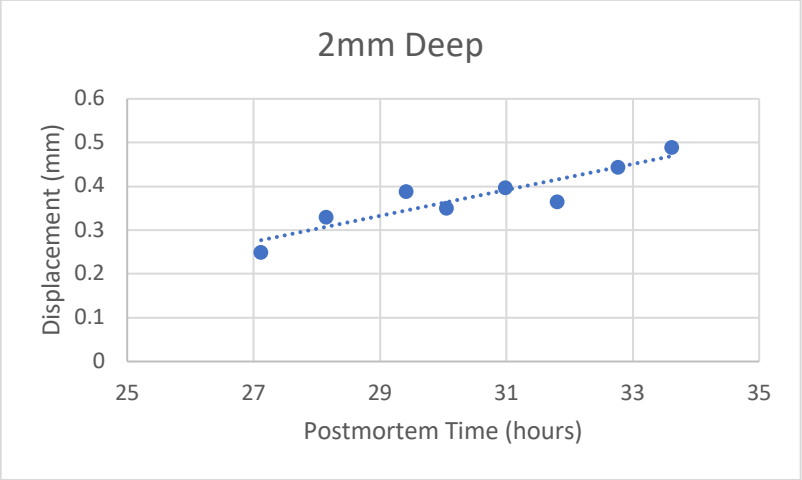

(c) 2 mm deep

Figure 44: Displacement of baseline tests measured at (a) the cortex surface, (b) 1mm deep in the cortex, and (c) 2 mm deep in the cortex versus postmortem time for subject 4

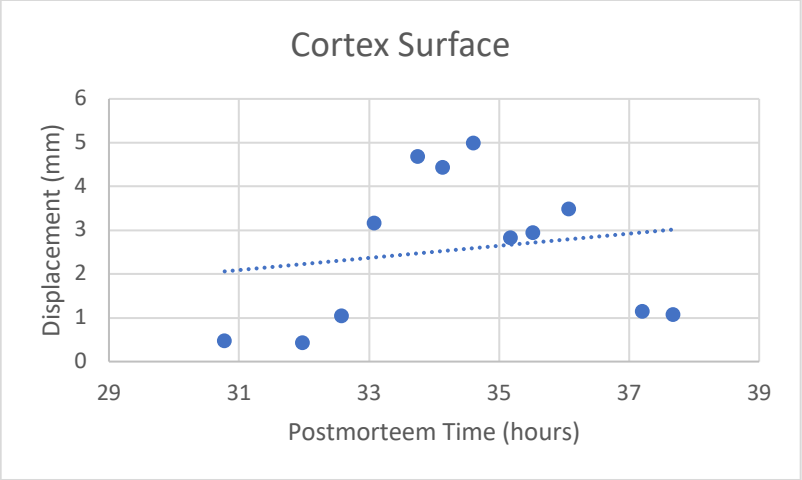

(a) cortex surface

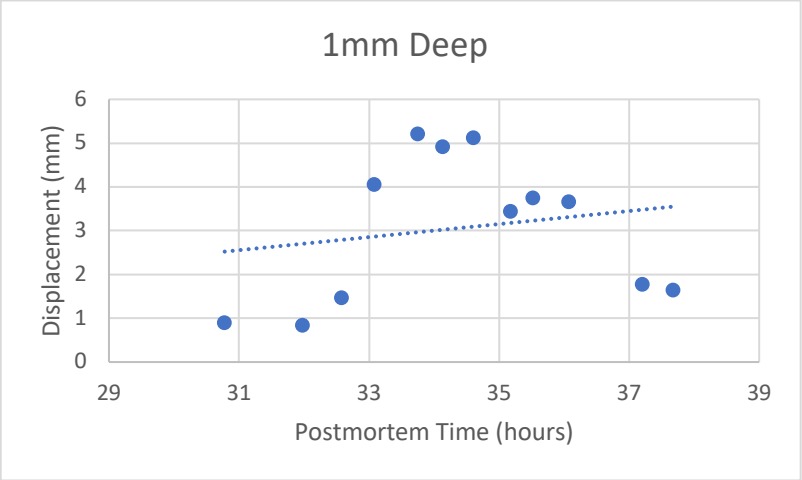

(b) 1 mm deep

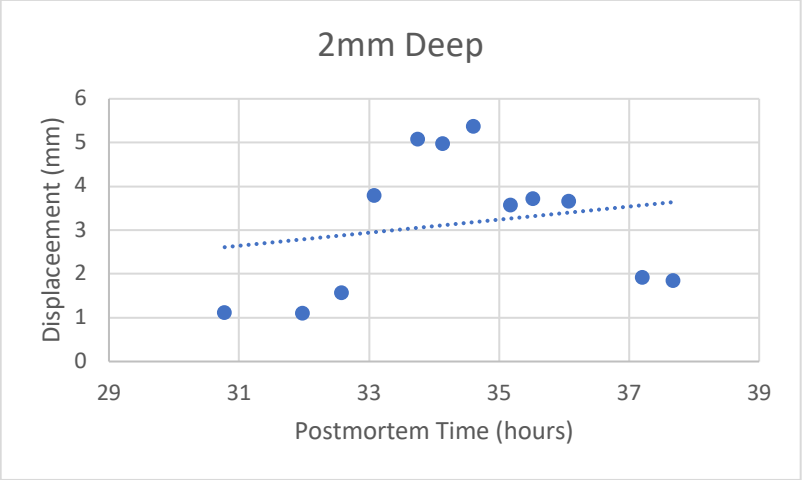

(c) 2 mm deep

Figure 45: Displacement of baseline tests measured at (a) the cortex surface, (b) 1mm deep in the cortex, and (c) 2 mm deep in the cortex versus postmortem time for subject 5

The combined baseline displacement data from all 5 subjects were then plotted against variables indicated as significant in the multiple regressions. Boxplots of the baseline displacements at all three tracked locations are plotted against postmortem time (Figure 46), BPF (Figure 47), and MOI (Figure 48). The number of individual tests in each x-axis category is indicated by the n-value and the number of subjects that had tests in those categories are indicated by the N-values.

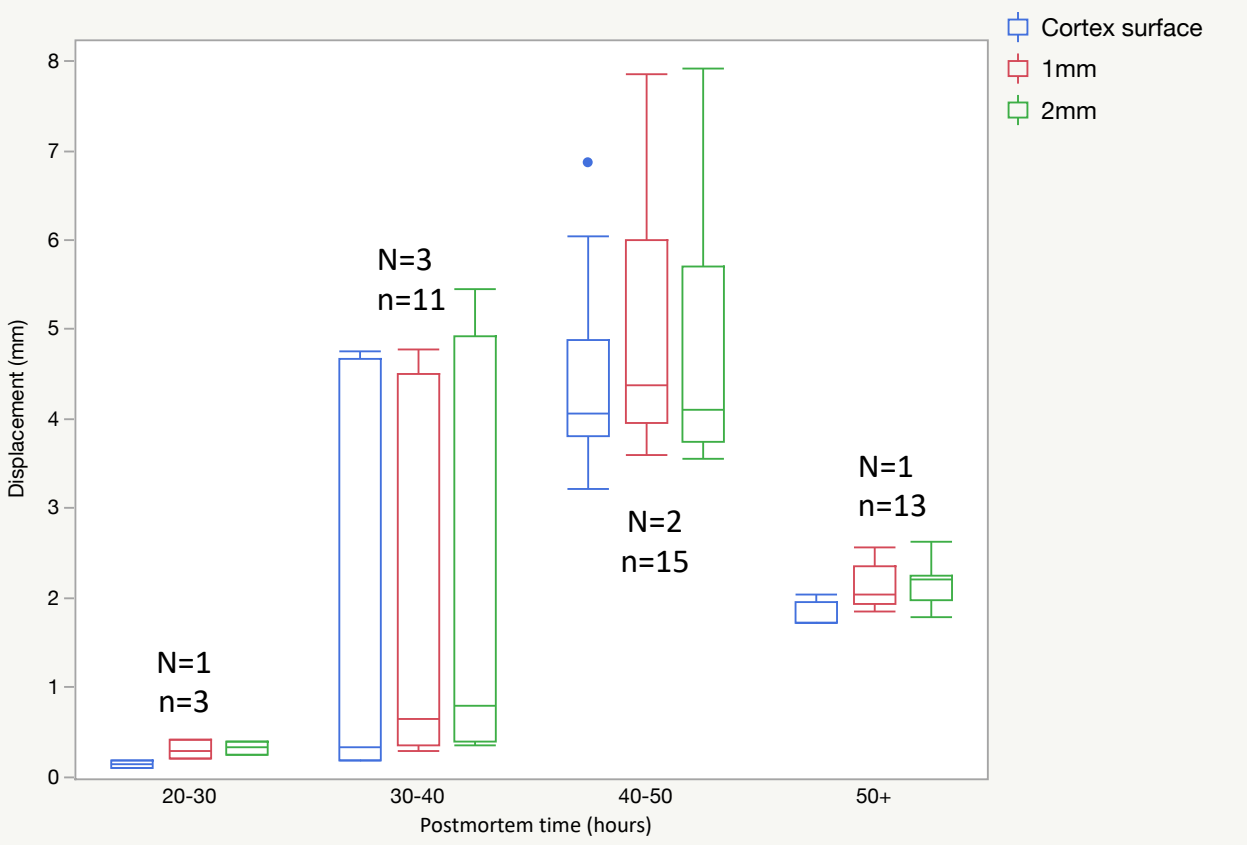

Figure 46: Boxplot of all trackable, non-damaged baseline displacement data versus postmortem time

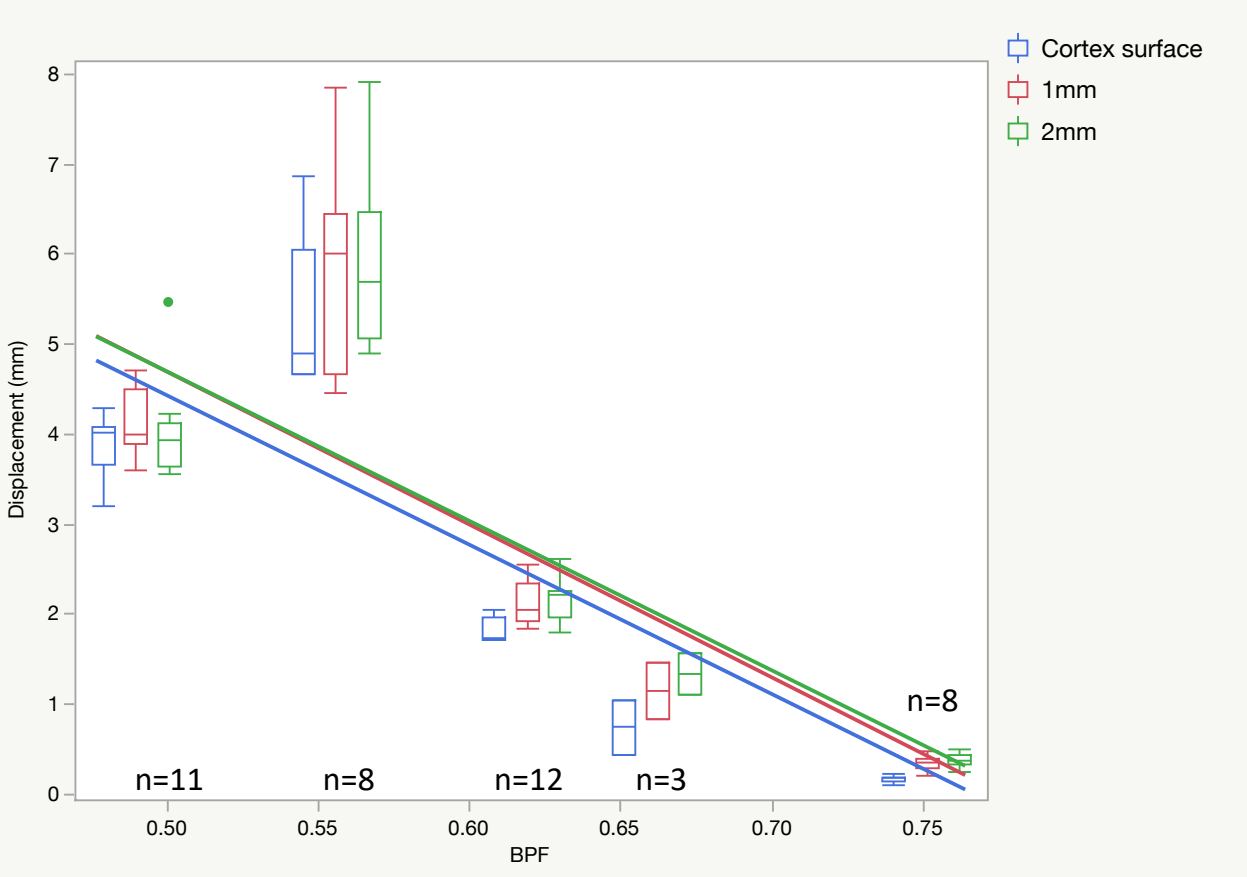

Figure 47: Boxplot of all trackable, non-damaged baseline displacement data versus BPF with trendlines of mean displacement at each tracked location

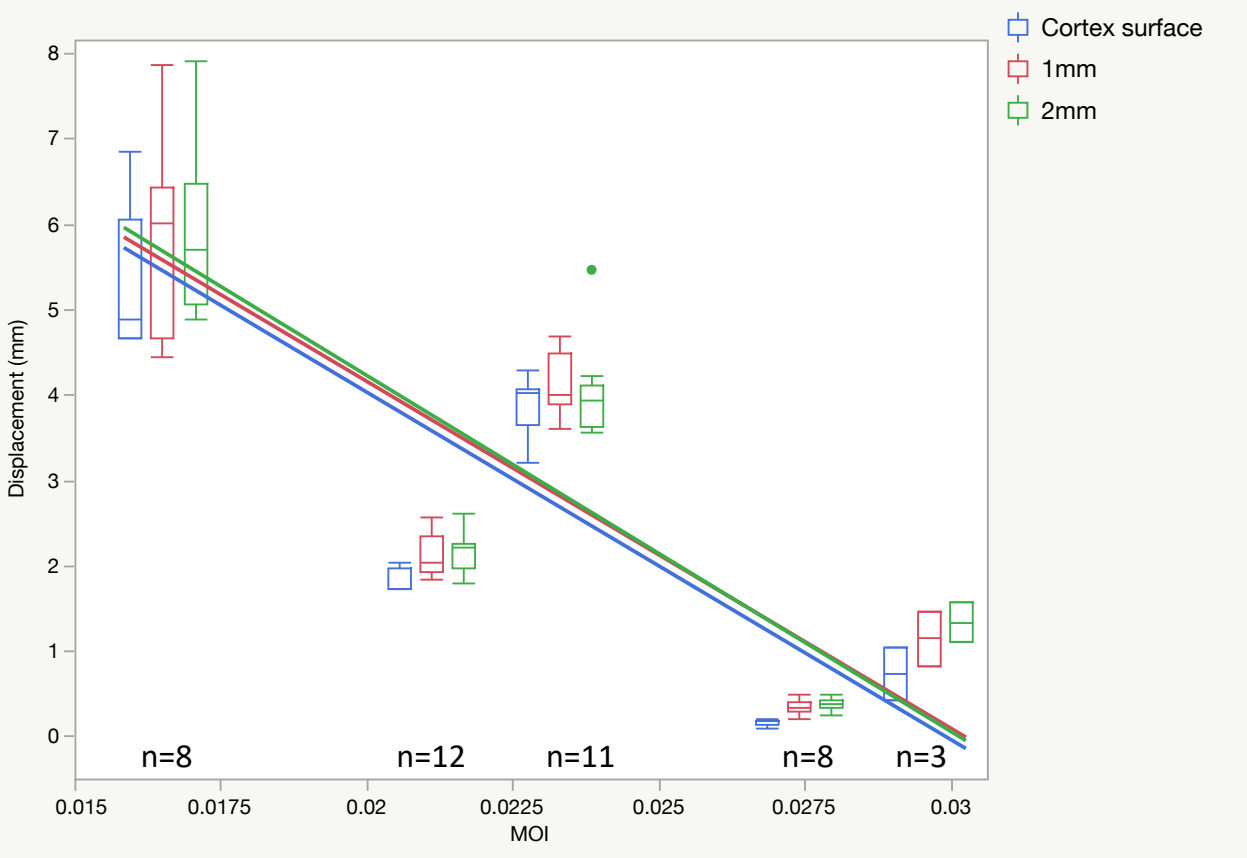

Figure 48: Boxplot of all trackable, non-damaged baseline displacement data versus MOI with trendlines of mean displacement at each tracked location

Though there is not a clear trend between baseline displacement and postmortem time, it was identified by the regression analysis as being statistically significant. Results show decreases in brain displacement at baseline severities with increases in BPF and MOI.

Comparison of higher-severity results

Higher-severity tests with comparable kinematics were chosen to further investigate displacement results across subjects. A summary of tests with higher-severity kinematics are

summarized in Table 14. The %CV for both rotational acceleration and rotational velocity for each test is less than 10%, indicating good kinematic repeatability.

Table 14: Summary of higher-severity tests with comparable kinematics

Subject Number	Test #	Rotational Acceleration (rad/s/s)		Rotational Velocity (rad/s)		Peak Displacement (mm)		
						Cortex surface	1 mm	2 mm
1	1	2040	1950 ± 139	18.7	18.8 ± 0.4	--	5.77	6.35
2		1997		19.3		9.54	10.1	9.6
3		2104		18.3		7.67	7.88	8.14
4		1839		19.3		0.522	0.824	0.839
5		1774		18.6		9.39	9.90	10.0
1	2	2372	2357 ± 173	21.5	20.6 ± 0.9	--	5.32	5.7
2		2463		19.8		10.5	10.4	11.2
3		2509		19.6		7.76	7.92	7.85
4		2376		20.8		0.967	1.04	1.07
1	3	2066	1869 ± 200	21.4	24.1 ± 1.3	8.36	9.07	9.87
2		1756		24.1		14.6	14.2	14.5
3		1737		25.6		8.59	8.71	8.46
4		1817		24.1		0.89	1.02	1.00
1	4	2164	2344 ± 256	22.5	24.3 ± 2.3	10.4	11.8	9.1
2		2229		27.3		15.5	15.4	15.1
3		2317		25.0		9.09	9.41	9.81
4		2120		22.7		1.30	1.39	1.45

4.3 PMHS Testing Discussion

4.3.1 Preliminary Fresh Subject Trial Discussion

To understand the potential effect of degradation on brain motion, further analysis was completed on the 10 lower-severity baseline tests that were conducted over a roughly 4-hour period from 50.3 hours to 54.1 hours postmortem. All the low-severity tests were analyzed to understand how motion results may be affected by postmortem tissue breakdown, and/or

potential damage from high-severity tests. Linear regressions were conducted to examine the relationships between angular velocity, angular acceleration, the number of tests run previously, and postmortem time with the amount of motion tracked at the cortex surface, 1 mm deep in the cortex, and 2 mm deep in the cortex for each test. Plots depicting displacement versus postmortem time for all the low-severity tests at the cortex surface, 1 mm deep, and 2 mm deep are shown in Figure 49.

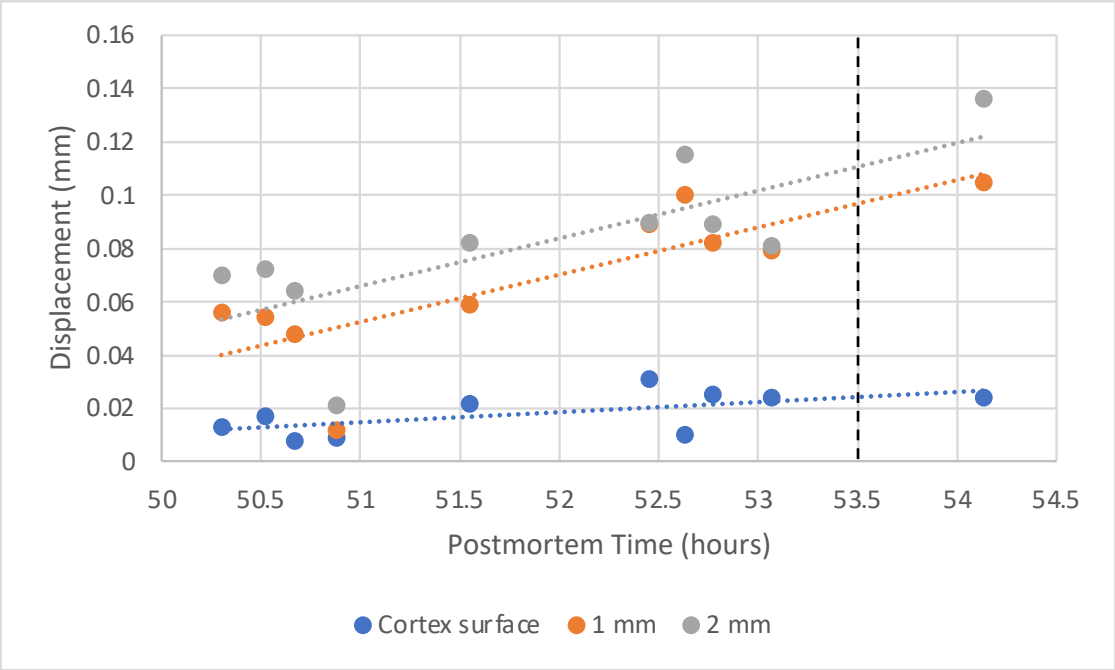

Figure 49: Displacement of fresh subject trial baseline tests vs. postmortem time. Higher-severity test indicated by vertical dashed line

Further, displacement values were plotted against rotational velocity (Figure 50), and rotational acceleration (Figure 51).

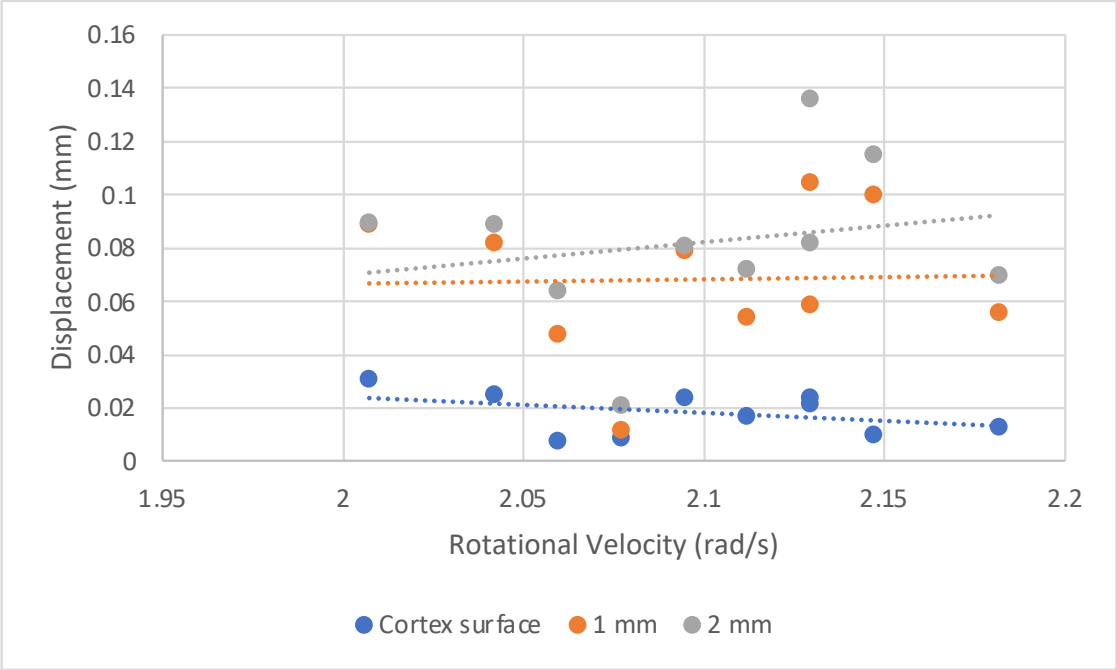

Figure 50: Displacement of fresh subject trial baseline tests vs. rotational velocity

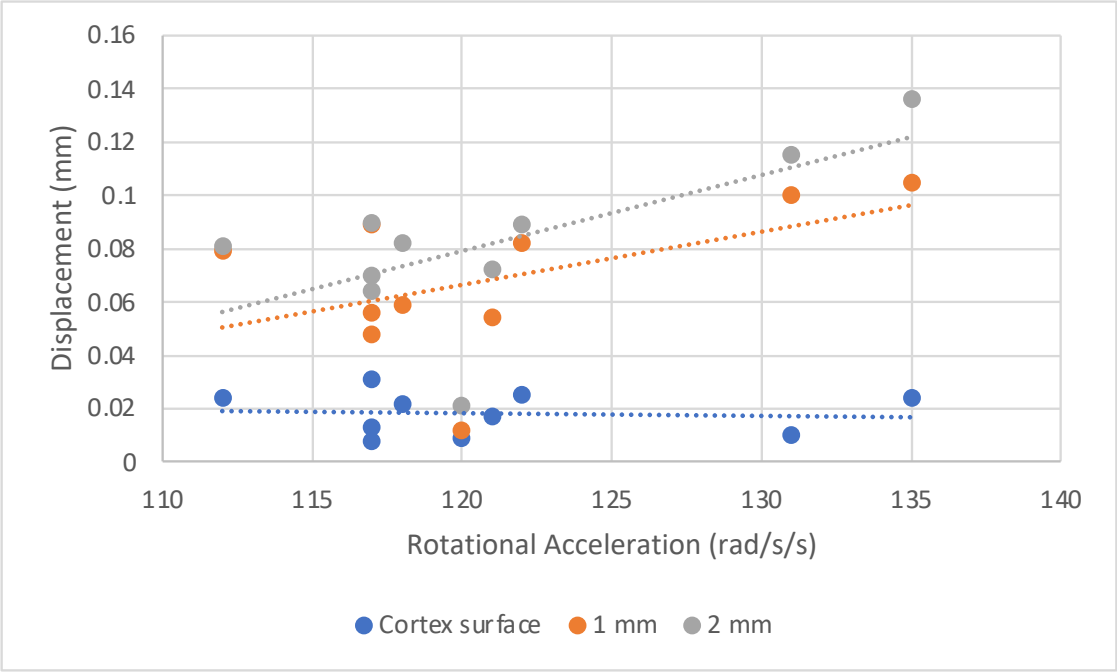

Figure 51: Displacement of fresh subject trial baseline tests vs. rotational acceleration

Generally, displacement increased with increased postmortem time, even over a 4-hour period. Comparing the R^2 values summarized in Table 15 suggests that elapsed postmortem time had a stronger correlation with displacement compared to test order, implying that tissue degradation has a bigger influence on increased motion results compared to repeat testing. Displacement did not seem to be affected by running higher-severity tests, noting that these tests showed similar displacement results that were comparable to other tests run in the same one-hour timeframe.

Table 15: R^2 values of fresh subject trial baseline test comparisons

	Cortex surface	**1 mm deep**	**2 mm deep**
Postmortem time vs. displacement	0.377	0.660	0.582
Rotational velocity vs. displacement	0.165	0.001	0.044
Rotational acceleration vs. displacement	0.006	0.250	0.429
# Tests vs. displacement	0.311	0.485	0.413

From Table 15, it can be noted that displacement values are more closely associated with postmortem time than by rotational velocity, rotational acceleration, or the number of previous tests run. Although conclusions are limited since these tests were only performed on a single subject over a 4-hour period, the results suggest that postmortem degradation may have a substantial effect on relative brain motion. These results emphasize the need for efforts to reduce postmortem degradation and to complete rotation testing as quickly as possible to minimize the effects of postmortem time.

Figure 52 shows displacement at 1 mm deep plotted against postmortem time, with the red circles encompassing a time frame of one hour.

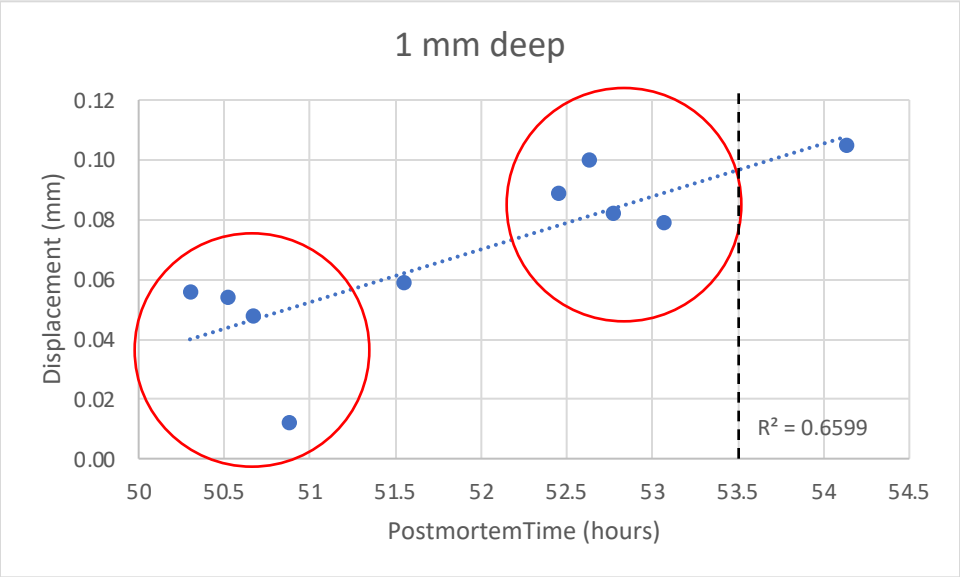

Figure 52: Displacement vs. postmortem time at 1 mm deep, 1-hour time frame in red circle. Higher-severity test indicated by vertical dashed line

Through the examination of the time points within the one-hour timeframe, it can be noted that there is not a strong correlation between displacement and postmortem time in these one-hour periods. This suggests that if tests are run within one-hour of each other, they can be compared without the confounding variable of postmortem time. This also supports that the most important tests in the test matrix should be completed within the first hour of testing to minimize the amount of postmortem time and to reduce the influence of multiple hits on the same subject.

Though this analysis was only performed with a single subject during one test series, the data were valuable in indicating the significance of postmortem time and the number of repeat tests run on displacement values measured at the surface of the brain. Though additional data points should be collected to explore these relationships further, these data emphasize the potentially large influence postmortem time especially has on displacement data. Efforts should

be made to prioritize the most important tests within the first hour of testing to minimize postmortem time and to reduce the effects of repeat testing on a single subject.

4.3.2 Fresh Subject Tests Discussion

A comprehensive understanding of how the whole-brain displaces under high-severity rotation is essential to predicting and mitigating injury. This dissertation work sought to fill the gap of missing surface-level brain displacement through the generation of over 300 displacement curves from 5 subjects varying in sex, age, and anthropometry that can be used to improve and validate finite element brain models.

As evidenced in this dissertation work and previous studies (Table 16), human variation widely differs. Differences in subject anthropometry and other subject-specific characteristics potentially result in a significant contribution to how much displacement occurs in the brain when subjected to dynamic rotational loading scenarios. Although hypothesized that BPF would have the largest effect on displacement outcomes, that was not the only conclusion drawn from this dissertation work. Rotational velocity, postmortem time, MOI, and BPF, were all shown to be significant contributors to peak displacement. Due to the large variance in displacement attributed to subject-specific parameters found between subjects even under repeatable loading conditions, a larger sample size is necessary to draw broader conclusions.

Table 16: Comparison of subject parameters from various studies

	Current study	Hardy et al. (2007)	Alshareef et al., (2020)	Mallory (2012)
Subject age (years)	84 ± 11	73 ± 10	64 ± 9	75 ± 18
Subject height (cm)	166 ± 9	166 ± 10	167 ± 8	162 ± 4
Subject weight (kg)	55.8 ±11.0	80.1 ± 25.1	74.3 ± 31.9	75.0 ± 11
Postmortem time when testing was complete (hours)	42 ± 10	--	59 ± 10	72 ± 19

Evaluation of damaged tests

One to three baseline tests were run at the beginning of the test matrix for each subject as a displacement reference for a test with the lowest possible postmortem time and without the influence of microdamage because of multiple tests run on the same subject. Subsequently, a baseline test was run between each higher-severity test. It was hypothesized that if a higher-severity tests resulted in damage, it would be evidenced by comparing the pre- and post-baseline test for the suspected damaging high-severity test. Results from the multiple regression analyses indicated that displacement has been shown to be significantly affected by increasing postmortem time, regardless of efforts to slow the influence of degradation on peak brain displacement. However, it is important to note that this dataset does not include a long-term study of baseline tests without higher-severity tests in between. Additionally, microdamage is known to occur from repeat testing as evidenced by the strain conditioning phenomenon first described by Darvish and Crandall (2001), so the accumulated microdamage from repeat testing should not be ignored.

Therefore, a quantitative methodology was developed to determine when a damaging test occurred. It should be noted that the determination of a damaging test is subject-specific, as it has not yet been established how parameters such as degradation status, MOI, and BPF influence peak displacement. The displacement of each baseline test was compared to the standard deviation of all previous baseline tests. By comparing to all previous baseline tests, the model considers both postmortem time and the cumulative microdamage due to multiple tests on a single subject.

The number of standard deviations each test is compared to the previous tests is summarized in Table 17.

Table 17: Comparison of subject 2 baseline standard deviations

	Displacement (mm)			Difference from previous test			Standard deviations away from previous test		
Test #	Cortex Surface	1mm deep	2mm deep	Cortex Surface	1mm deep	2mm deep	Cortex Surface	1mm deep	2mm deep
01	4.84	4.64	5.21	--	--	--	--	--	--
02	4.64	4.88	5.08	-0.09	-0.22	-0.39	--	--	--
03	4.89	4.85	4.82	0.01	0.33	-0.17	--	--	--
05	4.89	6.01	5.55	0.22	1.23	0.81	4.46	7.32	2.82
07	5.67	5.61	6.33	0.78	0.23	0.63	7.34	0.33	1.71
09	5.34	5.60	5.73	0.38	0.2	0.15	0.89	0.24	0.26
11	6.90	7.76	7.55	0.81	1.42	1.44	1.36	1.59	2.21
13	8.99	8.41	8.71	2.11	1.06	0.78	2.47	0.86	0.75
15	8.91	8.81	8.92	-0.19	-0.13	0.18	-0.13	-0.08	0.13
17	9.13	9.25	8.98	0.26	-0.86	0.1	0.15	-0.50	0.07
19	8.96	9.05	9.31	-0.04	1.11	0.33	-0.02	0.66	0.20
21	7.61	8.46	8.41	-1.46	-0.44	-0.72	-0.76	-0.25	-0.42
23	8.69	9.13	8.88	1.8	0.52	0.3	0.97	0.30	0.18
25	9.09	9.50	8.92	-0.24	0.37	0.05	-0.13	0.21	0.03
27	8.44	7.95	7.97	-0.64	-1.55	-0.96	-0.33	-0.85	-0.57
29	5.72	6.09	6.09	-3.23	-1.96	-1.72	-1.71	-1.11	-1.06
31	5.94	6.30	6.43	0.71	0.26	-0.16	0.38	0.01	-0.10
33	4.84	4.64	5.21	-0.37	0.19	0.34	-0.20	0.11	0.22

A plot of the standard deviation of the displacement values versus the number of tests run on subject 2 is shown in Figure 53.

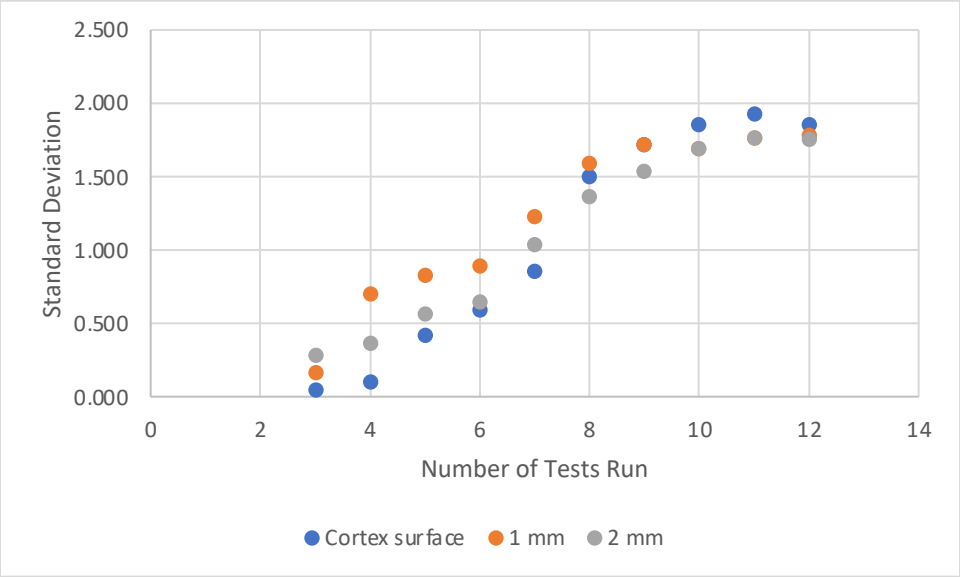

Figure 53: Damage estimation model for subject 2

The regression of the first 7 baseline tests demonstrates a strong linear relationship between the cumulative standard deviation versus the number of tests run previously, indicating that displacement changes are occurring because of the combination of increasing postmortem time and the number of tests being run on a single subject regardless of the severity of the tests. The jump between baseline tests 7 and 8 shows an increase in displacement that doesn't follow the previous trend, indicating that the excess motion that occurred in baseline test 8 was a result of the higher severity test run in between baselines 7 and 8.

The same type of analysis revealed damage in subject 5 that was not attributed to postmortem degradation or cumulative microdamage. The standard deviations are summarized in Table 18 and a plot of the standard deviation of the displacement values versus the number of tests run on subject 5 is shown in Figure 54.

Table 18:Comparison of subject 5 baseline standard deviations

	Displacement (mm)			Difference from previous test			Standard deviations away from previous test		
Test #	Cortex Surface	1mm deep	2mm deep	Cortex Surface	1mm deep	2mm deep	Cortex Surface	1mm deep	2mm deep
01	0.472	0.892	1.122	0.043	-0.062	-0.008	--	--	--
02	0.429	0.830	1.114	0.623	0.632	0.458	--	--	--
04	1.052	1.462	1.572	2.112	2.593	2.219	20.5	14.4	81.0
06	3.164	4.055	3.791	1.518	1.156	1.289	6.07	7.44	8.46
08	4.682	5.211	5.080	0.243	-0.302	-0.098	1.18	0.76	1.01
10	4.439	4.909	4.982	0.546	0.207	0.389	0.12	-0.14	-0.05
12	4.985	5.116	5.371	2.154	-1.684	-1.791	0.28	0.10	0.21
14	2.831	3.432	3.58	0.115	0.311	0.152	1.05	-0.82	-0.91
16	2.946	3.743	3.732	0.538	-0.093	-0.070	0.06	0.16	0.08
18	3.484	3.65	3.662	2.340	-1.884	-1.736	0.30	-0.05	-0.04
20	1.144	1.766	1.926	0.065	-0.124	-0.078	1.38	-1.11	-1.08
22	1.079	1.642	1.848	0.043	-0.062	-0.008	0.04	-0.07	-0.05

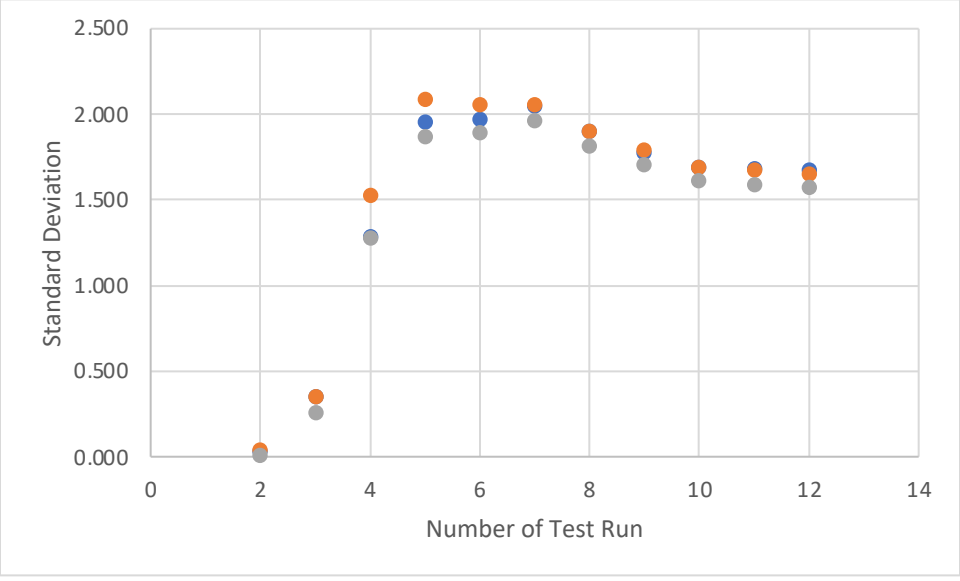

Figure 54: Damage estimation model for subject 5

Although it appears the damaging test occurred after baseline test 3, the damage in subject 5 occurred between baseline 2 and 3. Only two baseline tests were conducted before the first higher-severity tests for subject 5, but the first two baseline tests were run an hour apart. They did not show any significant differences in displacement. The cumulative standard deviation analysis revealed that the third baseline test that was run was more than 20 standard deviations away from the initial two baseline tests (Table 18), indicating the damage occurred from the first higher-severity test. The resulting increase from baseline 3 to 4 indicates that brain tissue may be even more susceptible to damage after an initial damaging event.

Despite the tests in the post-test matrix being likely unreliable due to potential tissue damage, the post-test matrix for subject 5 included repeat testing of tests with higher kinematics (approx. 22 rad/s and 2900 rad/s^2). Figure 55 shows the peak displacement of the four repeat tests versus postmortem time.

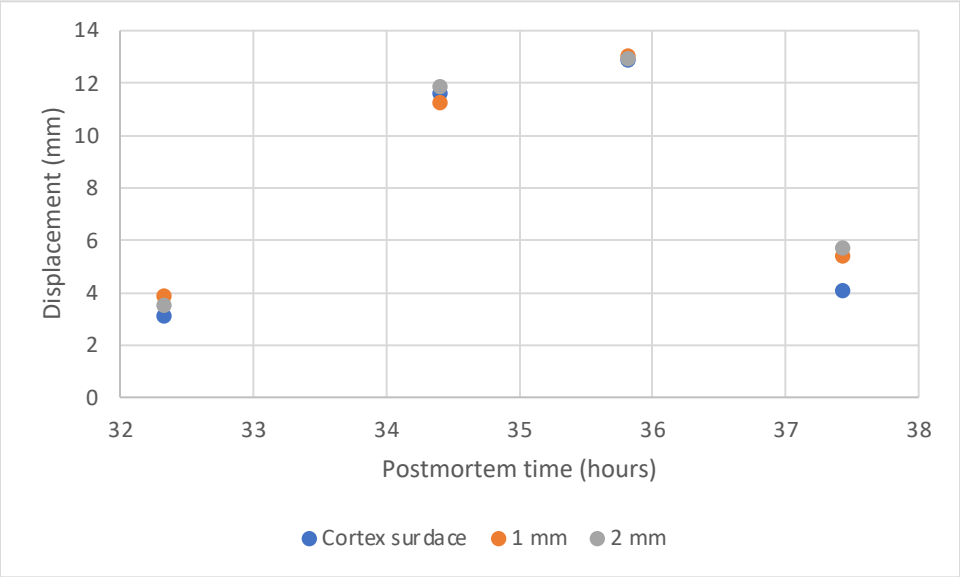

Figure 55: Peak displacement of tests with repeatable higher-severity kinematics at increasing postmortem times

These tests show the same trend as the baseline tests, with an initial increase in displacement as postmortem time increases, followed by a drop in peak displacement after approximately 36 hours of postmortem time.

Comparison of rotational kinematics

Experimental and analytical modeling results have indicated that brain injury is primarily produced through angular loading (Holbourn, 1943; Huang et al., 1999; Lee et al., 1987; Ommaya and Gennarelli, 1972; Zhang et al., 2006). However, it has been debated in the literature whether rotational acceleration or rotational velocity is the more dominant kinematic parameter influencing head and brain injury. Peak angular accelerations and decelerations have been cited as the injury mechanism for diffuse axonal injury and acute subdural hematoma in

animals (Gennarelli et al., 1972; Gennarelli et al., 1982; Lee et al., 1987; Miller et al., 1998), though these animal studies have suggested that a single metric, such as peak angular acceleration, may not be able to fully characterize brain injury. In a computational study, varying pulses with different peak rotational accelerations but equal changes in rotational velocity produced similar levels of brain strain, so it was concluded that rotational velocity may be a better metric of injury (Yoganandan et al., 2008). Several studies have investigated the relationship between cumulative strain density measure (CSDM) and rotational kinematics and found that higher CSDM values were more strongly correlated with rotational velocity compared to rotational acceleration (Takhounts et al., 2013; Knowles and Dennison, 2017; Gabler et al., 2018; Bian and Mao, 2020). However, there is a lack of conclusive evidence from experimental models about which parameter influences peak brain displacement specifically. One of the aims of this dissertation work was to further investigate which parameter is more dominant when it comes to peak displacement of surface-level brain tissue. For all trackable, non-damaged tests, it was found that rotational velocity was more strongly correlated to peak brain displacement compared to rotational acceleration across all subjects and loading severities (Figure 35, Table 12).

4.3.2.1 Analysis by Subject-Specific Characteristics

Postmortem Degradation

Though postmortem time was used as a "controlled" variable for subject-to-subject comparison, it is unclear how much degradation is associated with each hour of postmortem time, and if this is comparable between subjects. Softening of the brain tissue after death and the buildup of intracranial gasses as a byproduct contributed both to the potential alteration of

displacement results recorded during this dissertation as well as difficulties re-pressurizing the head to normal intracranial pressure and re-perfusing the subarachnoid space with aCSF+. Sufficient degradation also has been associated with changes in coupling between the brain and skull (Hrapko et al., 2008; Rashid et al., 2013). Degradation of brain tissue after death is a major concern in PMHS brain studies, and therefore efforts were taken to minimize its effects. To be considered for use in this dissertation work, subjects were required to be accessed at no greater than 36 hours postmortem. Procedures were streamlined to complete rotation testing as quickly as possible, resulting in the completion of rotation testing at less than 56 hours of postmortem time for all five subjects tested. Additionally, efforts were taken to keep the brain as close to 4 °C as possible, which has been shown in materials testing to reduce the effects of postmortem degradation and maintain the biofidelic material properties of brain tissue (Rashid et al., 2013). Further, sodium bicarbonate was added to all fluids entering the brain, as it has been showed to reduce the effects of postmortem degradation (Wetli et al., 2017)

The subjects used to complete this testing were obtained at various times postmortem, which was a parameter indicated by regression analyses to be a significant contributor to increased peak brain displacement over time. The qualitative state of the brain tissue at time of autopsy is shown in Figure 56.

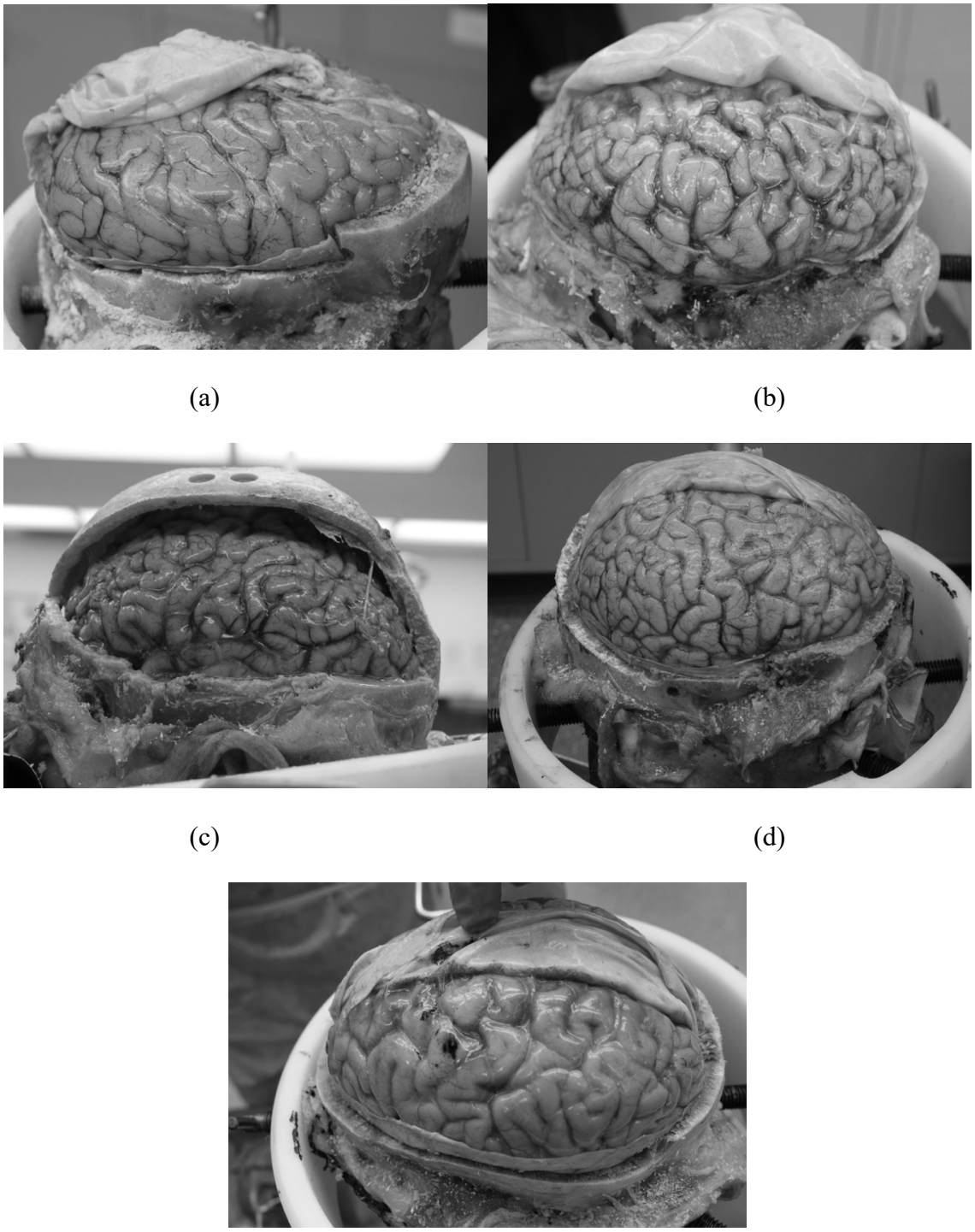

(a) (b)

(c) (d)

(e)

Figure 56: Qualitative state of brain tissue for each subject during autopsy (a) subject 1- 59 hours postmortem, (b) subject 2- 45 hours postmortem, (c) subject 3- 50 hours postmortem, (d) subject 4- 37 hours postmortem, (e) subject 5- 41 hours postmortem

A qualitative assessment of tissue state is consistent with the amount of displacement reported in this dissertation. Although subjects 2 and 5 did not have the highest postmortem time, both the spinal cord and brain tissue at autopsy indicated that degradation on these subjects were more advanced, consistent with the hypothesis that increased degradation leads to greater peak displacements.

The uncertainty of how postmortem time affects each subject individually makes comparing subjects difficult. Not only does the degradation from increased postmortem need to be considered, but the accumulation of microdamage from repeat testing on a single subject does as well. In this dissertation work, stiffness was not quantified but could significantly affect the peak displacement over time. Through the examination of the peak displacements from baseline testing versus postmortem time, a unique pattern was observed. This pattern was most closely observed in subject 2 and 5 and can be visualized in Figure 42 and Figure 45. Interestingly, peak displacement begins to decrease after a certain point, which may be attributed to the changes in stiffness that occurs postmortem according to the literature. Results from studies of isolated brain tissue samples have varied, with some studies reporting stiffness up to 10 hours after harvest (Rang et al., 2001; Hrapko et al., 2008), while other studies showed either little to no change in postmortem stiffness (Metz et al., 1970; Shen et al., 2006) or reported decreased stiffness from 3-4 hours postmortem to 3 days postmortem (Nicolle et al., 2004; Bentil et al., 2013). Darvish and Crandall (2001) reported decreased stiffness for postmortem times up to 16 days. While differences between these studies could be attributed to a wide variety of test techniques, preparation methods, and animal or human models used, still other differences could be attributed to subject-specific characteristics that were not quantified in those studies.

The decrease in peak displacement occurs at around 48 hours postmortem in subject 2- and 35-hours postmortem in subject 5. Also of note, this trend is most obvious in the two subjects that experienced a damaging test. The results from this dissertation in combination with the uncertainty in the literature suggests that the significance of stiffness with respect to peak displacement should be further explored.

The results of this dissertation work indicated postmortem time, which was used as a proxy for postmortem degradation, as a significant contributor to the increases seen in peak displacement. This conclusion was true for every subject analyzed in this dissertation work. The increases in displacement for all trackable, non-damaged tests were most strongly correlated with increasing rotational velocity (Table 12). Therefore, to further explore the influence of the effects of postmortem time, peak displacement was plotted against rotational speed, then further separated into bins of similar postmortem time (Figure 57).

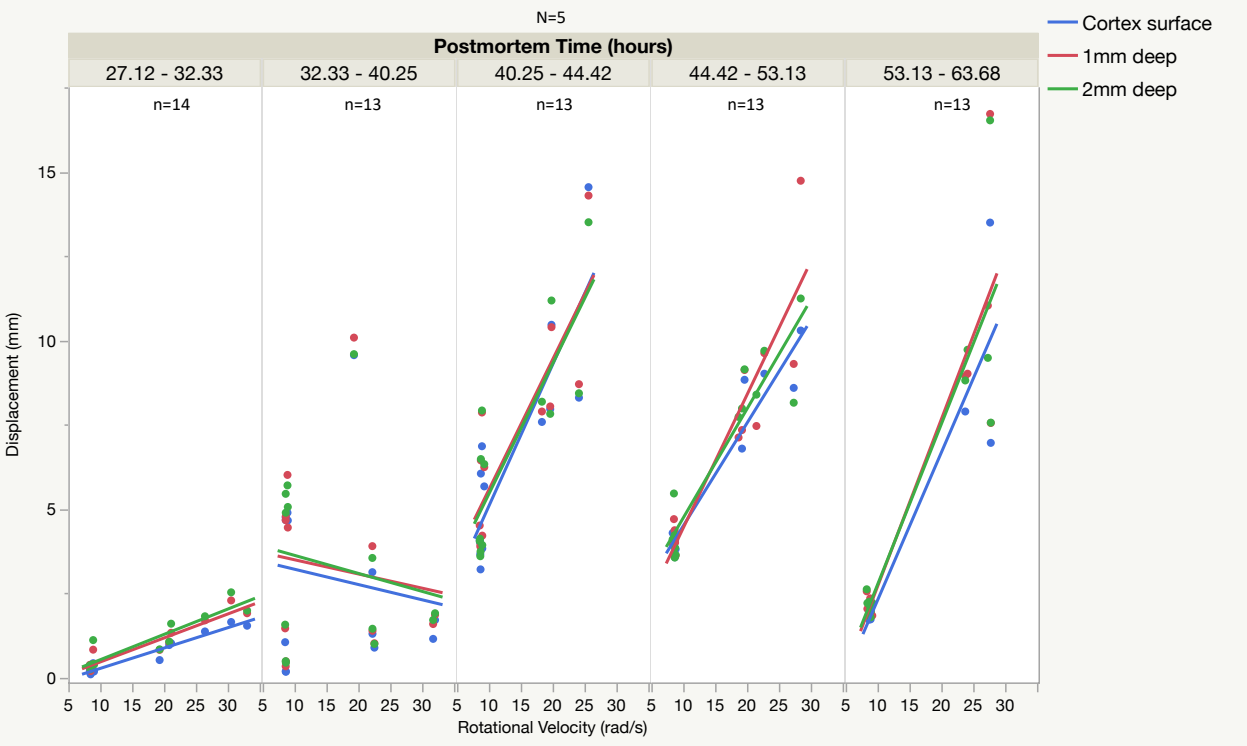

Figure 57: Peak displacement versus rotational velocity by postmortem time for all trackable, non-damaged tests

Each of the relationships shown in Figure 57 is statistically significant ($p<0.05$) except for the 32.33-40.25 postmortem time group, which requires further investigation into why the trend is not predictable given the postmortem time. From the slopes of the linear fit lines, it can be noted that the displacement has a higher rate of increase as rotational velocity increases when the postmortem time is higher (40+ hours) compared to the lower postmortem times. This is consistent with the hypothesis that higher postmortem times leads to greater postmortem degradation, resulting in greater peak displacements even at the same kinematic inputs. Additionally, this supports the conclusion that efforts to minimize the effects of postmortem

degradation during experimental PMHS tests are of the utmost importance, as displacement results are significantly affected by degradation. These results also suggest that experimental studies that report high postmortem times may be overpredicting brain displacements leading to overestimated injury outcomes.

MOI

The multiple regression analyses also indicated that the moment of inertia of the head and neck tissue that were rotated had a significant effect on peak displacement outcomes. Therefore, to further explore the influence of the effects of MOI at different rotational velocities, peak displacement was plotted against rotational velocity, then further separated into bins of similar postmortem time (Figure 58). All trackable, non-damaged tests were included in the analysis.

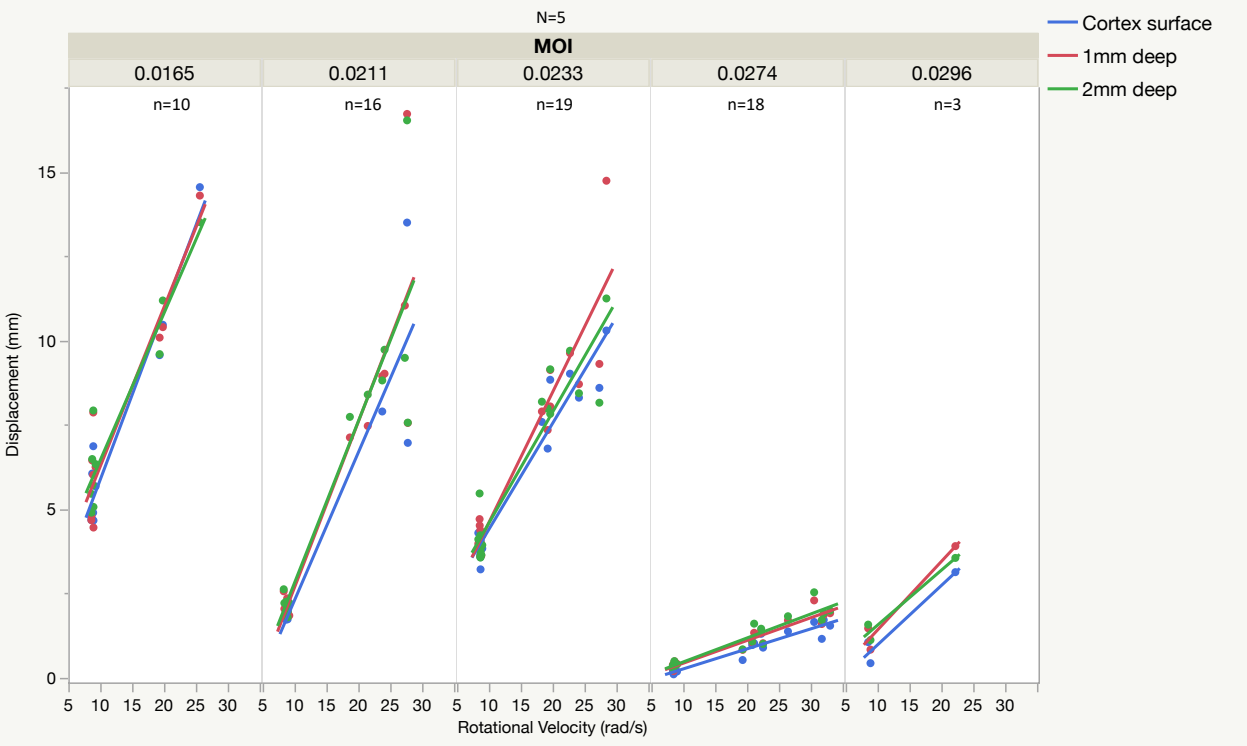

Figure 58: Peak displacement versus rotational velocity by MOI for all trackable, non-damaged tests

As the MOI of an object is its ability to resist change, it was hypothesized that a larger MOI value for a subject would result in less displacement. This trend was shown to be true through the regression analysis. Additionally, Figure 58 shows the effects of MOI to be dependent on the rotational velocity. For subjects with lower MOI, peak displacement is seen to be more sensitive to rotational velocity changes, as evidenced by the slope of the linear fit line. Conversely, subjects with higher MOI show less sensitivity to rotational velocity changes, conclusive with the hypothesis that subjects with higher MOI can resist the influence of rotation better, resulting in less peak displacement.

Though efforts were taken to minimize the amount of neck tissue that was kept during rotation testing, there is some neck tissue that accounts for the MOI reported for each subject in this dissertation work. As this MOI value was significant as a predictor for peak displacement, it is important that all future experimental brain tests quantify MOI and designate the contribution of neck mass. The isolated effects of MOI from the head and brain only may be better explored using human body models.

Atrophy

It has been postulated that the increase in ASDH resulting from bridging vein failure due to increase in age is primarily associated with age-related brain atrophy (Yamashima et al., 1984; Meany 1991; Kleiven et al., 2002; Hanif et al., 2009; Mallory et al., 2011; Zhou et al., 2021). This dissertation work explored the effects of atrophy on peak brain displacement under anterior-posterior rotation in attempt to close the gap between experimentally determining the relationship between relative brain motion and age.

A review of 95 studies of BPF by Vågberg and colleagues (2017) indicated that the calculation of BPF is significantly influenced by both image acquisition and imaging software methods used to calculate the BPF. Therefore, a study by Cook and colleagues (2017) created a dataset using a consistent scanning protocol and data processing protocol that characterized BPF change with age for healthy, older adults. The comparison of the Cook dataset (Cook et al., 2017) and the results from the current dissertation work are shown in Figure 59. These data are comparable as all MRI scans were completed on a 3T scanner using the same protocol. Additionally, the same processing software and technique were used.

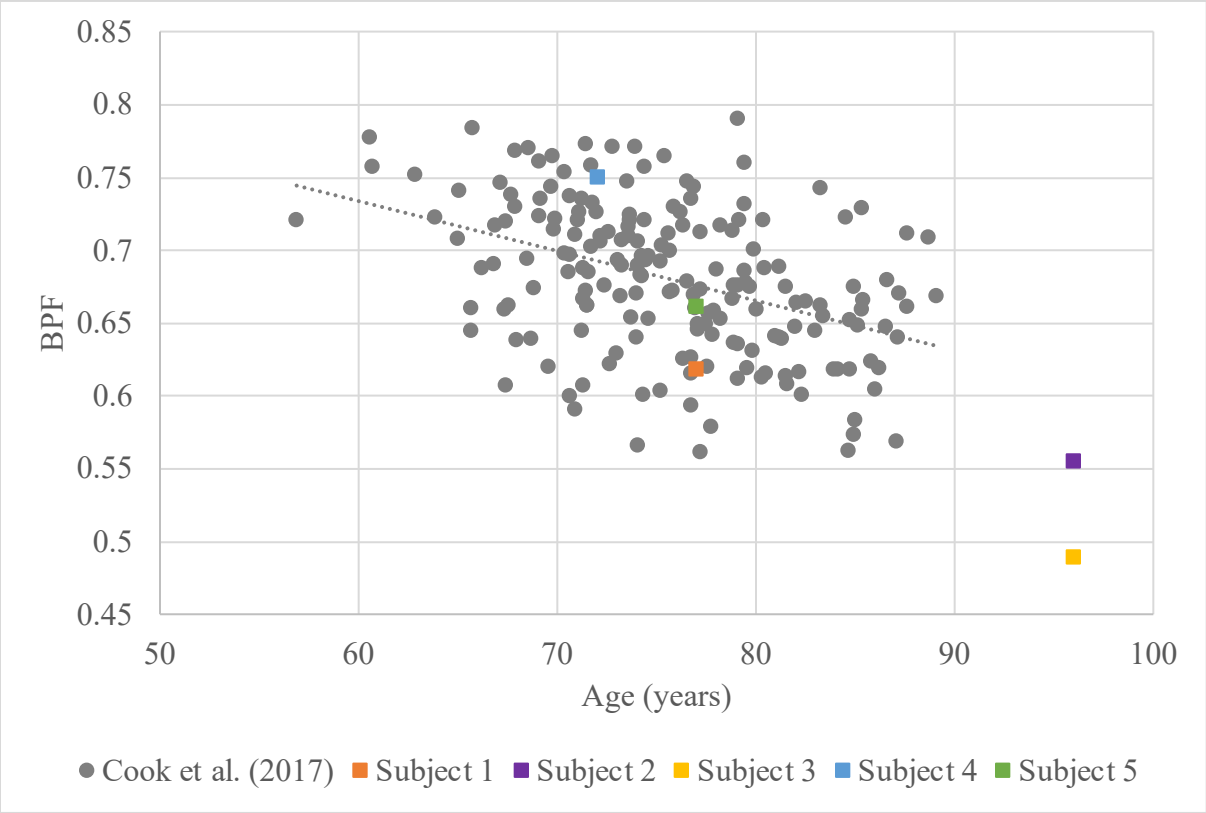

Figure 59: Comparison of BPF by age

It is important to note the wide range of BPF that can be observed at each age. This is significant as it demonstrates that age alone is not sufficient as a predictor for ASDH injury as evidenced in this dissertation. While subject numbers 2 and 3 do not fall within the range of previously collected data, the level of BPF for these subjects is consistent with the trend shown that BPF decreases as age increases.

As a qualitative assessment of how atrophy differed for the 5 subjects used in this dissertation, MR images are shown in Figure 60.

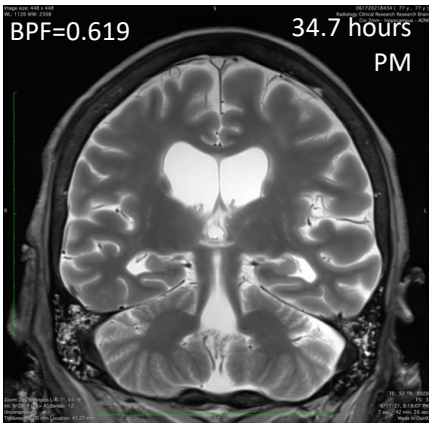

(a)

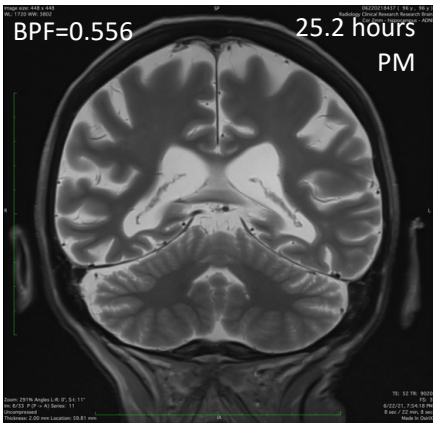

(b)

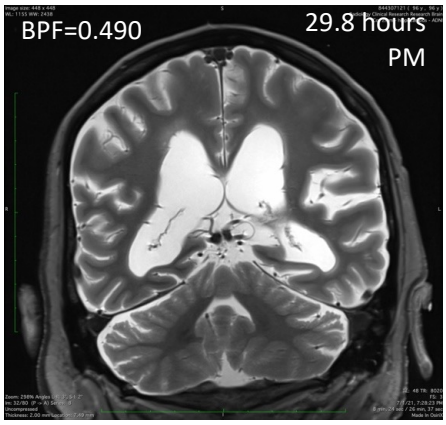

(c)

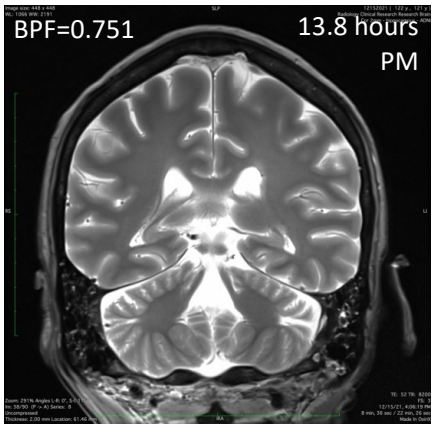

(d)

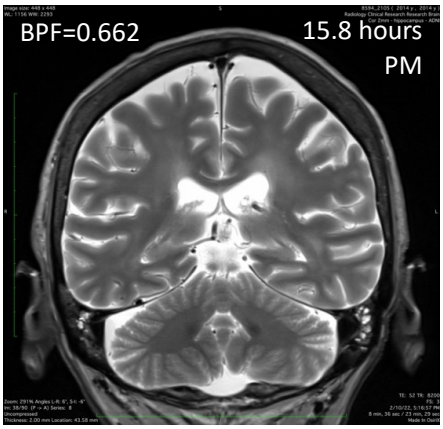

(e)

Figure 60: MR images from (a) subject 1, (b) subject 2, (c) subject 3, (d) subject 4, and (e) subject 5

Of note, it is possible that postmortem changes influenced the response of CSF, gray matter, and white matter tissue contrast which could potentially lead to variability in the analysis of these tissue volumes. A better understand of how postmortem time affects the brain is required to make more accurate comparisons between subjects.

It was hypothesized that a subject with a lower BPF would exhibit higher peak brain displacements than a subject with a higher BPF. Similar to the analysis shown above with postmortem time and MOI, peak displacements from all 5 subjects were plotted against rotational velocity then further segmented by BPF (Figure 61).

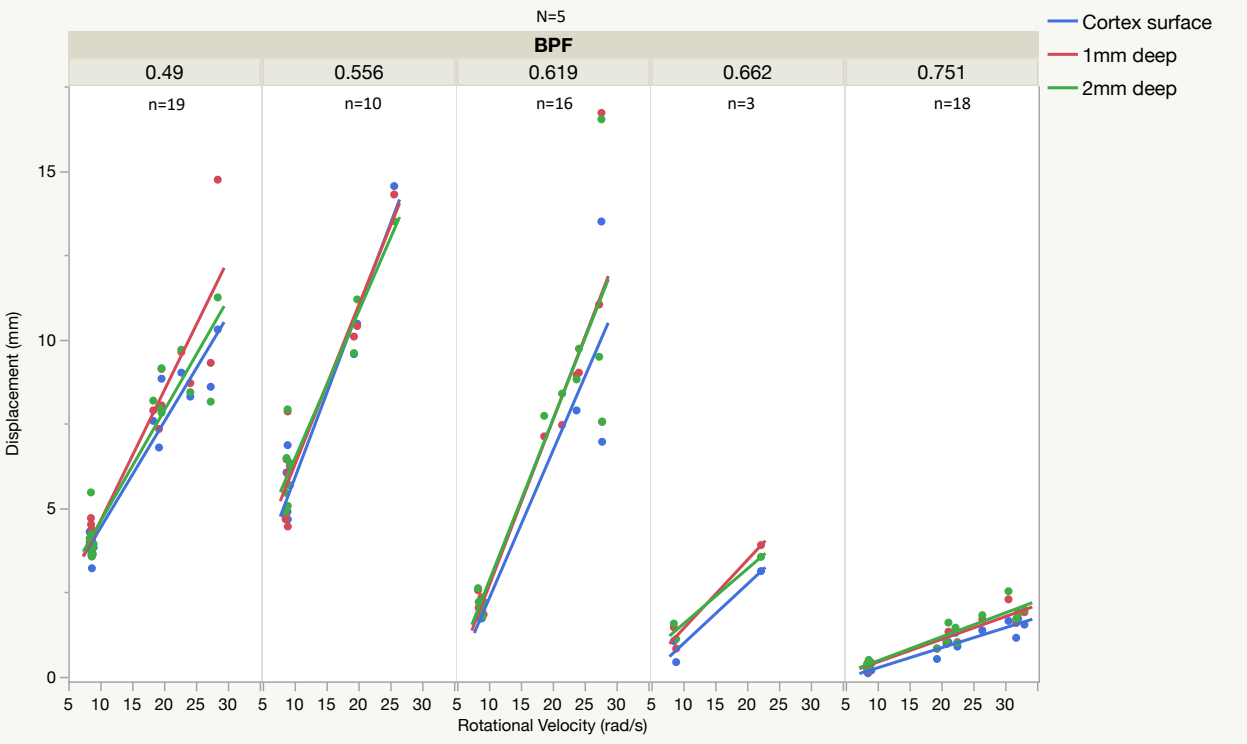

Figure 61: Peak displacement versus rotational velocity by MOI for all trackable, non-damaged tests

To further account for the effects of multiple variables, it should be noted that the subjects with the BPF values of 0.49 and 0.619 had similar MOI values (0.0233 kg-m^2 and 0.0211 kg-m^2, respectively), as did the subject with BPF values of 0.662 and 0.751 (0.0296 kg-m^2 and 0.0274 kg-m^2, respectively).

A comparison of the slopes of the linear fits indicates that subjects with lower BPF values show greater sensitivity to increasing rotational velocity compared to subjects with higher BPF values. In addition to the significance of the correlation between peak displacement and BPF, these results support the conclusion that subjects with greater BPF experience less peak displacement, even at comparable kinematic inputs.

4.3.3 Comparison to Previous Work

PMHS Tests

While previous human brain deformation studies conducted a wide variety of tests and severities, these studies of brain motion are limited by the lack of quantified brain motion near the surface of the brain and the failure to investigate subject-specific parameters that have a significant influence on the amount of brain displacement recorded (Pundez and Sheldon, 1944; Gosch et al., 1970; Nusholtz et al., 1984; Trosseille et al., 1992; Hardy et al., 2007; Alshareef et al, 2018, 2020). The regression analysis that was used to investigate the dependence on brain deformation and subject-specific parameters was simplistic and not intended to predict or interpolate brain deformations. Rather, it was through the comparison of tests across subjects run under repeatable kinematics that it was concluded that along with rotational kinematics, postmortem time, BPF, and MOI have a significant effect on brain displacement at and near the

surface of the cortex. This is a significant finding as previous brain displacement studies do not quantify some, or any, of the given parameters.

The selection of high-frequency, B-mode ultrasound has enabled the non-invasive measurement of surface-level brain motion under rotational loading. It has been used to track the shear motion of superficial brain tissue and the meningeal layers (Mallory, 2014). However, the ultrasound probe was mounted off-board, and a large section of the skull had to be removed to image the underlying tissue as the head rotated past the stationary probe. This limited data collection to low-level severities due to the bulging of the tissues and high relative velocities between the probe and the imaged tissue. The experimental plan was modified so instead the probe rotated with the skull and imaged the underlying tissue through a significantly smaller window opening, which allowed to for the quantification of surface-level brain motion up to 42.3 rad/s and 5800 rad/s^2, whereas Mallory (2014) was only able to quantify very small displacements (~0.2mm) under low-severities of 2.1 rad/s and 154 rad/s^2 due to limitations of the experimental methodology.

Deeper brain motion has been characterized at non-injurious levels with healthy volunteers (Bayly et al., 2006) and up to 50 rad/s and 10,000 rad/s^2 in primates and human cadavers (Löwenhielm, 1974; Ommaya et al., 2002; Depreitere et al., 2006; Hardy et al., 2007; Alshareef et al., 2018, 2020). As early as 1974, Shatsky and colleagues reported 2 to 3 mm of relative motion between the cerebral vasculature and the skull. Nusholtz and colleagues (1984) reported up to 6 mm of relative brain motion between the brain and skull for a case where skull fracture occurred. Hardy and colleagues (2007) reported displacements between 1.9 and 14.4 mm for locations deeper in the brain under moderate rotational velocities (20.3 ± 5.7 rad/s). Two tests in the Hardy (2007) study were intended to examine relative motion near the surface of the

brain. One subject demonstrated 9 to 11 mm of relative displacement at the surface of the cortex, while a second subject exhibited only 2 to 3 mm of relative brain motion at a location 10 mm deep in the cortex. The magnitude of the difference in subject-to-subject comparison is similar to the differences reported in this dissertation. However, subject-specific parameters such as postmortem time at which the subject was tested, BPF, and MOI were not reported, so a direct comparison to Hardy's work is difficult. General motion trends of the surface-level brain tissue followed the same trends as deeper brain tissues as described by Hardy and colleagues (2007). When the head begins to rotate, the local brain tissue retains its position and shape relative to the inertial reference frame, leading to relative motion between the brain and skull. In this dissertation work, the rotation fixture and braking systems were designed to allow for maximum "free flight" of the brain, meaning that the brain displacement reached its peak before the brake was engaged to ensure that peak brain displacement was not underestimated.

More recently, Alshareef and colleagues (2018, 2020) generated a dataset of brain motion under rotational loading at impact conditions considered injurious. Rotational pulses between 20 and 40 rad/s in the sagittal plane produced displacements between 0.3 and 12.2 mm at deeper locations in the brain measured using sonomicrometry. The input kinematics used, displacement results obtained, and the postmortem times at which subjects were tested are all comparable to this dissertation work, though the tracking locations are not. It is still unknown how motion at the surface of the brain is correlated to deeper brain motions. Though the distribution of age of the subjects used was similar to the ages of the subjects used in this dissertation work, BPF was not reported, which was demonstrated to be a significant parameter influencing the amount of brain displacement. The range of BPF across age has been shown to be quite large, so age alone is not a reliable source of comparison (Cook et al., 2017).

This dissertation work only tracked displacements up to 2 mm deep in the cortex. A limitation of using B-mode ultrasound to quantify brain displacement is the relatively shallow imaging area, and the lack of deeper displacement data in this dissertation makes comparison to previous work difficult. This emphasizes the need for collection of surface level brain motion, not only for the development of subdural injury risk, but also for further validation of human body models. However, it is still unclear how motion at the surface of the brain is related to the motion reported at deeper locations in the brain.

Modeling studies

Capturing the anatomical complexity of brain models are proving essential in the estimation of injury tolerances when using finite element (FE) models. Given the amount of potentially confounding variables that must be controlled during experimental PMHS testing, FE modeling provides a solution to these limitations by controlling those variables. However, large disparities exist among models when it comes to anatomical features included and material property values, which can potentially greatly influence results (Darvish and Crandall, 2001; Zhou 2019). Several FE models have been developed to predict ASDH in the elderly specifically, but consistent findings have not been reached.

Work by Zhou and colleagues (2019 & 2020) investigated the age-related ASDH mechanism through the utilization of three models with varying brain dimensions to simulate age-related brain atrophy. Both cortical relative motion and bridging vein strain were selected as ASDH indicators. The peak cortical displacement value for the model with the highest BPF was 7.6 mm, while the peak cortical displacement for the model with the lowest BPF was 9.2 mm.

Increased displacement with decreased BPF is consistent with the results presented in this dissertation.

Current study results related to BV failure limits

Due to differences between postmortem and in vivo head models, bridging vein failure cannot be recreated experimentally in PMHS. As parasagittal bridging veins originate in the cortical tissue then cross through the dura before entering the superior sagittal sinus, the relative motion between the surface of the cortex and the dura can be used to estimate the resulting stretch in the bridging veins. Using the failure properties of bridging veins reported in the literature, the probability of bridging vein failure given a level of rotational kinematics can be determined. A summary of bridging vein failure properties from the literature is summarized in Table 2.

It must be noted that isolated tests of bridging veins to failure have been tested in uniaxial tensile setup, which can only lead to one-dimensional properties. Though the properties described in Table 2 are a good starting point, they may not be physiologically realistic. Oka and colleagues (1985) reported that the direction of inflow from the bridging veins into the superior sagittal sinus shows high variability and is therefore unlikely if not impossible for BV to fail from pure uniaxial tension. Han and colleagues (2007) reported that only 18% (173/975) of bridging veins entered the superior sagittal sinus at a right angle. Due to various inflow angles, relative motion of the brain with respect to the skull in the sagittal plane will result in both tensile and shear loading of at least some of the bridging veins, resulting in possible failure. While more gradual damage models have been integrated with the nonlinear anisotropic models for

cardiovascular tissue, they have not yet been fitted for bridging veins specifically (Balzani et al., 2006; Weisbecker et al., 2012; Famaey et al., 2013; Famaey et al., 2014).

With the knowledge that one-third of ASDH are caused by the rupture of bridging veins (Maxeiner, 1997; Depreitere et al., 2006), a complete understanding of how peak brain displacement relates to bridging vein tolerance is a logical step. Experimental testing of bridging vein tolerance lacks repeatability and the opportunity to test bridging veins in a realistic failure scenario. Typical linear elastic and failure properties such as Young's modulus, ultimate stress and strain, and yield stress and strain have been reported (Table 2), but results vary due to differences in experimental methodology between research groups.

It has been proposed that peak brain displacement can be related to bridging vein failure by utilizing the failure parameters reported in the literature (Mallory, 2104, Famaey et al., 2014, Zhou, 2019). However, the simple linear elastic properties reported are widely variable and do not properly represent how bridging veins fail in vivo. Though nonlinear anisotropic failure models exist, they are not yet fit for bridging veins (Famaey et al., 2014). Future work should collect bridging vein failure properties from a combination of uniaxial and shear testing to make a more reasonable comparison between peak displacement and bridging vein failure in the context of ASDH injury risk.

4.3.4 Limitations

This dissertation work was not without its challenges and limitations. Although the use of postmortem human subjects is necessary for studying the high-level impacts associated with injurious MVCs, the limitations of using PMHS for this research must be addressed. Differences between an in vivo and postmortem model that are expected to contribute the most to differences

in brain motion include pressurization and perfusion differences, and the degradation of brain tissues, vessels, and the meningeal connections.

4.3.4.1 Limitations of using PMHS

It must be addressed that a PMHS model is not able to provide an injury response. Though data were collected to develop injury-level tolerances, there does not yet exist a reference for injury. However, the data collected here will contribute to further development towards defining a given parameter to predict injury.

Pressurization

Efforts were taken to minimize the differences between the postmortem human subjects and an in vivo human head through the pressurization of each subject. Intravascular and intraparenchymal pressures have been reported to affect overall relative brain-skull motion (Stalnaker et al., 1977; Viano et al., 1997; Depreitere et al., 2006; Monea et al., 2012). Previous efforts of re-pressurizing the head via the vasculature in whole-body PMHS tests utilized balloon catheters with pressure monitors inserted to monitor fluid pressures in the common carotid arteries (Stalnaker et al., 1977; Nusholtz et al., 1984; Trosseille et al., 1992). In isolated head testing, Hardy and colleagues additionally connected fluid inputs to the jugular veins to raise the pressure in the PMHS heads to an average arterial and venous blood pressure, leaving the vertebral arteries open to bleed gasses from the system (Hardy et al., 2007). In the current dissertation work, the vascular system was returned to physiological intracranial pressures rather than vascular pressures that have been targeted in previous studies. An intracranial pressure of 5-

15 mmHg (Raboel et al., 2012) was targeted rather than vascular pressure because it is thought that intracranial pressure has a more direct effect on brain motion than vascular pressure.

The ICP of each subject was brought into the physiological range before each rotation test and then monitored throughout the rotation test. A pre-test pressurization trial was conducted before the rotation testing for each subject to obtain the amount of time and the fluid height necessary to raise the pressure of the brain to ICP. Additionally, a post-test pressurization trial was conducted to check the reliability of the pressure sensor, and to ensure the brain was not over pressurized due to consecutive pressurized tests on a single subject. As pressure changes in the brain under dynamic loading were not a variable of interest in the dissertation work, time-histories of the transient pressure response are not reported.

The first subject used as a preliminary trial subject was not pressurized for rotation testing. Therefore, tests with similar kinematics were chosen for further comparison between the non-pressurized trial subject and the 5 pressurized subjects. A summary of tests chosen for further comparison are shown in Table 19.

Table 19: Comparison of pressurized/perfused and non-pressurized/perfused tests

Subject Number	Test Number	Pressurized? Perfused?	Rotational Acceleration (rad/s^2)	Rotational Velocity (rad/s)	Peak Displacement (mm)		
					Cortex Surface	1 mm	2 mm
Trial	Test 1	No	3120	26	2.00	3.28	3.41
1	Test 4	Yes	2290	27	10.4	11.8	11.2
2	Test 3	Yes	1790	26	2.89	4.85	4.82
3	Test 3	Yes	1890	24	8.59	8.46	9.71
Average			**2273**	**26**	**5.97**	**7.10**	**7.29**
STDEV			**605**	**1.3**	**4.15**	**3.81**	**3.75**
% CV			**26.6**	**4.9**	**69.6**	**53.7**	**51.5**

It should be noted that kinematic replication of tests between the preliminary trial subject and subsequent tests was not targeted. Therefore, while the repeatability in terms of the angular velocity is good (CV<5%), rotational acceleration is not repeatable (CV>10%). The sample size available for this comparison is small, so no insight can be gained from statistical analysis; however, the displacement plot comparing the non-pressurized test to the pressurized test is provided (Figure 62).

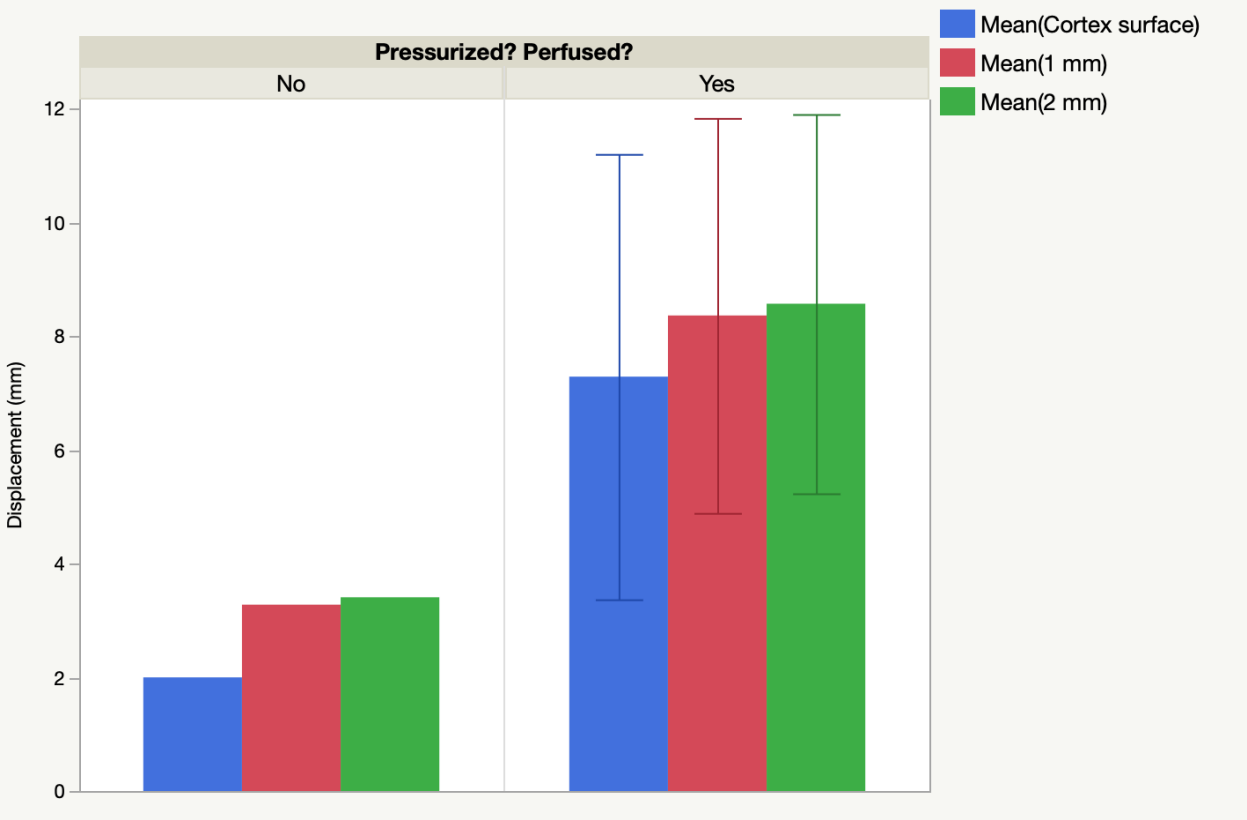

Figure 62: Displacement comparison of non-pressurized and non-perfused trial subject test versus pressurized and perfused tests with comparable kinematics

On average, the pressurized tests showed greater displacement than the non-pressurized test, consistent with findings reported in the literature. Further testing comparing non-pressurized and pressurized tests is required to draw more definite conclusions.

aCSF Perfusion

To further increase the biofidelity of a PMHS brain, artificial cerebrospinal fluid was reintroduced into the cranial subarachnoid space via the spinal subarachnoid space. In vivo, cerebrospinal fluid is contained in the subarachnoid space, over the surface of the brain, in the sulci, and in the ventricles to cushion the brain against sudden impact or injury. When measuring relative motion at the surface of the brain, maintaining this biofidelic condition is imperative. The resistance in tangential motion at the brain-skull interface has been shown to be attributed to the shear stress generated in the CSF and the frictional force in proportion to the pressure at the surface of the brain (Zhou, 2019). However, perfusing the subdural space rather than the subarachnoid space with aCSF+ may result in displacement values that overestimate the true displacement results, as evidenced by subject 1.

The effectiveness of aCSF+ perfusion was investigated during post-test dissection The aCSF+ fluid was dyed a dark green color to assist in the differentiation between it, pressurization fluids, and other fluids contained in the head. During dissection, the brain and sulci were inspected for evidence of green dye, though it is possible that since the subarachnoid space is so small, not enough dyed fluid was contained in the area, especially after rotation testing. Next, the spinal cord, cerebellum, and basilar surface of the skull were visually inspected for evidence of green dye before ultimately slicing the cerebrum to investigate evidence of green-dyed aCSF+ in the ventricles.

Success in the perfusion of aCSF in the subarachnoid space was limited. It was believed that in subject 1, it was the subdural space rather than the subarachnoid space being perfused due to the rate at which aCSF was flowing into the brain. Because the subarachnoid space is so small, it is not expected that a large amount of fluid, such as was recorded during subject 1, is necessary to re-perfuse the space. Perfusion of the subdural space in subject 1 was further confirmed using the ultrasound images of the surface level brain tissues (Figure 63).

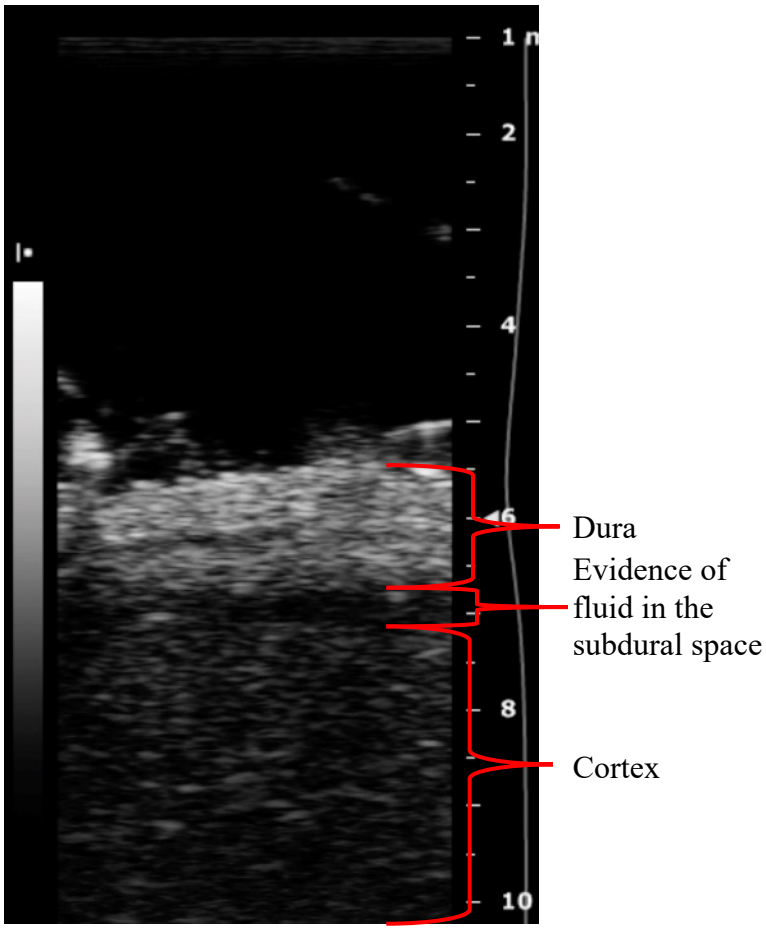

Figure 63: Ultrasound view of subject 1 showing evidence of fluid in the subdural space

As noted in Figure 63, there is a dark space underneath the dura without the cortex speckle pattern, corresponding to fluid in the subdural space. Over the course of rotation testing, the evidence of fluid under the dura diminished over time (Figure 64).

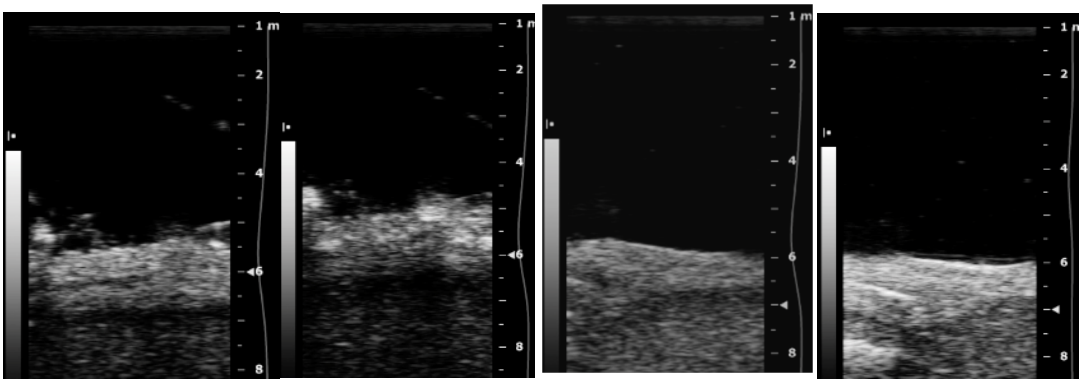

Figure 64: First frame of ultrasound videos from subsequent baseline testing. From left to right, test 1, test 5, test 9, and test 13

Because of the presence of the fluid under the dura during the main test matrix, cortex surface points were not tracked until visible, during the post-test matrix.

The first subject used as a preliminary trial subject was not perfused for rotation testing (Table 19). On average, the perfused tests showed greater displacement than the non-perfused test (Figure 62), consistent with findings reported in the literature. Further testing comparing non-perfused and perfused tests is required to draw more definite conclusions.

Although success in re-perfusion of the 5 subjects varied due to differences in the status of vessel degradation, the perfusion of the subarachnoid space is essential for returning the relationships between the meningeal layers to their in vivo state for accurate displacement

measurements. Future work investigating relative brain motion should continue efforts to re-perfuse the subarachnoid space.

4.3.4.2 Limitations of Measurement Technique

An advantage of using high-frequency B-mode ultrasound is the ability to capture tissue motion at high rates; however, this necessitates a narrow field of view across the width of the image. To maximize frame rate, an image width of 4.08 mm was used consistently throughout this dissertation, though recorded peak displacements were often larger. As described in Chapter 3: Validation of the Ultrasound Measurement Technique, as tracked points moved out of frame, additional points were tracked at the same depth. The time displacement of the previously tracked points was curve-fit using a shape-preserving piecewise cubic interpolation function. As the ultrasound image is created by a collection of single images, this means that points being imaged at the leading edge of the probe are collected earlier than points near the trailing edge. Points were tracked across the entire width of the image to ensure that the true peak displacement was captured, and the spline fit minimizes the error along the true curve. As was true in the validation study, the tracking errors were normally distributed about 0.

Studies of motion of deeper brain tissue have demonstrated out-of-plane motion up to 3 mm under anterior-posterior rotational loading at rotational velocities of 20 rad/s (Alshareef et al., 2018, 2020), though none of the reported displacement curves are near enough to the surface of the brain to draw conclusions that out-of-plane motion is comparable at the surface of the brain. Though rotations were constrained to a single plane and all tests in this dissertation work were able to be tracked, it is still possible that out-of-plane motion of the tissue occurred, which may influence the peak displacement results reported in this dissertation.

The peak displacement data was calculated from data that was obtained through semi-automatic tracking efforts, so, a possible limitation of the ultrasound measurement method is the subjectivity of point selection. Therefore, the intra-observational error was calculated using the technical error of measurement (TEM) (Weinberg et al., 2005). The differences in tracking the same tests were normally distributed, indicating user bias was not present. On average across all tests from all 5 subjects, the TEM was 0.12 mm which is consistent with other ultrasound validation studies (Korstanje et al., 2010; Mallory et al., 2018), demonstrating good repeatability between tracking efforts. Only one person tracked all the tests reported in this dissertation, so inter-observational error was not quantified.

3.2.4.3 Limitations of Methodology

The experimental methodology outlined in this dissertation was developed to minimize differences between subjects. The Head Alignment Tool (HAT) was developed for aligning each subject on its axis of rotation while maintaining an 8 cm radial location where brain motion was measured. While this technique ensures that the radial acceleration at the measured location is comparable between subjects, differences in head and brain sizes among subjects results in differences in the distance between the selected axis of rotation and a subject's center of gravity when compared between subjects. Future work should investigate if the CG location relative to the center of rotation is a significant contributor to the differences seen in peak displacement.

Furthermore, peak displacement results are only recorded from a single location based on external skull landmarks. The window location for all 5 subjects was determined using the sagittal suture with the assumption that the falx lies directly beneath it; however, upon inspection

of the MRIs for each subject, it was found that there is an offset between the sagittal suture and the underlying falx that ranges between 0.94 and 2.07 mm

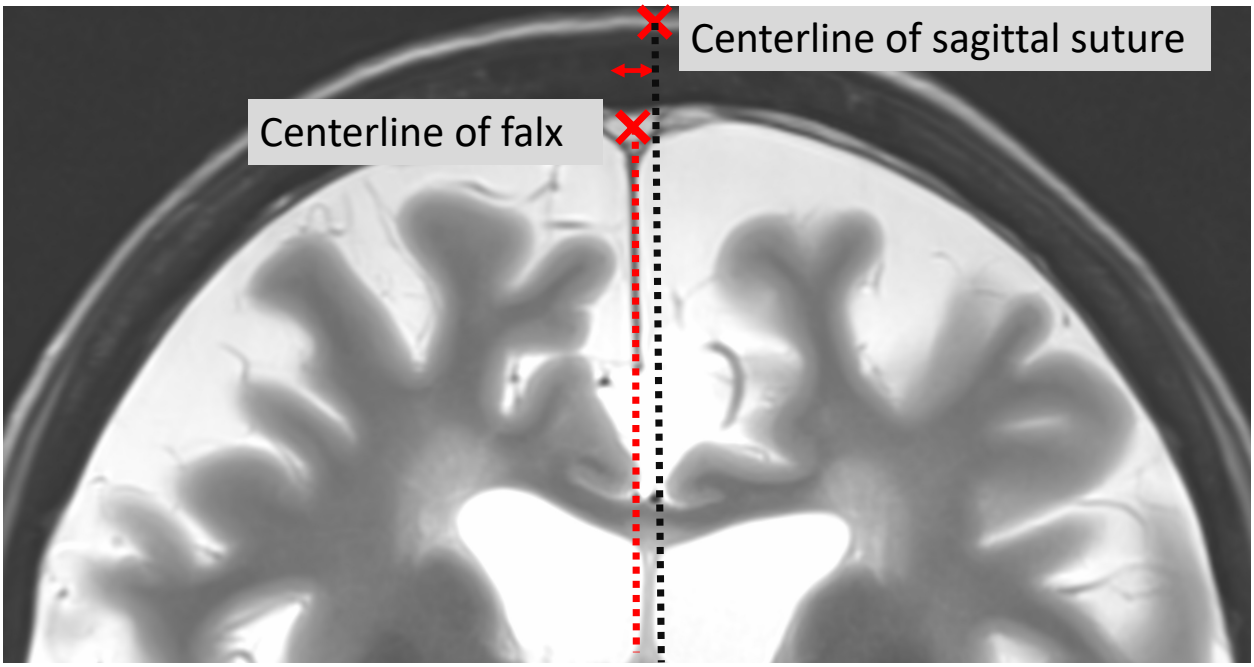

Figure 65: Offset observed between sagittal suture (black) and falx cerebri (red)

Although a linear relationship between the falx offset and the peak displacement was weak ($R^2<0.3$) for all three tracked depths (Figure 66), the relationship was statistically significant ($p<0.05$). This indicates that this offset contributes to the variability recorded between subjects, which is supported in the literature through the documentation that the falx cerebri influences brain tissue displacement (Yamashima et al., 1984, Hardy et al., 2007).

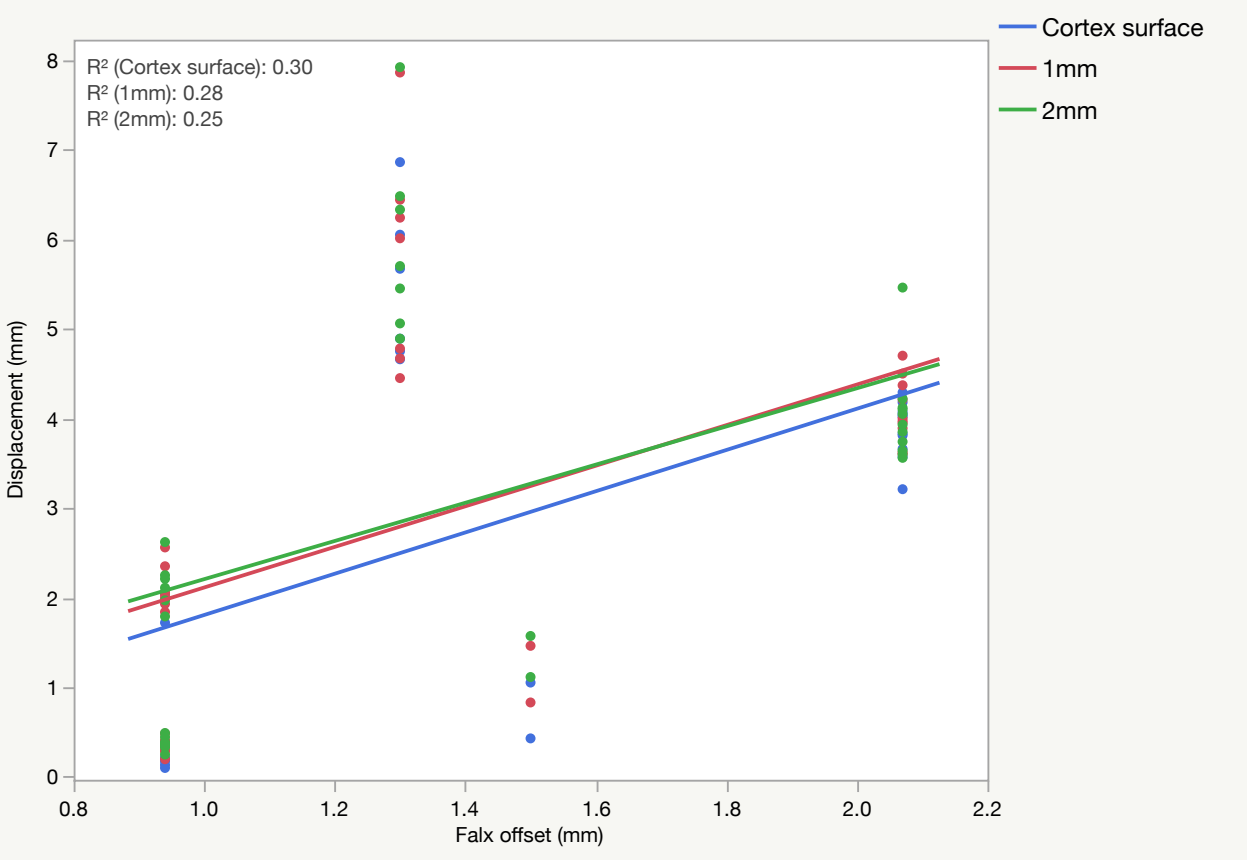

Figure 66: Relationship between falx distance and displacement for all trackable, non-damaged baseline tests

3.2.4.4 Limitations of Analysis Using Confounding Variables

Confounding variables such as age, BPF, head and brain mass, MOI, brain temperature, and the amount of postmortem time may account for many of the discrepancies in experimental brain research. It was not possible to vary each parameter that was studied in this dissertation work independently. Ideally, a sufficiently large sample size is required to evaluate the effects of these variables; however, a small sample size is a common limitation in PMHS studies. Efforts were taken to account for confounding variables in each analysis, and the limitations of each

confounding variable was acknowledged throughout this dissertation. The effects of these variables may be better explored through FE modeling, where the variables can be controlled independently. The data provided in this dissertation can be used to further validate FE head models to explore the effects of potentially confounding variables more accurately.

Because of the small sample size, multiple tests were run on each subject to maximize the amount of data collected. The repeat testing introduces another potentially confounding variable, as it is still unknown the amount of microdamage that results from multiple tests using a single subject. Therefore, for tests that are utilized for injury assessment development, it is recommended that only the first higher-severity test is utilized. However, additional testing can still be completed to continue investigating the influence of the variables mentioned above.

Chapter 5: Conclusions

5.1 Summary and Major Contributions

This dissertation work provides a novel, validated methodology to non-invasively quantify surface-level brain motion in postmortem human subjects using high-frequency B-mode ultrasound. The peak brain displacement dataset of 5 subjects under various loading conditions provides a significant contribution to the data available for validation of human body models. Analyses revealed the significance of subject characteristics such as degradation from a combination of postmortem time and cumulative microdamage, BPF, and MOI, which are not characterized in other brain motion studies. These parameters have a significant effect on the measurement of peak displacement, which may contribute to previous unexplained variability in PMHS brain experimental studies.

The first objective of this dissertation was to validate the use of high-frequency B-mode ultrasound as a measurement technique for quantifying surface-level brain motion under high-rate rotational motion. A custom validation fixture was fabricated to evaluate the validity of the ultrasound probe in the same manner that it is utilized for PMHS testing. The following were concluded:

- There was, on average, less than a 1.5% difference between the peak displacement of a tracking phantom calculated for the ultrasound measurement and a reference measurement system (linear potentiometer)

- Ultrasound overcomes the limitations of other measurement techniques such as sonomicrometry and high-speed biplanar x-ray by non-invasively measuring displacement at the surface of the brain
- With the ultrasound probe rotating at rotational velocities between 13.9 and 35.4 rad/s and rotational acceleration between 1490 and 3558 rad/s^2, lateral displacement of a phantom moving between 1 and 15 mm were accurate with 0.09 mm on average compared to the linear potentiometer

A second objective was to collect surface-level brain motion between the cortex and the skull under a variety of loading conditions to provide novel data for the further validation of human body models and to further the understanding of kinematics resulting in ASDH in the elderly. This dissertation provides over 300 displacement curves from 5 subjects varying in age, sex, and anthropometry that can be used to improve and validate human body models. Other studies had characterized whole-brain displacement but were limited when it came to providing surface-level displacement data. Not only does this work fill that gap for the betterment of all FE brain models, but more specifically, these data are another step towards understanding subdural hematoma injury risk assessment based on age and kinematic inputs. From the experimental rotation testing, the following were concluded:

- Subject-specific parameters such as postmortem time at which the data were collected, BPF, and MOI were all significant predictors of peak brain displacement, indicating that these parameters should continue to be quantified during experimental brain testing
- Rotational velocity was a better predictor of peak brain displacement compared to rotational acceleration

- As postmortem time increased, peak brain displacement of tests run with comparable kinematics also increased
- As BPF increased, peak brain displacement decreased
- As MOI increased, peak brain displacement decreased.

Results indicated human variation is widespread and has a significant contribution to how much displacement occurs in the brain when subjected to dynamic rotation. This makes the quantification of degradation even more difficult, as results here indicated that the effects of postmortem time are subject-dependent. Though degradation was not objectively quantified in this dissertation, the relationship between displacement and postmortem time was significant for peak brain displacement. This is a noteworthy finding as it further informs future experimental brain researchers on parameters that should be quantified to continue exploring this relationship. Though degradation was not quantified in this dissertation work, efforts were taken to ensure the effects of degradation were minimized. These efforts included:

- Limiting subject selection so that access is at no greater than 36 hours postmortem
- Streamlining procedures to minimize total accumulated postmortem time
- Prioritizing each test matrix, so the most important tests are collected first, thus minimizing the effects of postmortem time and accumulation of microdamage
- Adding preservatives to pressurization and perfusion fluids to slow the effects of degradation
- Monitoring and controlling temperature of the subjects throughout both preparation and testing, as colder temperatures have been shown to reduce the effects of postmortem degradation

5.2 Future Work

A comprehensive understanding of how the entire brain displaces under high-severity rotation is essential to predicting and mitigating injury. While the data provided in this dissertation fills a gap by providing surface-level displacement data, further investigation is necessary to understand how subject-specific parameters such as postmortem time, BPF, and MOI influence subject-to-subject displacement comparison. Understanding how brain stiffness changes with postmortem time is a logical next step that would better inform experimental results.

While the data provided does begin to fill the research gap, ultrasound is limited in only being able to quantify more superficial displacement. Therefore, future work should investigate the relationship between surface-level brain displacement and deeper brain displacements. Additionally, the small sample size provided in this dissertation limits the conclusions that can be drawn. More experimental data may strengthen the conclusions drawn here; however, with the data provided, these relationships could be more effectively explored using FE modeling. Future work should also explore brain motion under a larger range of severities, especially in the ranges known to result in subdural hematomas and other brain injuries.

References

AAAM. (2015). The Abbreviated Injury Scale – 2015 Revision. Association for the Advancement of Automotive Medicine, Des Plaines IL.

Abu-Zidan, F. M., Hefny, A. F., Corr, P. (2011) "Clinical ultrasound physics." J Emerg Trauma Shock. 2011 Oct-Dec; 4(4): 501–503.doi: 10.4103/0974-2700.86646: 10.4103/0974-2700.86646

Alshareef, A., Giudice, J.S., Forman, J., Salzar, R.S., and Panzer, M.B.(2018). A novel method for quantifying human in situ whole brain deformation under rotational loading using sonomicrometry. J. Neurotrauma 35, 780–789

Alshareef, A., Giudice, J. S., Forman, J., Shedd, D. F., Reynier, K. A., Wu, T., Sochor, S., Sochor, M. R., Salzar, R. S., & Panzer, M. B. (2020). Biomechanics of the Human Brain during Dynamic Rotation of the Head. *Journal of neurotrauma*, *37*(13), 1546–1555. https://doi.org/10.1089/neu.2019.6847

Andeweg J (1996) The anatomy of collateral venous flow from the brain and its value in aetiological interpretation of intracranial pathology. Neuroradiol 38:621–628

Balzani, D., Schröder, J., Gross, D. Simulation of discontinuous damage incorporating residual stresses in circumferentially overstretched atherosclerotic arteries., Acta biomaterialia 2 (6) (2006) 609–18.

Bayly, P. V., T. S. Cohen, E. P. Leister, D. Ajo, E. C. Leuthardt and G. M. Genin (2005). "Deformation of the Human Brain Induced by Mild Acceleration." Journal of Neurotrauma 22(8): 845-56

Beillas P, Helfenstein C, Rongieras F, Gennisson J L and Tanter M (2013). "A new method to assess the deformations of internal organs of the abdomen during impact." Computer Methods in Biomechanics and Biomedical Engineering 16 (sup1) 202–3

Bian K, Mao H. Mechanisms and variances of rotation-induced brain injury: a parametric investigation between head kinematics and brain strain. Biomech Model Mechanobiol. 2020 Dec;19(6):2323-2341. doi: 10.1007/s10237-020-01341-4. Epub 2020 May 24. PMID: 32449073

Bentil, S. and Dupaix, R. "Exploring the Mechanical Behavior of Degrading Swine Neural Tissue at Low Strain Rates Via the Fractional Zener Constitutive Model." Journal of the Mechanical Behavior of Biomedical Materials 30(2014):83-90.

Bergeron E, Rossignol M, et al. Improving the TRISS methodology by restructuring age categories and adding comorbidities. *J Trauma.* 2004;56(4):760–7.

Brockmann, C., Kunze, S., Scharf, J. (2011). "Computed tomographic angiography of the superior sagittal sinus and bridging veins., Surgical and radiologic anatomy": SRA 33 (2) 129–34.

Bullock MR, Chesnut R, Ghajar J, et al. Surgical management of acute subdural hematomas. Neurosurgery. 2006; 58:16–24

Chiewvit, P., Tritakarn, S.O., Nanta-aree, S., and Suthipongchai, S. (2010). "Degree of midline shift from CT scan predicted outcome in patients with head injuries." J. Med. Assoc. Thai. 93, 99–107.

Cook, B., Mallory, A., Moorhouse, K., Kang, Y. "The Relationship of Brain Atrophy and Age to aid in Subdural Hematoma Injury Risk Prediction." Poster Presentation, Injury Biomechanics Symposium, 2017.

Coronado, V. G., K. E. Thomas, R. W. Sattin and R. L. Johnson (2005). "The CDC Traumatic Brain Injury Surveillance System: Characteristics of Persons Aged 65 Years and Older Hospitalized with a TBI." Journal of Head Trauma Rehabilitation 20(3): 215- 228.

Csönge, L., Pellet, S., Szenes, A., Istvan, J., (1995). Antibiotics in the preservation of allograft and xenograft skin. Burns, Volume 21, Issue 2, Pages 102-105, ISSN 0305-4179.

Darvish, K. and Crandall, J. (2001). "Nonlinear Viscoelastic Effects in Oscillatory Shear Deformation of Brain Tissue." Medical Engineering and Physics, 23(9):633-645.

Daugherty J, Waltzman D, Sarmiento K, Xu L. "Traumatic Brain Injury-Related Deaths by Race/Ethnicity, Sex, Intent, and Mechanism of Injury - United States, 2000-2017". MMWR Morb Mortal Wkly Rep. 2019 Nov 22;68(46):1050-1056. doi: 10.15585/mmwr.mm6846a2. PMID: 31751321; PMCID: PMC6871899.

Delye, H., Goffin, J., Verschueren, P., Vander Sloten, J., Van der Perre, G., Alaerts, H. Verpoest, I., Berckmans, D. Biomechanical properties of the superior sagittal sinus-bridging vein complex., Stapp car crash journal 50 (November) (2006) 625–36.

Depreitere, B., C. Van Lierde, P. Verschueren, H. Delye, D. Berckmans, I. Verpoest, J. Vander Sloten, G. Van der Perre and J. Goffin (2005). "Cerebral Bridging Vein Rupture in Humans: An Experimental Evaluation." In IUTAM Symposium on Impact Biomechanics, M. D. Gilchrist, Springer: 305-12.

Depreitere, B., Van Lierde, C., Vander Sloten, J., Van Audekercke, R., Van der Perre, G., Plets, C., Goffin, J. Mechanics of acute subdural hematomas resulting from bridging vein rupture., Journal of neuro- surgery 104 (6) (2006) 950–6.

Divani, A.A., Majidi, S., Luo, X., Souslian, F.G., Zhang, J., Abosch, A., and Tummala, R.P. (2011). The ABCs of accurate volumetric measurement of cerebral hematoma. Stroke 42, 1569–1574

Ehrlich E, Maxeiner H, Lange J. Postmortem radiological investigation of bridging vein ruptures. Leg Med (Tokyo). 2003 Mar;5 Suppl 1: S225-7. doi: 10.1016/s1344-6223(02)00118-9. PMID: 12935596.

Famaey, N., Vander Sloten, J., Kuhl, E., A three-constituent damage model for arterial clamping in computer-assisted surgery., Biomechanics and modeling in mechanobiology 12 (1) (2013) 123–36.

Famaey N, Ying Cui Z, Umuhire Musigazi G, Ivens J, Depreitere B, Verbeken E, Vander Sloten J. Structural and mechanical characterization of bridging veins: A review. J Mech Behav Biomed Mater. 2015 Jan; 41:222-40. doi: 10.1016/j.jmbbm.2014.06.009. Epub 2014 Jul 11. PMID: 25052244.

Faul, M., Xu, L., Wald, M., and Coronado, V. (2010). “Traumatic Brain Injury in the United States: Emergency Department Visits, Hospitalizations, and Deaths”. Centers for Disease Control and Prevention, National Center for Injury Prevention and Control: Atlanta.

Feng, Y., T. M. Abney, R. J. Okamoto, R. B. Pless, G. M. Genin and P. V. Bayly (2010). "Relative Brain Displacement and Deformation During Constrained Mild Frontal Head Impact." Journal of the Royal Society Interface 7(53): 1677-88.

Ferrer, I., Santpere, G., Arzberger, T., Bell, J., Blanco, R., Boulda, S., Budka, H., Carmona, M., Giaccone, G., Krebs, B., Limido, L., Parchi, P., Ouig, B., Strammiello, R., Ströbel, T., Kretzschmar, H. (2007). "Brain Protein Preservation Largely Depends on the Postmortem Storage Temperature: Implications for Study of Proteins in Human Neurologic Diseases and Management of Brain Banks: A BrainNet Europe Study." J. Neuropathol Exp Neurol 66(1):35-46.

Fletcher, A. E., S. Khalid, et al. (2007). "The epidemiology of severe traumatic brain injury among persons 65 years of age and older in Oklahoma, 1992-2003." Brain Inj21(7): 691-9.

Fountain, D., Kolias, A., Lecky, F., Bouamra, O., Lawrence, T., Adams, H., Bond, S., Hutchinson, P. (2017). “Survival Trends Aftere Surgery for Acute Subdural Hematoma in Adults Over a 20-year Period.” Annals of Surgery 265(3).

Gabler LF, Crandall JR, Panzer MB. Development of a Metric for Predicting Brain Strain Responses Using Head Kinematics. Ann Biomed Eng. 2018 Jul;46(7):972-985. doi: 10.1007/s10439-018-2015-9. Epub 2018 Mar 28. PMID: 29594689.

Garo, A., Hrapko, M., Van Dommelen, J. and Peters, G. (2007). "Towards a Reliable Characterisation of the Mechanical Behaviour of Brain Tissue: The Effects of Post-Mortem Time and Sample Preparation." Biorheology, 44(1):51-58.

Gennarelli, T., Thibault, L., Ommaya, A. K. Pathophysiologic responses to rotational and translational accelerations of the head, Stapp car crash journal 16 (1972) 296–308.

Gennarelli, T. A., G. M. Spielman, T. W. Langfitt, P. L. Gildenberg, T. Harrington, J. A. Jane, L. F. Marshall, J. D. Miller, and L. H. Pitts (1982). "Influence of the Type of Intracranial Lesion on Outcome from Severe Head Injury." Journal of Neurosurgery 56(1): 26-32.

Gennarelli, T. A. and L. E. Thibault (1982). "Biomechanics of Acute Subdural Hematoma." Journal of Trauma-Injury Infection & Critical Care 22(8): 680-6.

Gosch, H. H., E. Gooding, and R. C. Schneider (1970). "The Lexan Calvarium for the Study of Cerebral Responses to Acute Trauma." Journal of Trauma-Injury Infection & Critical Care 10(5): 370-6.

Grossman, M., Miller, D., Scaff, D., Arcona, S. “When Is an Elder Old? Effect of Preexisting Conditions on Mortality in Geriatric Trauma.” The Journal of Trauma: Injury, Infection, and Critical Care: February 2002 - Volume 52 - Issue 2 - p 242-246

Guerrero, J. L., D. J. Thurman, et al. (2000). "Emergency department visits associated with traumatic brain injury: United States, 1995-1996." Brain Inj14(2): 181-6.

Han, H., Tao, W., Zhang, M. The dural entrance of cerebral bridging veins into the superior sagittal sinus: an anatomical comparison between cadavers and digital subtraction angiography., Neuroradiology49 (2) (2007) 169–75.

Hardy, W. N., C. D. Foster, M. Mason, K. H. Yang, A. I. King, and S. Tashman (2001). "Investigation of Head Injury Mechanisms Using Neutral Density Technology and High- Speed Biplanar X-Ray." Stapp Car Crash Journal 45: 1-32.

Hardy, W. N., M. J. Mason, C. D. Foster, C. S. Shah, J. M. Kopacz, K. H. Yang, A. I. King, J. Bishop, M. Bey, W. Anderst and S. Tashman (2007). "A Study of the Response of the Human Cadaver Head to Impact." Stapp Car Crash Journal 51: 17-80.

Helfenstein-Didier C, Tanter M, Gennisson J-L and Beillas P 2015. “Observation of the internal response of the kidney during compressive loading using ultrafast ultrasonography.” J. Biomech. 48 1852–9

Hodgson, V. R., E. S. Gurdjian and L. M. Thomas (1966). "Experimental Skull Deformation and Brain Displacement Demonstrated by Flash X-Ray Technique." Journal of Neurosurgery 25(5): 549-52

Holbourn, A.H.S. (1943) Mechanics of head injury. *The Lancet* (9 October): pp.438–441.

Horgan, T. J., and M. D. Gilchrist. The creation of three-dimensional finite element models for simulating head impact biomechanics. J. Crashworthiness, 8(4):353–366, 2003

Hrapko, M., Van Dommelen, J., Peters, G. and Wismans, J. (2008). "The Influence of Test Conditions on Characterization of the Mechanical Properties of Brain Tissue." Journal of Biomechanical Engineering, 130(3).

Huang, H.-M. M., (1999). "Three-Dimensional Finite Element Analysis of Subdural Hematoma." Journal of Trauma-Injury Infection & Critical Care: 538-544.

Hukkelhoven, C. W., E. W. Steyerberg, A. J. Rampen, E. Farace, J. D. Habbema, L. F. Marshall, G. D. Murray, and A. I. Maas (2003). "Patient Age and Outcome Following Severe Traumatic Brain Injury: An Analysis of 5600 Patients." Journal of Neurosurgery 99(4): 666-73.

Ibrahim, N. G., R. Natesh, S. E. Szczesny, K. Ryall, S. A. Eucker, B. Coats, and S. S. Margulies (2010). "In Situ Deformations in the Immature Brain During Rapid Rotations." Journal of Biomechanical Engineering 132(4): 044501.

Jack CR Jr, Bernstein MA, Fox NC, Thompson P, Alexander G, Harvey D, Borowski B, Britson PJ, L Whitwell J, Ward C, Dale AM, Felmlee JP, Gunter JL, Hill DL, Killiany R, Schuff N, Fox-Bosetti S, Lin C, Studholme C, DeCarli CS, Krueger G, Ward HA, Metzger GJ, Scott KT, Mallozzi R, Blezek D, Levy J, Debbins JP, Fleisher AS, Albert M, Green R, Bartzokis G, Glover G, Mugler J, Weiner MW. "The Alzheimer's Disease Neuroimaging Initiative (ADNI): MRI methods." J Magn Reson Imaging. 2008 Apr;27(4):685-91. doi: 10.1002/jmri.21049. PMID: 18302232; PMCID: PMC2544629.

Jacobs, B., Beems, T., van der Vliet, T.M., Diaz-Arrastia, R.R., Borm, G.F., and Vos, P.E. (2011). Computed tomography and outcome in moderate and severe traumatic brain injury: hematoma volume and midline shift revisited. J Neurotrauma 28, 203–215.

Jager, T. E., H. B. Weiss, et al. (2000). "Traumatic brain injuries evaluated in U.S. emergency departments, 1992-1994." Acad Emerg Med7(2): 134-40.

Jain, V., Langham, M. C., & Wehrli, F. W. (2010). MRI Estimation of Global Brain Oxygen Consumption Rate. Journal of Cerebral Blood Flow & Metabolism, 30(9), 1598–1607. https://doi.org/10.1038/jcbfm.2010.49

Ji, S., D. W. Roberts, A. Hartov and K. D. Paulsen (2009). "Brain-Skull Contact Boundary Conditions in an Inverse Computational Deformation Model." Medical Image Analysis 13(4): 659-72.

Ji, S., Q. Zhu, L. Dougherty, and S. S. Margulies (2004). "In Vivo Measurements of Human Brain Displacement." Stapp Car Crash Journal 48: 227-37.

Kang YS, Moorhouse K, Bolte JH IV. Instrumentation technique for measuring six degrees of freedom head kinematics in impact conditions using six-accelerometers and three-angular rate sensors (6aω configuration) on a lightweight tetrahedron fixture. Paper presented at: 24th International Technical Conference on the Enhanced Safety of Vehicles (ESV); Gothenburg, Sweden, June 8–11, 2015.

Kang, Y., Agnew, A., Hong, C. B., Icke, K., Bolte, J. "Elderly PMHS Thoracic Responses and Injuries in Frontal Impacts." Proceedings of the 2017 International IRCOBI Conference on the Biomechanics of Injury.

Kleiven, S. (2006). "Evaluation of Head Injury Criteria Using a Finite Element Model Validated against Experiments on Localized Brain Motion, Intracerebral Acceleration, and Intracranial Pressure." International Journal of Crashworthiness 11(1): 65-79.

Kleiven, S. and W. N. Hardy (2002). "Correlation of an FE Model of the Human Head with Local Brain Motion--Consequences for Injury Prediction." Stapp Car Crash Journal 46: 123-44.

Kleiven, S. and H. von Holst (2002). "Consequences of Head Size Following Trauma to the Human Head." Journal of Biomechanics 35(2): 153-60.

Kleiven, S. and H. von Holst (2002). "Consequences of Reduced Brain Volume Following Impact in Prediction of Subdural Hematoma Evaluated with Numerical Techniques." Traffic Injury Prevention 3: 303-310.

Kleiven, S. (2006). "Evaluation of Head Injury Criteria Using a Finite Element Model Validated against Experiments on Localized Brain Motion, Intracerebral Acceleration, and Intracranial Pressure." International Journal of Crashworthiness 11(1): 65-79.

Kleiven, S. Predictors for traumatic brain injuries evaluated through accident reconstructions. Technical report, SAE Technical Paper, 2007.

Knowles BM, Dennison CR. "Predicting Cumulative and Maximum Brain Strain Measures from Hybrid-III Head Kinematics: A Combined Laboratory Study and Post-Hoc Regression Analysis." Ann Biomed Eng. 2017 Sep;45(9):2146-2158. doi: 10.1007/s10439-017-1848-y. Epub 2017 May 11. PMID: 28497321; PMCID: PMC5569695.

Korstanje JW, Selles RW, Stam HJ, Hovius SE, Bosch JG. Development and validation of ultrasound speckle tracking to quantify tendon displacement. J Biomech. 2010 May 7;43(7):1373-9. doi: 10.1016/j.jbiomech.2010.01.001. Epub 2010 Feb 11. PMID: 20152983.

Le Ruyet A and Beillas P (2015). "Estimation of 2D strain in abdominal organs during an impact based on ultrafast ultrasound images: a physical landmark-based approach." Computer Methods in Biomechanics and Biomedical Engineering 18 (sup1) 2048–9

Lee, M. C., and R. C. Haut (1989). "Insensitivity of Tensile Failure Properties of Human Bridging Veins to Strain Rate: Implications in Biomechanics of Subdural Hematoma." Journal of Biomechanics 22(6-7): 537-42.

Lissner, H. R., Lebow, M., and Evans, F. G., (1960). “Experimental studies on the relation between acceleration and intracranial pressure changes in man.” Surgery, gynecology, and obstetrics, 111, 329.

Löwenhielm, P. (1974). "Dynamic Properties of the Parasagittal Bridging Veins." Zeitschrift fur Rechtsmedizin. Journal of Legal Medicine 74(1): 55-62.

Löwenhielm, P. (1974). "Strain Tolerance of the Vv. Cerebri Sup. (Bridging Veins) Calculated from Head-on Collision Tests with Cadavers." Zeitschrift fur Rechtsmedizin. Journal of Legal Medicine 75(2): 131-44.

Maas, A.I., Hukkelhoven, C.W., Marshall, L.F., and Steyerberg, EW. (2005). Prediction of outcome in traumatic brain injury with computed tomographic characteristics: a comparison between the computed tomographic classification and combinations of computed tomographic predictors. Neurosurgery 57, 1173–1182.

Maas, A.I., Steyerberg, E.W., Butcher, I., Dammers, R., Lu, J., Mar-marou, A., Mushkudiani, N.A., McHugh, G.S., and Murray, G.D. (2007). Prognostic value of computerized tomography scan characteristics in traumatic brain injury: results from the IMPACT study. J. Neurotrauma 24, 303–314

Madhukar, A., Ostoja-Starzewski, M. (2019) “Finite Element Methods in Human Head Impact Simulations: A Review.” Annals of Biomedical Engineering. Vol. 47, No. 9, pp. 1832–1854

Maier, S. E., C. J. Hardy and F. A. Jolesz (1994). "Brain and Cerebrospinal Fluid Motion: Real-Time Quantification with M-Mode MR Imaging." Radiology 193(2): 477-83.

Mallory, A. (2010). "Head Injury and Aging: The Importance of Bleeding Injuries." Annals of Advances in Automotive Medicine 54: 51-60.

Mallory, A., R. Herriott and H. Rhule (2011). "Subdural Hematoma and Aging: Crash Characteristics and Associated Injuries." 22nd International Technical Conference on the Enhanced Safety of Vehicles (ESV). Washington, DC: Paper Number 11-0399.

Mallory, A. (2014). “Measurement of meningeal motion using B-mode ultrasound as a step toward understanding the mechanism of subdural hematoma.” *PhD Dissertation* The Ohio State University

Mallory, A., Donnelly, B., Liu, J., Bahner, D., Moorhouse, K., Dupaix, R. (2018) “Addressing spatiotemporal distortion of high-speed tissue motion in B-mode ultrasound.” *Biomed. Phys. Eng. Express* 4 057003.

Marshall, L. F., T. Gautille, M. R. Klauber, H. M. Eisenberg, J. A. Jane, T. G. Luerssen, A. Marmarou and M. A. Foulkes (1991). "The Outcome of Severe Closed Head Injury." Journal of Neurosurgery 75: S28-S36.

Maxeiner, H. (1997). "Detection of Ruptured Cerebral Bridging Veins at Autopsy." Forensic Science International 89(1-2): 103-10.

Maxeiner, H. (1998). "Subdural Hematomas in Victims with and without Cerebral Contusions - Comparison of Two Types of Head Injuries." Rechtsmedizin 9(1): 14-20.

Maxeiner, H., and M. Wolff (2002). "Pure Subdural Hematomas: A Postmortem Analysis of Their Form and Bleeding Points." Neurosurgery 50(3): 503-509.

McElhaney, J.H., Melvin, J.W., Roberts, V.L., Portnoy, H.D., 1973. Dynamic characteristics of the tissues of the head. Kenedi, R. M., ed. Perspectives in Biomedical Engineering. Proceedings of a Symposium. Macmillan press Ltd., London, 215–222.

Meaney, D. F. (1991). "Biomechanics of Acute Subdural Hematoma in the Subhuman Primate and Man." Ph.D. Dissertation, Bioengineering, University of Pennsylvania.

Meder JF, Chiras J, Roland J, et al (1994) Venous territories of the brain. J Neuroradiol 21:118–133

Metz, H., McElhaney, J., and Ommaya, A.K. (1970). "A Comparison of the Elasticity of Live, Dead, and Fixed Brain Tissue." Journal of Biomechanics, (3):453-458.

Miller, D. J., I. R. Piper, and P. A. Jones (1996). "Pathophysiology of Head Injury." In Neurotrauma, R. K. Narayan, J. E. Wilberger, and J. T. Povlishock (Eds.), New York, McGraw Hill: 61-69.

Monea, A.G., Baeck, K., Verbeken, E., Verpoest, I., Sloten, J.V., Goffin, J., Depreitere, B. The biomechanical behaviour of the bridging vein-superior sagittal sinus complex with implications for the mechanopathology of acute subdural haematoma., Journal of the mechanical behavior of biomedical materials 32C (2014) 155–165.

Monea, A. G., I. Verpoest, J. Vander Sloten, G. Van der Perre, J. Goffin, and B. Depreitere (2012). "Assessment of Relative Brain-Skull Motion in Quasistatic Circumstances by Magnetic Resonance Imaging." Journal of Neurotrauma 29(13): 2305- 2317.

Monson, K. L., W. Goldsmith, N. M. Barbaro, and G. T. Manley (2005). "Significance of Source and Size in the Mechanical Response of Human Cerebral Blood Vessels." Journal of Biomechanics 38(4): 737-744.

Moore, K. L., Dalley, A. F., & Agur, A. M. (2013). Clinically oriented anatomy.

Mosenthal, A. C., R. F. Lavery, M. Addis, S. Kaul, S. Ross, R. Marburger, E. A. Deitch and D. H. Livingston (2002). "Isolated Traumatic Brain Injury: Age Is an Independent Predictor of Mortality and Early Outcome." Journal of Trauma-Injury Infection & Critical Care 52(5): 907-11.

NCIPC. Web-based Injury Statistics Query and Reporting System (WISQARS) [Internet]. www.cdc.gov. http://www.cdc.gov/injury/wisqars/ (accessed January 2022).

Nahum, A.; Smith, R.; Ward, C. Proc. 21st Stapp Car Crash Conference. Society of Automotive Engineers; Warrendale, PA: 1977. Intracranial pressure dynamics during head impact; p. 337-366.

Newman, J. A. (1998). "Kinematics of Head Injury." In Frontiers of Head and Neck Trauma: Clinical and Biomechanical, N. Yoganandan, F. A. Pintar, S. J. Larson, and A. Sances (Eds.), Burke, Virginia, IOS Press Inc.: 200-214.

Nicolle, S., M. Lounis and R. Willinger (2004). "Shear Properties of Brain Tissue over a Frequency Range Relevant for Automotive Impact Situations: New Experimental Results." Stapp Car Crash Journal 48: 239.

Nusholtz, G. S., P. Lux, P. Kaiker and M. A. Janicki (1984). "Head Impact Response - Skull Deformation and Angular Accelerations." Stapp Car Crash Conference, Society of Automotive Engineers: 41-74.

Oka KA, Rhoton AL, Barry M, et al (1985) Microsurgical anatomy of the superficial veins of the cerebrum. Neurosurgery 17:711–748

Ommaya, A. K., F. Faas and P. Yarnell (1968). "Whiplash Injury and Brain Damage: An Experimental Study." JAMA: Journal of the American Medical Association 204(4): 285- 9.

Ommaya, A. K., W. Goldsmith, and L. Thibault (2002). "Biomechanics and Neuropathology of Adult and Paediatric Head Injury." British Journal of Neurosurgery 16(3): 220-242.

Pentland, B., P. A. Jones, et al. (1986). "Head injury in the elderly." Age Ageing15(4): 193-202.

Peters, G., Meulman, J. and Sauren, A. (1997). "The Applicability of the Time/Temperature Superposition Principle to Brain Tissue." Biorheology, 34(2):127-138.

Poncelet, B. P., V. J. Wedeen, R. M. Weisskoff and M. S. Cohen (1992). "Brain Parenchyma Motion: Measurement with Cine Echo-Planar MR Imaging." Radiology 185(3): 645-51.

Pudenz, R. H. and C. H. Shelden (1946). "The Lucite Calvarium; a Method for Direct Observation of the Brain; Cranial Trauma and Brain Movement." Journal of Neurosurgery 3(6): 487-505.

Puymirat, J., Javoy-Agid, F., Gaspar, P., Ploska, A., Prochiantz, A., Agid, Y. (1979). "Post Mortem Stability and Storage in the Cold of Brain Enzymes." Journal of Neurochemistry 32:449-454.

Raboel, P., J. Bartek, M. Andresen, B. Bellander and B. Romner (2012). "Intracranial Pressure Monitoring: Invasive Versus Non-Invasive Methods—a Review." Critical care research and Practice 2012.

Rang, E. M., Lippert, S. A. and Grimm, M. J. (2001). "The Degradation of Material Properties of Brain Tissue as a Function of Time Postmortem." ASME Bioengineering Conference. Snowbird, Utah.

Rashid, B., Destrade, M. and Gilchrist, M. D. (2013). "Influence of Preservation Temperature on the Measured Mechanical Properties of Brain Tissue." Journal of Biomechanics, 46(7):1276-1281.

Rhoton AL (2002) The cerebral veins. Neurosurgery 51 [4 Suppl]: S159–205

Roozenbeek B, Maas AI, Menon DK. “Changing patterns in the epidemiology of traumatic brain injury”. Nat Rev Neurol. 2013 Apr;9(4):231-6. doi: 10.1038/nrneurol.2013.22. Epub 2013 Feb 26. PMID: 23443846.

SAE (2007). "J211/1 200707: Instrumentation for Impact Test Part 1 - Electronic Instrumentation." Warrendale, PA.

Sampei, T., Yasui, N., Okudera, T., Fukasawa, F. Anatomic study of anterior frontal cortical bridging veins with special reference to the frontopolar vein., Neurosurgery 38 (5) (1996) 971–5.

Sass, D. J., P. Corrao and A. K. Ommaya (1971). "Brain Motion During Vibration of Water Immersed Rhesus Monkeys." Journal of Biomechanics 4(5): 331-4.

Sawauchi, S. and T. Abe (2008). "The Effect of Haematoma, Brain Injury, and Secondary Insult on Brain Swelling in Traumatic Acute Subdural Haemorrhage." Acta Neurochirurgica 150(6): 531-6; discussion 536.

Seelig, J. M., D. P. Becker, J. D. Miller, R. P. Greenberg, J. D. Ward, and S. C. Choi (1981). "Traumatic Acute Subdural Hematoma: Major Mortality Reduction in Comatose Patients Treated within Four Hours." New England Journal of Medicine 304(25): 1511-8.

Shatsky, S. A., W. A. Alter, III, D. E. Evans, V. Armbrustmacher and G. Clark (1974). "Traumatic Distortions of the Primate Head and Chest: Correlation of Biomechanical, Radiological and Pathological Data." Stapp Car Crash Conference, Society of Automotive Engineers: 351-381.

Shatsky, S. A., D. E. Evans, F. Miller, and A. N. Martins (1974). "High-Speed Angiography of Experimental Head Injury." Journal of Neurosurgery 41(5): 523-30.

Sheldon, C. H., R. H. Pudenz, J. S. Restarski and W. M. Craig (1944). "The Lucite Calvarium - a Method for Direct Observation of The Brain. I. The Surgical and Lucite Processing Techniques" Journal of Neurosurgery 1(1): 67-75.

Shen, F., Tay, T., Li, J., Nigen, S., Lee, P. and Chan, H. (2006). "Modified Bilston Nonlinear Viscoelastic Model for Finite Element Head Injury Studies."

Shugar, T. (1977), "A finite element head injury model. Vol I: Theory, development, and results." Tech. rep. Dept. Of Transportation Report No. DOT-HS-289-3-550-IA.

Smith, C. D., H. Chebrolu, et al. (2007). "Age and gender effects on human brain anatomy: A voxel-based morphometric study in healthy elderly." Neurobiology of Aging28: 1075-1087.

Stalnaker, R. L., J. W. Melvin, G. S. Nusholtz, N. M. Alem and J. B. Benson (1977). "Head Impact Response." Stapp Car Crash Conference, Society of Automotive Engineers: 305-335.

Stitzel, J. D., P. D. Kilgo, K. A. Danelson, C. P. Geer, T. Pranikoff and J. W. Meredith (2008). "Age Thresholds for Increased Mortality of Three Predominant Crash Induced Head Injuries." Annual proceedings of the Association for the Advancement of Automotive Medicine 52: 235-44.

Strik, H.M., Borchert, H., Fels, C., Knauth, M., Rienhoff, O., Ba¨hr, M., and Verhey, J.F. (2005). Three-dimensional reconstruction and volumetry of intracranial haemorrhage and its mass effect. Neuroradiology 47, 417–424

Sucu, H.K., Gokmen, M., and Gelal, F. (2005). The value of XYZ/2technique compared with computer-assisted volumetric analysis to estimate the volume of chronic subdural hematoma. Stroke 36, 998–1000.

Sugawara, O., Y. Atsuta, T. Iwahara, T. Muramoto, M. Watakabe and Y. Takemitsu (1996). "The Effects of Mechanical Compression and Hypoxia on Nerve Root and Dorsal Root Ganglia. An Analysis of Ectopic Firing Using an in Vitro Model." Spine 21(18): 2089-94.

Takhounts, E.G., Craig, M.J., Moorhouse, K., McFadden, J., Hasija, V. (2013) Development of Brain Injury Criteria (BrIC). Stapp Car Crash Journal, 57: pp.243–266.

Taussky, P., H. R. Widmer, J. Takala and J. Fandino (2008). "Outcome after Acute Traumatic Subdural and Epidural Haematoma in Switzerland: A Single-Centre Experience." Swiss Med Wkly 138(19-20): 281-5.

Taylor CA, Bell JM, Breiding MJ, Xu L. Traumatic Brain Injury–Related Emergency Department Visits, Hospitalizations, and Deaths — United States, 2007 and 2013. MMWR Surveill Summ 2017;66(No. SS-9):1–16.

Trosseille, X., C. Tarriére, F. Lavaste, F. Guillon and A. Domont (1992). "Development of a F.E.M. Of the Human Head According to a Specific Test Protocol." Stapp Car Crash Conference.

Urban, J., Whitlow, C., Edgerton, C., Powers, A., Maldjian, J., Stitzel, J (2012). "Motor Vehicle Crash-Related Subdural Hematoma from Real-World Head Impact Data." Journal of Neurotrauma 29:2774-2781.

United States Census Bureau. "Population Estimates Program (PEP)." March 2021.

Vågberg, M., Granåsen, G., and Svenningsson, A. (2017). Brain parenchymal fraction in healthy adults - a systematic review of the literature. PLoS ONE 12 (1): e0170018. doi:10.1371/journal. pone.0170018.

Vignes, J.-R., Dagain, A., Gúerin, J., Liguoro, D. "A hypothesis of cerebral venous system regulation based on a study of the junction between the cortical bridging veins and the superior sagittal sinus. Laboratory investigation." Journal of neurosurgery 107 (6) (2007) 1205–10.

Visualsonics (2009). "Vevo2100 Transducers V1.9." VisualSonics. Toronto, Ontario.

Vollmer, D. G., J. C. Torner, J. A. Jane, B. Sadovnic, D. Charlebois, H. M. Eisenberg, M. A. Foulkes, A. Marmarou and L. F. Marshall (1991). "Age and Outcome Following Traumatic Coma: Why Do Older Patients Fare Worse." Journal of Neurosurgery 75: S37- S49.

Walcott BP, Khanna A, Kwon C-S, et al. Time interval to surgery and outcomes following the surgical treatment of acute traumatic subdural hematoma. J Clin Neurosci. 2014; 21:2107–2111

Weinberg, SM., Scott, NM., Neiswanger, K., Marazita, ML. (2005). "Intraobserver error associated with measurements of the hand." J. Hum Biol. May-Jun; 17(3):368-71

Weisbecker, H., Pierce, D., Regitnig, P., Holzapfel, G. Layer-specific damage experiments and modeling of human thoracic and abdominal aortas with non-atherosclerotic intimal thickening., Journal of the mechanical behavior of biomedical materials 12 (2012) 93–106.

Wetli, A., Cook, B., Mallory, A., Moorhouse, K., Kang, Y. "Developing a Method of Slowing Brain Tissue Degradation through Temperature, Sodium Bicarbonate and Antibiotics for Traumatic Brain Injury Testing."Poster Presentation, Injury Biomechanics Symposium, 2017.

Wilberger JE, Harris M, Diamond DL. Acute subdural hematoma: morbidity, mortality, and operative timing. J Neurosurg. 1991; 74:212–218

Wilson MH, Kolias AG, Hutchinson PJ. Neurotrauma - a multidisciplinary disease. Int J Clin Pract. 2014 Jan;68(1):5-7. doi: 10.1111/ijcp.12246. PMID: 24341298.

Yamashima, T., Friede, R. L. Why do bridging veins rupture into the virtual subdural space? Journal of neurology, neurosurgery, and psychiatry 47 (2) (1984) 121–7.

Zafrullah Arifin M, Ginowan W. Analysis of pre surgery time as a prognostic factor in traumatic acute subdural hematoma. J Neurosurg Sci. 2013;57:277–280.

Zhang, J., Yoganandan, N., Pintar, F. A., Guan, Y., Shender, B., Paskoff, G. and Laud, P. (2011). "Effects of Tissue Preservation Temperature on High Strain-Rate Material Properties of Brain." Journal of Biomechanics, 44(3):391-396.

Zhong, X., C. H. Meyer, D. J. Schlesinger, J. P. Sheehan, F. H. Epstein, J. M. Larner, S. H. Benedict, P. W. Read, K. Sheng and J. Cai (2009). "Tracking Brain Motion During the Cardiac Cycle Using Spiral Cine-Dense MRI." Medical Physics 36(8): 3413-9.

Zhou, C., Khalil, T. B., King, A. I. (1995). "A New Model Comparing Impact Responses of the Homogeneous and Inhomogeneous Human Brain." Proceedings of the 39th Stapp Car Crash Conference, SAE Technical Paper 952714: pg. 121-37.

Zhou, Z., 2019. Evaluation of Fluid-Structure Interaction and Biofidelity of Finite Element Head Models. Ph.D. Thesis, KTH Royal Institute of Technology, Stockholm, Sweden.

Zhou, Z., Li., X., Klieven, S. (2020). "Evaluation of brain-skull interface modelling approaches on the prediction of acute subdural hematoma in the elderly." Journal of Biomechanics. Volume 105, 2020, 109787, ISSN 0021-9290.

Zoghi-Moghadam, M., Sadegh, A.M. (2009) "Global/local head models to analyse cerebral blood vessel rupture leading to ASDH and SAH." Computer Methods in Biomechanics and Biomedical Engineering 12 (1) 1– 12

Zou, H., J. P. Schmiedeler and W. N. Hardy (2007). "Separating Brain Motion into Rigid Body Displacement and Deformation under Low-Severity Impacts." Journal of Biomechanics 40(6): 1183-91.

Appendix A: Validation Results

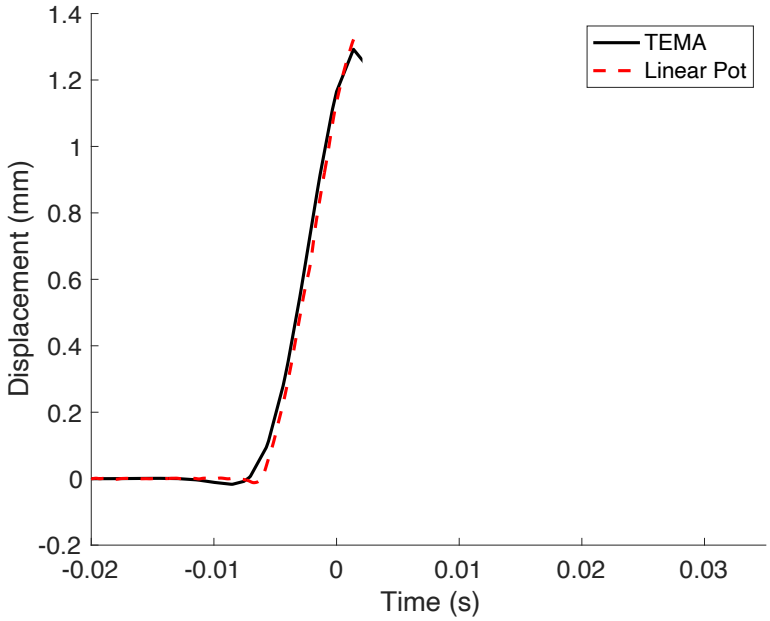

(a) Test 1

Figure 67: Comparison of displacement time histories from tracked ultrasound data (black) and a linear potentiometer (red dashed) for validation tests 1-27 (a-aa)

Figure 67 continued

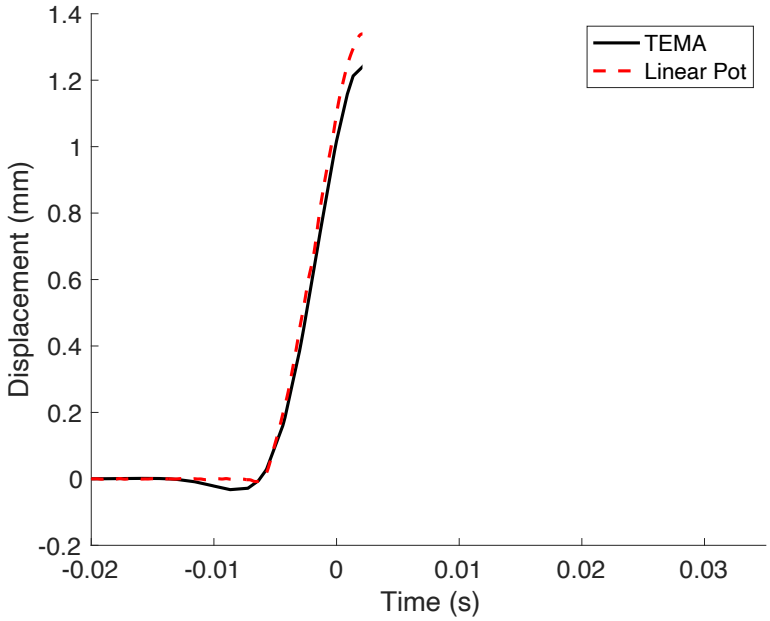

(b) Test 2

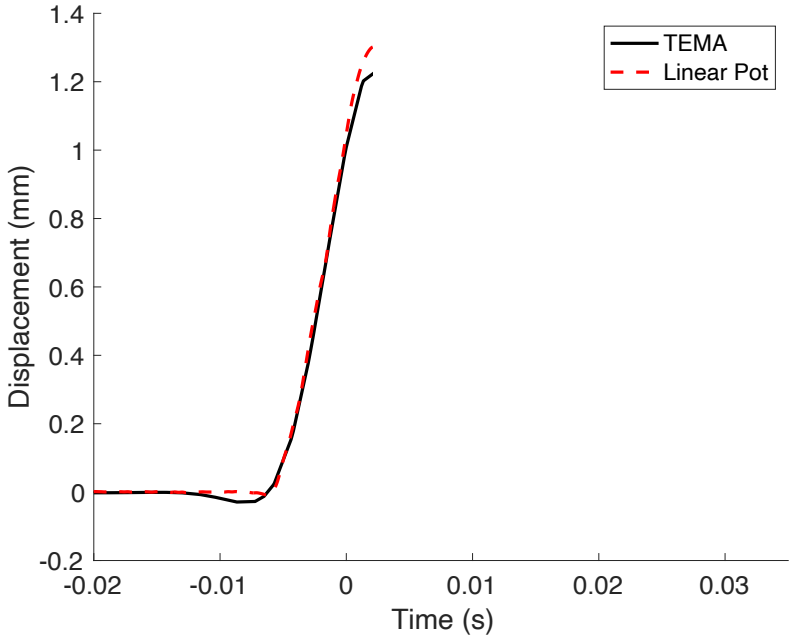

(c) Test 3

Figure 67 continued

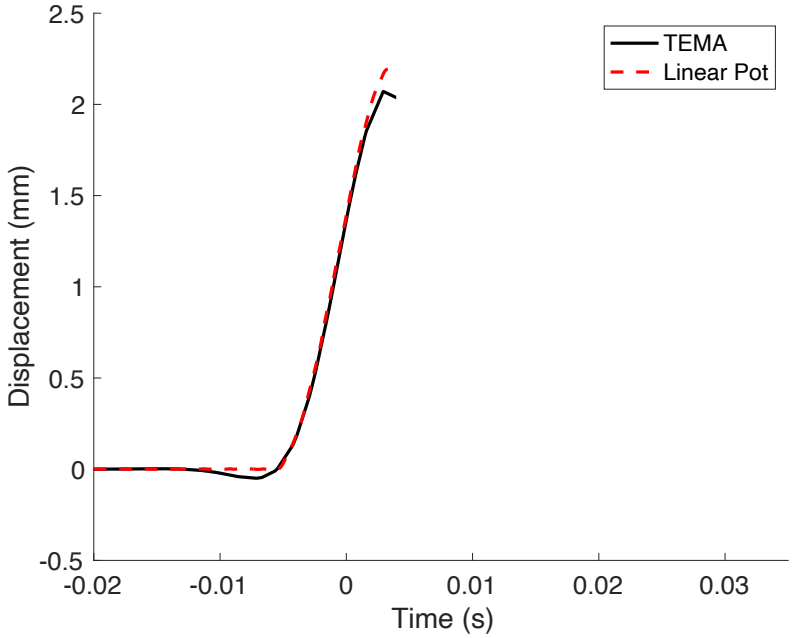

(d) Test 4

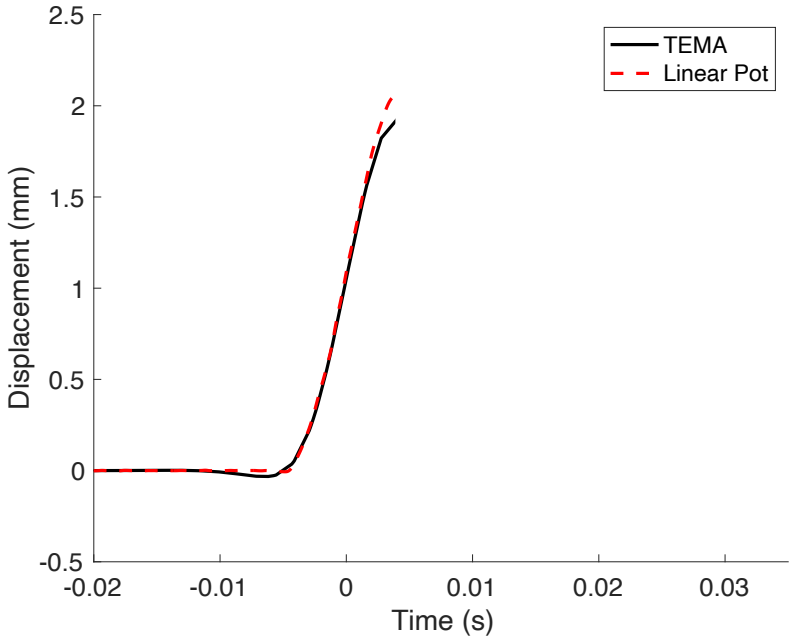

(e) Test 5

Figure 67 continued

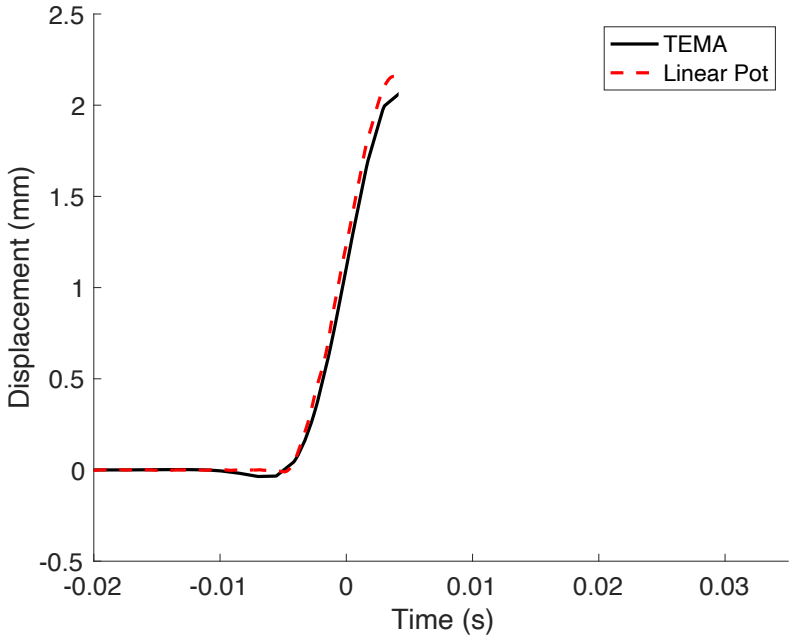

(f) Test 6

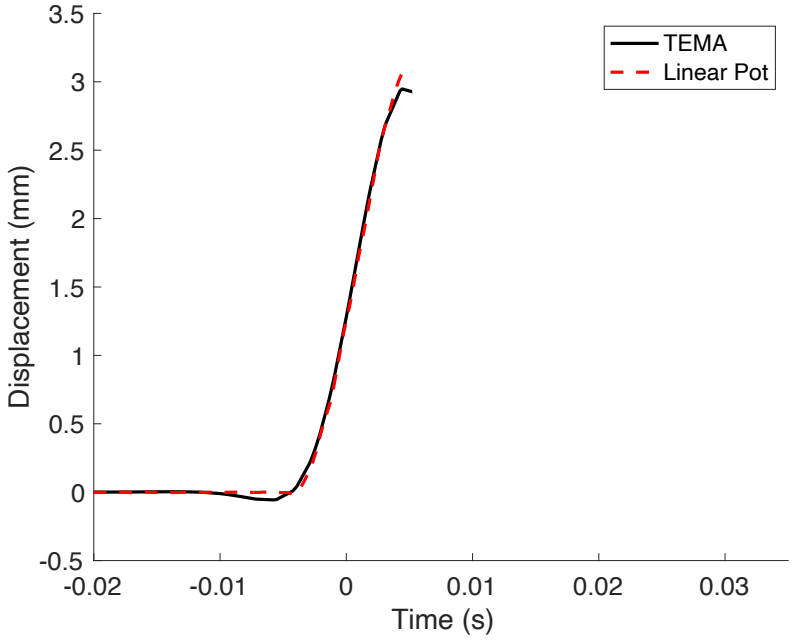

(g) Test 7

Figure 67 continued

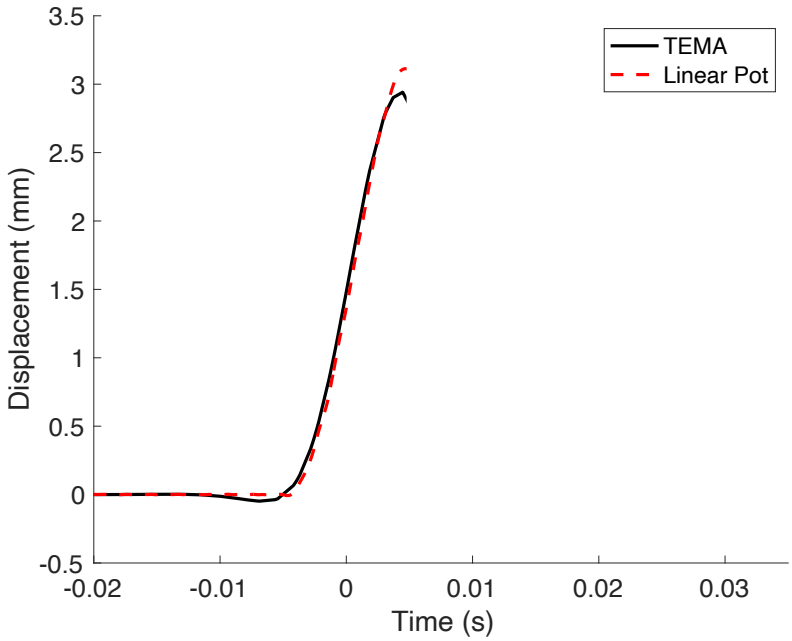

(h) Test 8

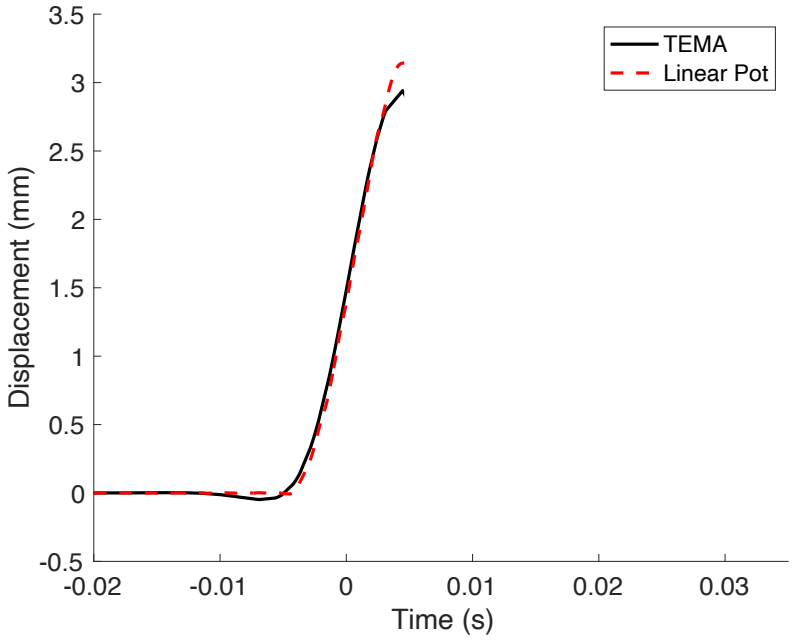

(i) Test 9

Figure 67 continued

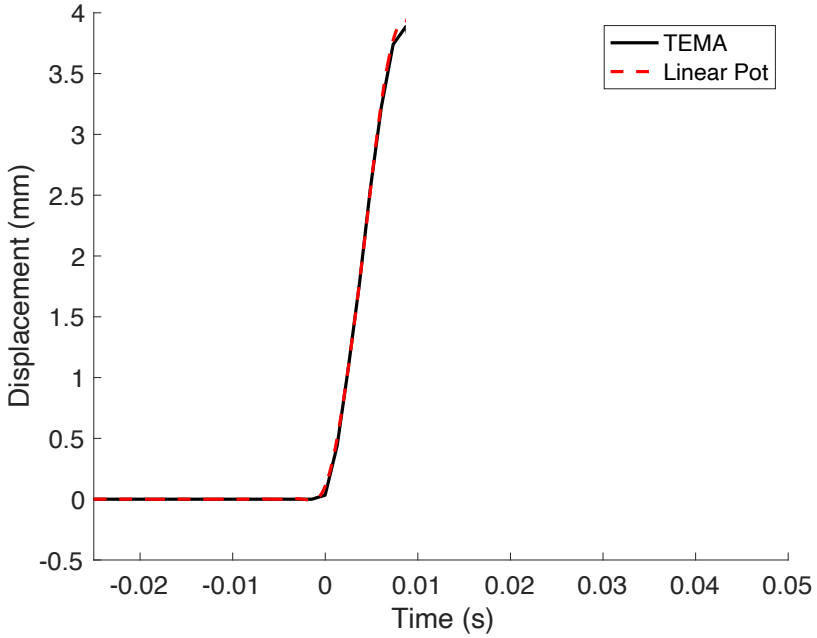

(j) Test 10

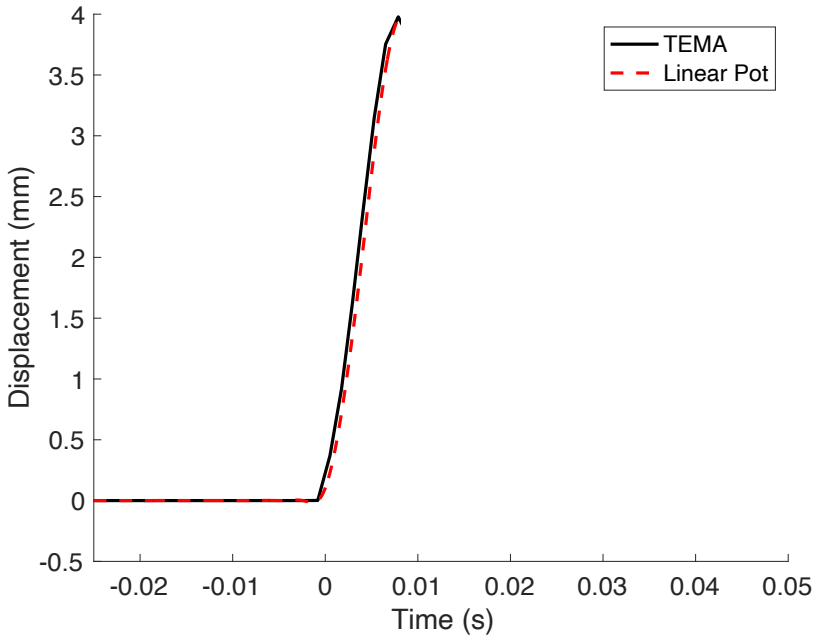

(k) Test 11

Figure 67 continued

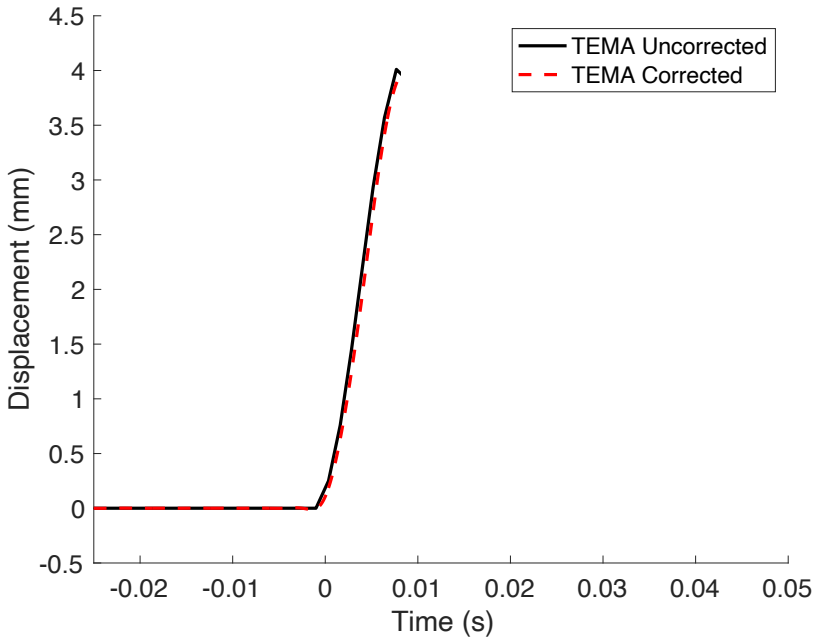

(l) Test 12

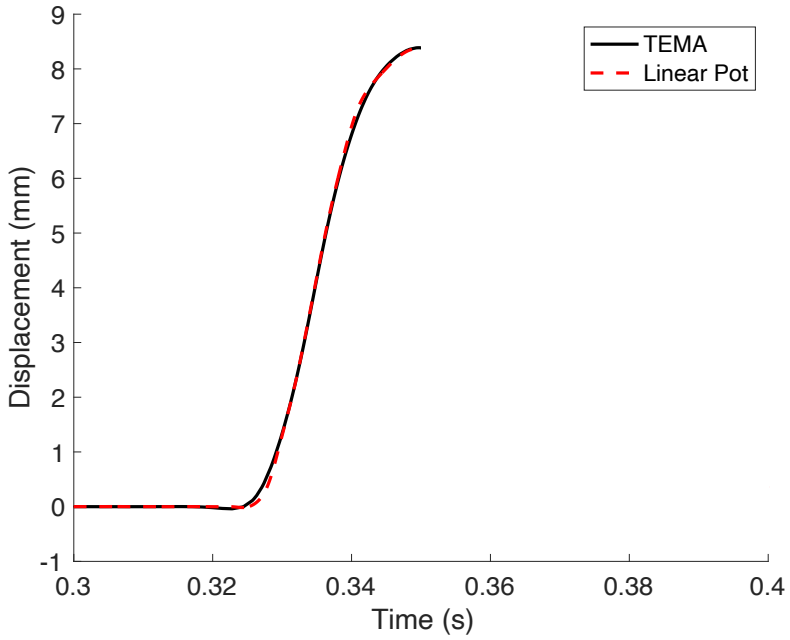

(m) Test 13

Figure 67 continued

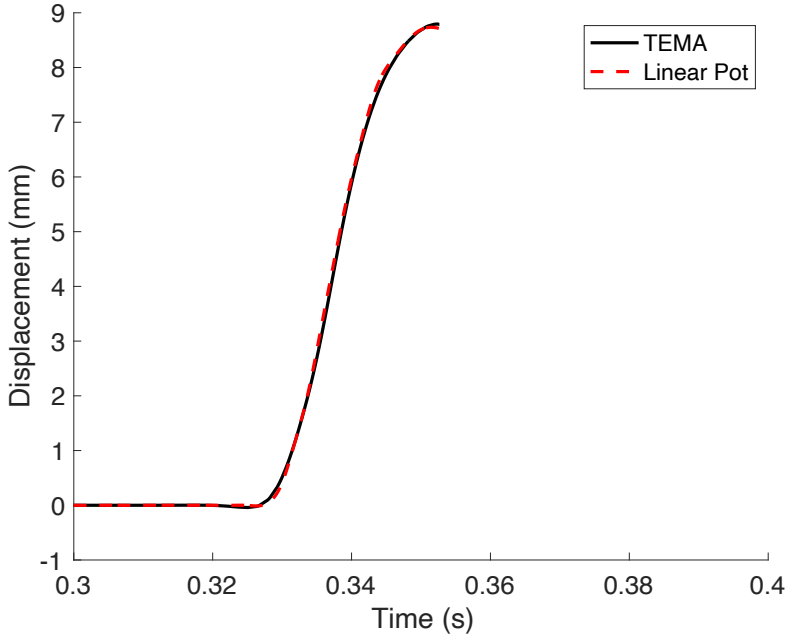

(n) Test 14

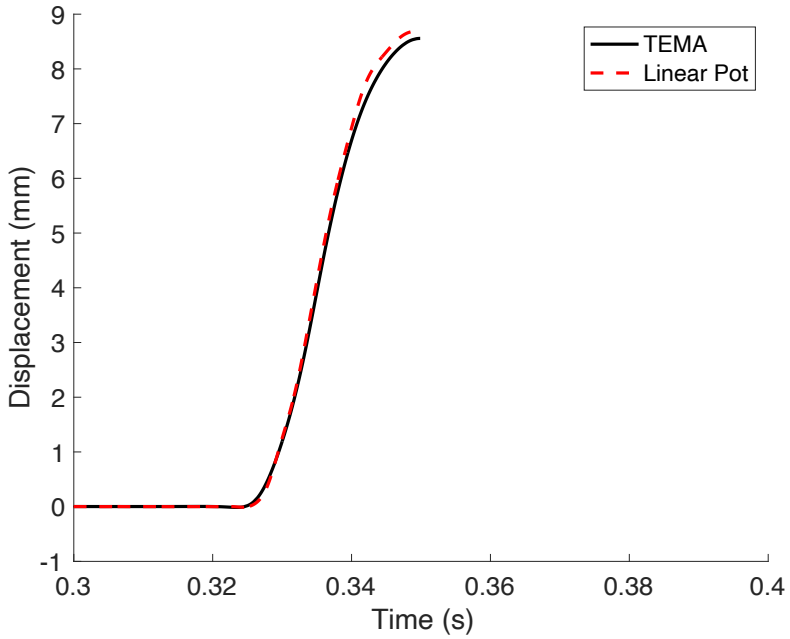

(o) Test 15

Figure 67 continued

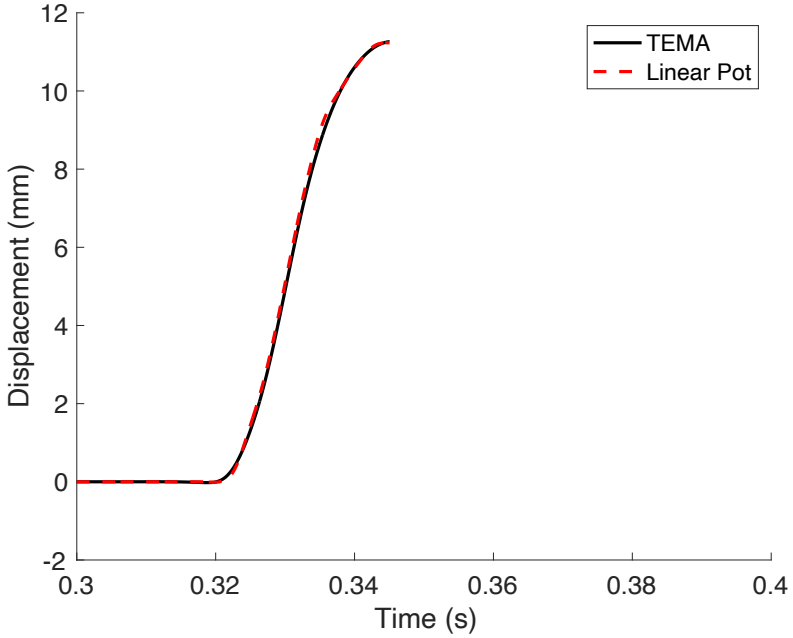

(p) Test 16

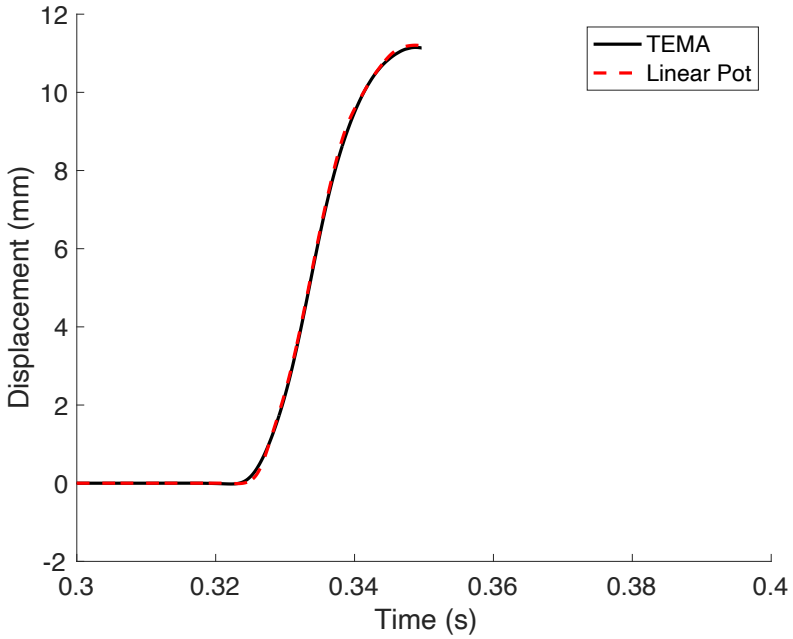

(q) Test 17

Figure 67 continued

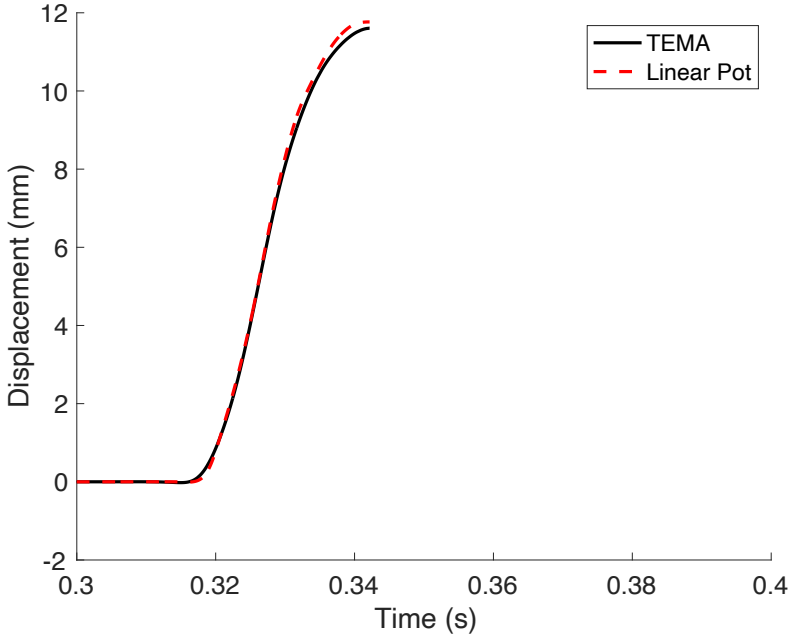

(r) Test 18

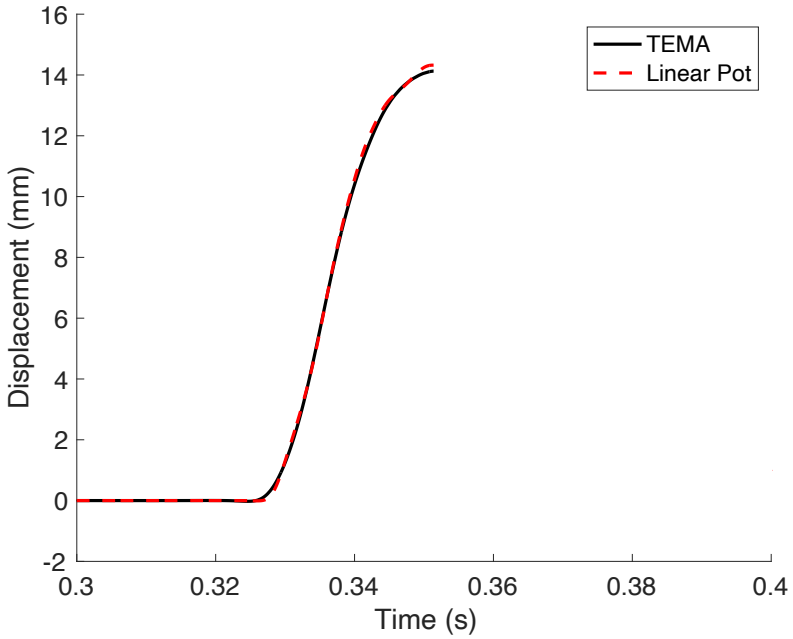

(s) Test 19

Figure 67 continued

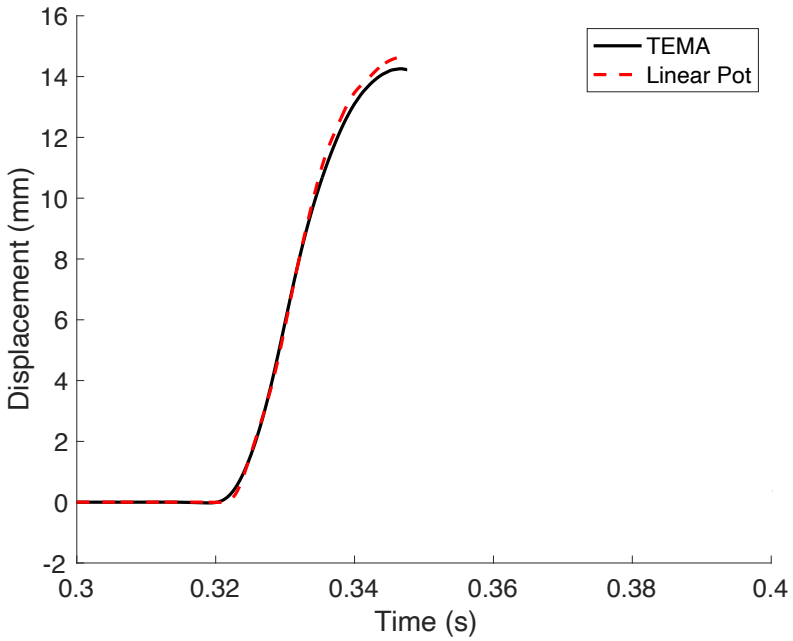

(t) Test 20

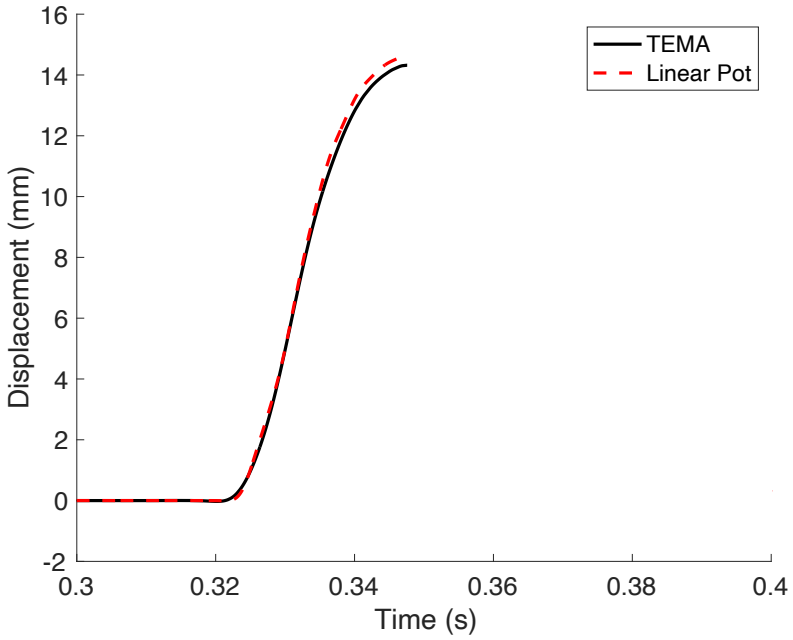

(u) Test 21

Figure 67 continued

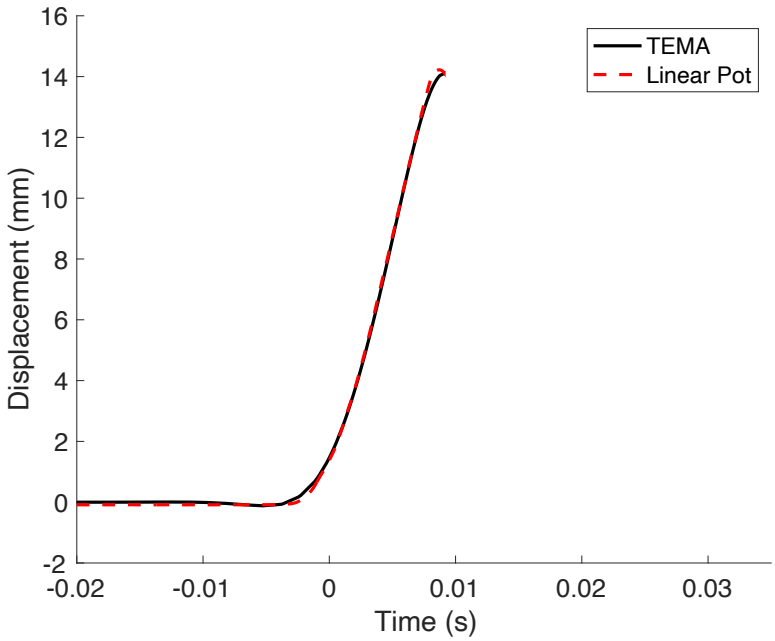

(v) Test 22

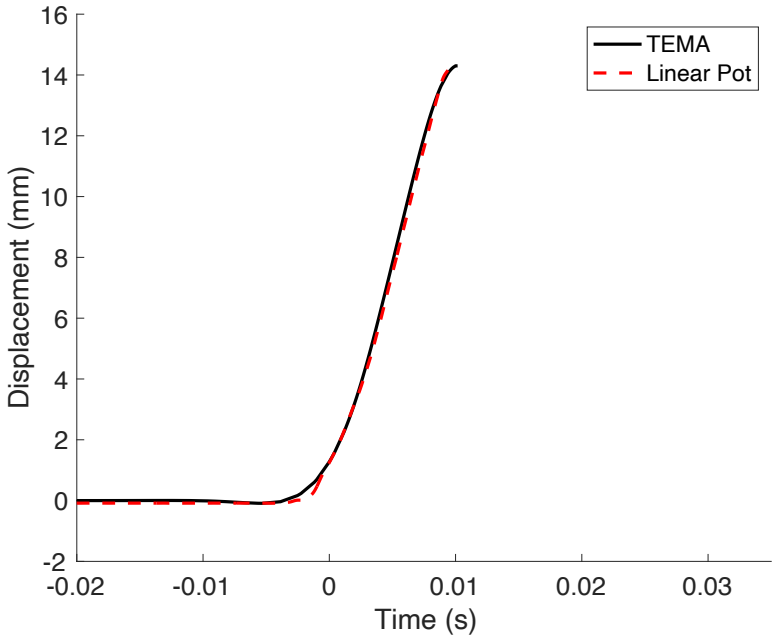

(w) Test 23

Figure 67 continued

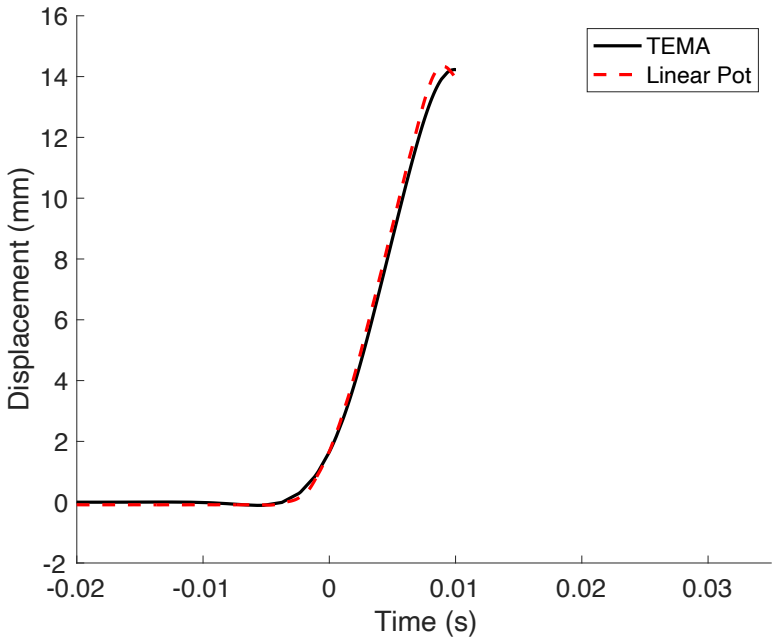

(x) Test 24

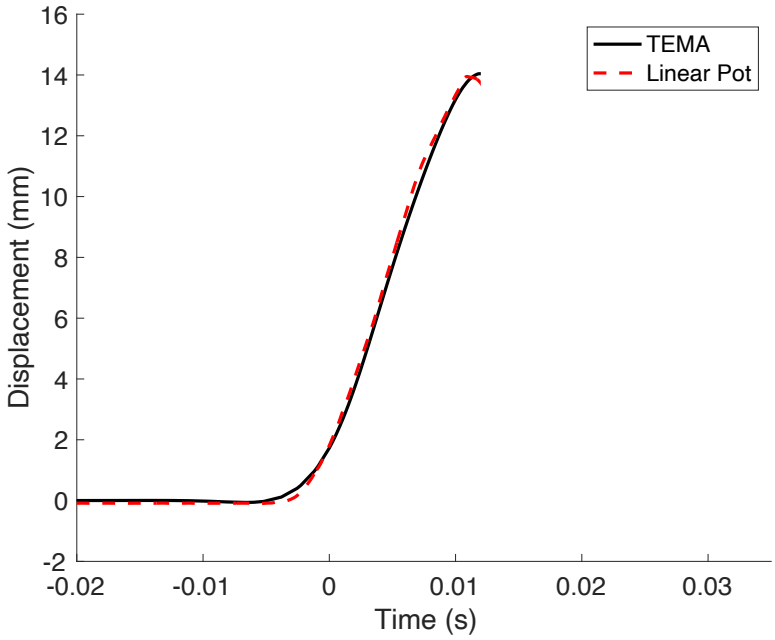

(y) Test 25

Figure 67 continued

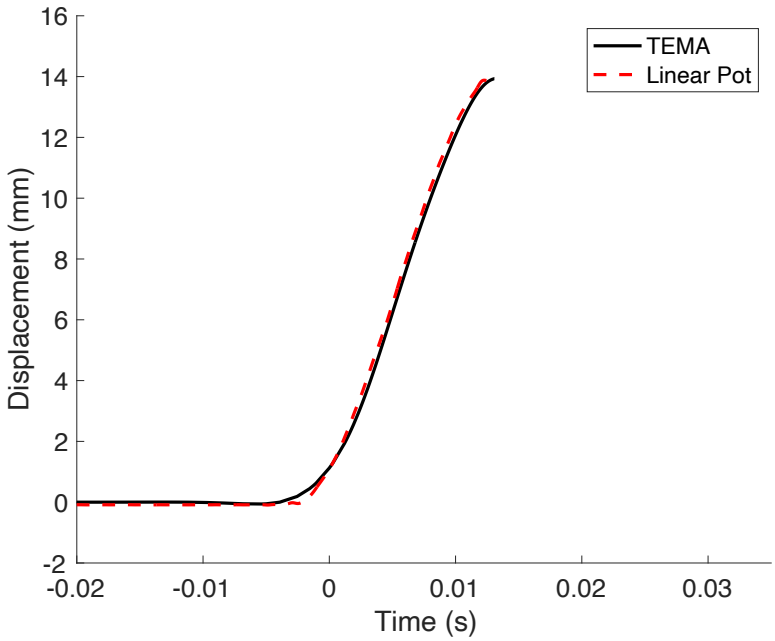

(z) Test 26

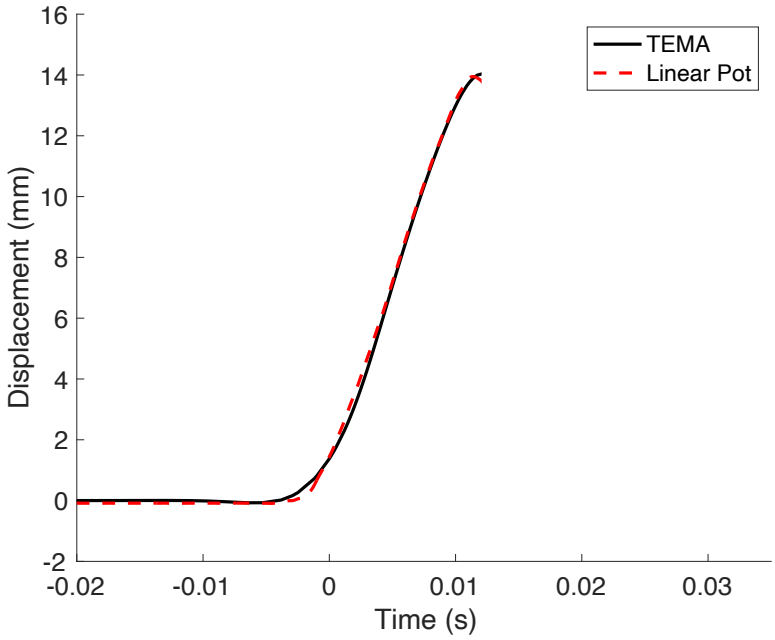

(aa) Test 27

Appendix B: Subject 1 Results

Table 20: Main test matrix results for subject 1

					Displacement (mm)		
Test #	Description	Postmortem time (hours)	Rotational Acceleration (rad/s^2)	Rotational Velocity (rad/s)	Cortex Surface	1mm deep	2mm deep
01	Baseline	50.75	784	8.89	--	3.82	3.83
02	Baseline	51.13	754	8.73	--	3.10	3.53
03	Baseline	51.37	797	8.99	--	2.80	3.18
04	Test 1	51.67	2000	18.7	--	5.77	6.35
05	Baseline	52.12	1011	9.15	--	2.18	2.18
06	Test 2	52.70	2378	21.5	--	5.32	5.7
07	Baseline	53.13	906	9.17	--	1.85	2.26
08	Test 3	54.28	1785	24.1	8.36	9.07	9.87
09	Baseline	54.95	812	8.30	2.17	2.53	2.64
10	Test 4	56.40	2285	27.3	10.4	11.8	9.10
11	Baseline	57.10	902	8.40	1.68	1.89	2.25

Table 21: Post-test matrix results for subject 1

					Displacement (mm)		
Test #	Description	Postmortem time (hours)	Rotational Acceleration (rad/s^2)	Rotational Velocity (rad/s)	Cortex Surface	1mm deep	2mm deep
2101_12	Post-test 1	58.18	2574	27.6	13.5	16.7	16.5
2101_13	Baseline	58.61	991	9.02	2.06	2.40	2.53
2101_14	Post-test 2	59.23	2138	27.7	6.96	7.55	7.56
2101_15	Baseline	60.11	759	8.94	1.73	1.82	2.00
2101_16	Post-test 3	60.61	2795	23.8	Not trackable		
2101_17	Baseline	61.00	926	8.91	1.72	1.94	1.81
2101_18	Post-test 4	61.35	2843	23.7	7.43	8.94	8.82
2101_19	Baseline	61.58	795	8.84	2.04	2.34	2.11
2101_20	Post-test 5	62.41	2327	29.8	5.04	6.37	6.26
2101_21	Baseline	63.68	884	8.66	1.73	2.03	2.15
2101_22	Post-test 6	64.20	2285	29.8	6.91	7.47	7.72

Table 22: Comparison of baseline results for subject 1

					Displacement (mm)		
Test #	Description	Postmortem time (hours)	Rotational Acceleration (rad/s^2)	Rotational Velocity (rad/s)	Cortex Surface	1mm deep	2mm deep
2101_01	Baseline	50.75	784	8.89	--	3.82	3.83
2101_02	Baseline	51.13	754	8.73	--	3.10	3.53
2101_03	Baseline	51.37	797	8.99	--	2.80	3.18
2101_05	Baseline	52.12	1011	9.15	--	2.18	2.18
2101_07	Baseline	53.13	906	9.17	--	1.85	2.26
2101_09	Baseline	54.95	812	8.3	2.17	2.53	2.64
2101_11	Baseline	57.10	902	8.4	1.68	1.89	2.25
2101_13	Baseline	58.61	991	9.02	2.06	2.40	2.53
2101_15	Baseline	60.11	759	8.94	1.73	1.82	2.00
2101_17	Baseline	61.00	926	8.91	1.72	1.94	1.81
2101_19	Baseline	61.58	795	8.84	2.04	2.34	2.11
2101_21	Baseline	63.68	884	8.66	1.73	2.03	2.15
		Average	**860**	**8.82**	**1.88**	**2.39**	**2.54**
		Std. dev.	**88.7**	**0.26**	**0.21**	**0.60**	**0.64**
		% CV	**10.3**	**2.99**	**10.94**	**25.16**	**25.24**

The %CV of rotational velocity was <5%, indicating very good repeatability of the fixture kinematics for the baseline tests. Time history plots of rotational acceleration and rotational velocity for all baseline tests for subject 1 are shown in Figure 68.

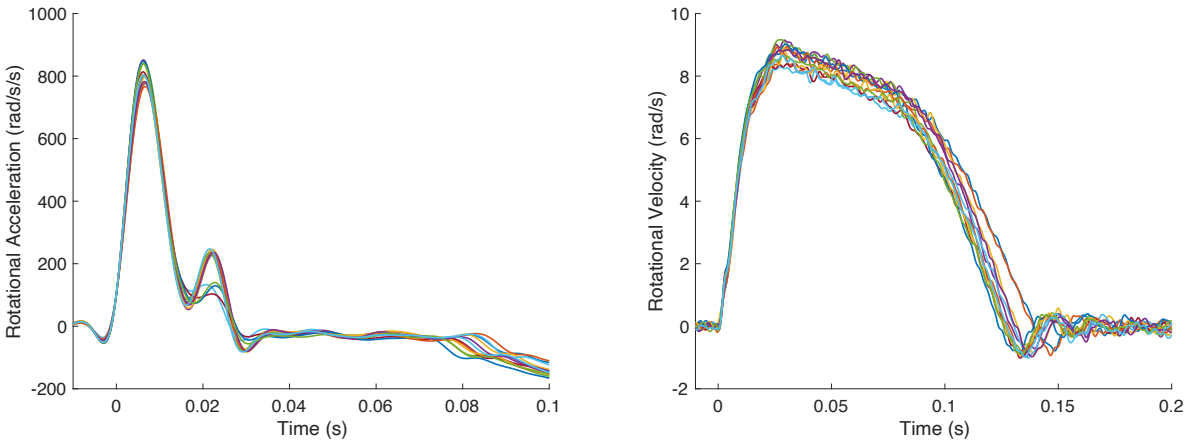

Figure 68: Comparison of baseline kinematics for subject 1

The spread of displacement values for the baselines tests at each tracked location is shown graphically in a boxplot in Figure. On average, peak displacements tracked at the cortex surface were the smallest, while peak displacement tracked 2mm deep in the cortex were the largest.

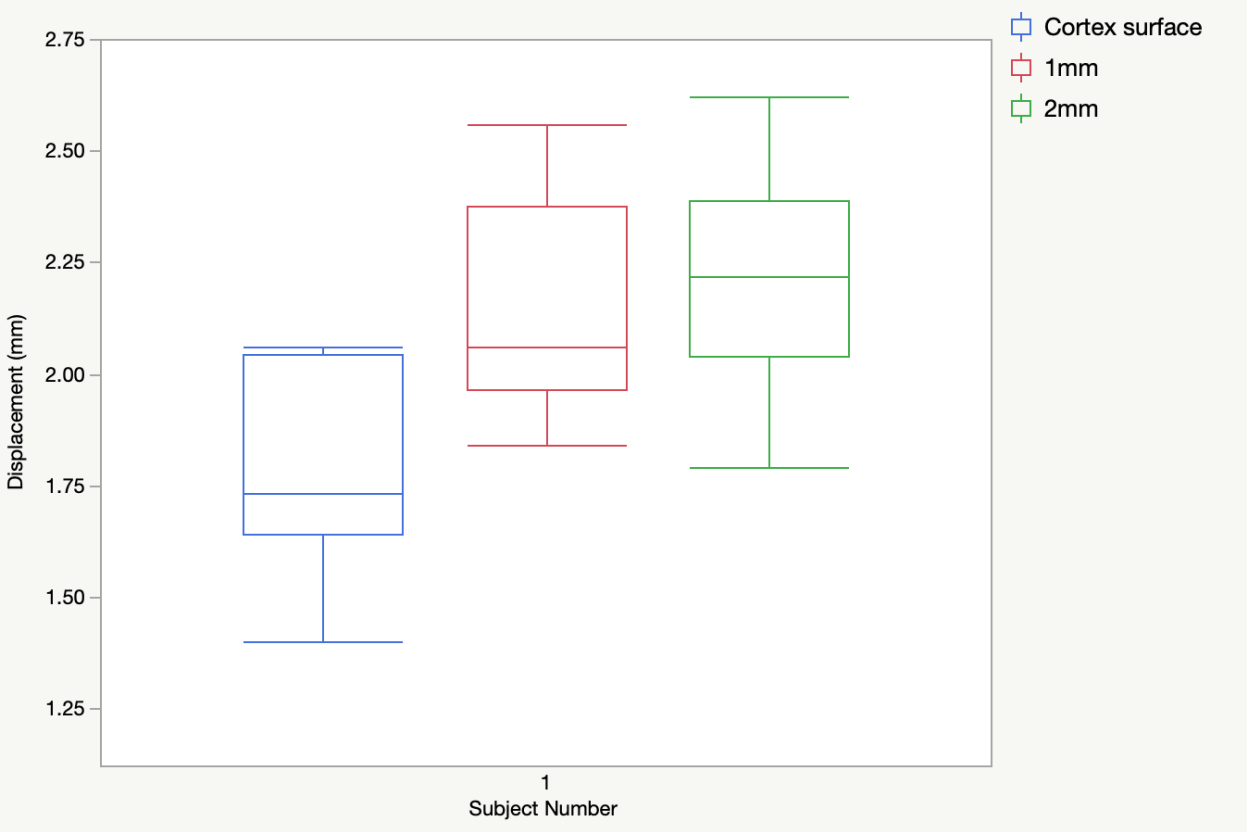

Figure 69: Boxplot of subject 1 baseline peak displacements at the three tracked locations

Table 23: Linear regression results for subject 1 displacements versus postmortem time, rotational velocity, and rotational acceleration

	Postmortem time	Rotational Velocity	Rotational Acceleration
	R^2		
Cortex surface	0.09	0.62*	0.11
1 mm deep	0.02	0.10	0.00
2 mm deep	0.14	0.12	0.14

*Indicates statistical significance ($p<0.05$)

The linear regression results indicate that peak displacement is correlated with both rotational velocity at the cortex surface. Rotational acceleration and postmortem time did not have a significant effect on the outcome of peak displacement at any tracked point location.

Additionally, the peak brain displacement for every test was utilized in a multiple linear regression to determine the dependence of brain deformation on angular head kinematics and postmortem time. The model fits had an R^2 ranging from 0.668-0.744. Coefficient values are presented in Table 24.

Table 24: Multiple regression summary statistics for subject 1

	Analysis of Variance		**Summary of Fit**		**Parameter Estimates**			
					intercept	**Postmortem time (hours)**	**Rotational Velocity (rad/s)**	**Rotational Acceleration (rad/s^2)**
	F-ratio	**df**	**Adjusted R^2**	**RMSE**	**estimate (p-value)**			
Cortex surface	<0.001*	13	0.736	1.986	20.74 (0.082)	-0.371 (0.0679)	0.220 (0.280)	0.0017 (0.519
1mm	<0.001*	20	0.744	1.791	6.163 (0.260)	-0.125 (0.206)	0.380 (0.0138*)	-0.0001 (0.933)
2mm	<0.001*	20	0.668	2.188	7.749 (0.247)	-0.150 (0.212)	0.431 (0.0205*)	-0.0007 (0.745)
*Indicates statistical significance ($p<0.05$)								

The multiple regression analysis was statistically significant for all three locations tracked as evidenced by the F-ratio value for each test. The regressions showed a dependence of peak brain displacement on angular velocity.

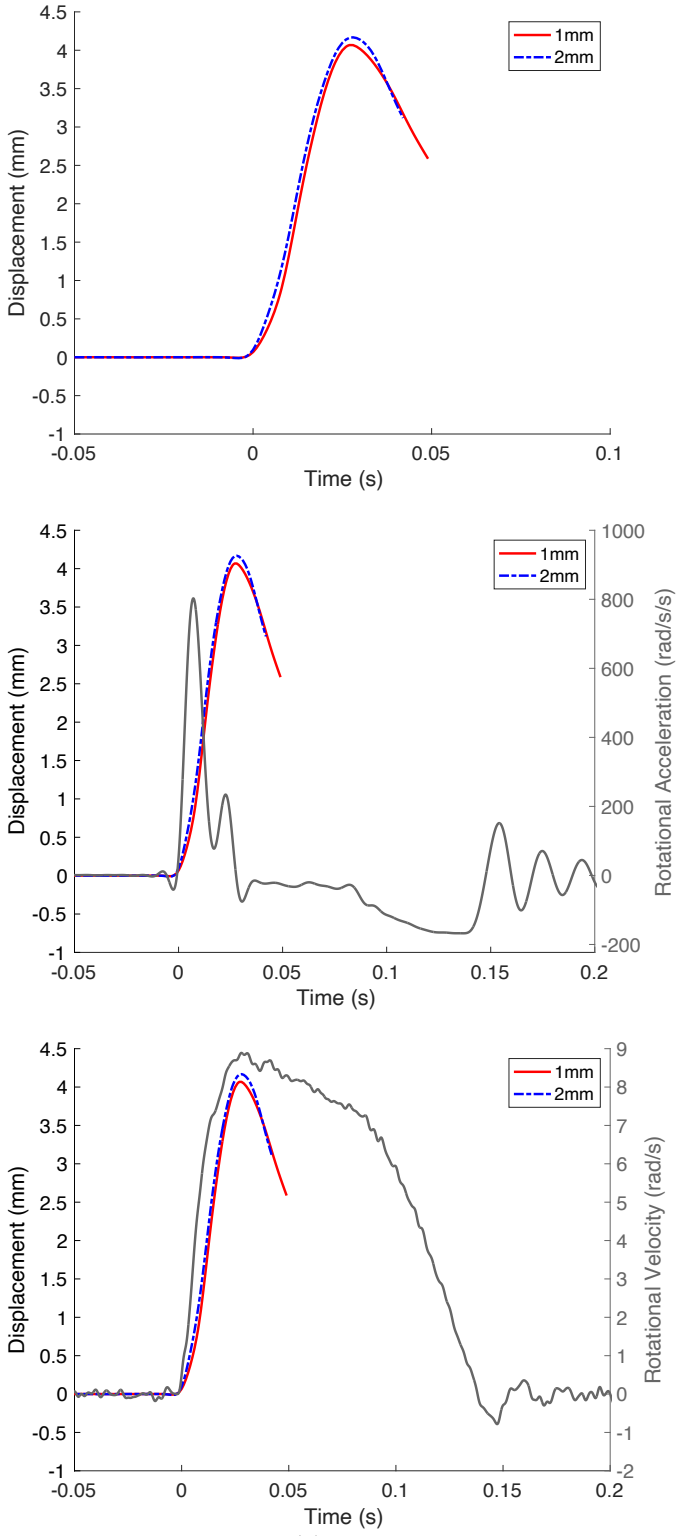

(a) Test 1

Figure 70: Time history of displacement (top), displacement compared to rotational acceleration (middle) and displacement compared to rotational velocity (bottom) for subject 1

Figure 70 continued

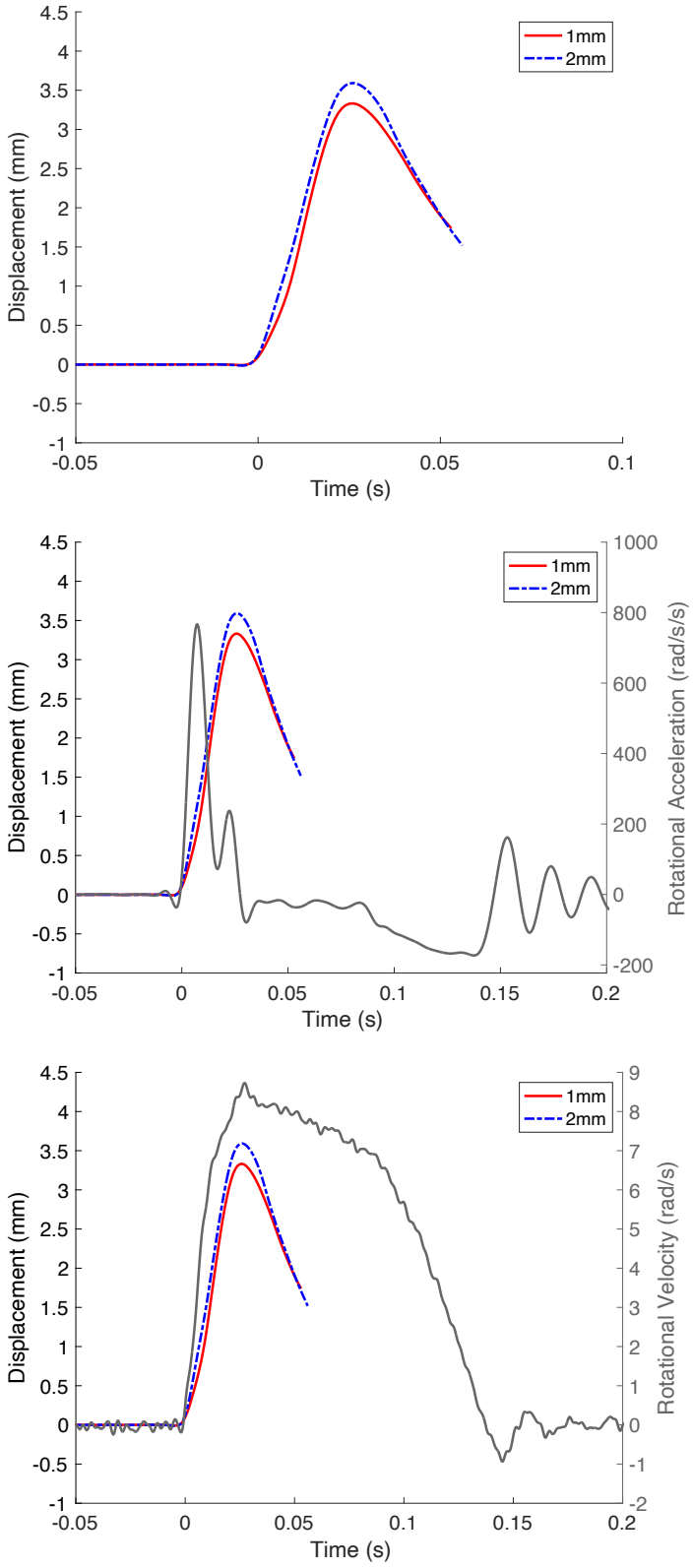

(b) Test 2

Figure 70 continued

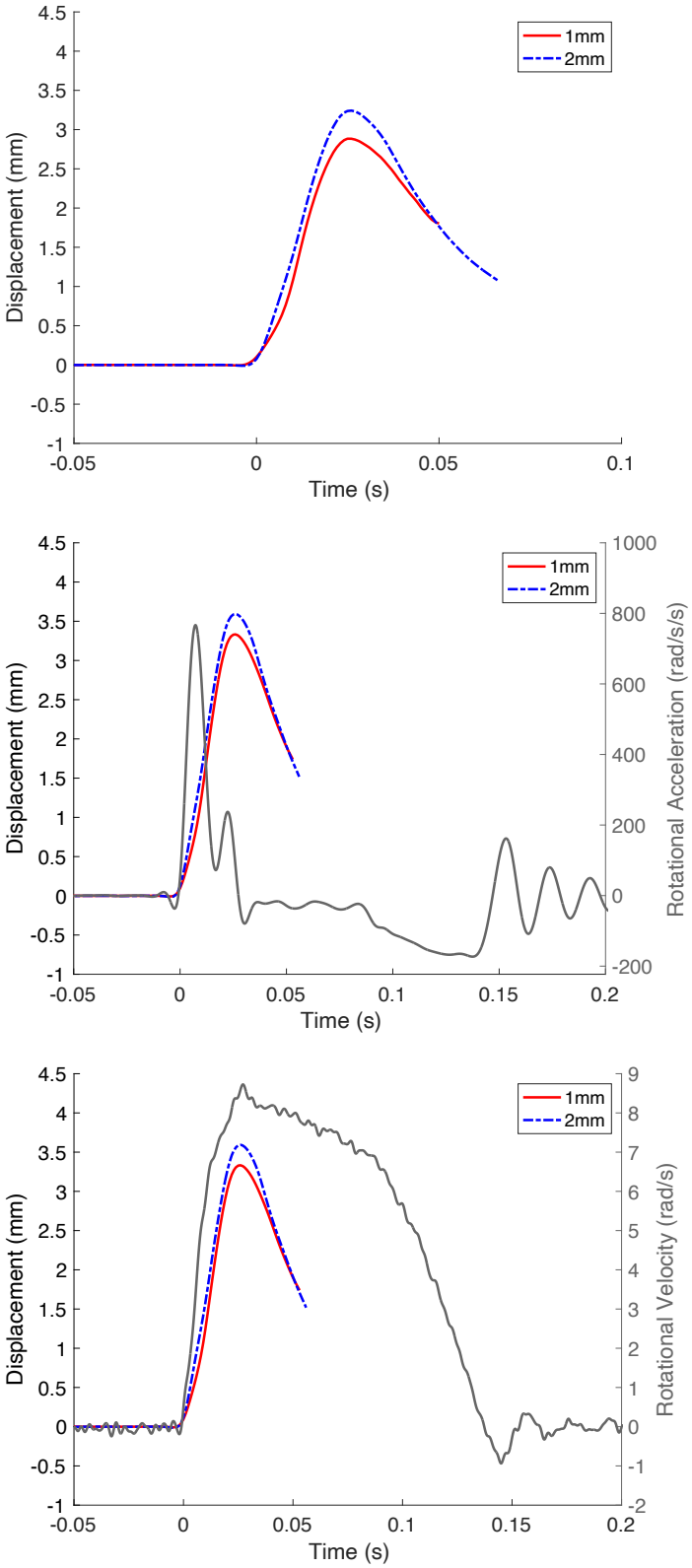

(c) Test 3

Figure 70 continued

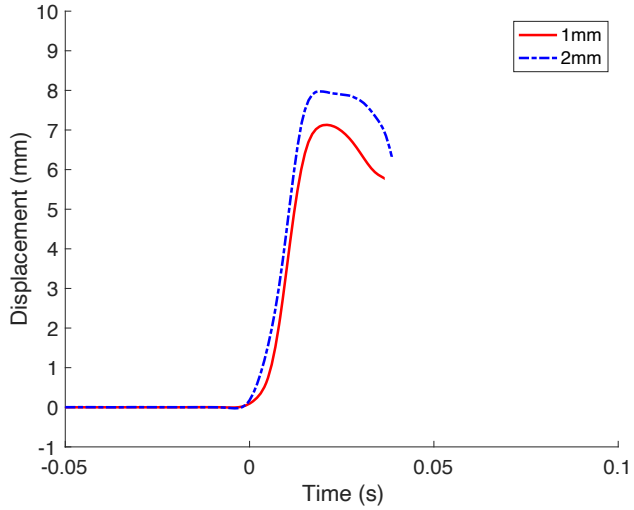

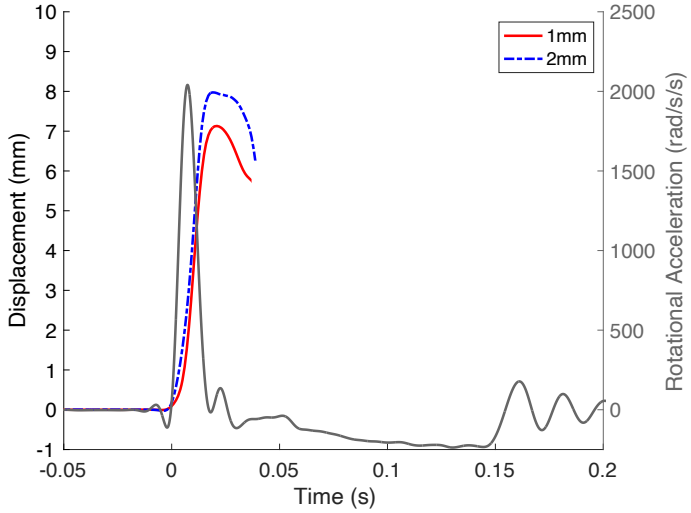

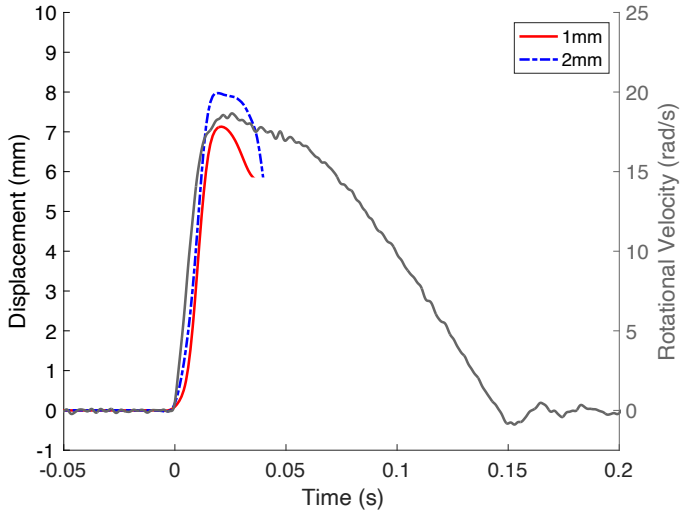

(d) Test 4

Figure 70 continued

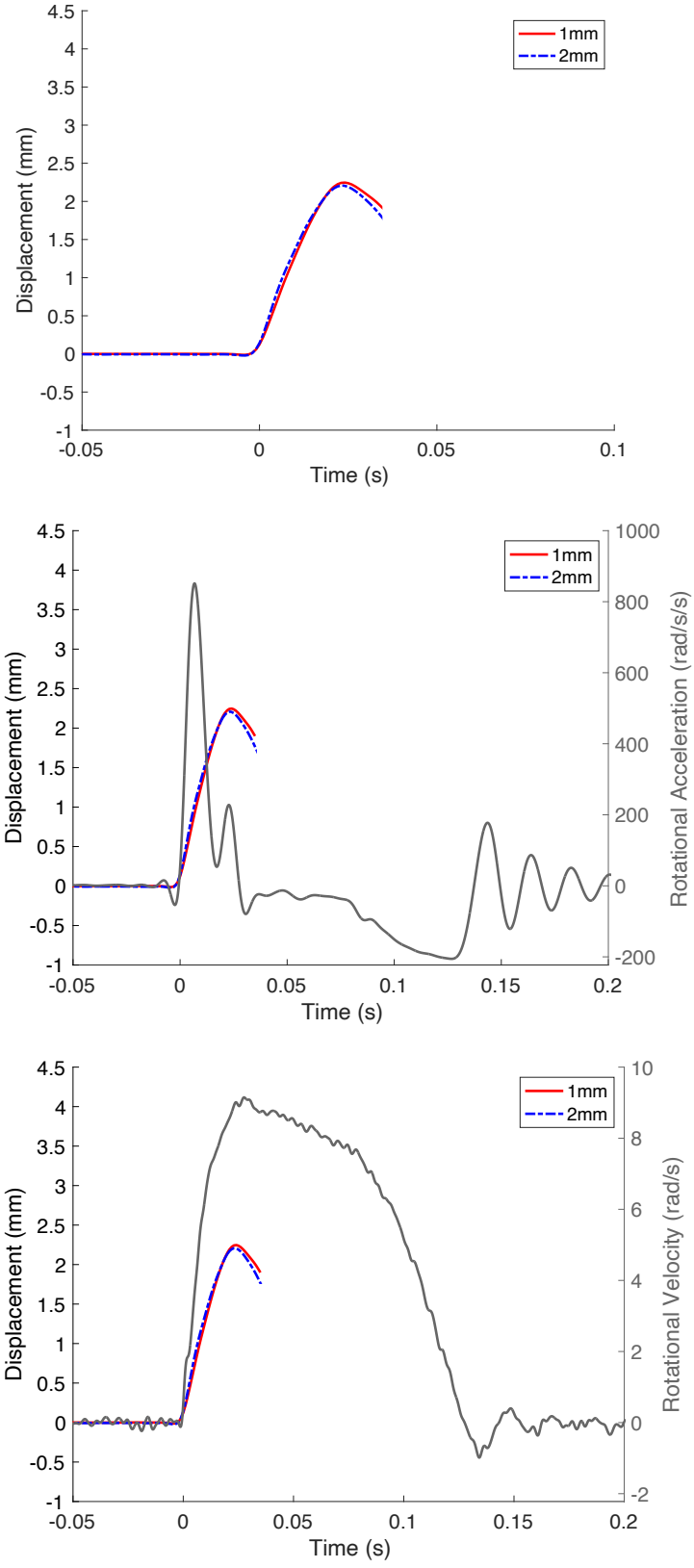

(e) Test 5

Figure 70 continued

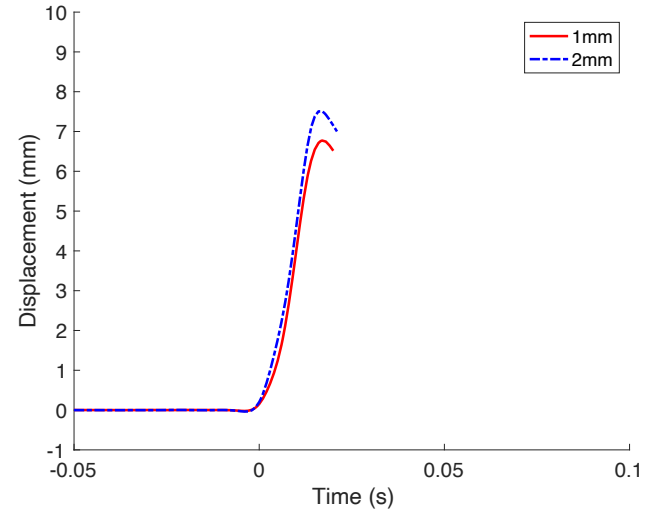

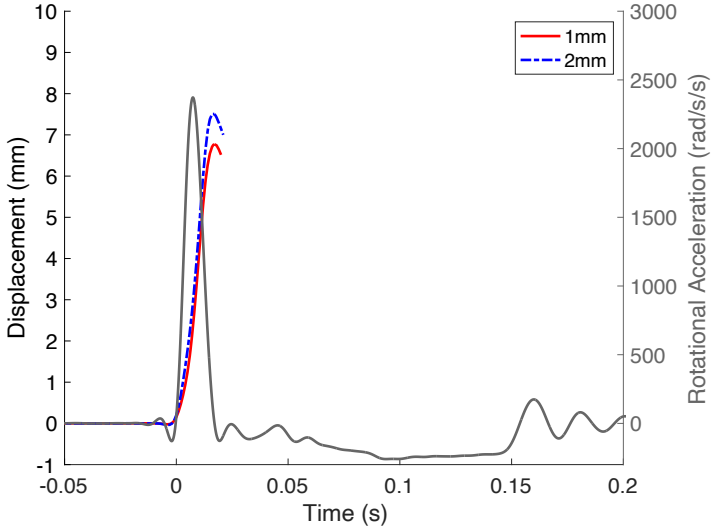

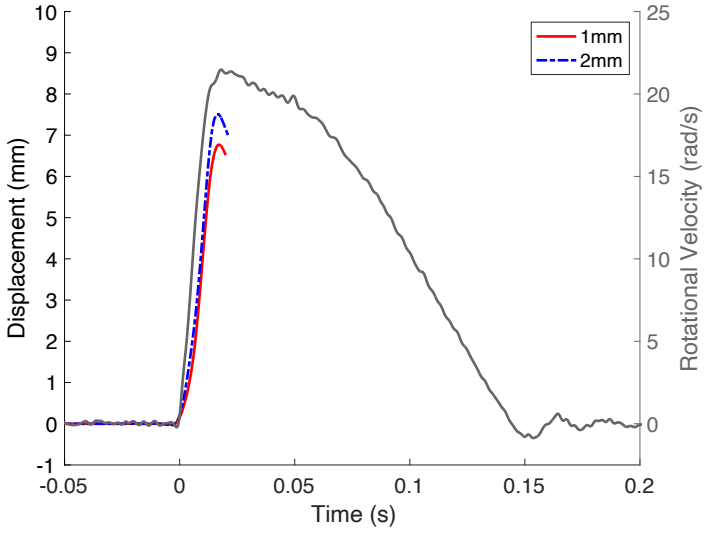

(f) Test 6

Figure 70 continued

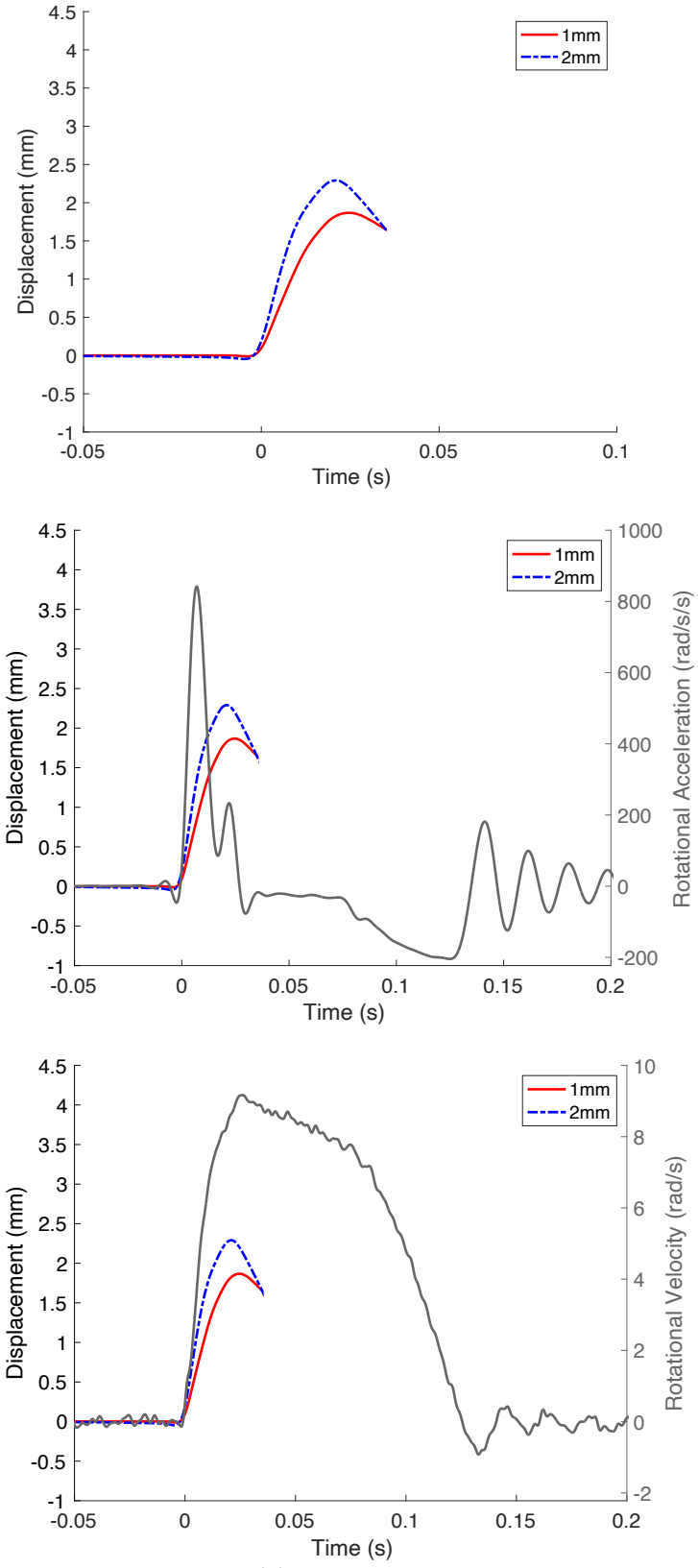

(g) Test 7

Figure 70 continued

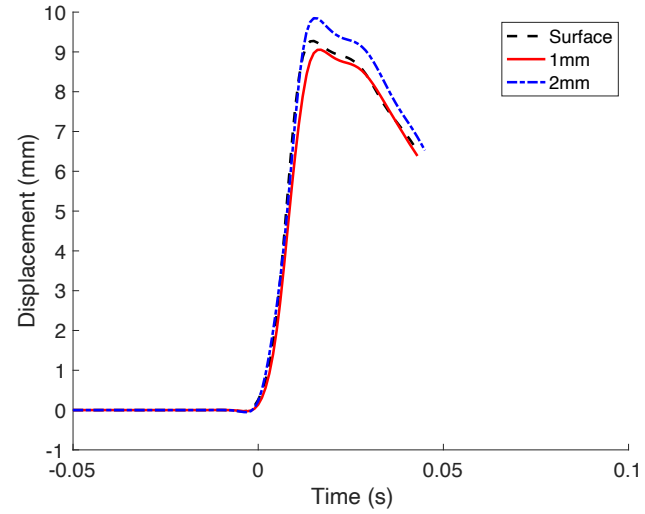

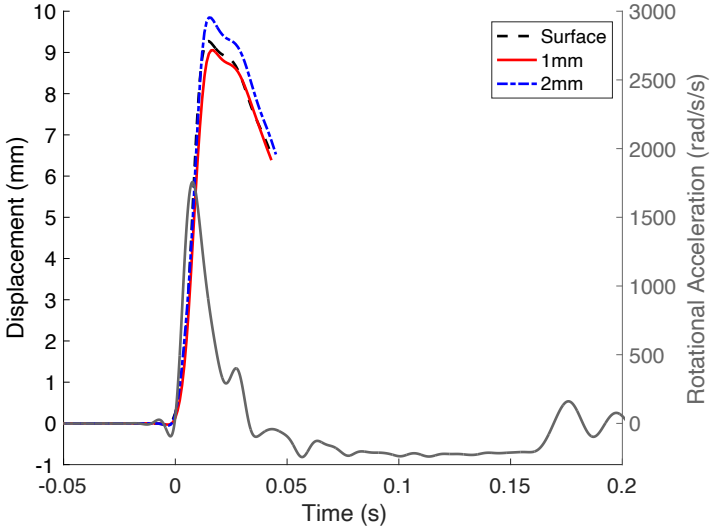

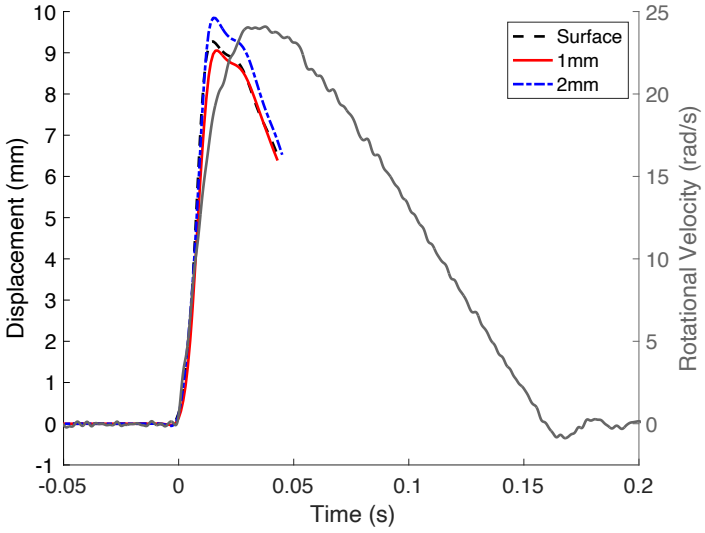

(h) Test 8

Figure 70 continued

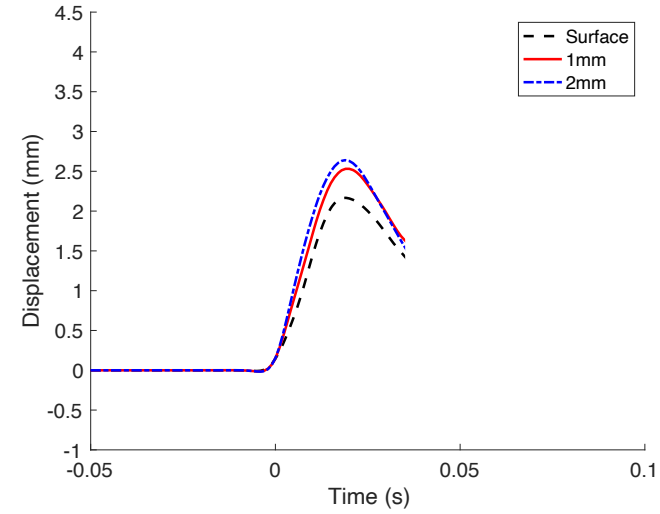

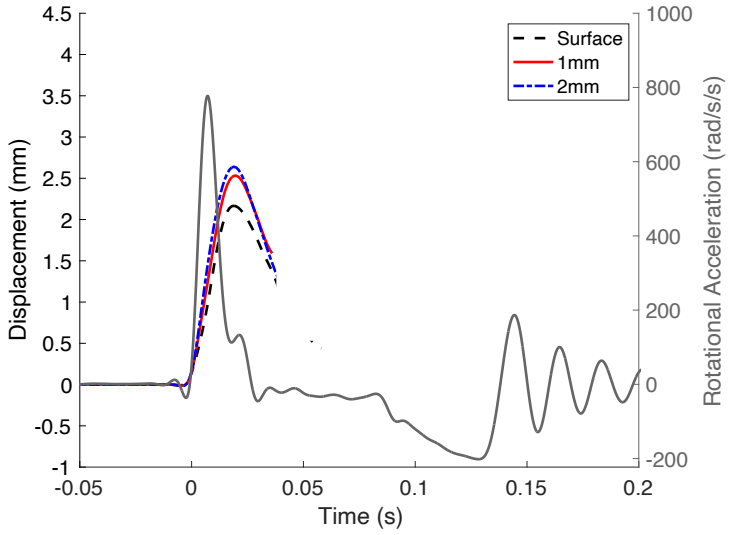

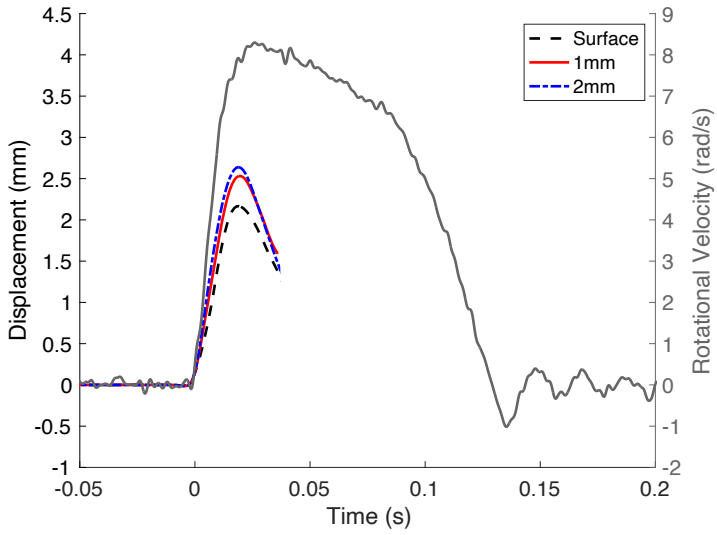

(i) Test 9

Figure 70 continued

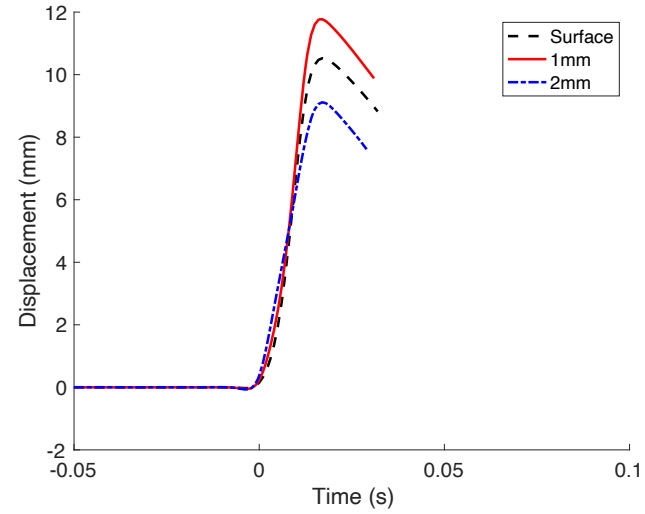

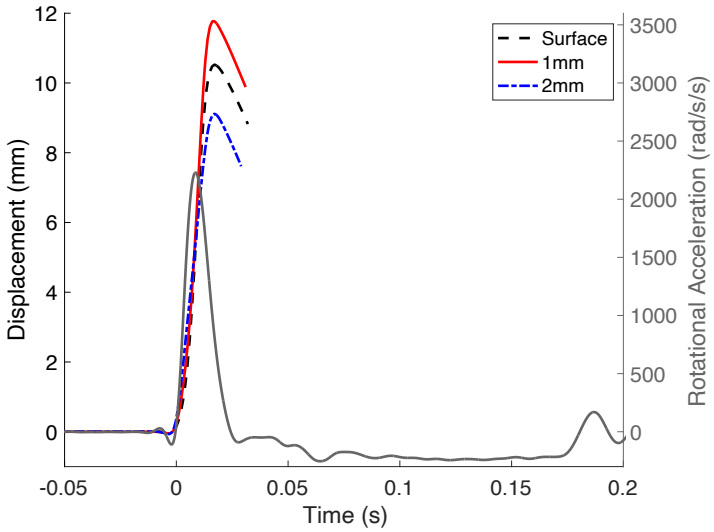

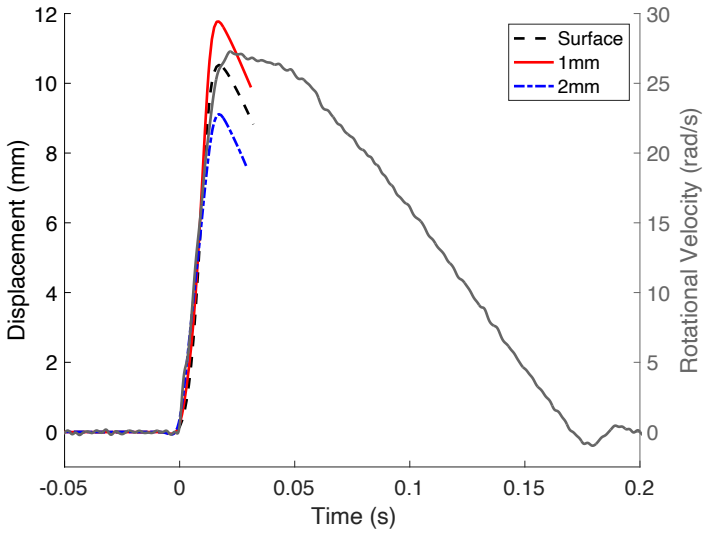

(j) Test 10

Figure 70 continued

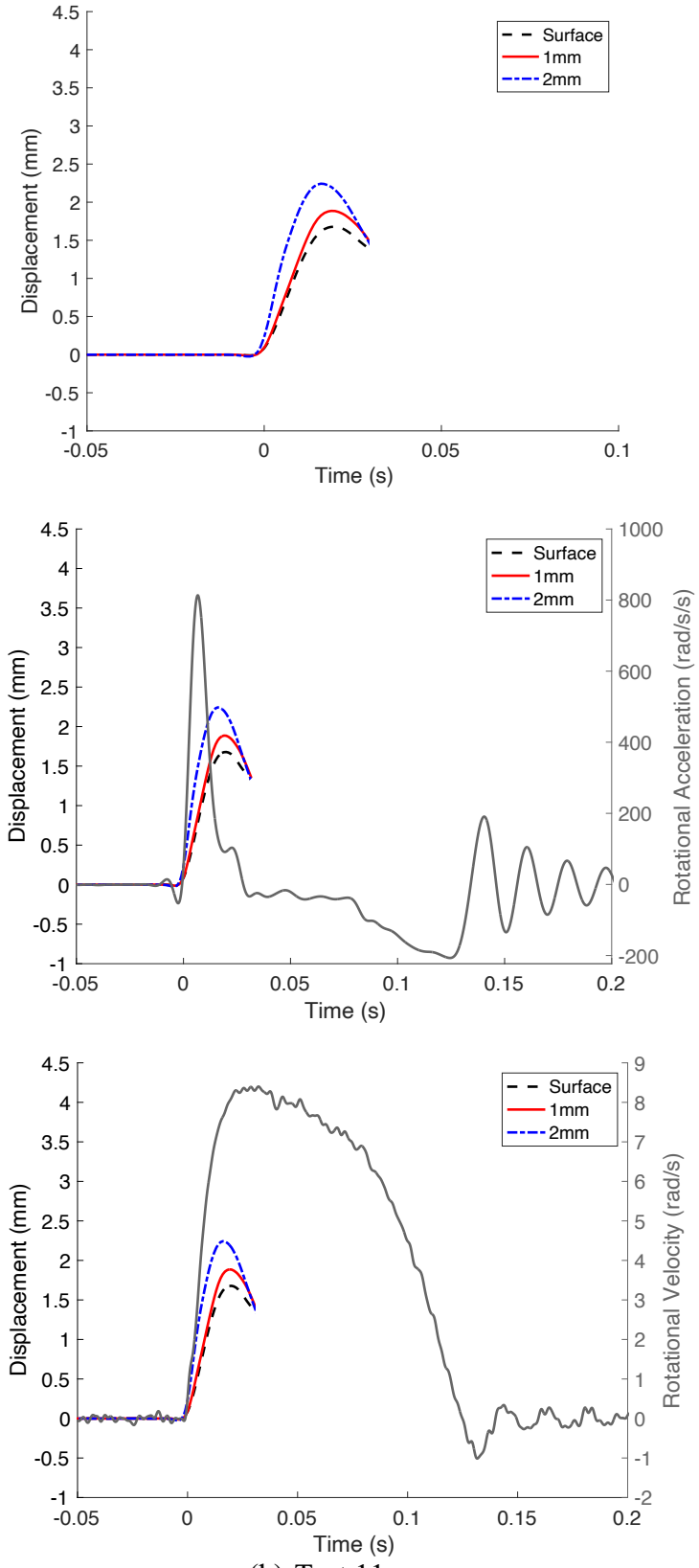

(k) Test 11

Figure 70 continued

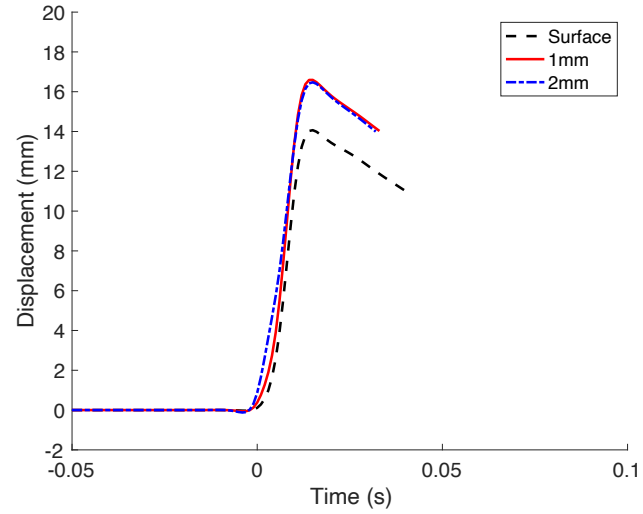

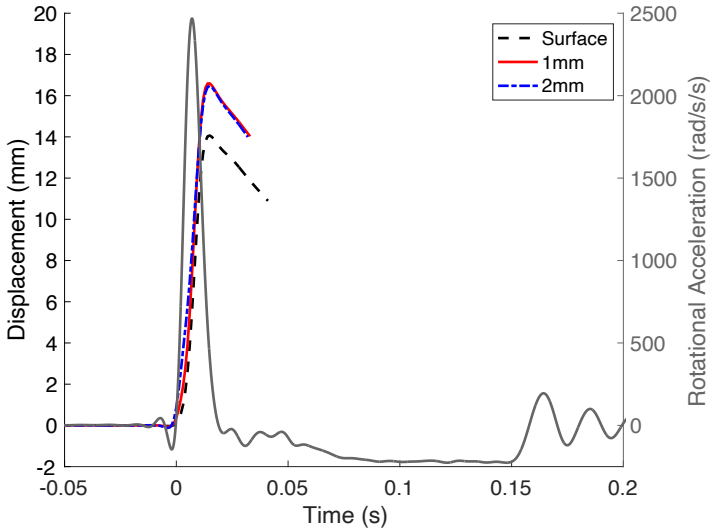

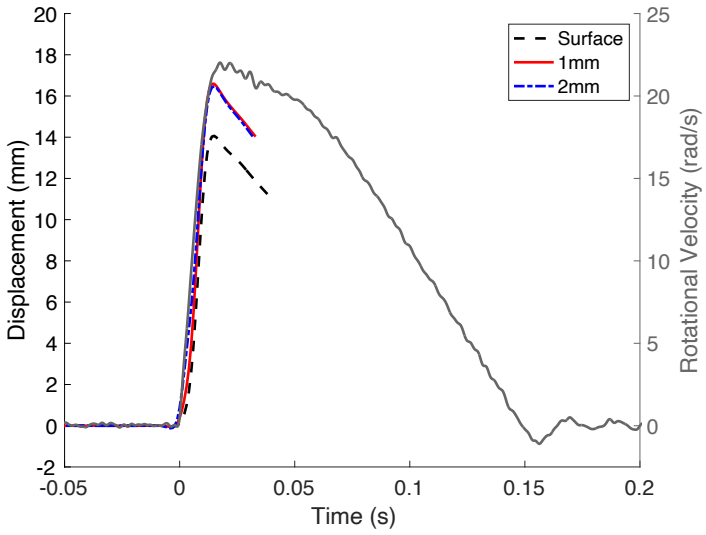

(l) Test 12

Figure 70 continued

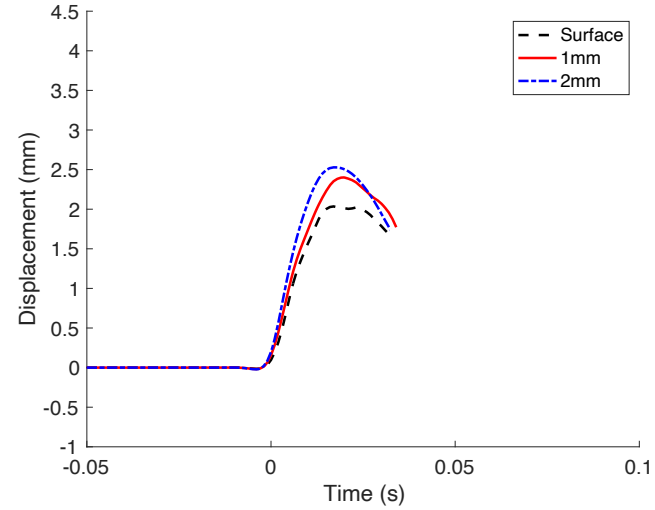

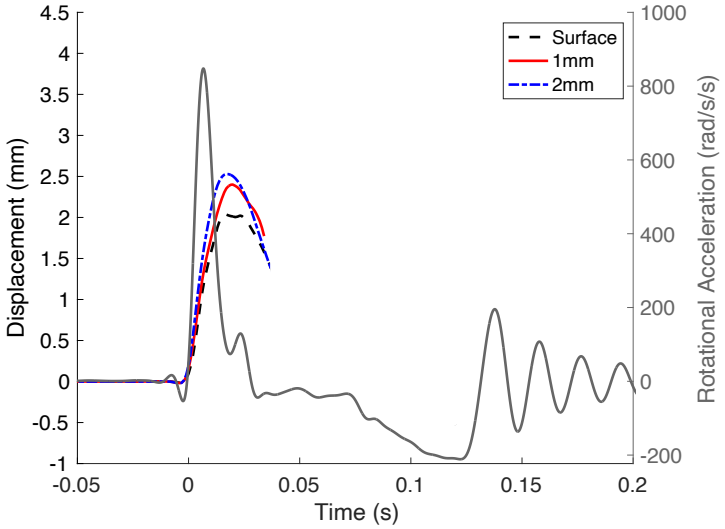

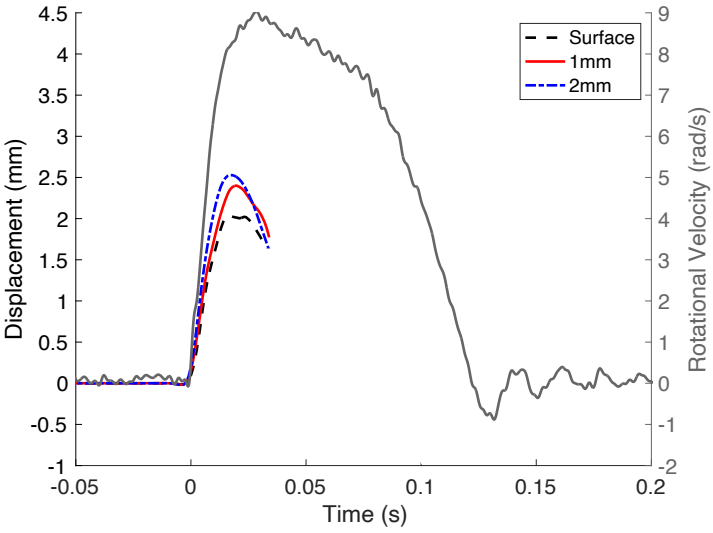

(m)Test 13

Figure 70 continued

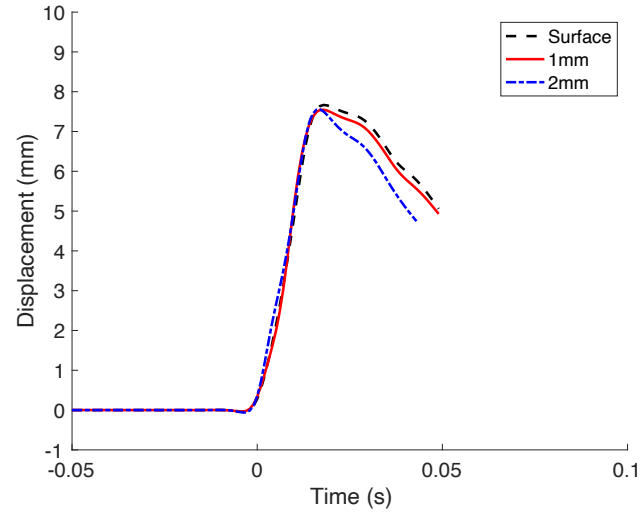

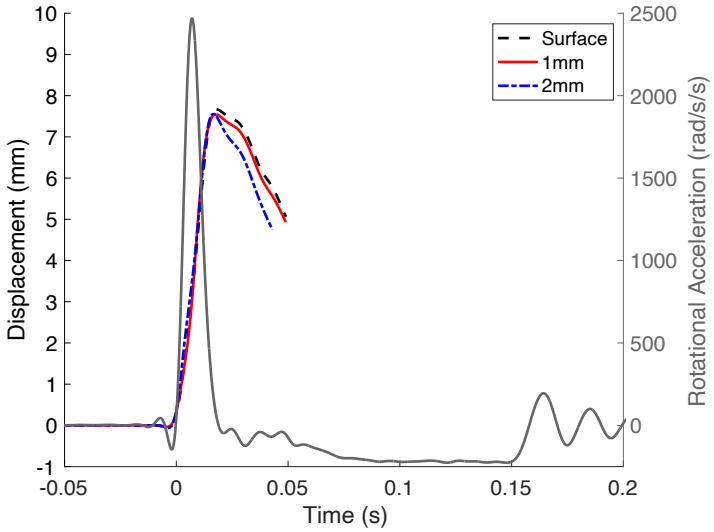

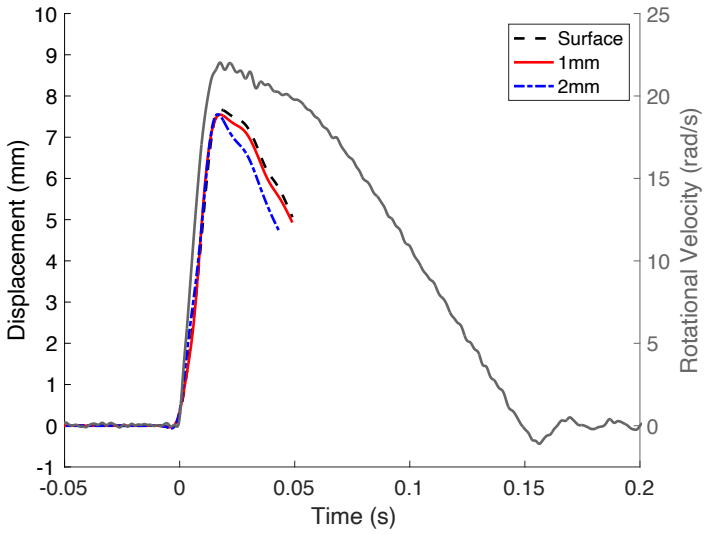

(n) Test 14

Figure 70 continued

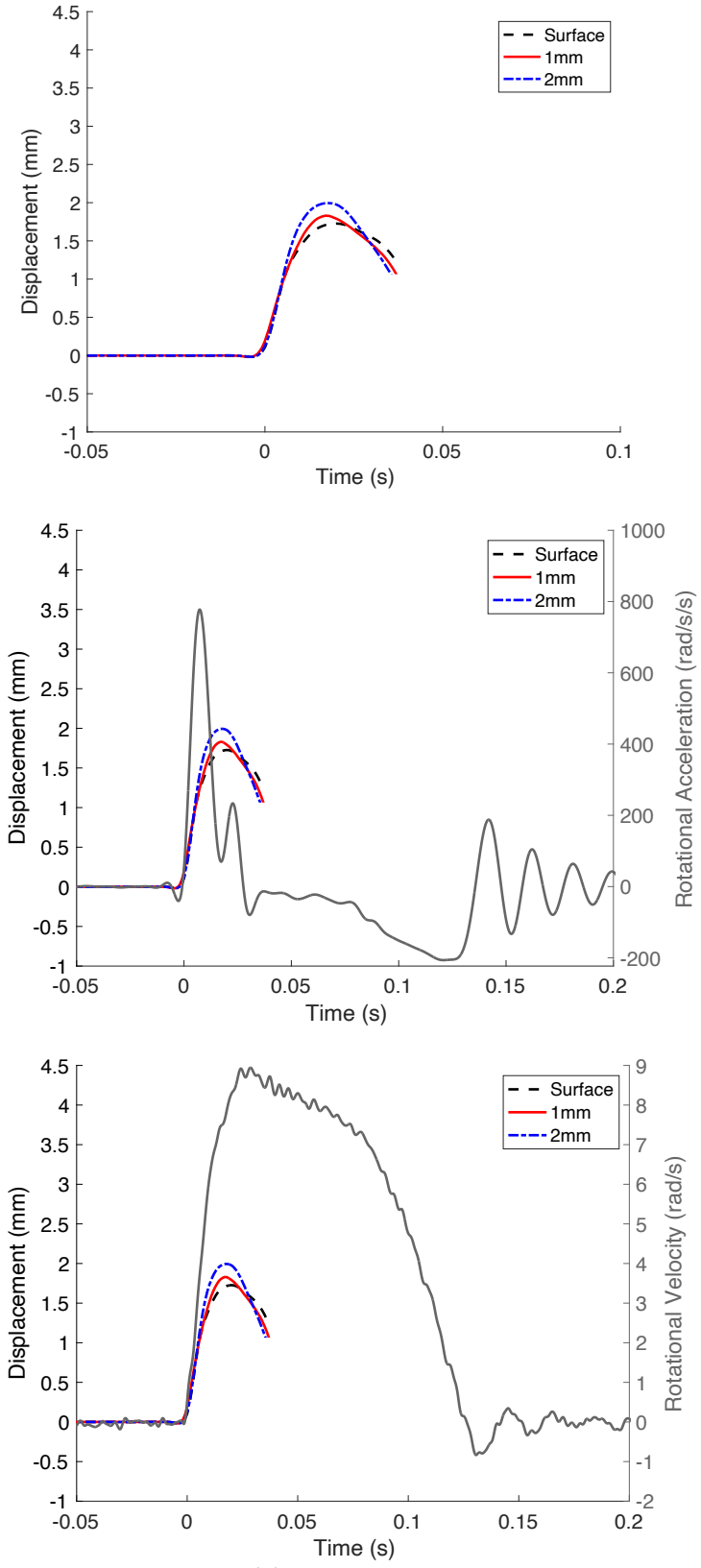

(o) Test 15

Figure 70 continued

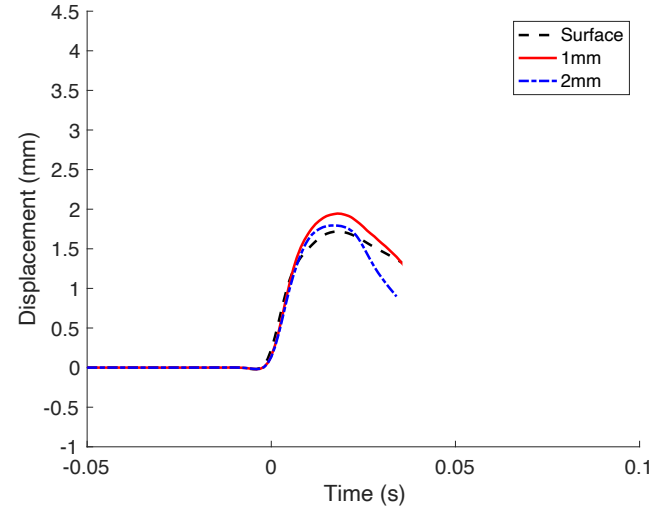

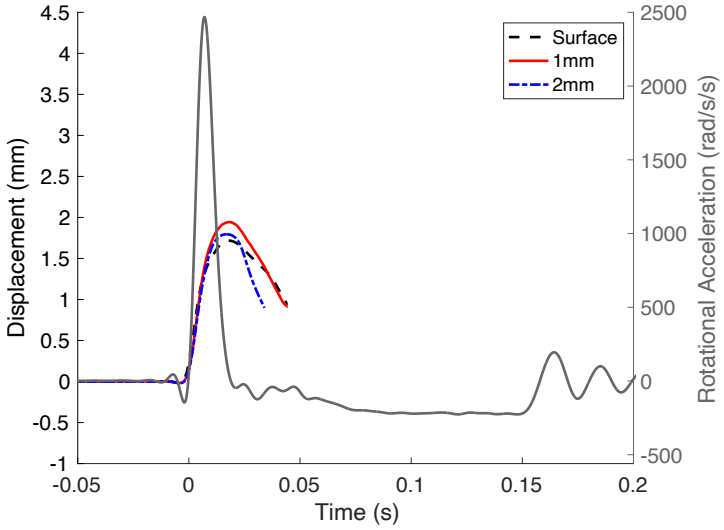

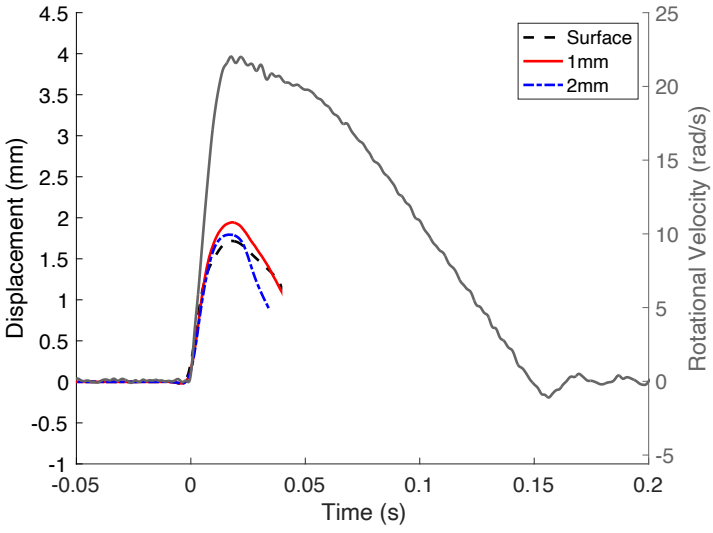

(p) Test 17

Figure 70 continued

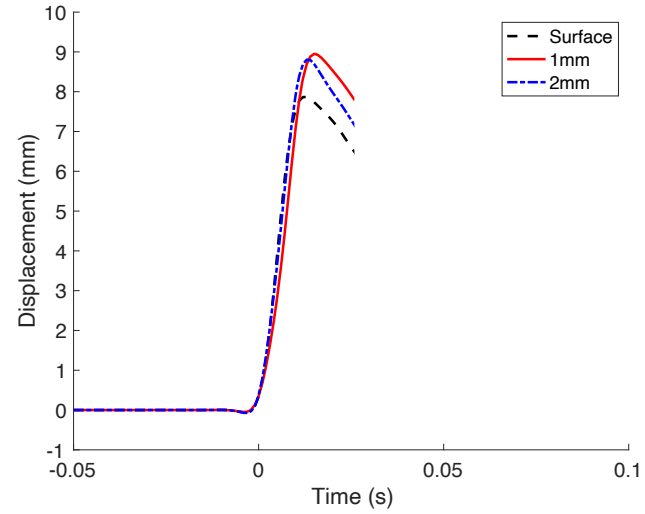

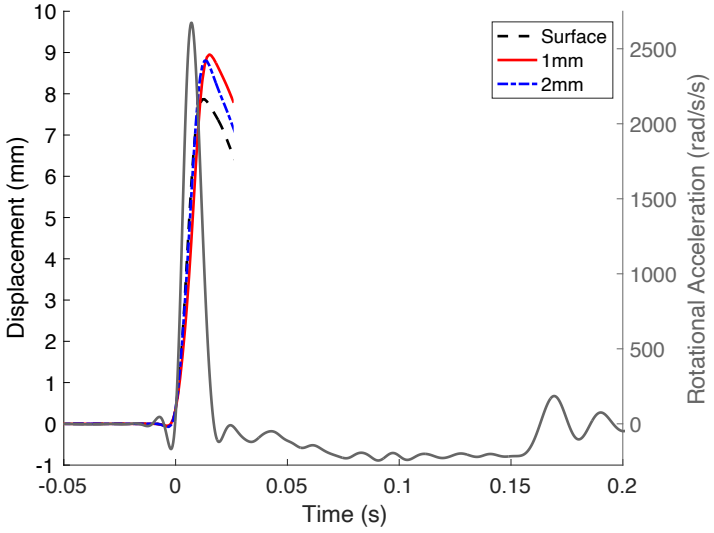

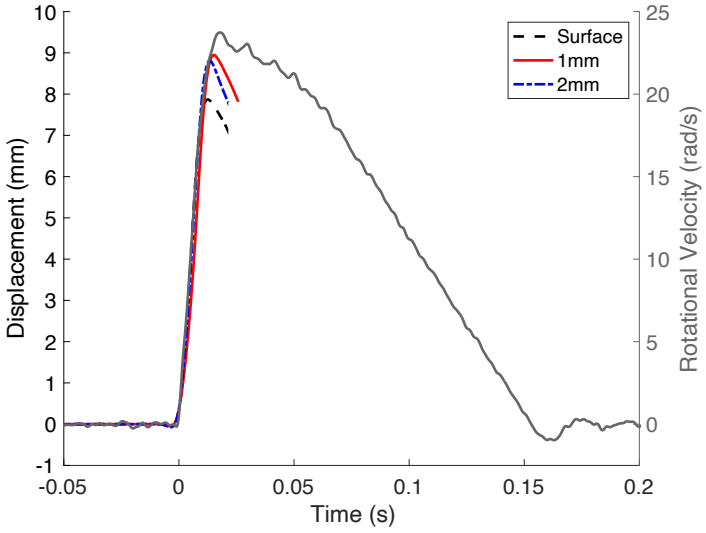

(q) Test 18

Figure 70 continued

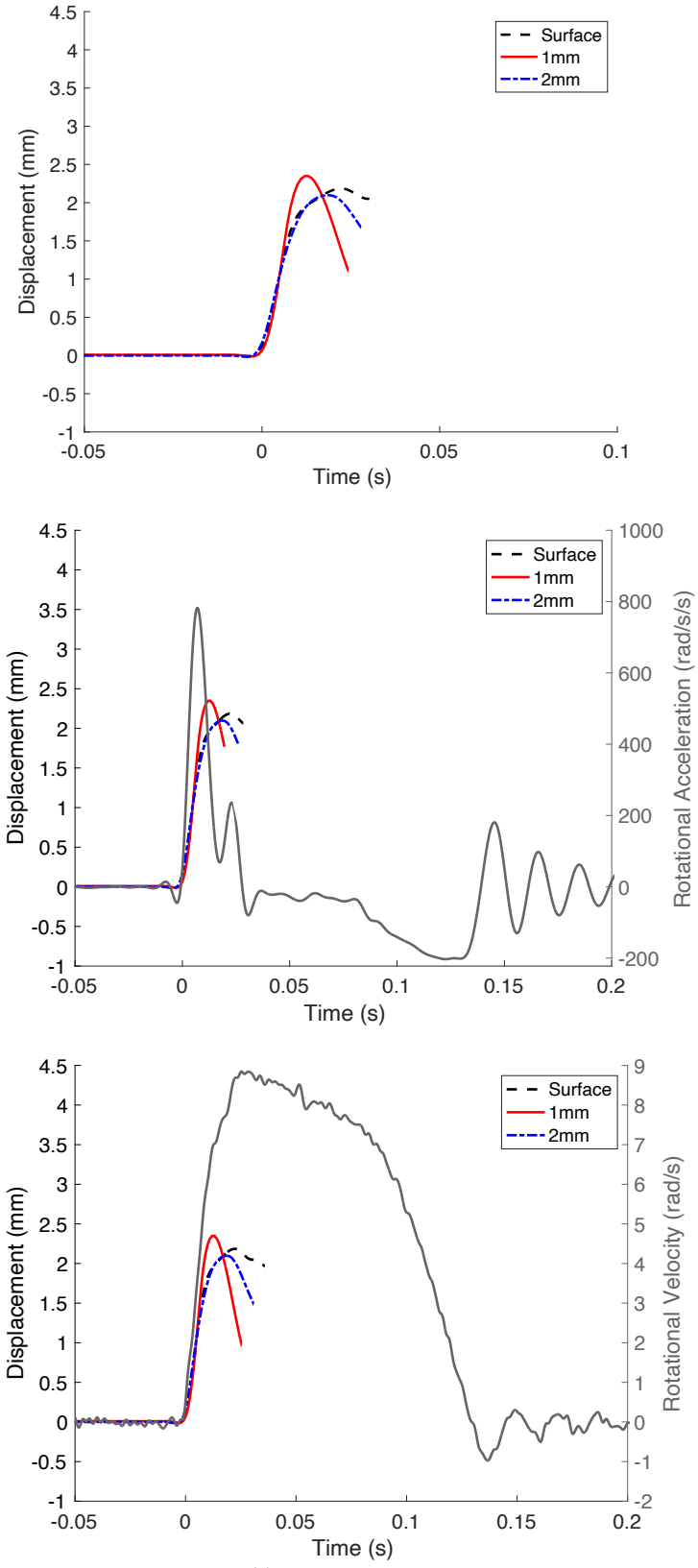

(r) Test 19

Figure 70 continued

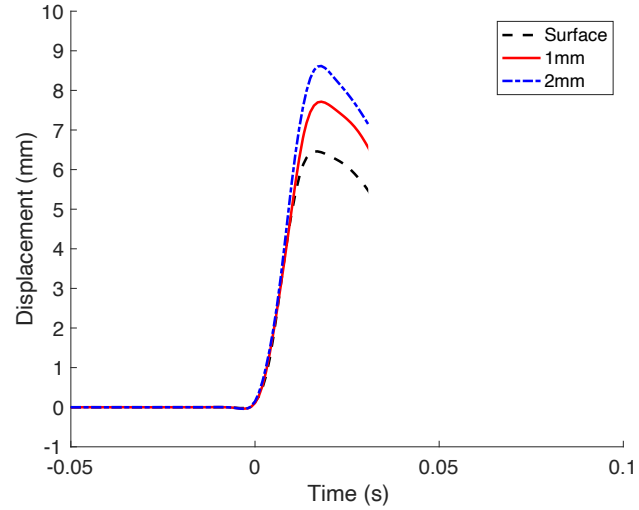

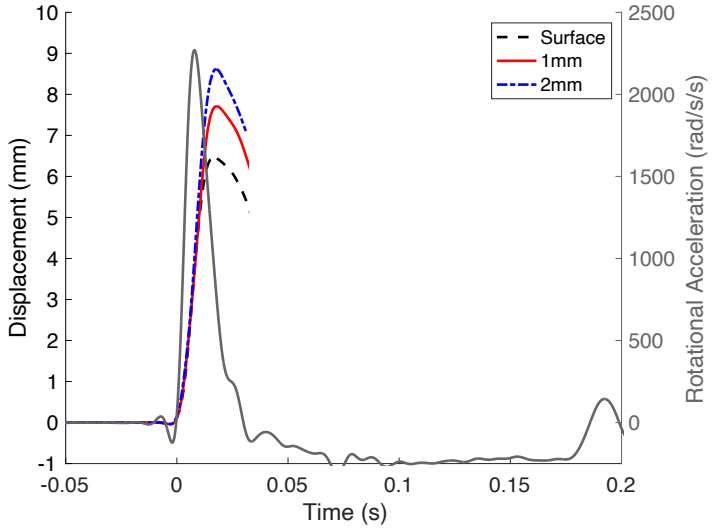

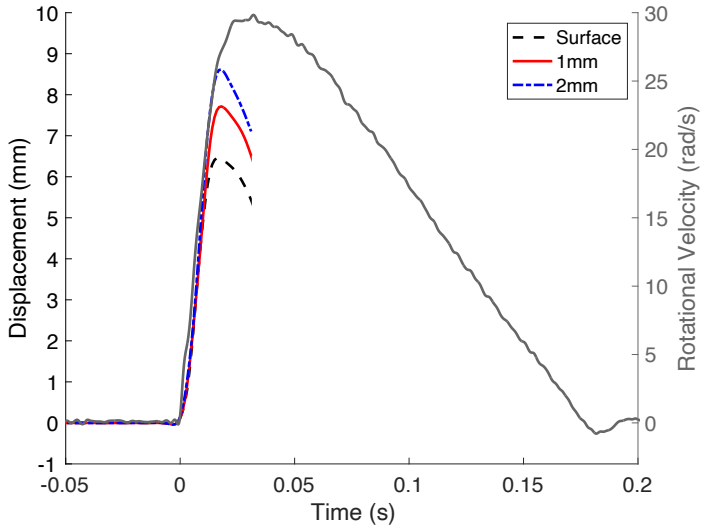

(s) Test 20

Figure 70 continued

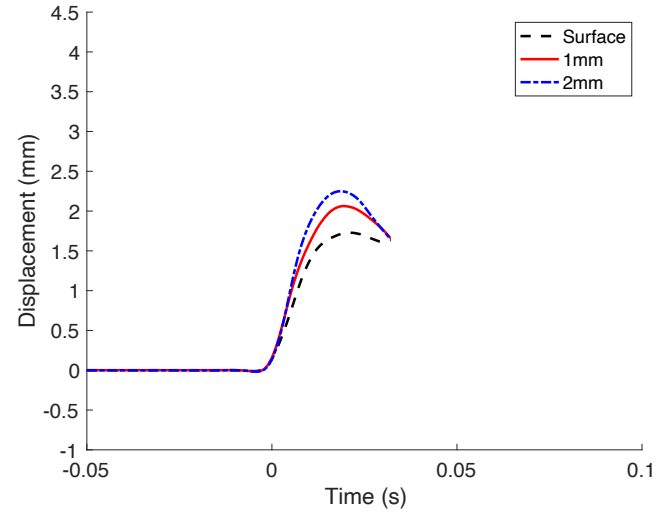

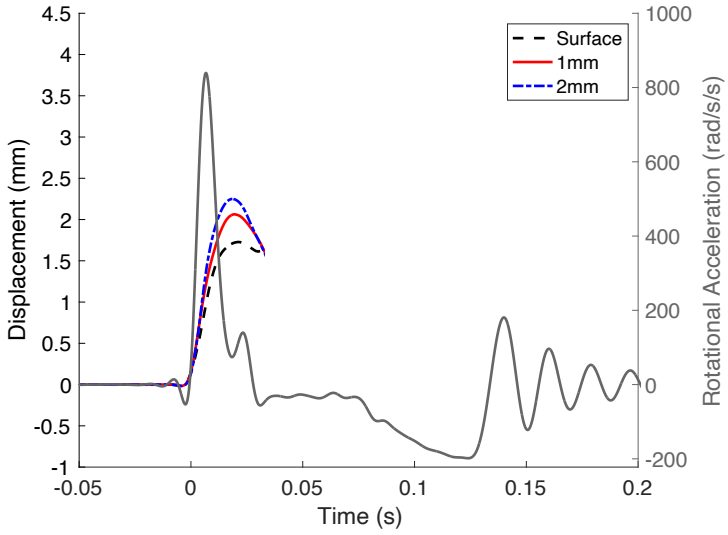

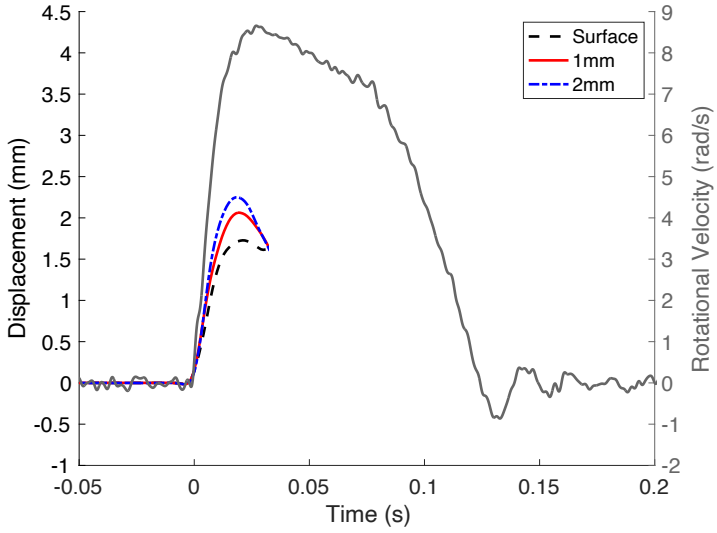

(t) Test 21

Figure 70 continued

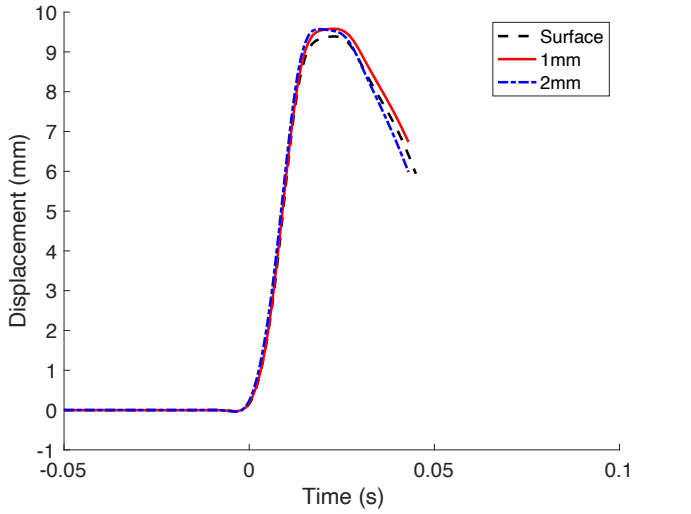

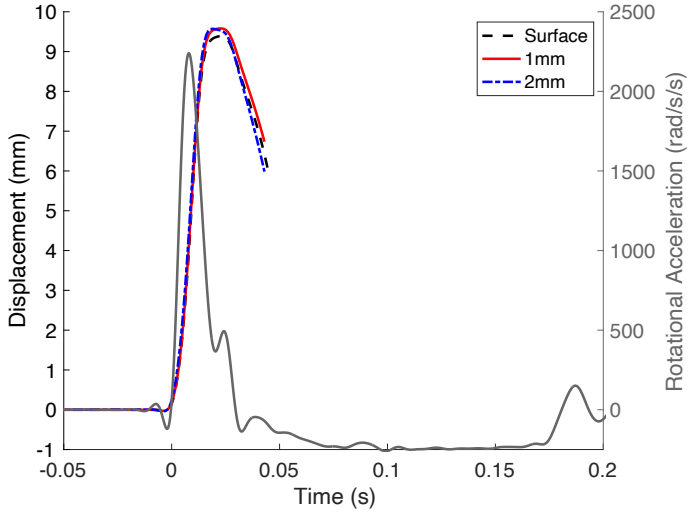

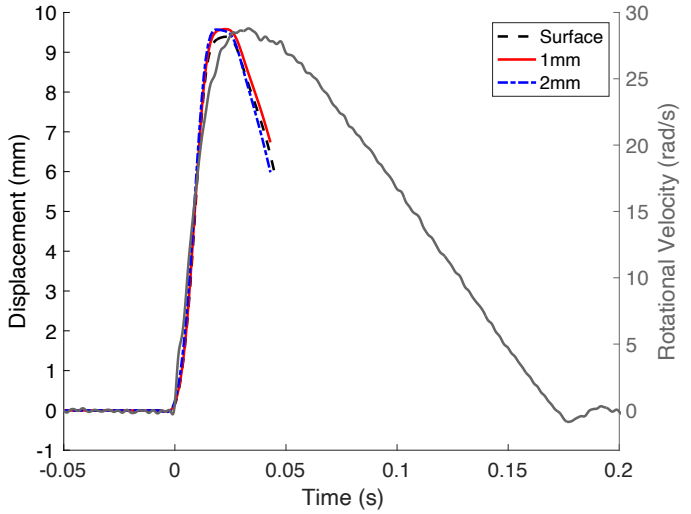

(u) Test 22

Appendix C: Subject 2 Results

Table 25: Main matrix results for subject 2

					Displacement (mm)		
Test #	Description	Postmortem time (hours)	Rotational Acceleration (rad/s^2)	Rotational Velocity (rad/s)	Cortex Surface	1mm deep	2mm deep
01	Baseline	39.30	783	8.61	4.84	4.64	5.21
02	Baseline	39.45	831	8.94	4.64	4.88	5.08
03	Baseline	39.60	787	8.62	4.89	4.85	4.82
04	Test 1	39.85	2074	19.3	9.54	10.1	9.60
05	Baseline	40.03	757	8.89	4.89	6.01	5.55
06	Test 2	40.25	2420	19.8	10.5	10.4	11.3
07	Baseline	40.58	1007	9.27	5.67	5.61	6.33
08	Test 3	41.07	1791	25.6	14.6	14.2	14.5
09	Baseline	41.58	746	8.74	5.34	5.60	5.73
10	Test 4	42.20	2452	25.0	15.5	15.4	15.1
11	Baseline	42.83	941	8.91	6.90	7.76	7.55

Table 26: Post-test matrix results for subject 2

					Displacement (mm)		
Test #	Description	Postmortem time (hours)	Rotational Acceleration (rad/s^2)	Rotational Velocity (rad/s)	Cortex Surface	1mm deep	2mm deep
2102_12	Post-test 1	43.15	2584	22.5	Not trackable		
2102_13	Baseline	43.38	753	9.03	8.99	8.41	8.71
2102_14	Post-test 2	43.71	2251	28.5	Not trackable		
2102_15	Baseline	44.06	916	8.81	8.91	8.81	8.92
2102_16	Post-test 3	44.26	2750	23.9	Not trackable		
2102_17	Baseline	44.45	787	9.27	9.13	9.25	8.98
2102_18	Post-test 4	44.76	2494	30.2	20.01	19.69	18.68
2102_19	Baseline	45.13	829	9.41	8.96	9.05	9.31
2102_20	Post-test 5	45.50	2935	30.2	19.21	18.99	20.00
2102_21	Baseline	45.86	800	9.34	7.61	8.46	8.41
2102_22	Post-test 6	46.23	2549	31.2	21.13	22.85	21.71
2102_23	Baseline	46.60	751	8.96	8.69	9.13	8.88
2102_24	Post-test 7	46.96	3018	27.3	19.18	20.29	20.75
2102_25	Baseline	47.33	797	9.06	9.09	9.50	8.92
2102_26	Post-test 8	47.70	2809	33.0	24.07	21.77	23.77
2102_27	Baseline	48.06	1143	8.85	8.44	7.95	7.97
2102_28	Post-test 9	48.43	3261	28.4	22.62	23.74	23.47
2102_29	Baseline	48.80	1020	8.59	5.23	5.98	6.26
2102_30	Post-test 10	49.16	3189	25.8	24.51	22.73	24.51
2102_31	Baseline	49.53	1070	9.33	5.72	6.09	5.72
2102_32	Post-test 11	49.90	2983	26.0	24.84	24.52	24.84
2102_33	Baseline	50.26	1030	8.92	5.94	6.30	5.94

Table 27: Comparison of baseline results for subject 2

					Displacement (mm)		
Test #	Description	Postmortem time (hours)	Rotational Acceleration (rad/s^2)	Rotational Velocity (rad/s)	Cortex Surface	1mm deep	2mm deep
2102_01	Baseline	39.30	783	8.61	4.84	4.64	5.21
2102_02	Baseline	39.45	831	8.94	4.64	4.88	5.08
2102_03	Baseline	39.60	787	8.62	4.89	4.85	4.82
2102_05	Baseline	40.03	757	8.89	4.89	6.01	5.55
2102_07	Baseline	40.58	1007	9.27	5.67	5.61	6.33
2102_09	Baseline	41.58	746	8.74	5.34	5.60	5.73
2102_11	Baseline	42.83	941	8.91	6.90	7.76	7.55
2102_13	Baseline	43.38	753	9.03	8.99	8.41	8.71
2102_15	Baseline	44.06	916	8.81	8.91	8.81	8.92
2102_17	Baseline	44.45	787	9.27	9.13	9.25	8.98
2102_19	Baseline	45.13	829	9.41	8.96	9.05	9.31
2102_21	Baseline	45.86	800	9.34	7.61	8.46	8.41
2102_23	Baseline	46.60	751	8.96	8.69	9.13	8.88
2102_25	Baseline	47.33	797	9.06	9.09	9.50	8.92
2102_27	Baseline	48.06	1143	8.85	8.44	7.95	7.97
2102_29	Baseline	48.80	1020	8.59	5.72	6.09	6.09
2102_31	Baseline	49.53	1070	9.33	5.94	6.30	6.43
2102_33	Baseline	50.26	1030	8.92	4.84	4.64	5.21
		Average	**875**	**8.98**	**6.98**	**7.19**	**7.23**
		Std. dev.	**128**	**0.27**	**1.81**	**1.75**	**1.63**
		% CV	**14.6**	**2.99**	**25.86**	**24.38**	**22.51**

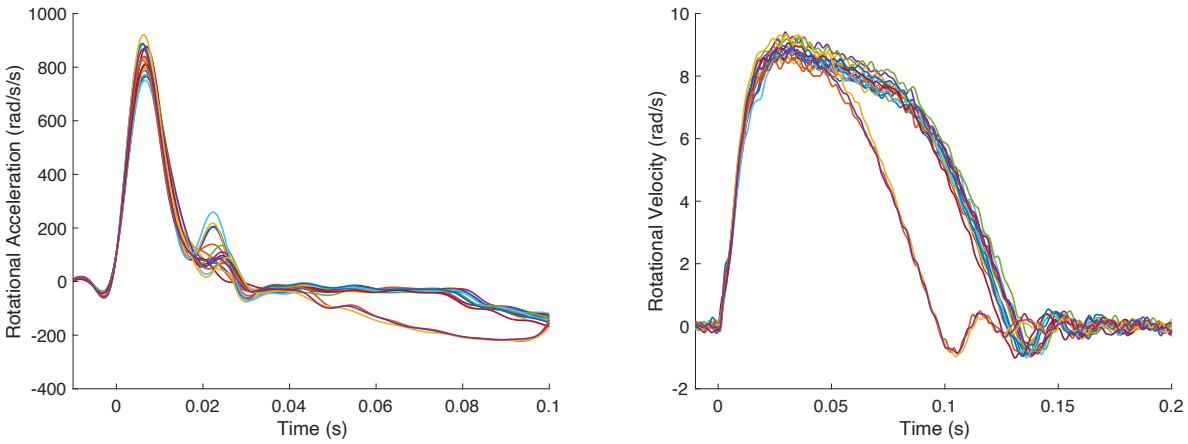

Figure 71: Comparison of baseline kinematics for subject 2

Of note, the tests show in orange and yellow (Figure 71) have a shorter pulse duration due to adjustment of the braking system to allow for higher kinematic tests in the post-test matrix.

Post-test 1 was determined to be a damaging test (see 4.3. PMHS Testing Discussion *Evaluation of Damaged Tests*). Therefore, tests 13-33 are not included in the subsequent analysis.

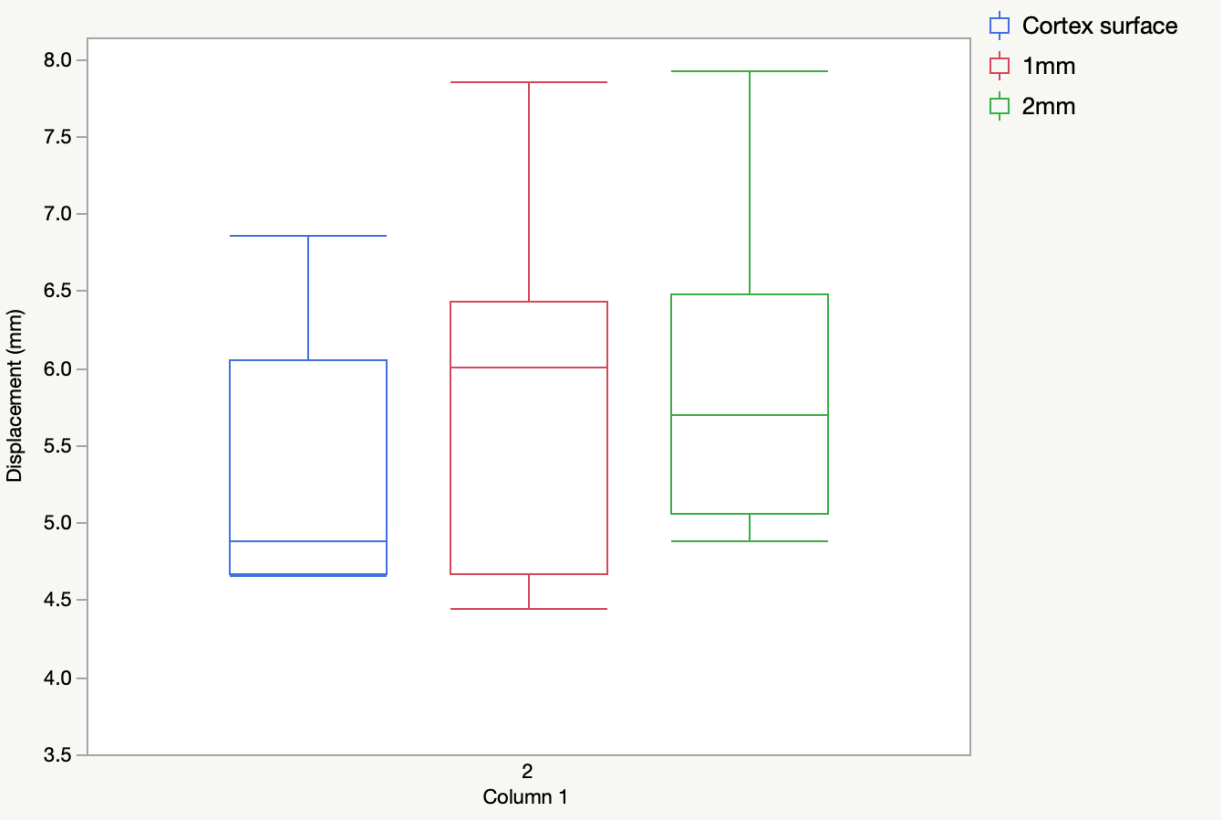

Figure 72: Boxplot of subject 2 baseline peak displacements at the three tracked locations

Table 28: Linear regression results for subject 2 displacements versus postmortem time, rotational velocity, and rotational acceleration

	Postmortem time	Rotational Velocity	Rotational Acceleration
	R^2 (p-value)		
Cortex surface	0.97*	0. 10	0.21
1 mm deep	0.90*	0.14	0.13
2 mm deep	0.92*	0.12	0.22

*Indicates statistical significance ($p<0.05$)

The linear regression results indicate that peak displacement is strongly correlated with postmortem time. Rotational kinematics did not have a significant effect on the outcome of peak displacement at any tracked point location. Regressions with statistical significance are shown in Figure 73.

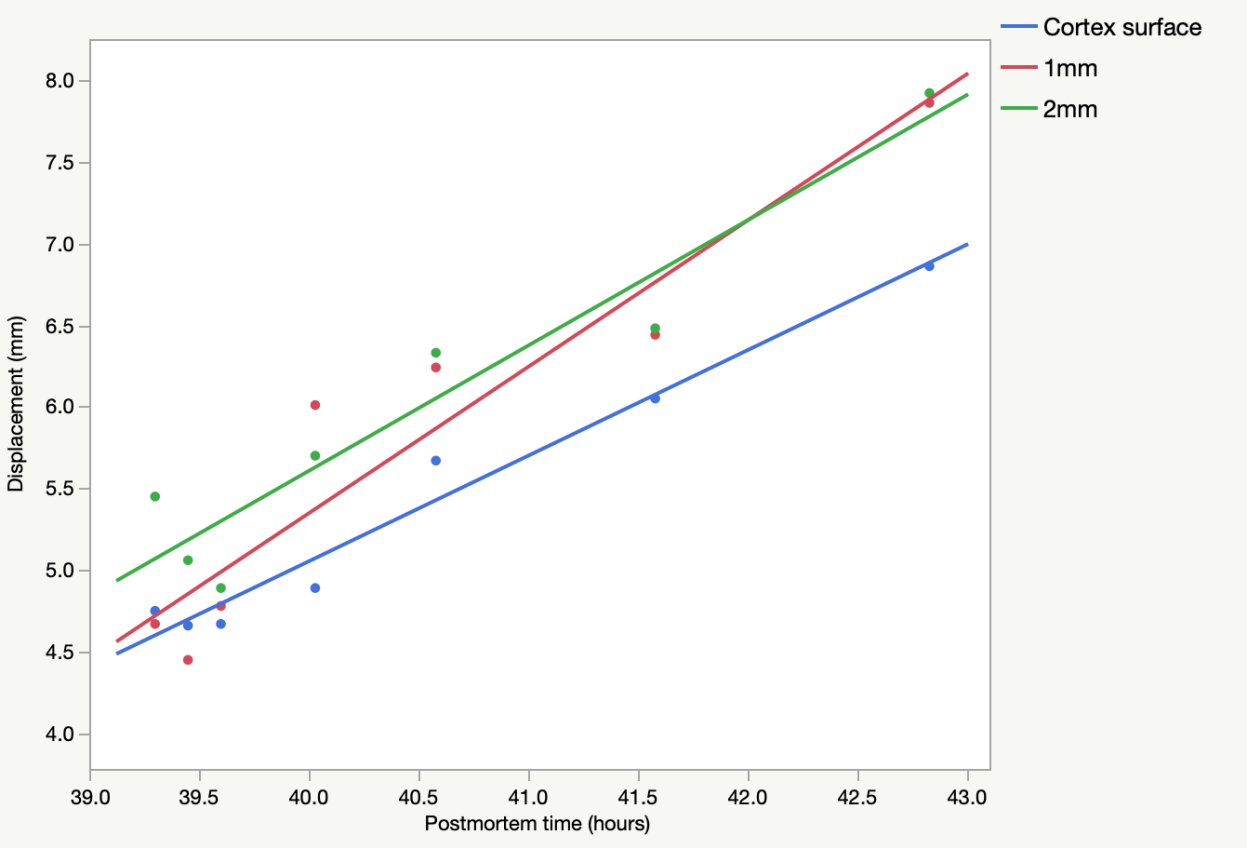

Figure 73: Statistically significant relationships for baseline data from subject 2

Table 29: Multiple regression summary statistics for subject 2

	Analysis of Variance		Summary of Fit		Parameter Estimates			
					intercept	Postmortem time (hours)	Rotational Velocity (rad/s)	Rotational Acceleration (rad/s/s)
	F-ratio	df	Adjusted R^2	RMSE	estimate (p-value)			
Cortex surface	<0.001*	10	0.992	0.356	-29.30 (<0.001*)	0.744 (<0.001*)	0.563 (<0.001*)	0.00039 (0.214)
1mm	<0.001*	10	0.991	0.364	-36.20 (<0.001*)	0.932 (<0.001*)	0.508 (<0.001*)	0.00040 (0.441)
2mm	<0.001*	10	0.979	0.535	-34.79 (<0.001*)	0.505 (<0.001*)	0.400 (<0.001*)	0.00059 (0.297)
*Indicates statistical significance ($p<0.05$)								

The multiple regression analysis was statistically significant for all three locations tracked as evidenced by the F-ratio value for each test. The regressions showed a dependence of peak brain displacement on angular velocity and postmortem time.

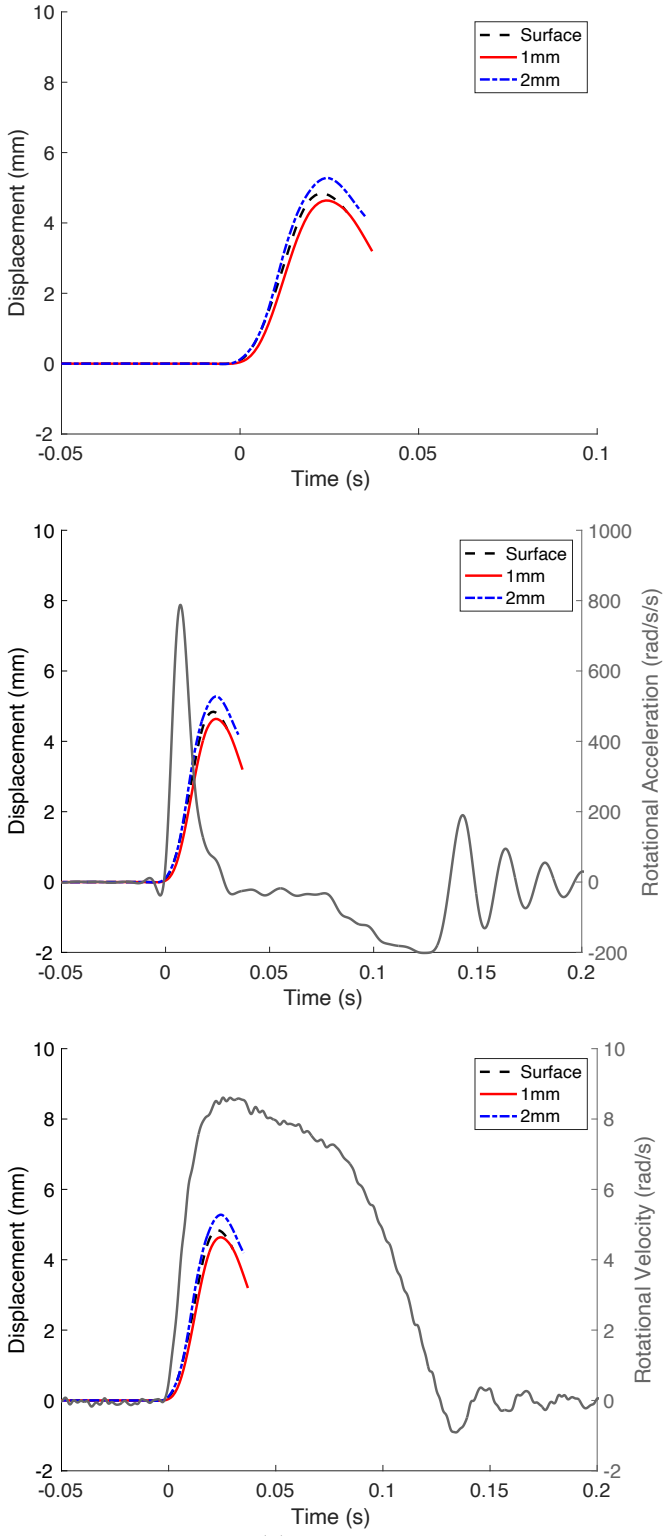

(a) Test 1

Figure 74: Time history of displacement (top), displacement compared to rotational acceleration (middle) and displacement compared to rotational velocity (bottom) for subject 2

Figure 74 continued

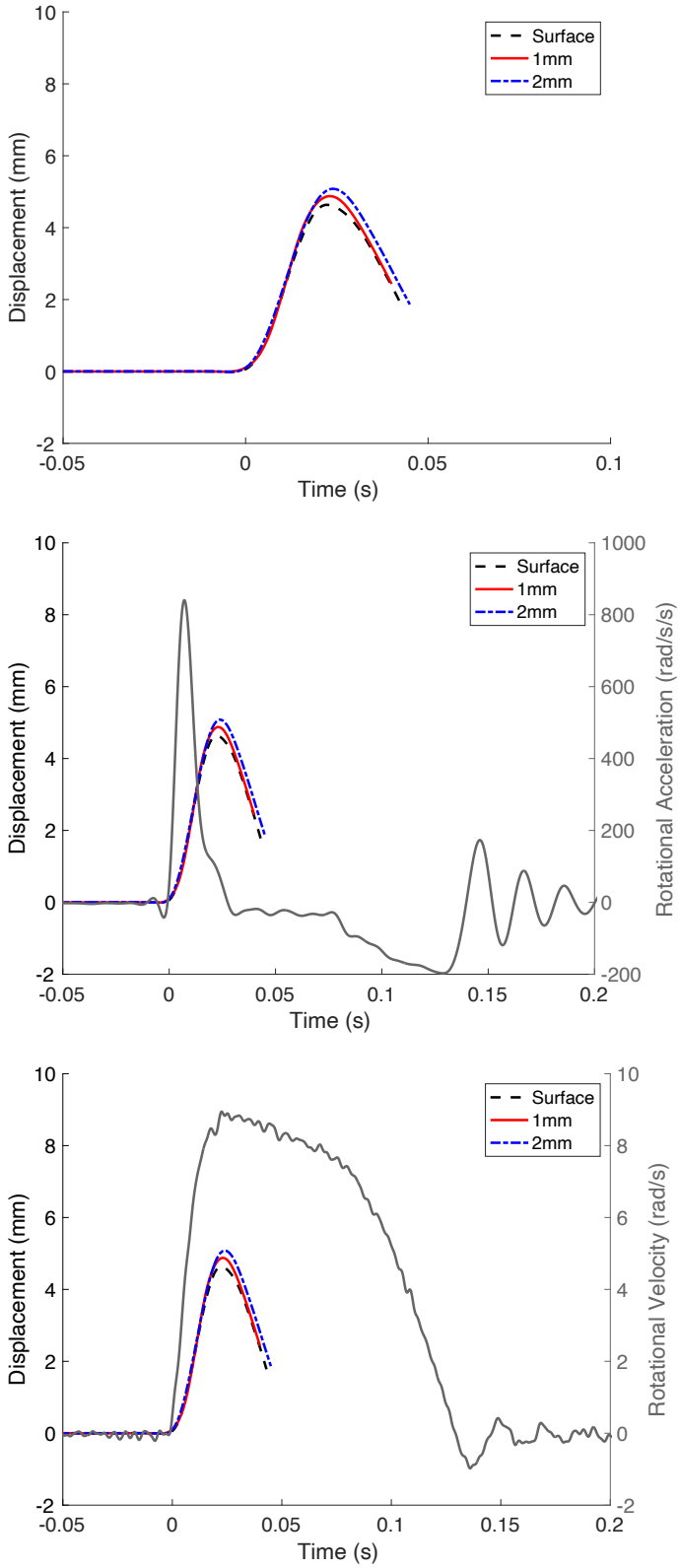

(b) Test 2

Figure 74 continued

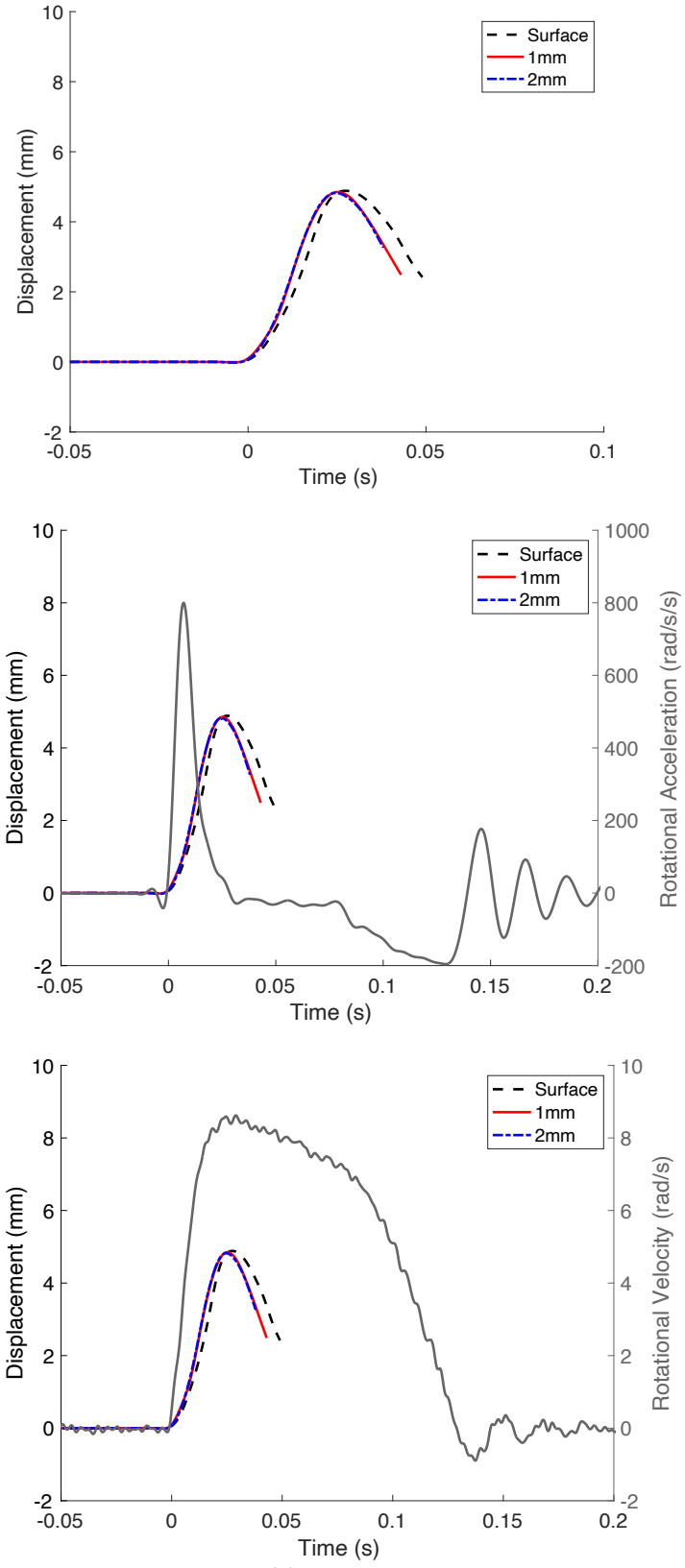

(c) Test 3

Figure 74 continued

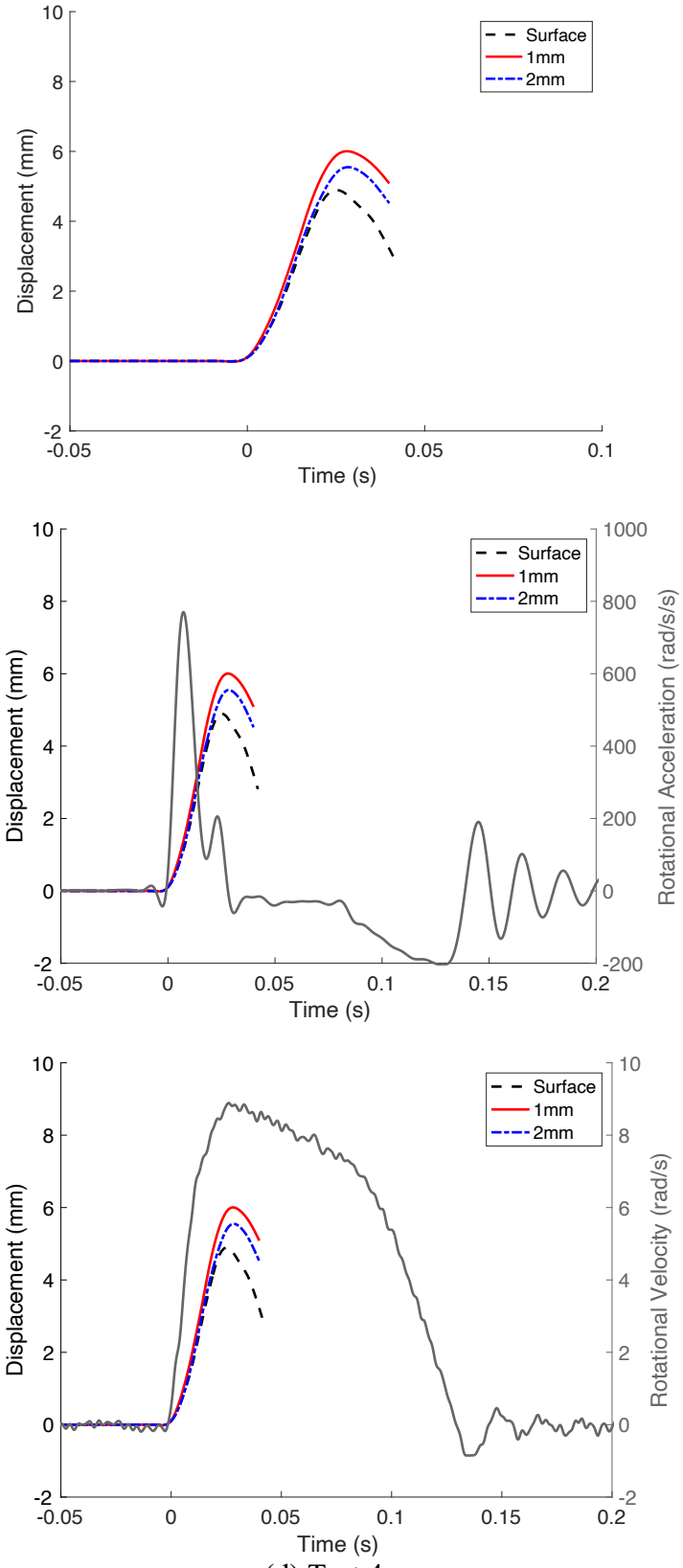

(d) Test 4

Figure 74 continued

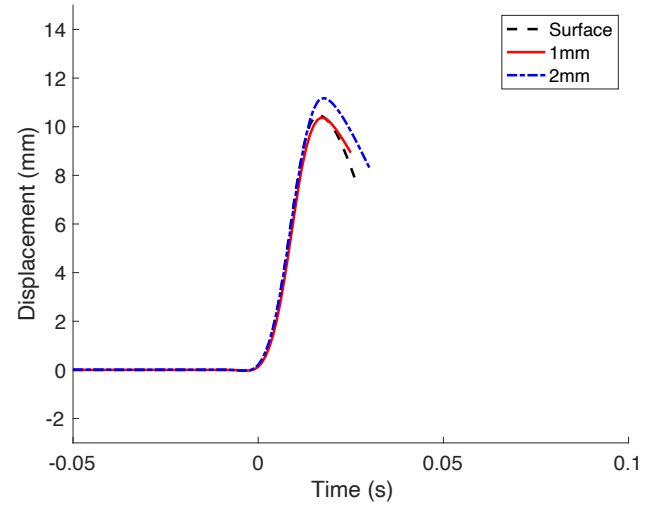

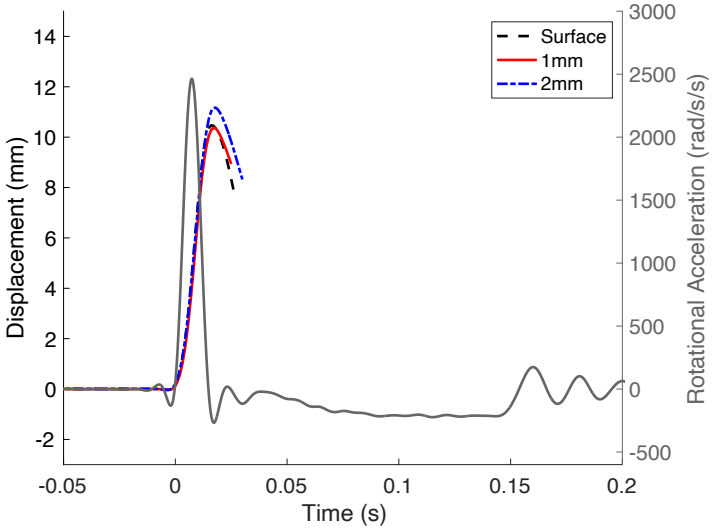

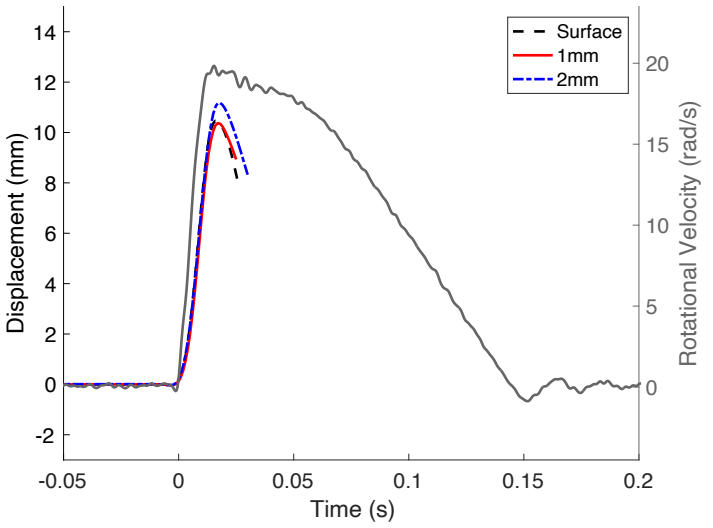

(e) Test 5

Figure 74 continued

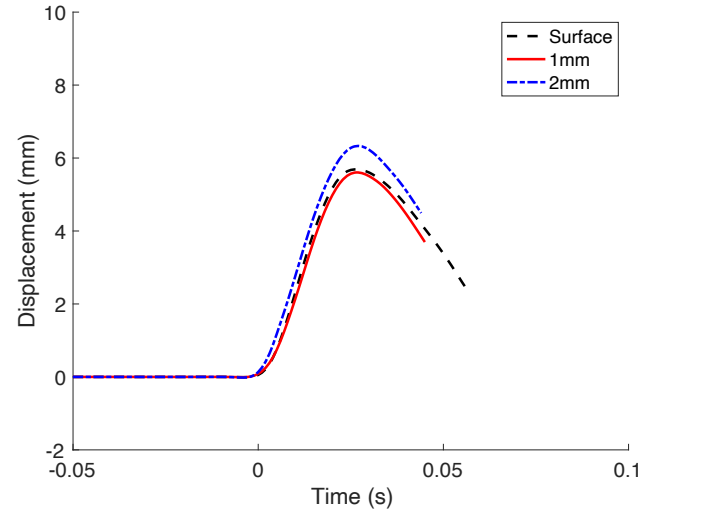

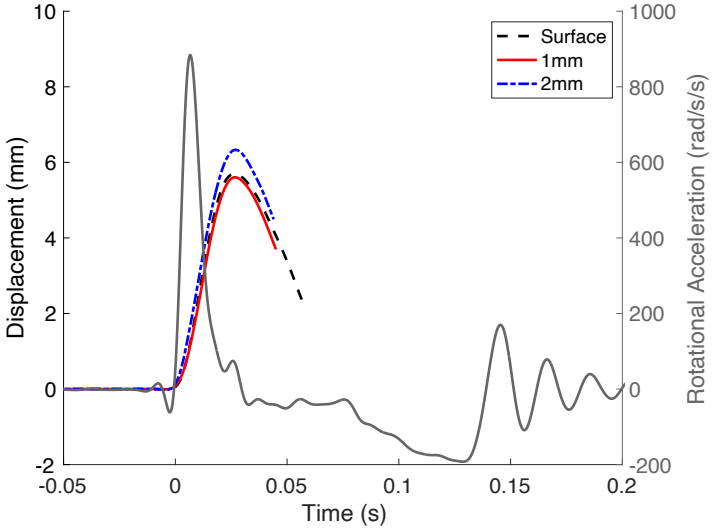

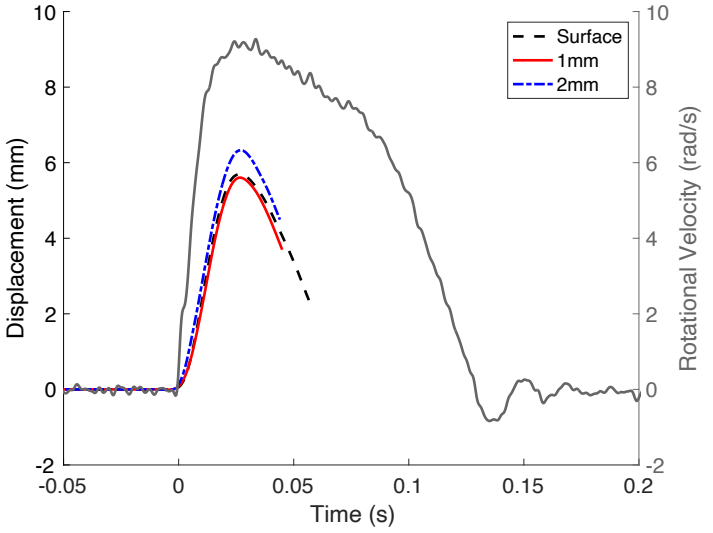

(f) Test 6

Figure 74 continued

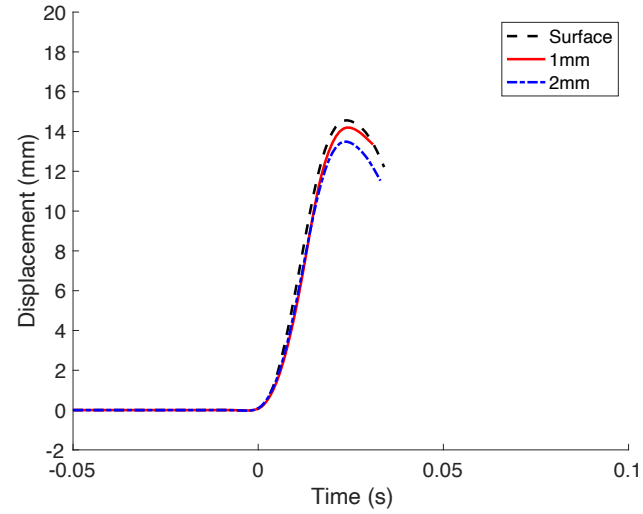

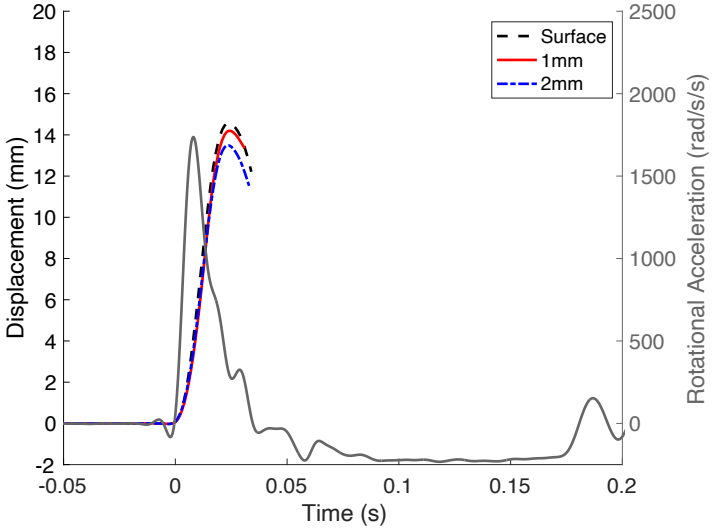

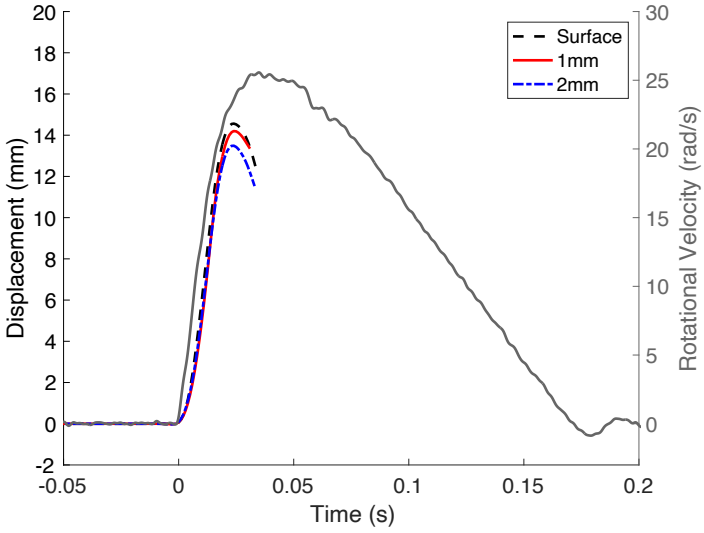

(g) Test 7

Figure 74 continued

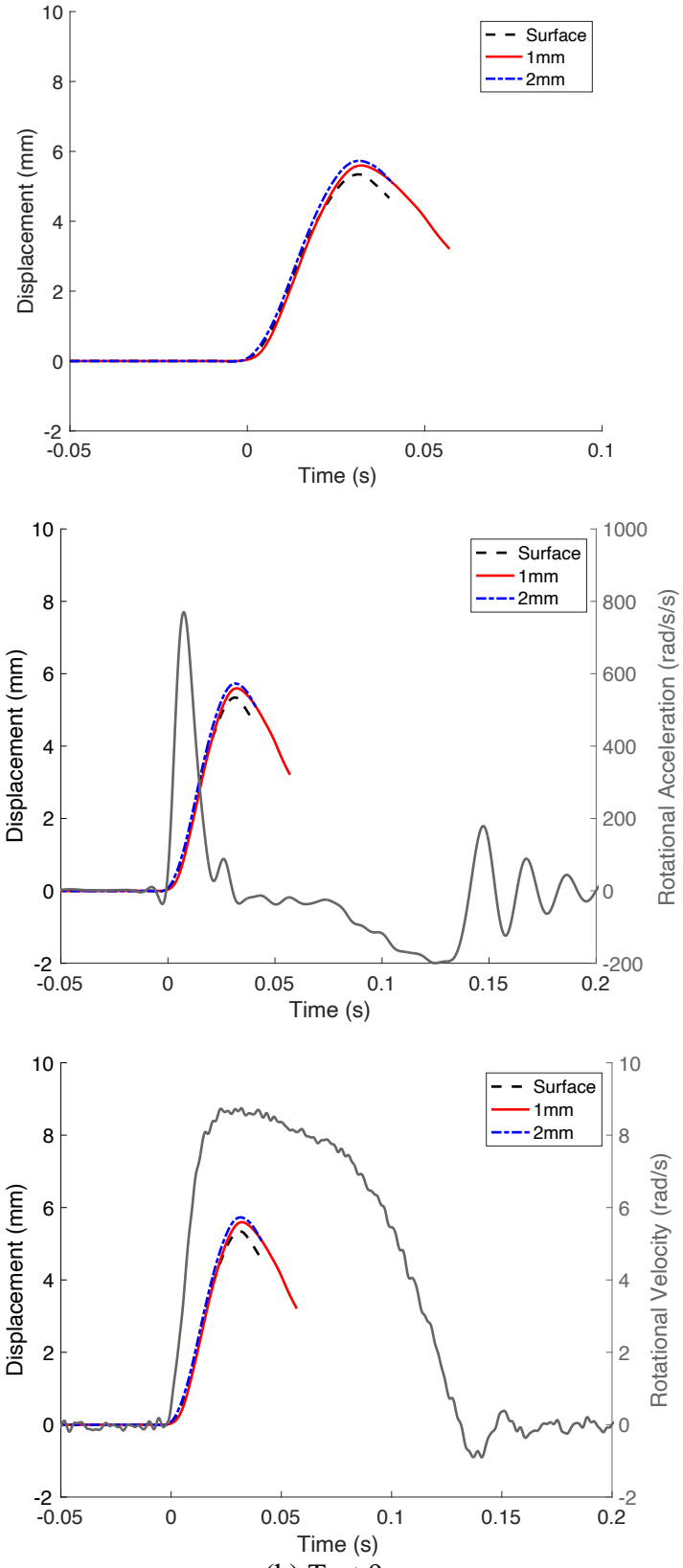

(h) Test 9

Figure 74 continued

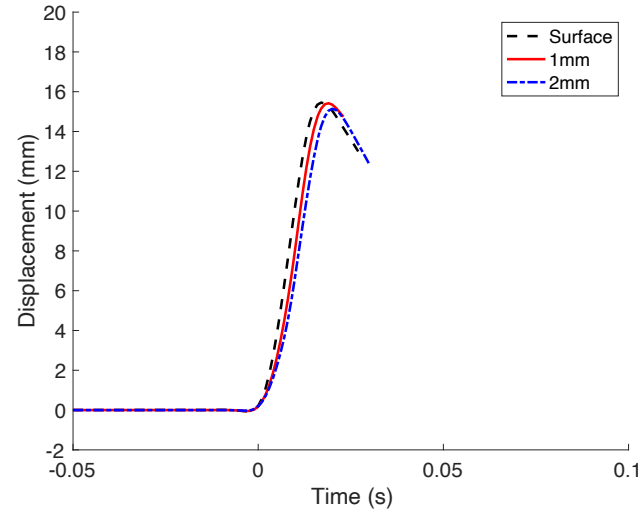

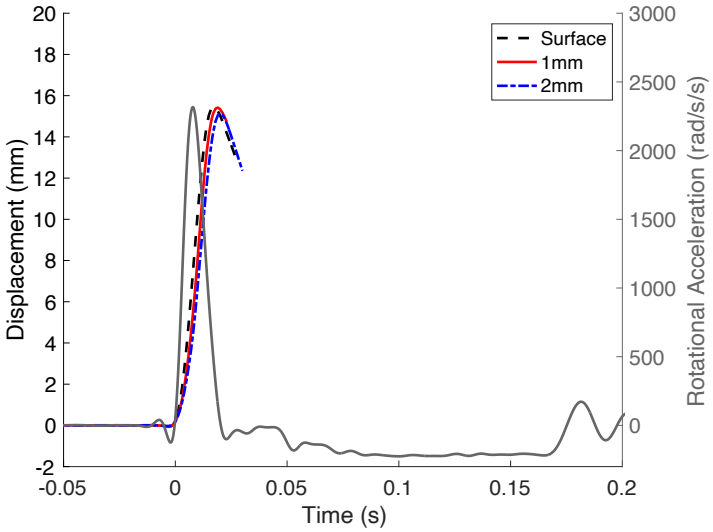

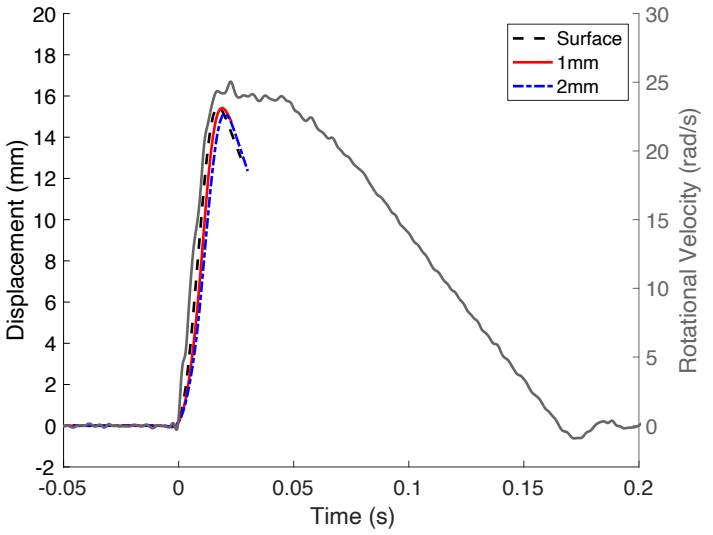

(i) Test 10

Figure 74 continued

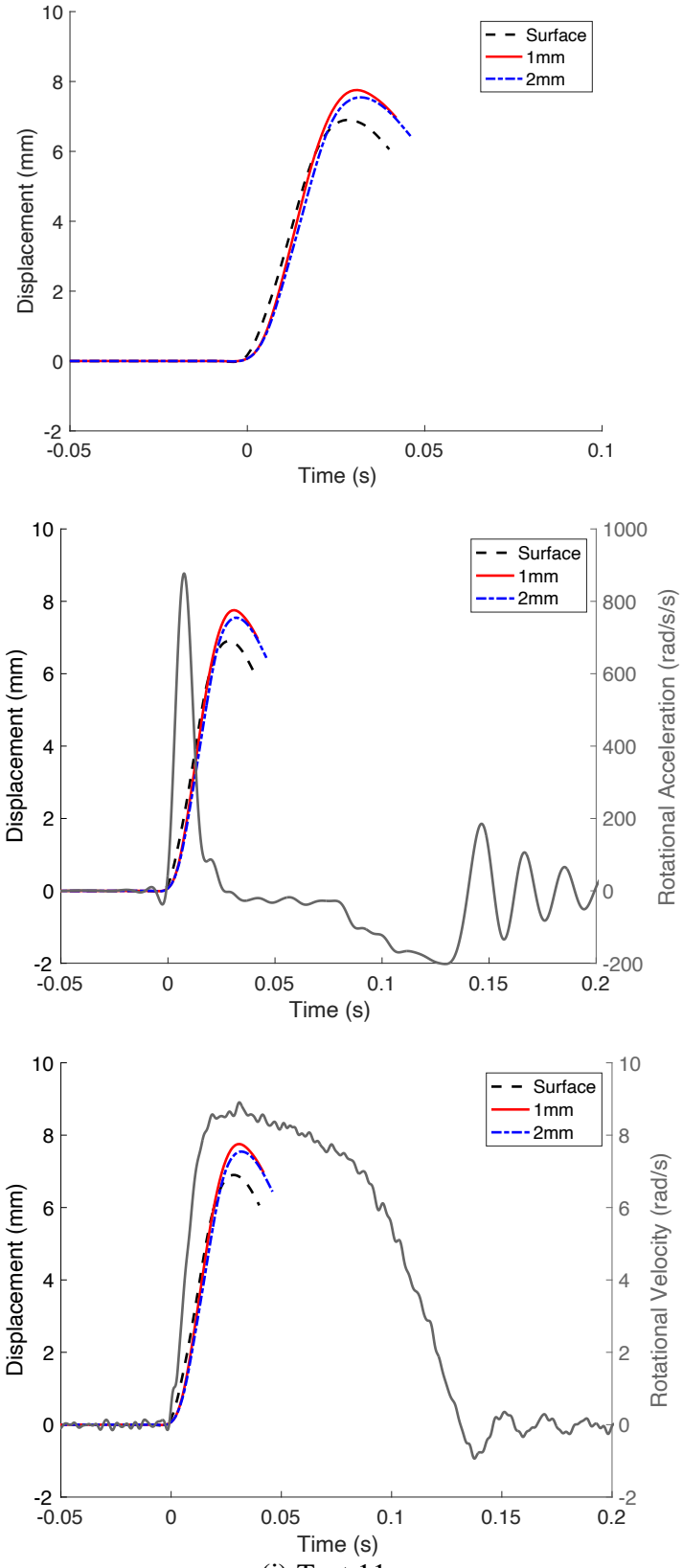

(j) Test 11

Figure 74 continued

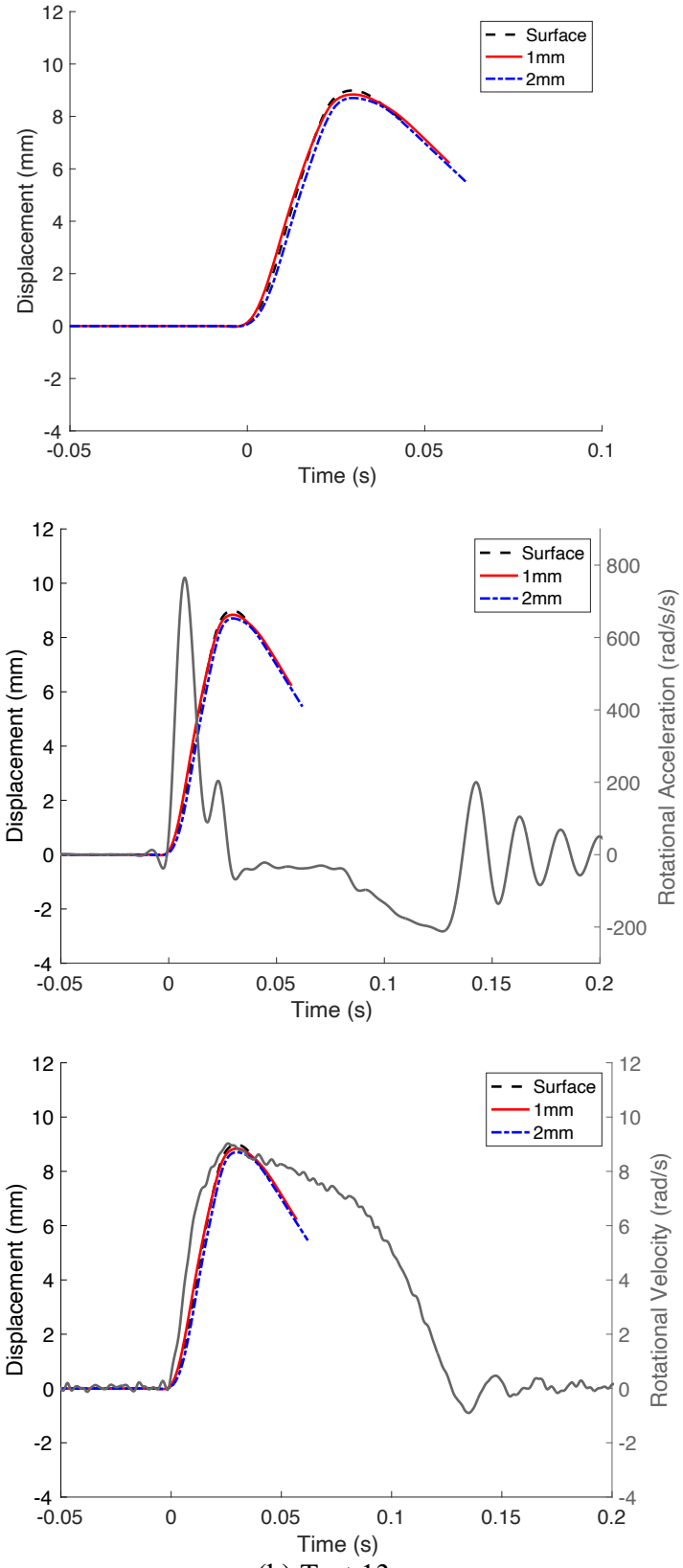

(k) Test 13

Figure 74 continued

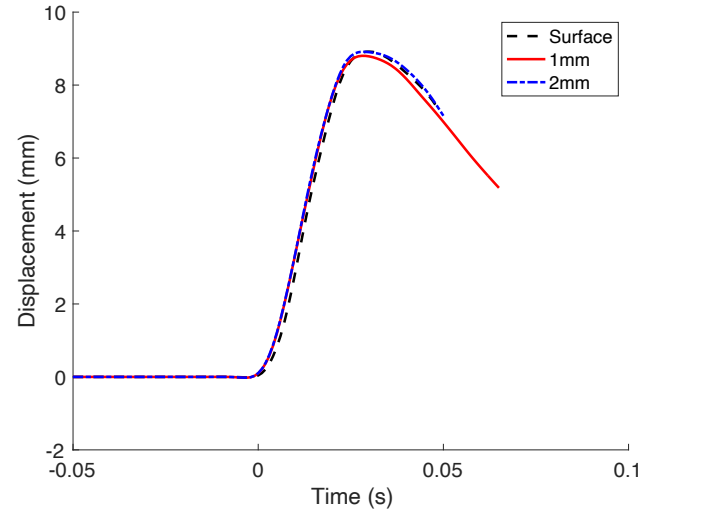

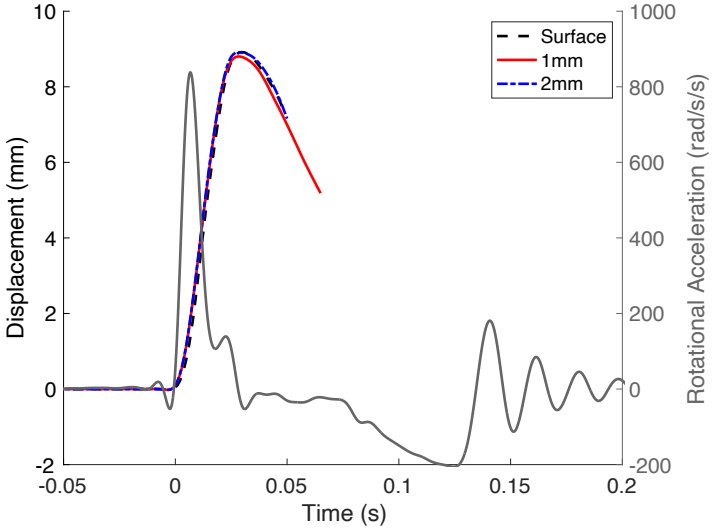

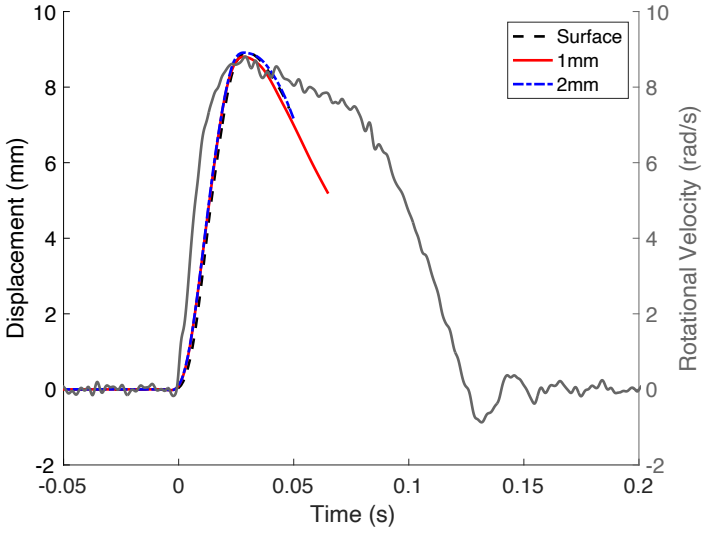

(l) Test 15

Figure 74 continued

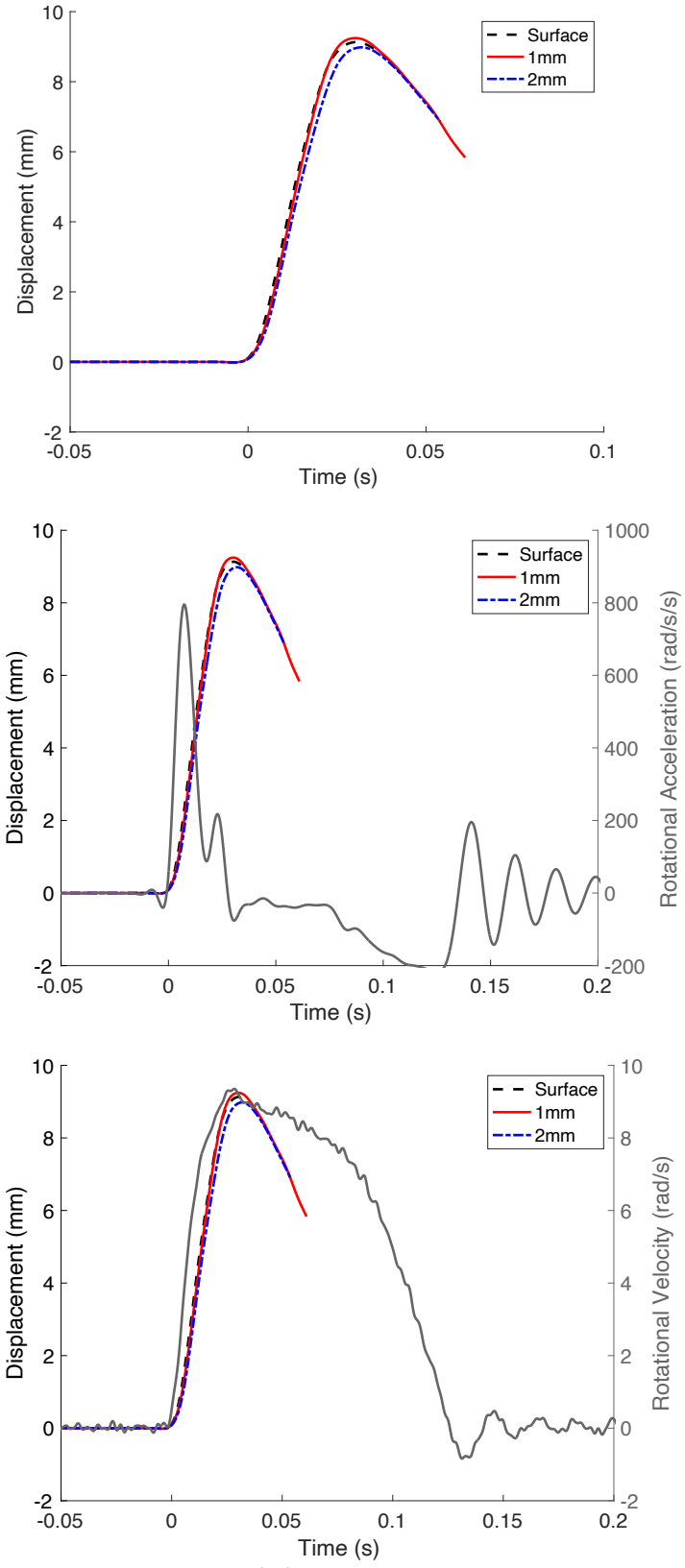

(m) Test 17

Figure 74 continued

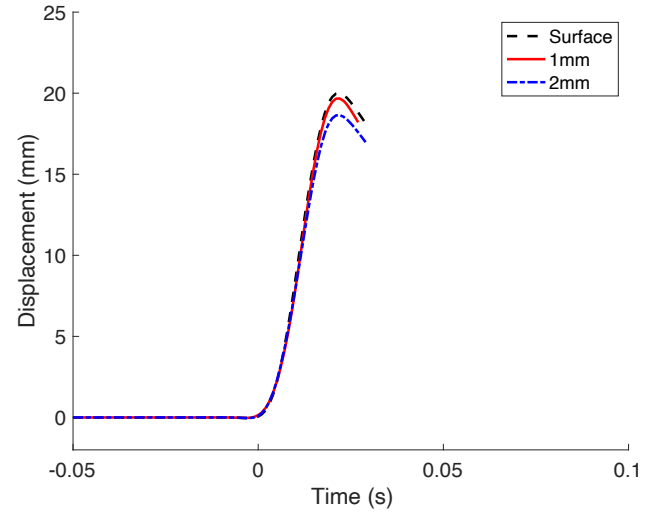

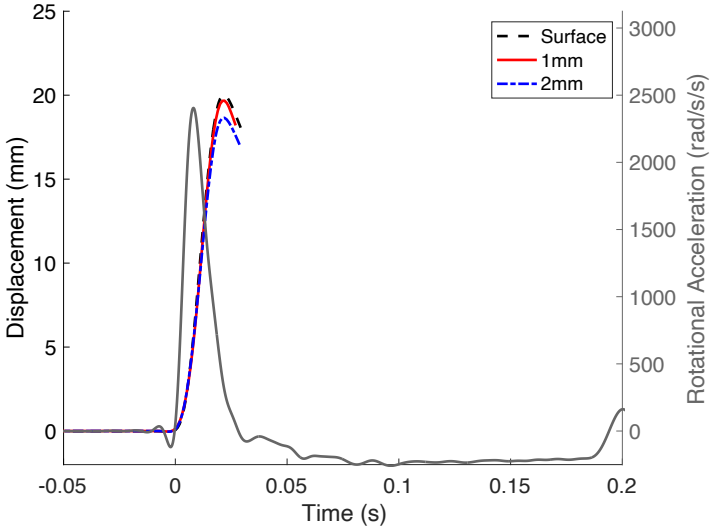

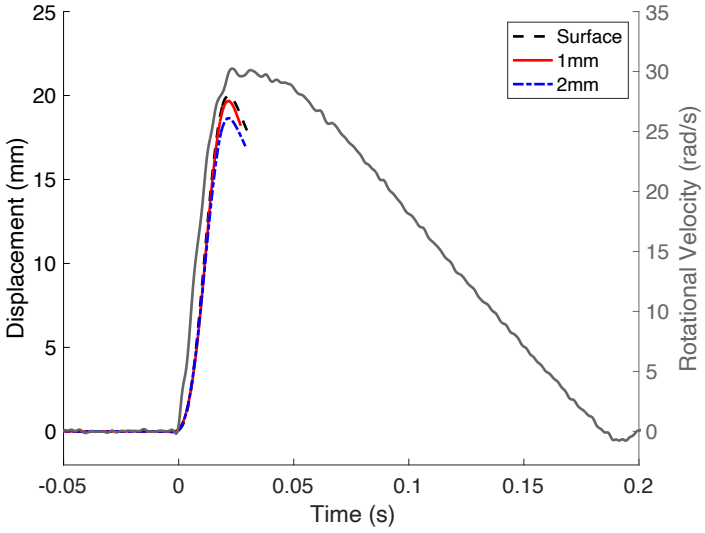

(n) Test 18

Figure 74 continued

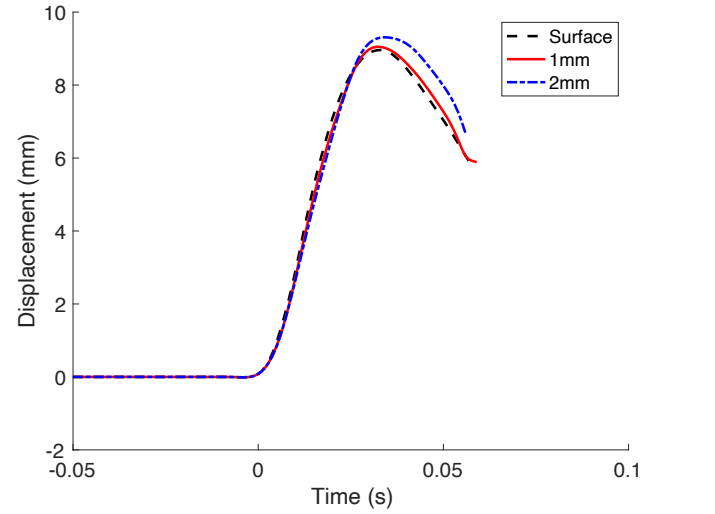

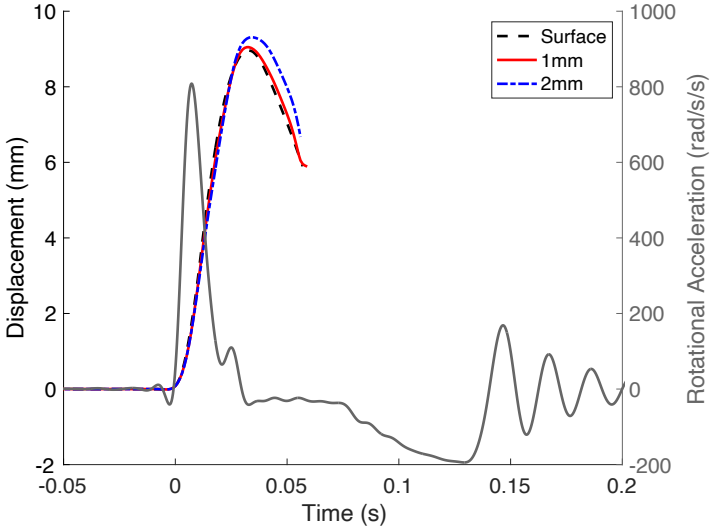

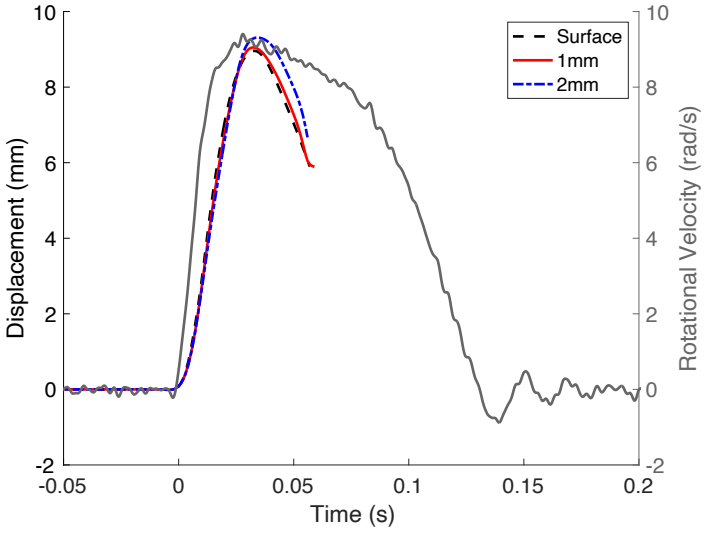

(o) Test 19

Figure 74 continued

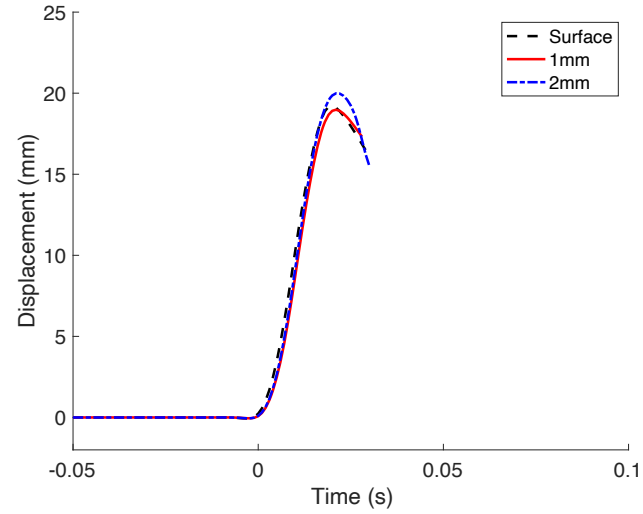

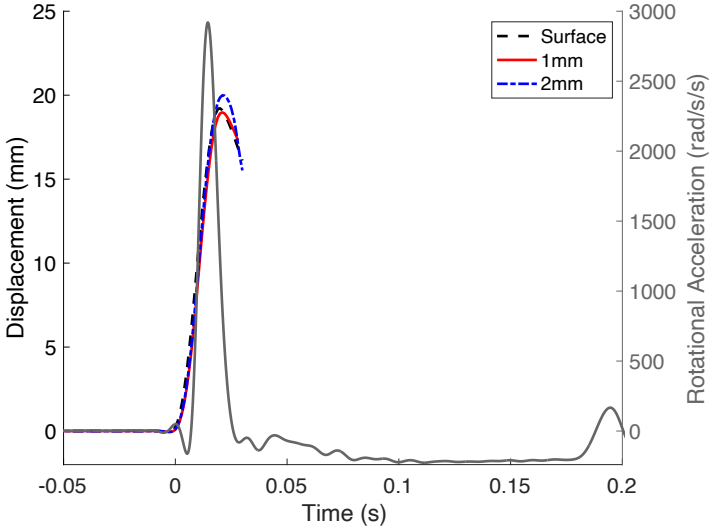

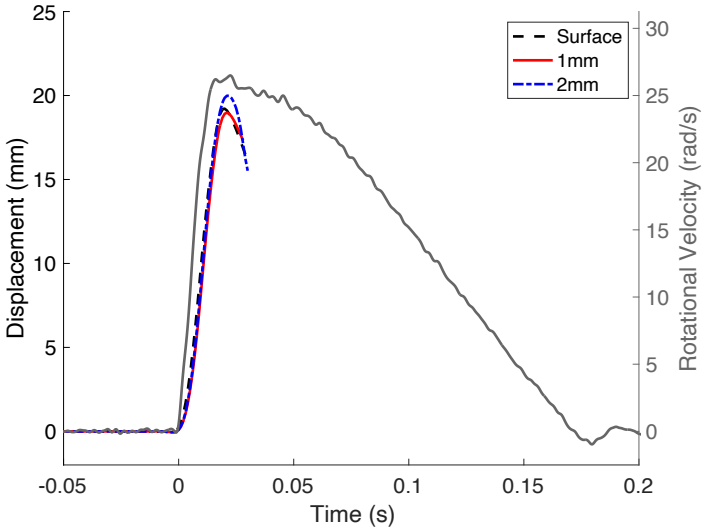

(p) Test 20

Figure 74 continued

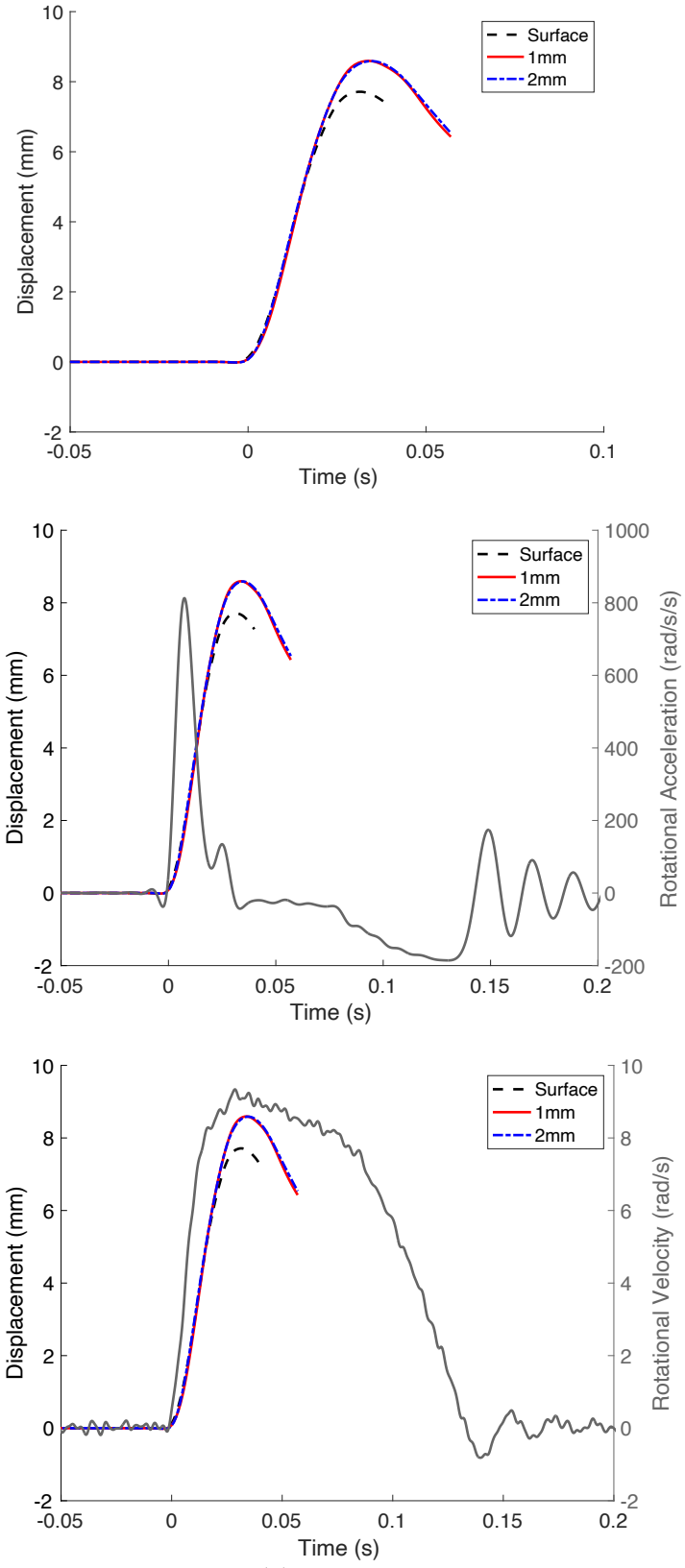

(q) Test 21

Figure 74 continued

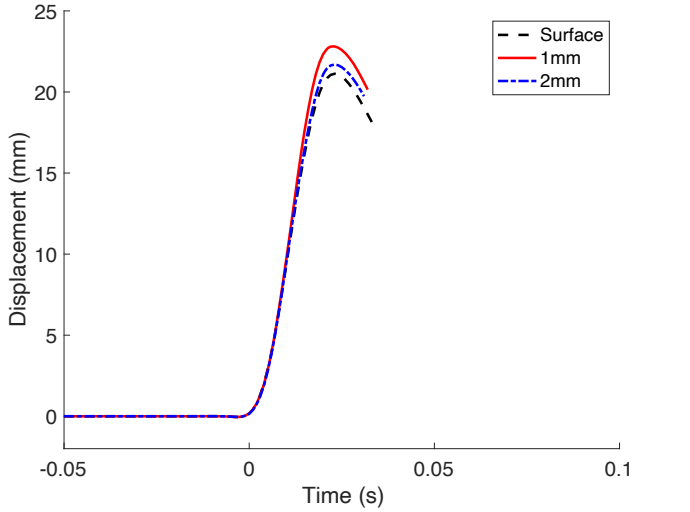

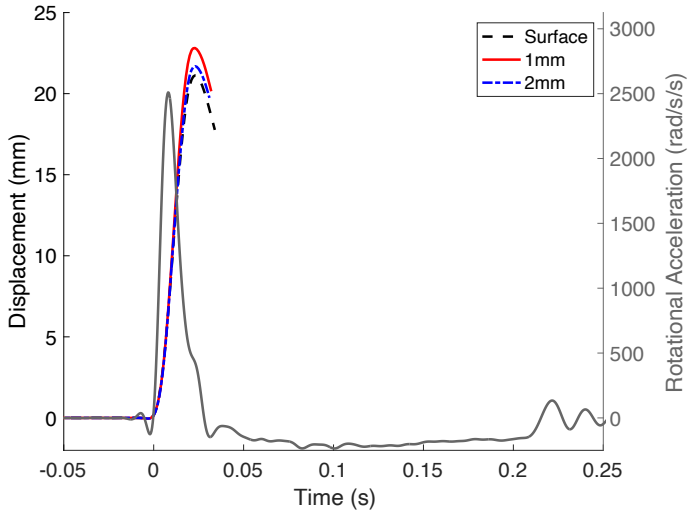

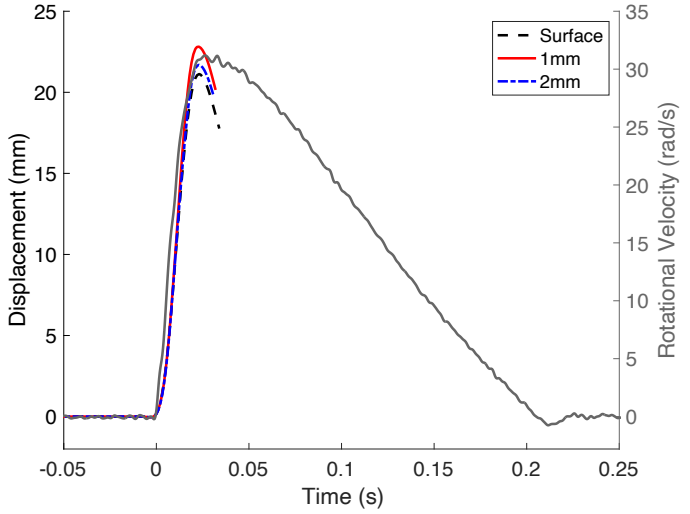

(r) Test 22

Figure 74 continued

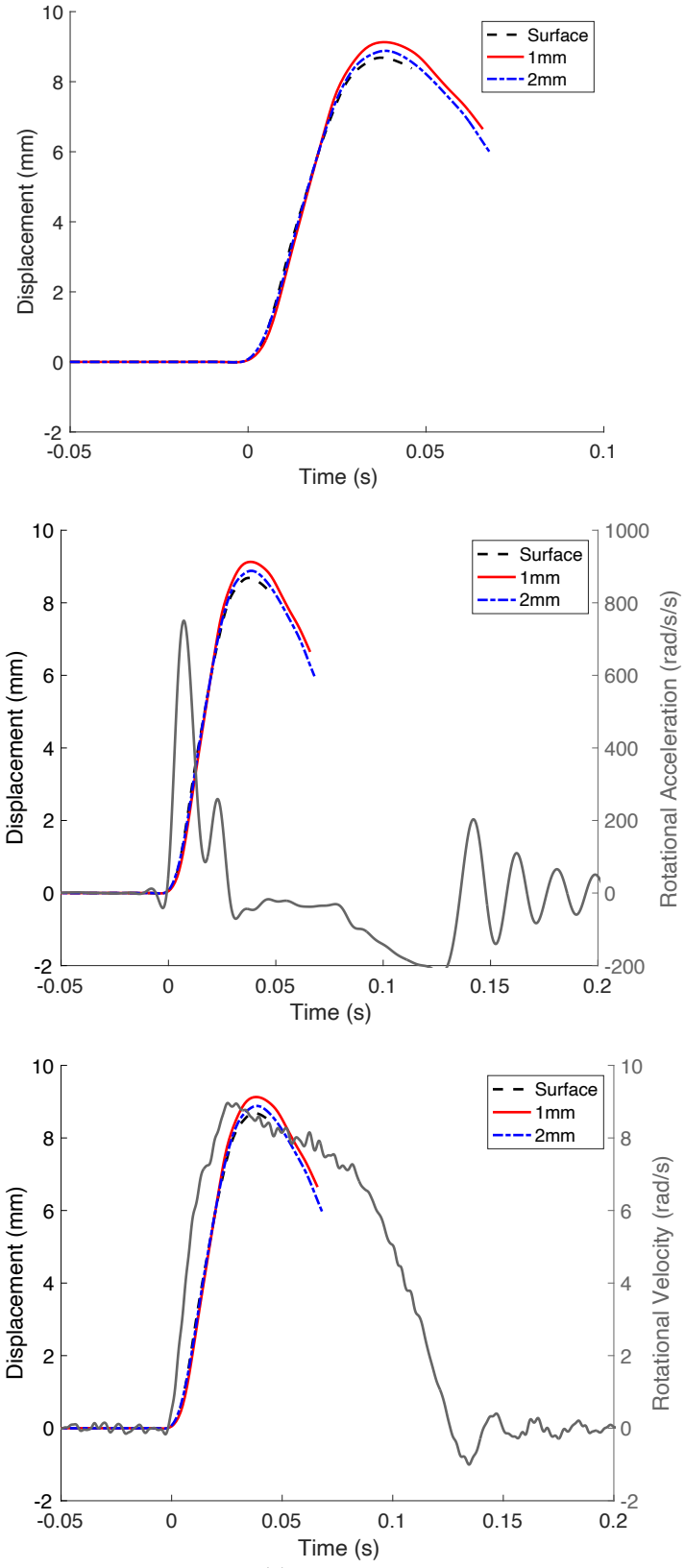

(s) Test 23

Figure 74 continued

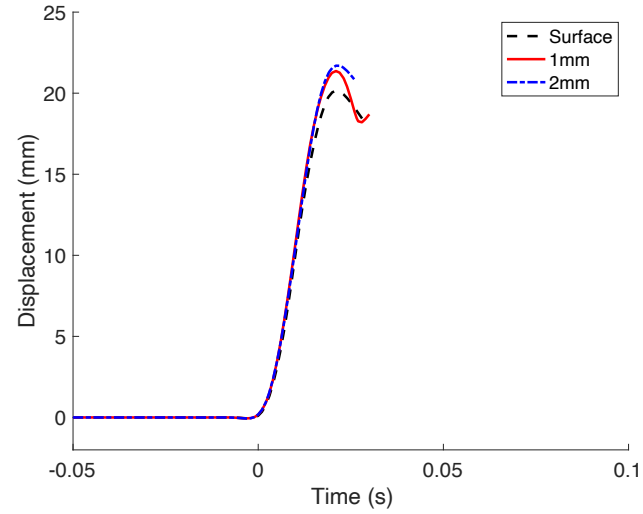

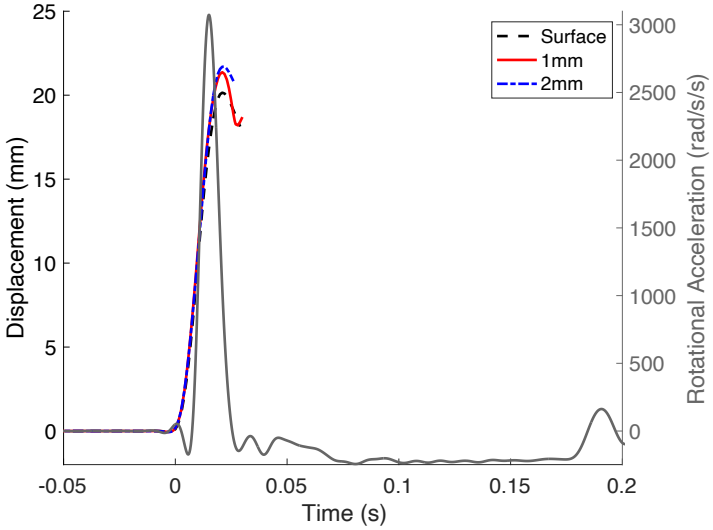

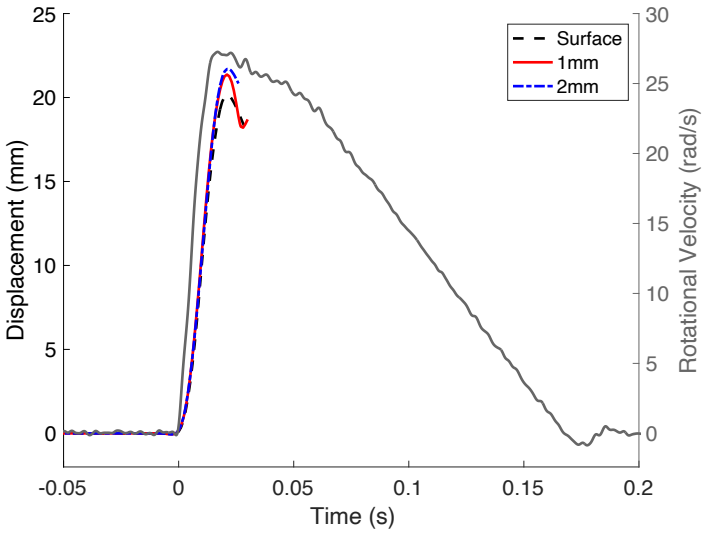

(t) Test 24

Figure 74 continued

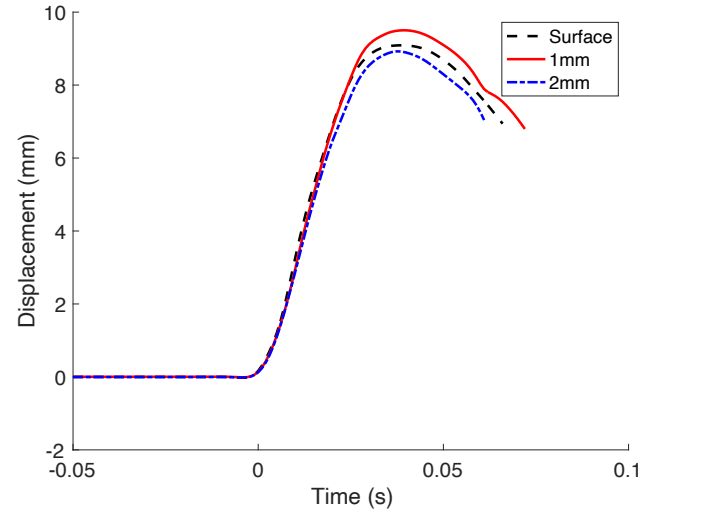

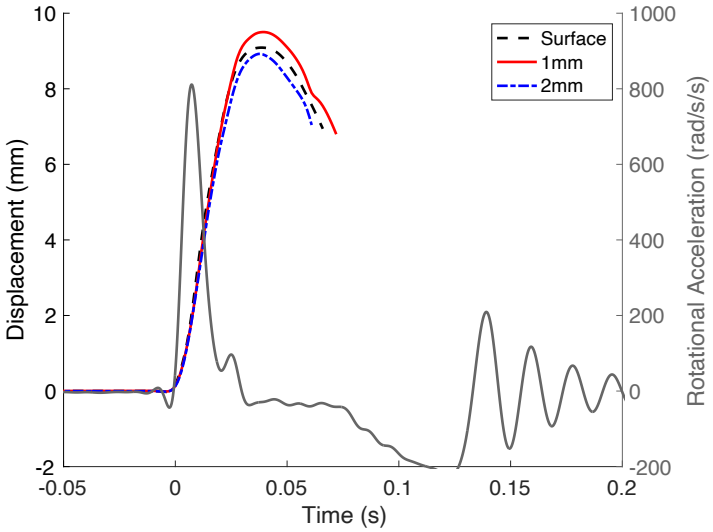

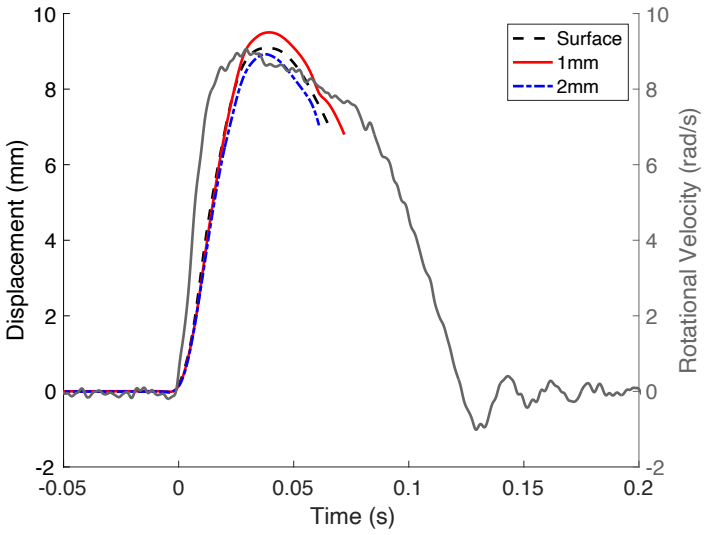

(u) Test 25

Figure 74 continued

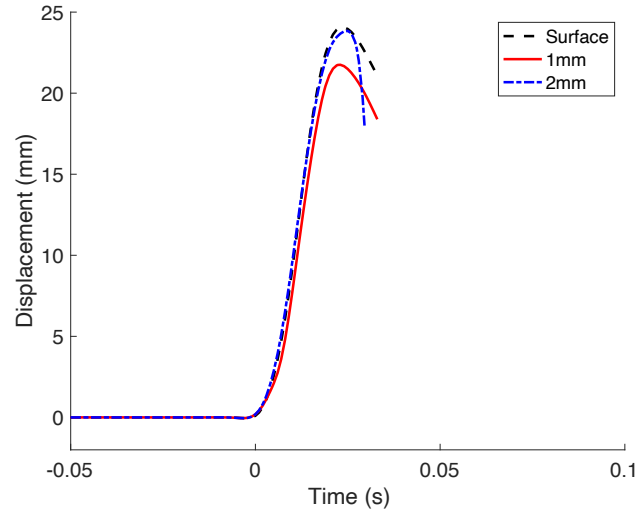

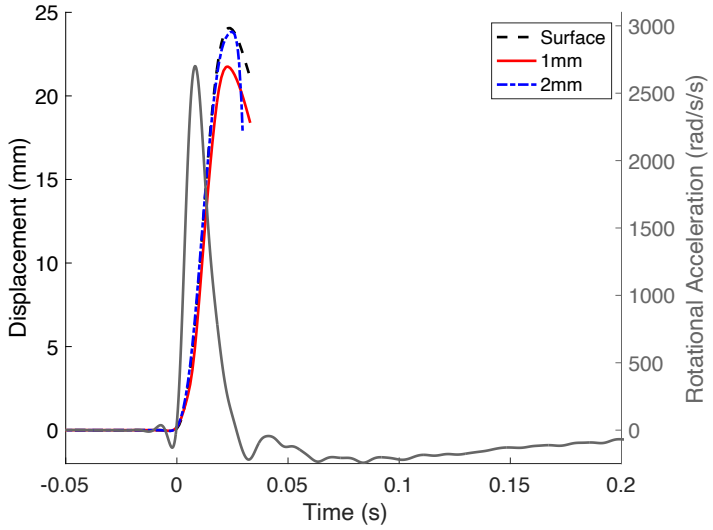

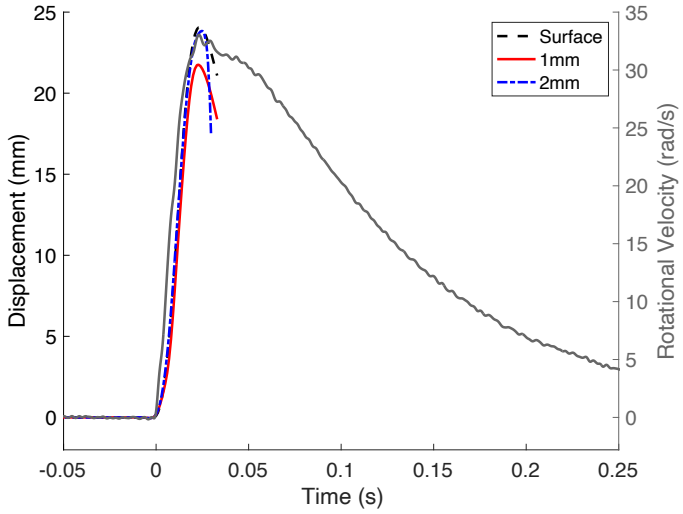

(v) Test 26

Figure 74 continued

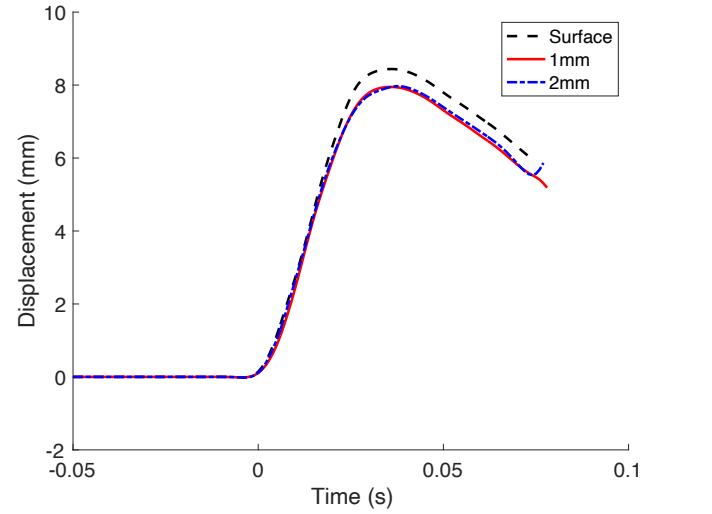

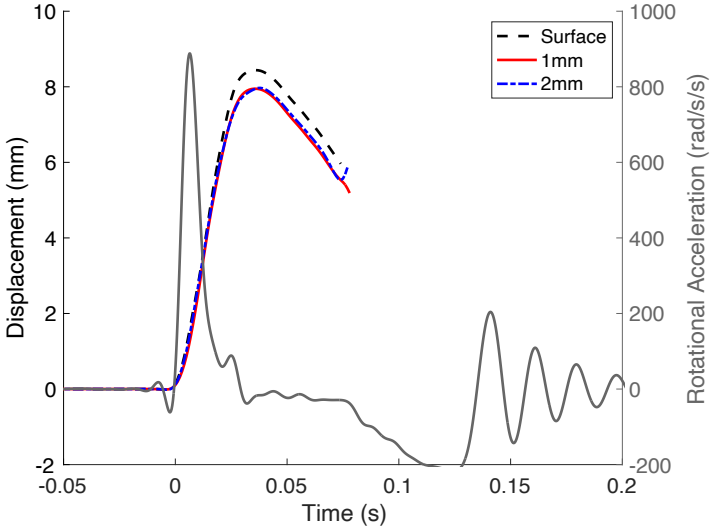

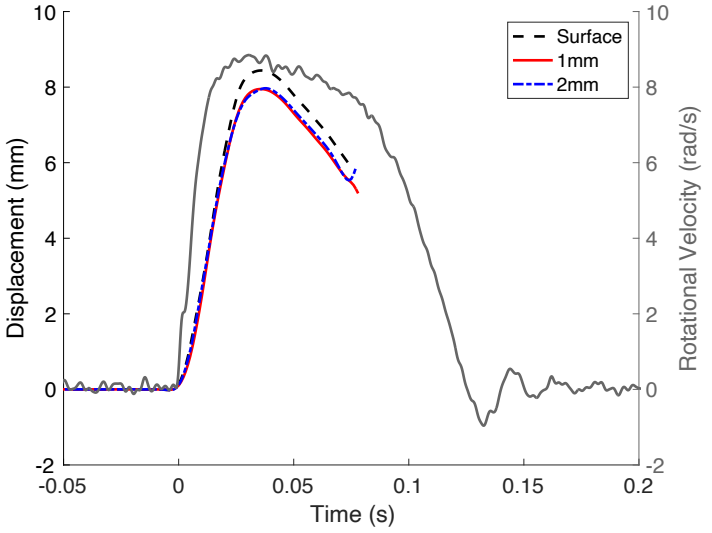

(w) Test 27

Figure 74 continued

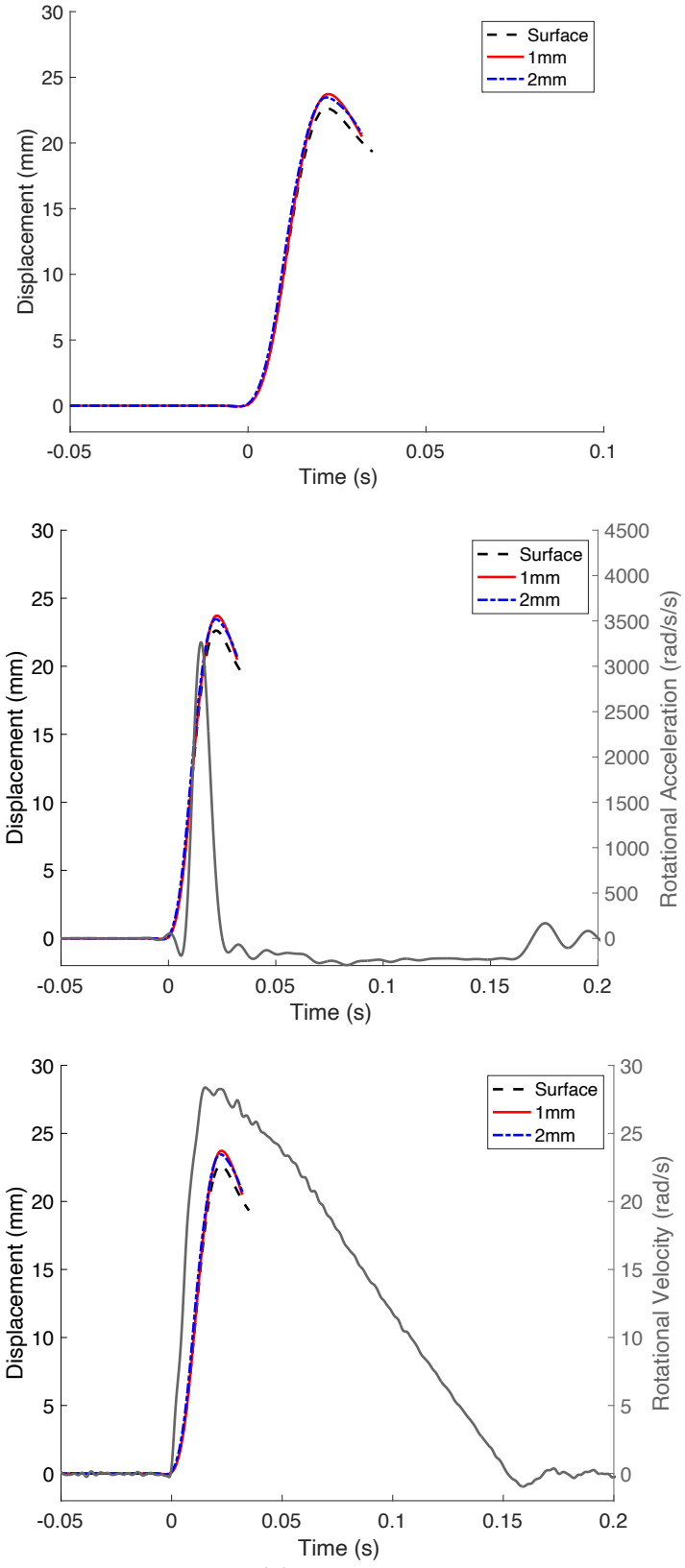

(x) Test 28

Figure 74 continued

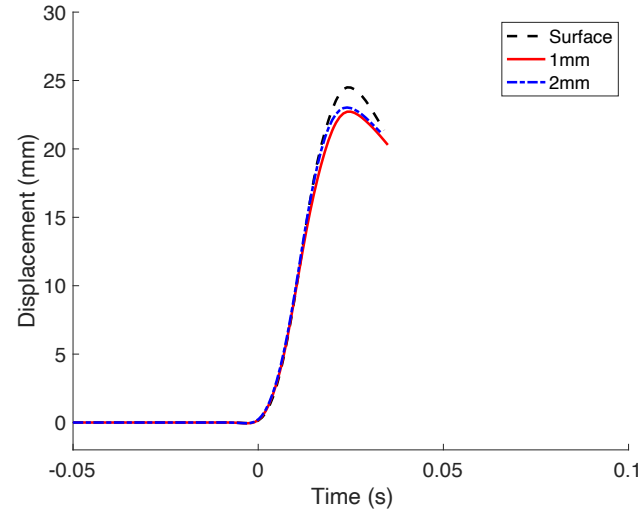

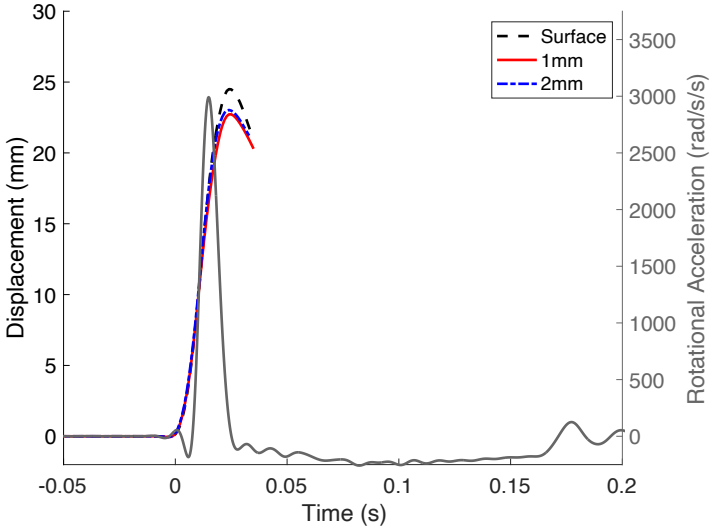

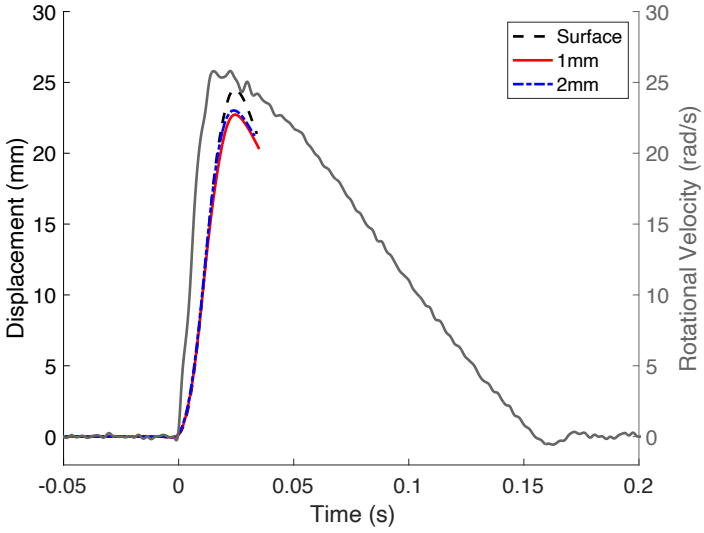

(z) Test 30

Figure 74 continued

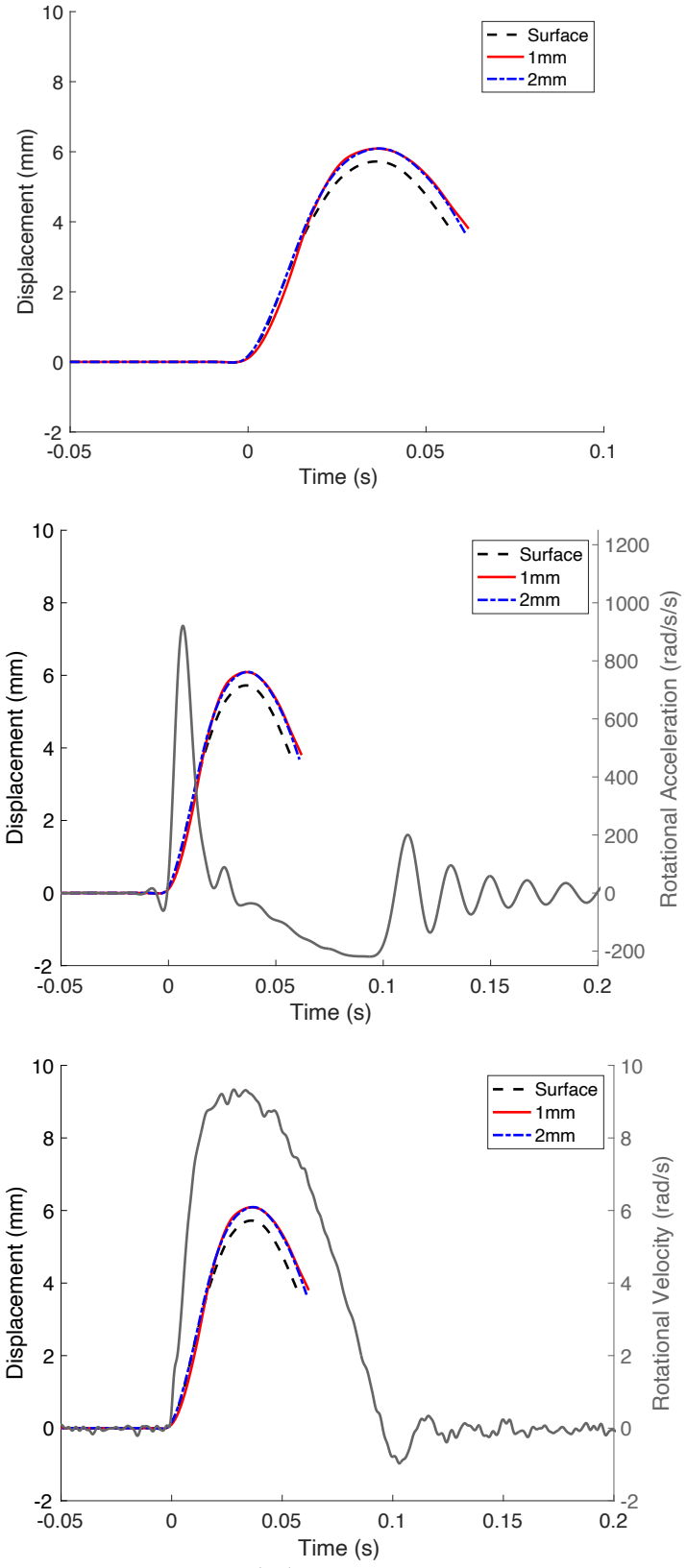

(aa) Test 31

Figure 74 continued

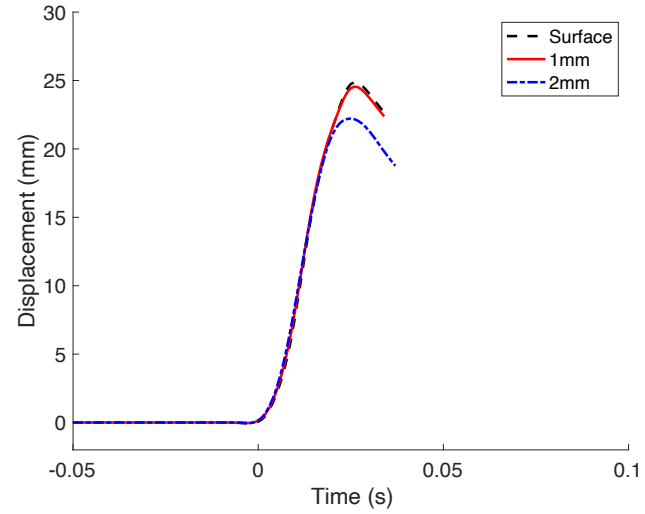

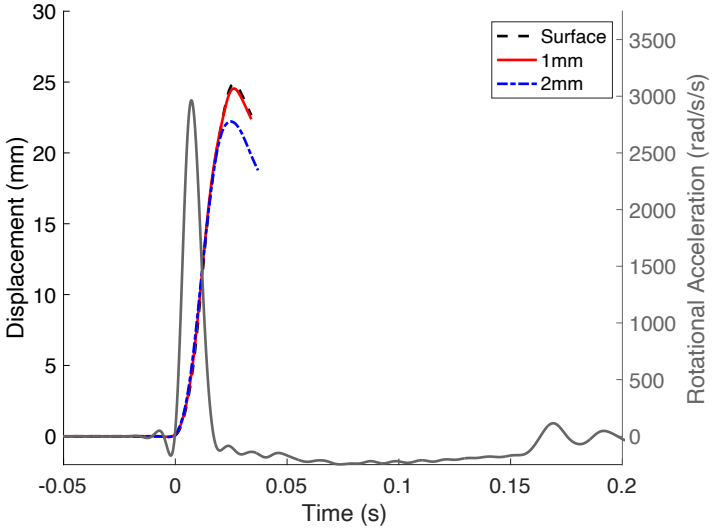

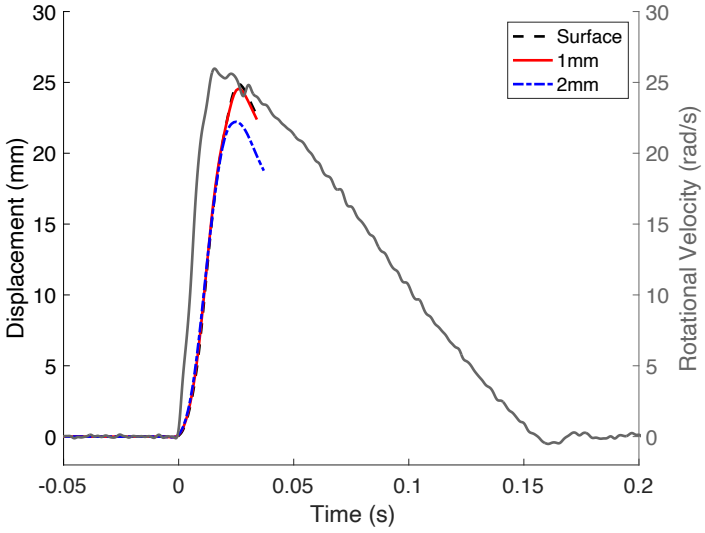

(ab) Test 32

Figure 74 continued

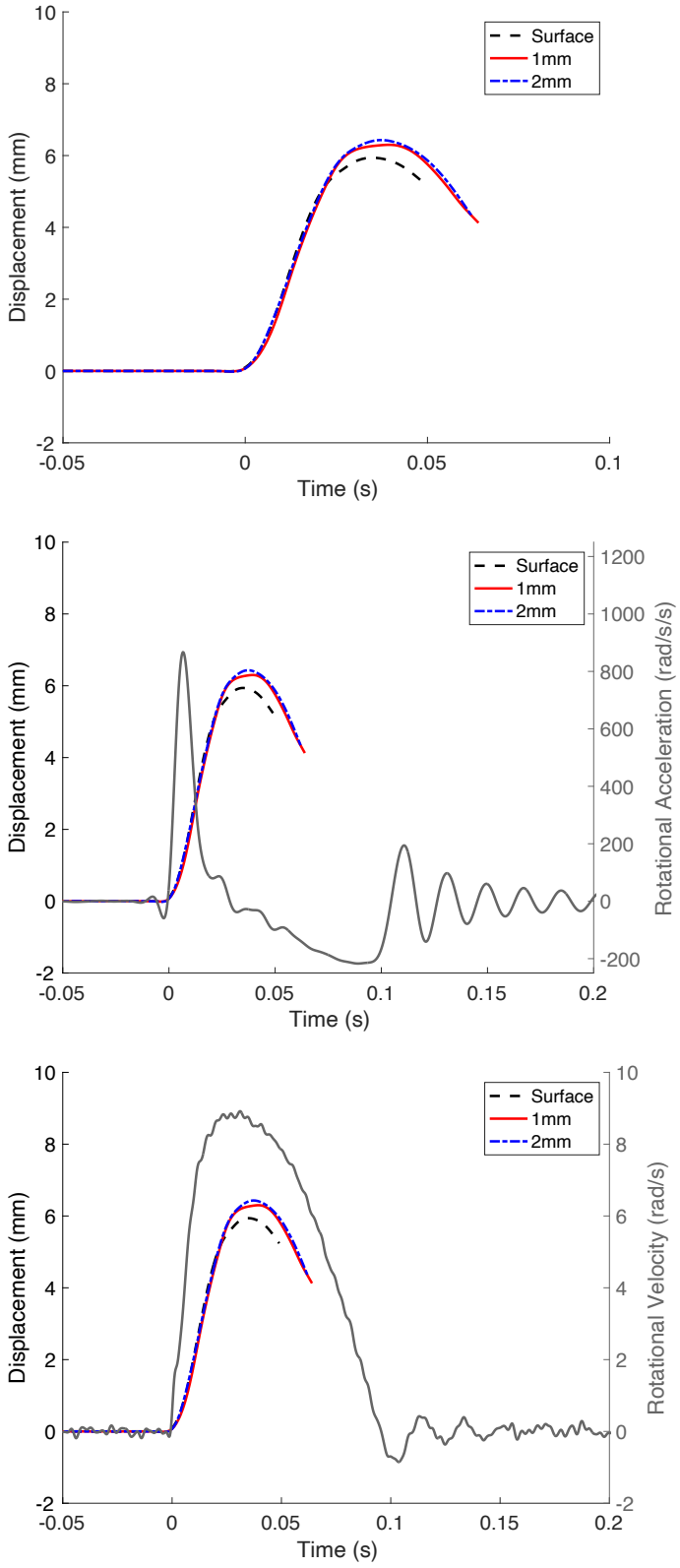

(ac) Test 33

Appendix D: Subject 3 Results

Table 30: Main matrix results for subject 3

					Displacement (mm)		
Test #	Description	Postmortem time (hours)	Rotational Acceleration (rad/s^2)	Rotational Velocity (rad/s)	Cortex Surface	1mm deep	2mm deep
2103_01	Baseline	41.97	999	8.69	3.19	4.36	3.74
2103_02	Baseline	42.20	961	8.65	3.65	4.31	3.66
2103_03	Baseline	42.39	995	8.96	3.75	4.71	3.88
2103_04	Test 1	42.57	2100	18.3	7.67	7.88	8.14
2103_05	Baseline	42.82	990	8.56	4.21	5.47	4.13
2103_06	Test 2	43.15	2581	19.6	7.76	7.92	7.85
2103_07	Baseline	43.49	1046	8.59	4.10	5.84	4.22
2103_08	Test 3	44.04	1898	24.1	8.59	8.71	8.46
2103_09	Baseline	44.42	779	8.34	4.05	4.68	4.14
2103_10	Test 4	44.80	2262	22.7	9.09	9.41	9.81
2103_11	Baseline	45.24	999	8.72	4.00	4.34	3.91

Table 31: Post-test matrix results for subject 3

					Displacement (mm)		
Test #	Description	Postmortem time (hours)	Rotational Acceleration (rad/s^2)	Rotational Velocity (rad/s)	Cortex Surface	1mm deep	2mm deep
2103_12	Post-test 1	45.79	2262	19.2	6.79	8.29	7.96
2103_13	Baseline	46.17	766	8.67	3.57	3.86	3.53
2103_14	Post-test 2	46.69	2715	27.3	8.60	9.57	8.27
2103_15	Baseline	47.15	752	8.81	3.81	3.83	3.57
2103_16	Post-test 3	47.78	2401	19.6	8.83	8.84	9.21
2103_17	Baseline	48.39	997	8.54	4.57	5.05	4.54
2103_18	Post-test 4	48.61	3021	28.4	10.29	13.77	11.20
2103_19	Baseline	48.84	1100	8.65	4.19	4.71	4.04

Table 32: Comparison of baseline results for subject 3

					Displacement (mm)		
Test #	Description	Postmortem time (hours)	Rotational Acceleration (rad/s^2)	Rotational Velocity (rad/s)	Cortex Surface	1mm deep	2mm deep
2103_01	Baseline	41.97	999	8.69	3.19	4.36	3.74
2103_02	Baseline	42.20	961	8.65	3.66	3.89	3.60
2103_03	Baseline	42.39	995	8.96	3.75	4.71	3.88
2103_05	Baseline	42.82	990	8.56	4.21	5.47	4.13
2103_07	Baseline	43.49	1046	8.59	4.10	5.84	4.22
2103_09	Baseline	44.42	779	8.34	4.05	4.68	4.14
2103_11	Baseline	45.24	766	8.72	4.00	4.34	3.91
2103_13	Baseline	46.17	752	8.67	3.57	3.86	3.53
2103_15	Baseline	47.15	997	8.81	3.81	3.83	3.57
2103_17	Baseline	48.39	1100	8.54	4.57	5.05	4.54
2103_19	Baseline	48.84	903	8.65	4.19	4.71	4.04
		Average	**935**	**8.65**	**3.94**	**4.69**	**3.97**
		Std. dev.	**119**	**0.16**	**0.38**	**0.64**	**0.31**
		% CV	**12.8**	**1.82**	**9.69**	**13.74**	**7.84**

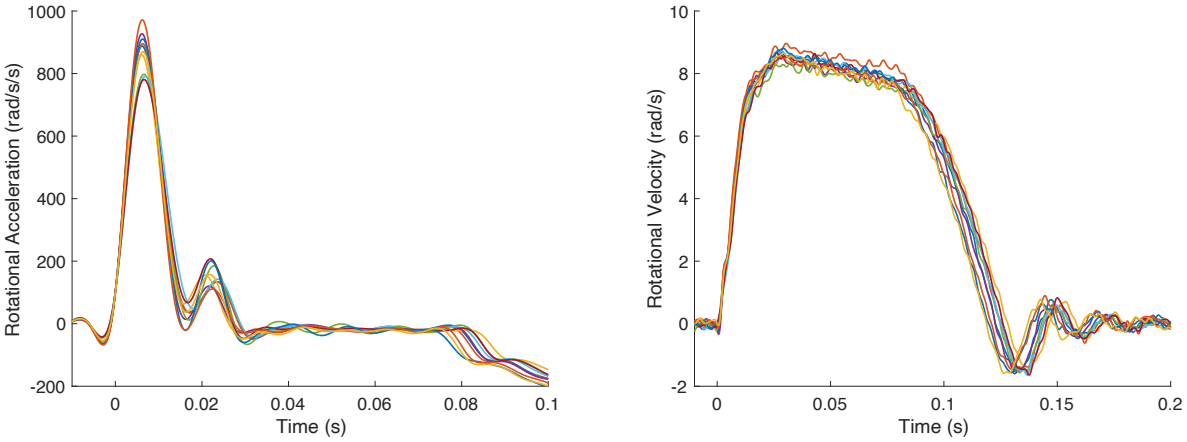

Figure 75: Comparison of baseline kinematics for subject 3

The spread of displacement values for the baselines tests at each tracked location is shown graphically in a boxplot in Figure 76. On average, peak displacements tracked at the cortex surface were the smallest, while peak displacement tracked 1mm deep in the cortex were the largest.

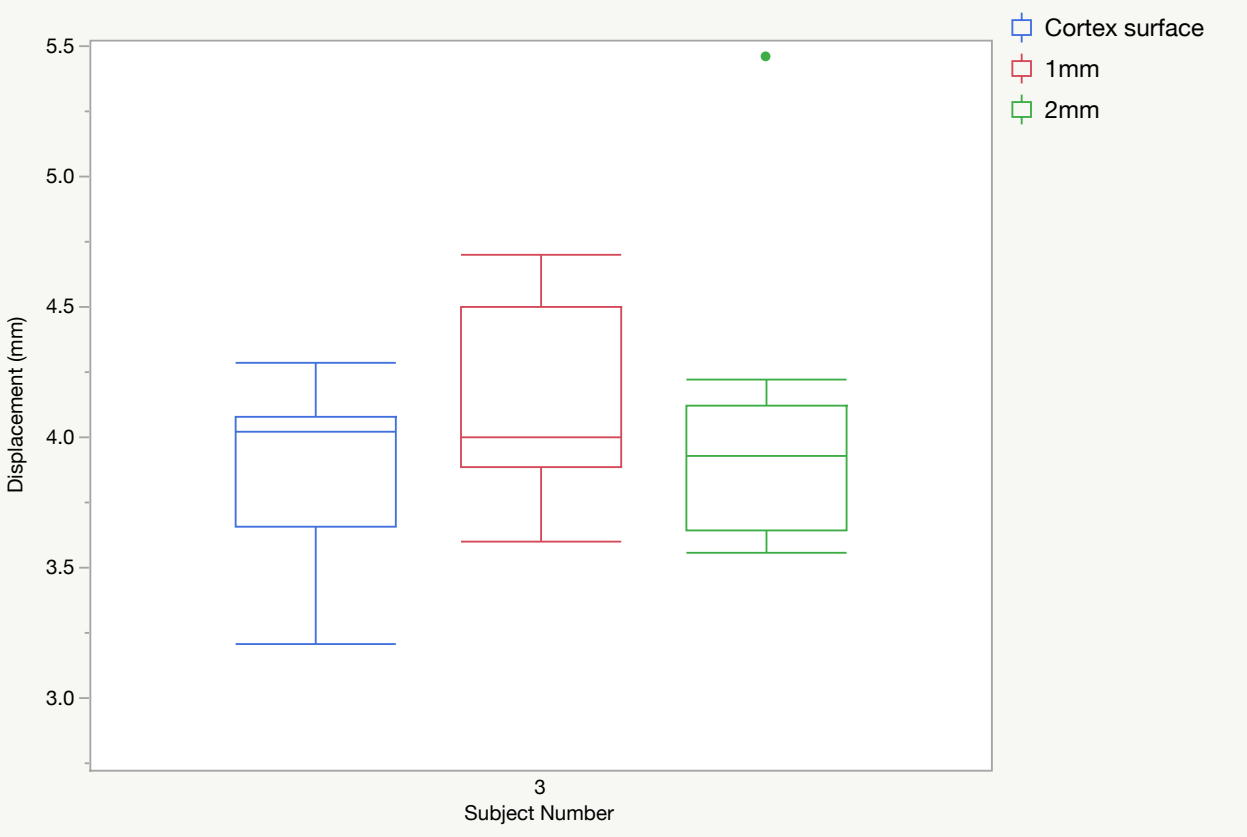

Figure 76: Boxplot of subject 3 baseline peak displacements at the three tracked locations

Table 33: Linear regression results for subject 3 displacements versus postmortem time, rotational velocity, and rotational acceleration

	Postmortem time	Rotational Velocity	Rotational Acceleration
	R^2		
Cortex surface	0.16	0. 19	0.00
1 mm deep	0.01	0.07	0.33
2 mm deep	0.22	0.14	0.34
*Indicates statistical significance ($p<0.05$)			

Table 34: Multiple regression summary statistics for subject 3

	Analysis of Variance		**Summary of Fit**		**Parameter Estimates**			
					intercept	**Postmortem time (hours)**	**Rotational Velocity (rad/s)**	**Rotational Acceleration (rad/s/s)**
	F-ratio	**df**	**Adjusted R^2**	**RMSE**	**estimate (p-value)**			
Cortex surface	<0.001*	18	0.947	0.550	0.114 (0.996)	0.0260 (0.662)	0.223 (<0.001*)	0.0009 (0.0318*)
1mm	<0.001*	18	0.905	0.838	-0.786 (0.844)	0.0535 (0.555)	0.217 (0.0038*)	0.00119 (0.0483*)
2mm	<0.001*	18	0.946	0.604	1.581 (0.584)	-0.0106 (0.870)	0.186 (0.001*)	0.0010 (0.0026*)
*Indicates statistical significance ($p<0.05$)								

The multiple regression analysis was statistically significant for all three locations tracked as evidenced by the F-ratio value for each test. The regressions showed a dependence of peak brain displacement on angular velocity.

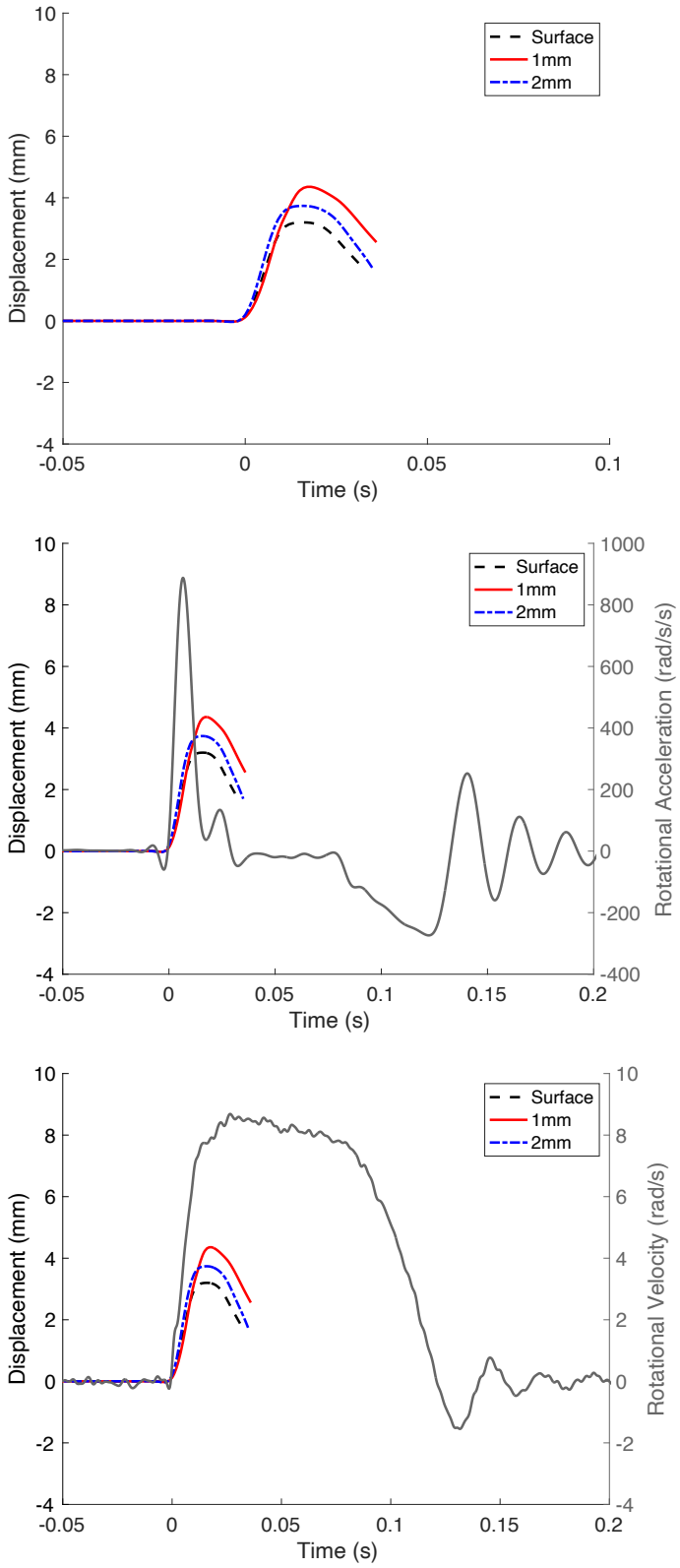

(a) Test 1

Figure 77: Time history of displacement (top), displacement compared to rotational acceleration (middle) and displacement compared to rotational velocity (bottom) for subject 3

Figure 77 continued

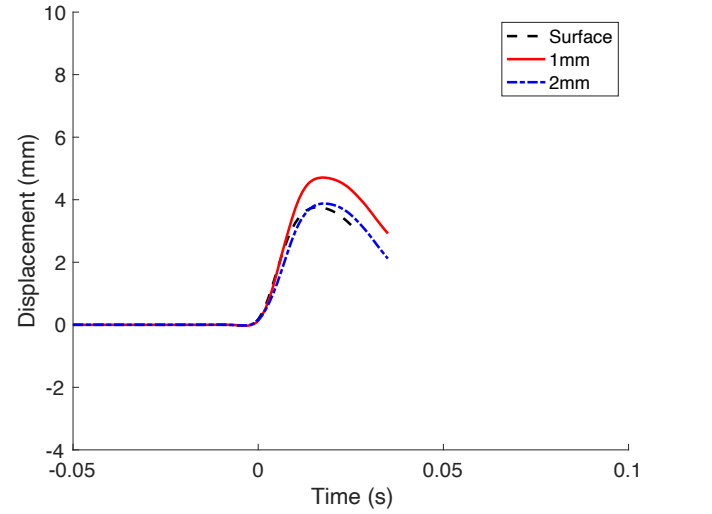

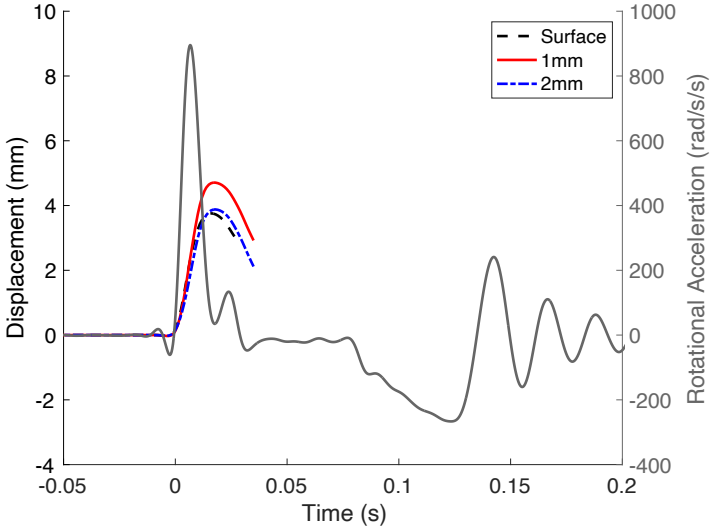

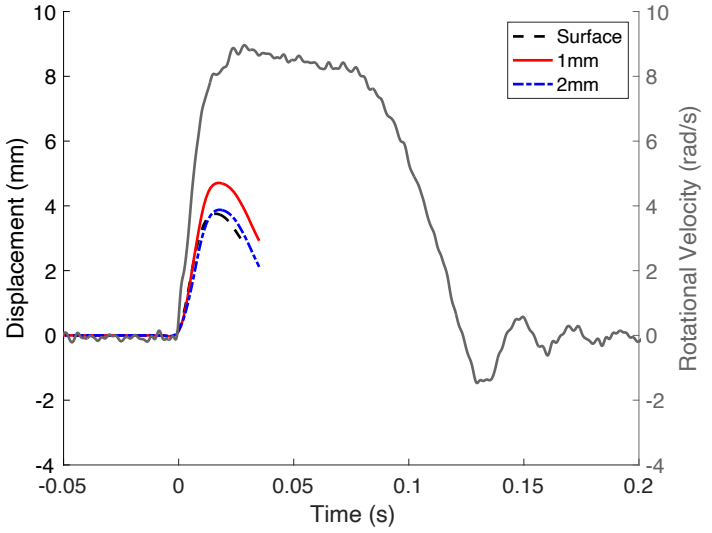

(c) Test 3

Figure 77 continued

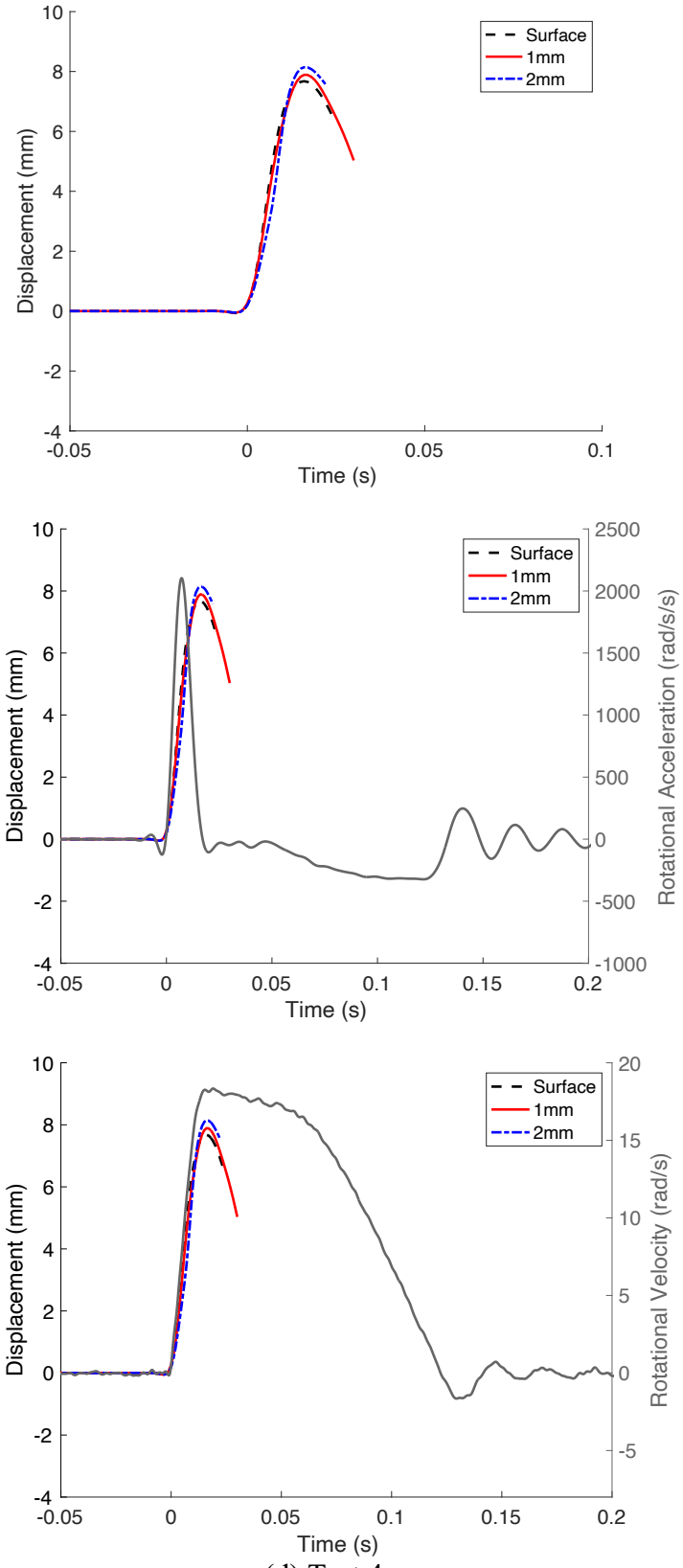

(d) Test 4

Figure 77 continued

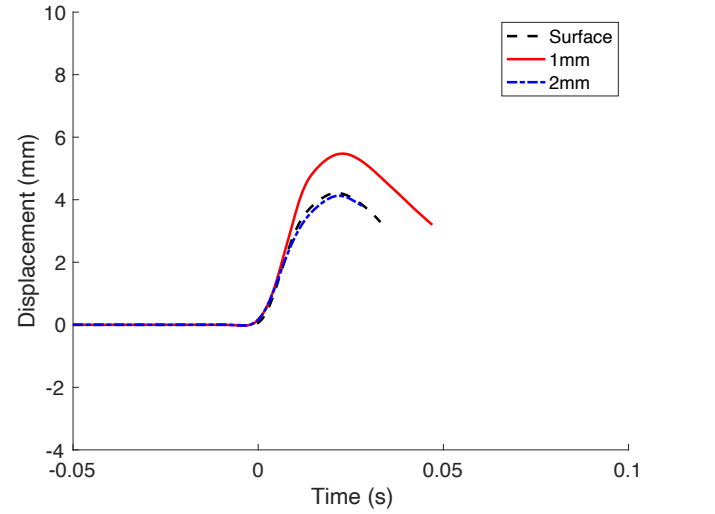

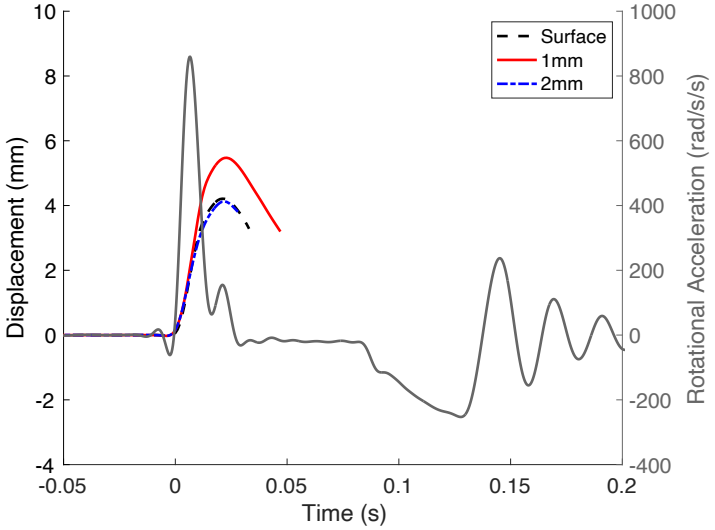

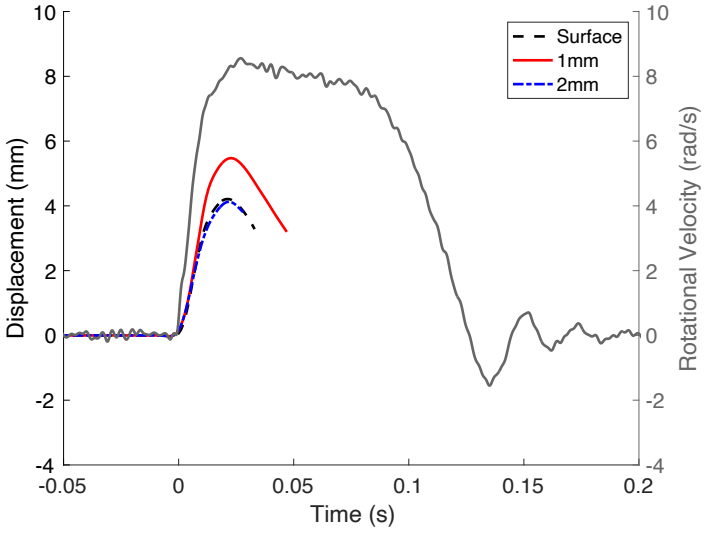

(e) Test 5

Figure 77 continued

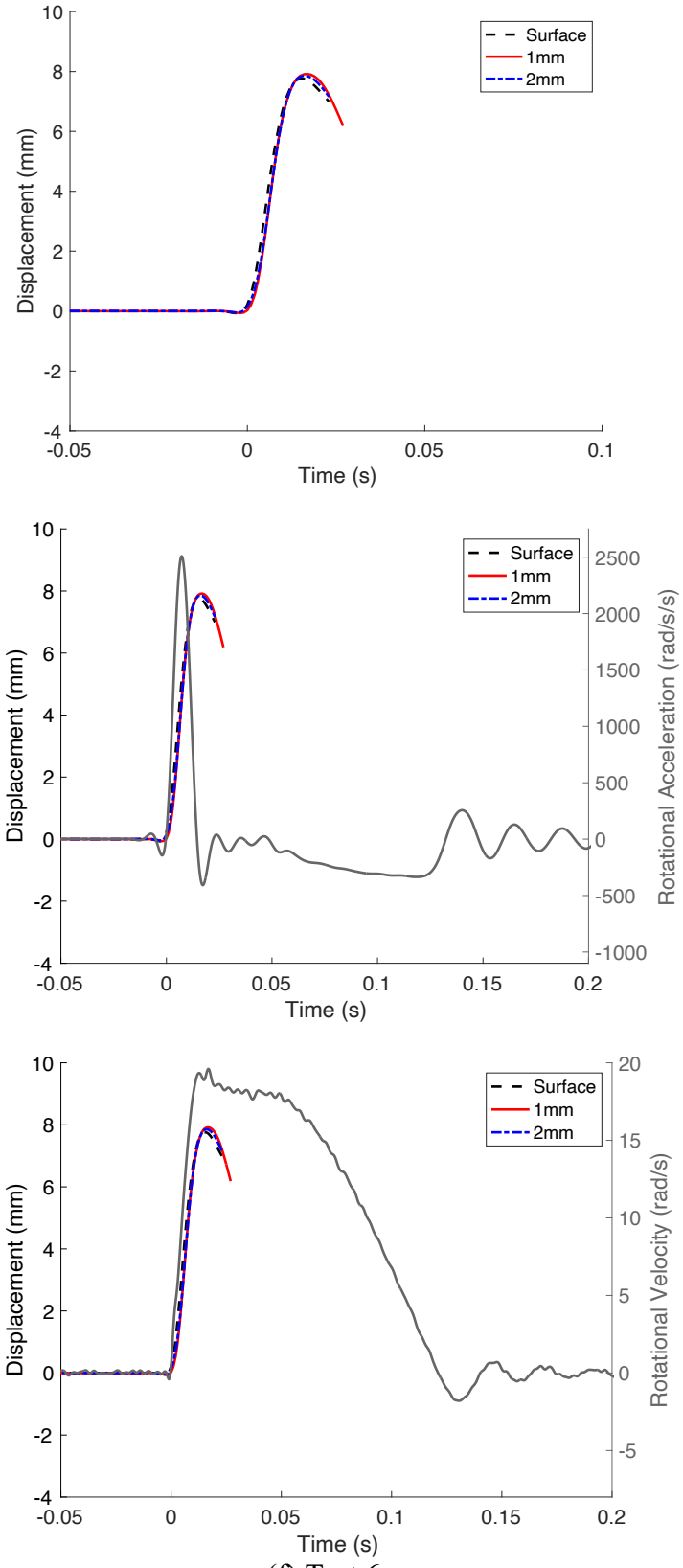

(f) Test 6

Figure 77 continued

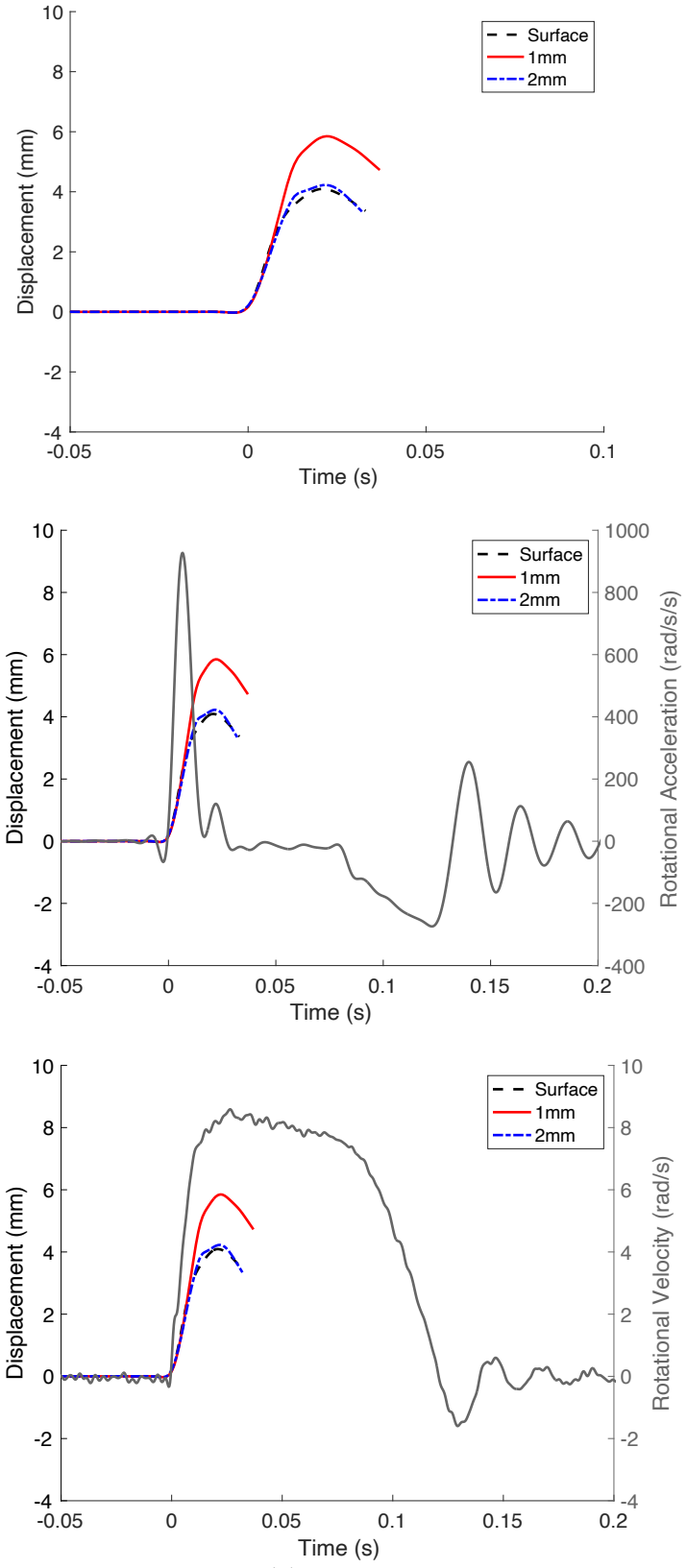

(g) Test 7

Figure 77 continued

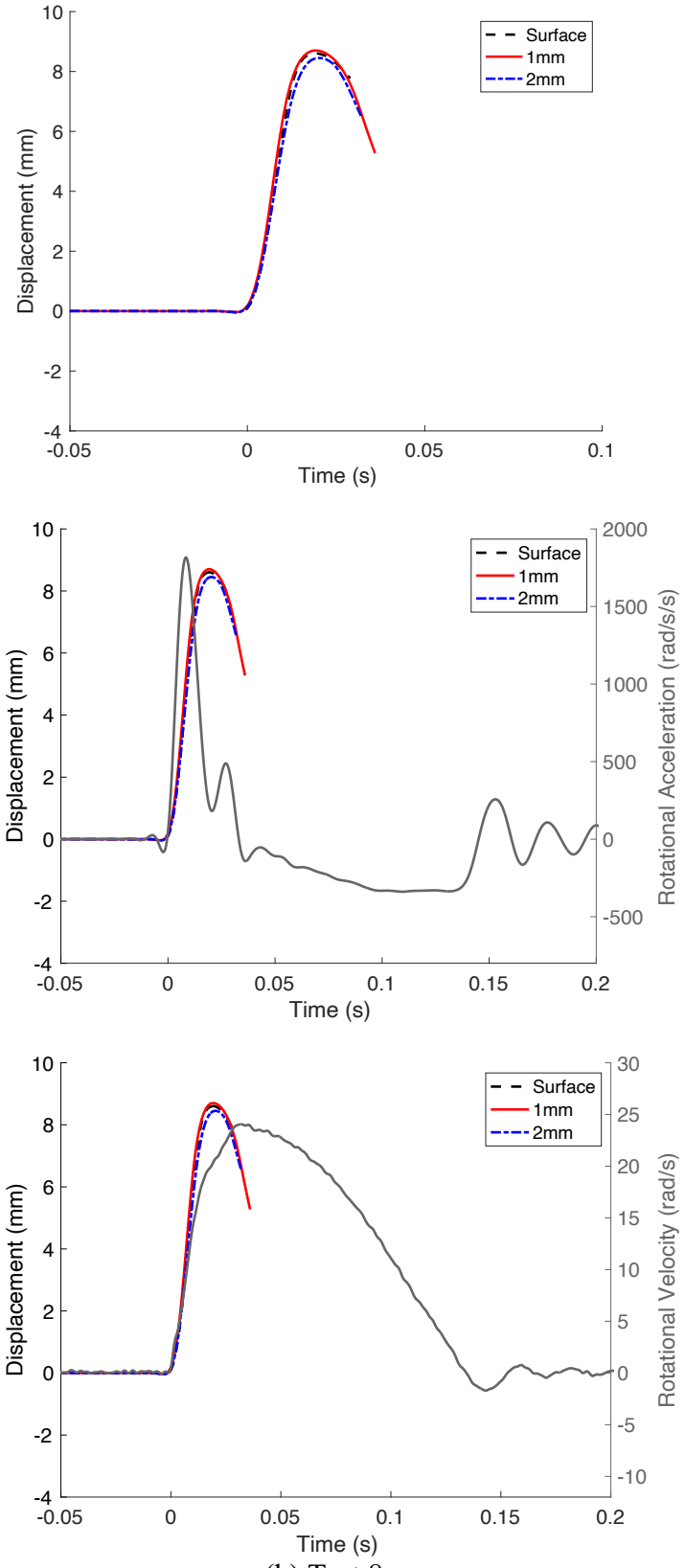

(h) Test 8

Figure 77 continued

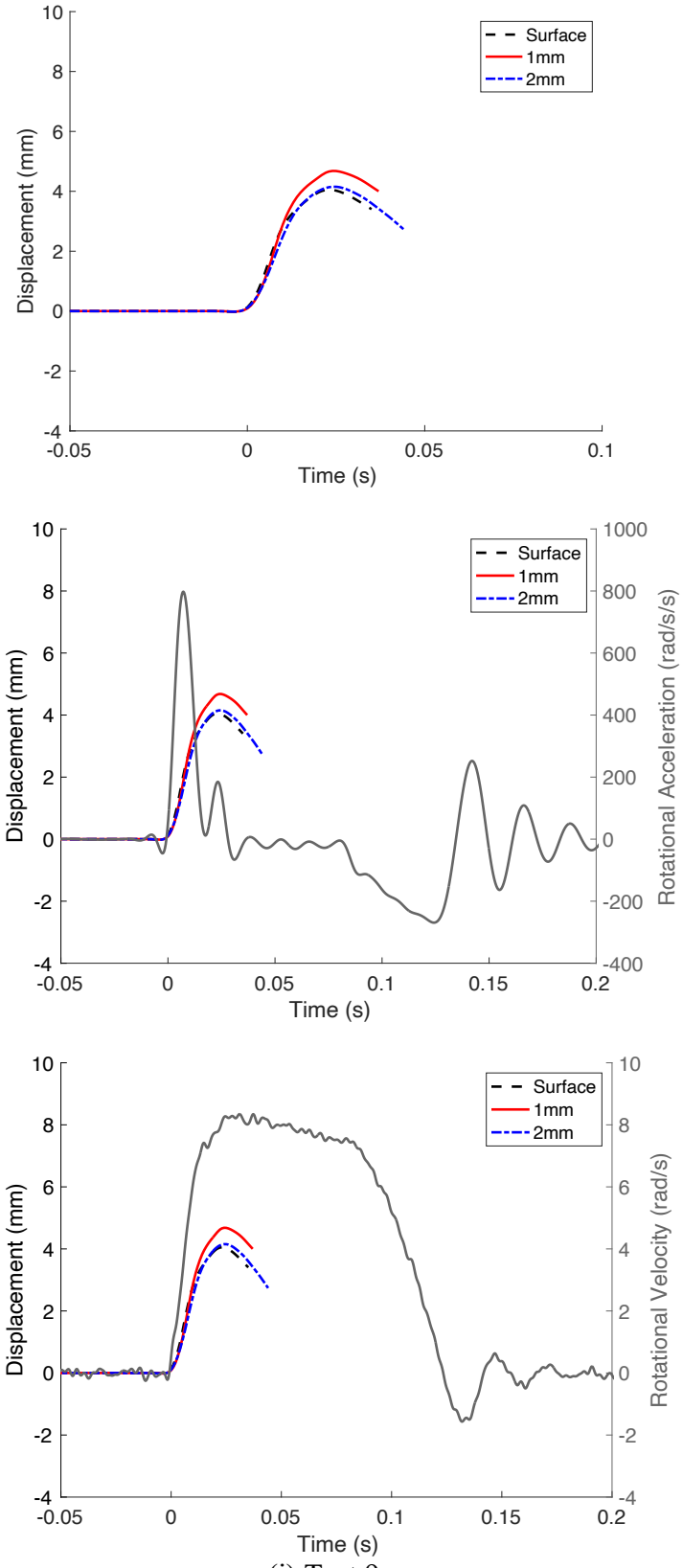

(i) Test 9

Figure 77 continued

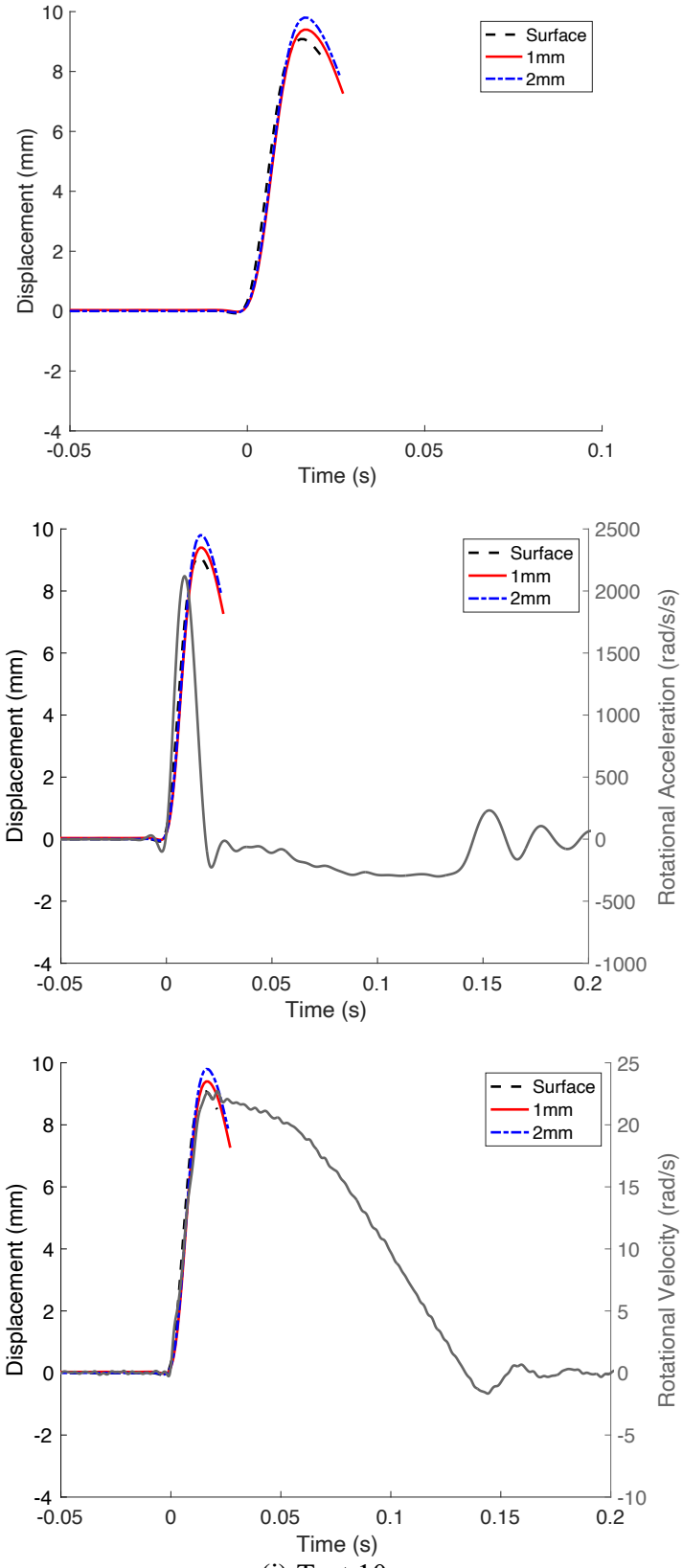

(j) Test 10

Figure 77 continued

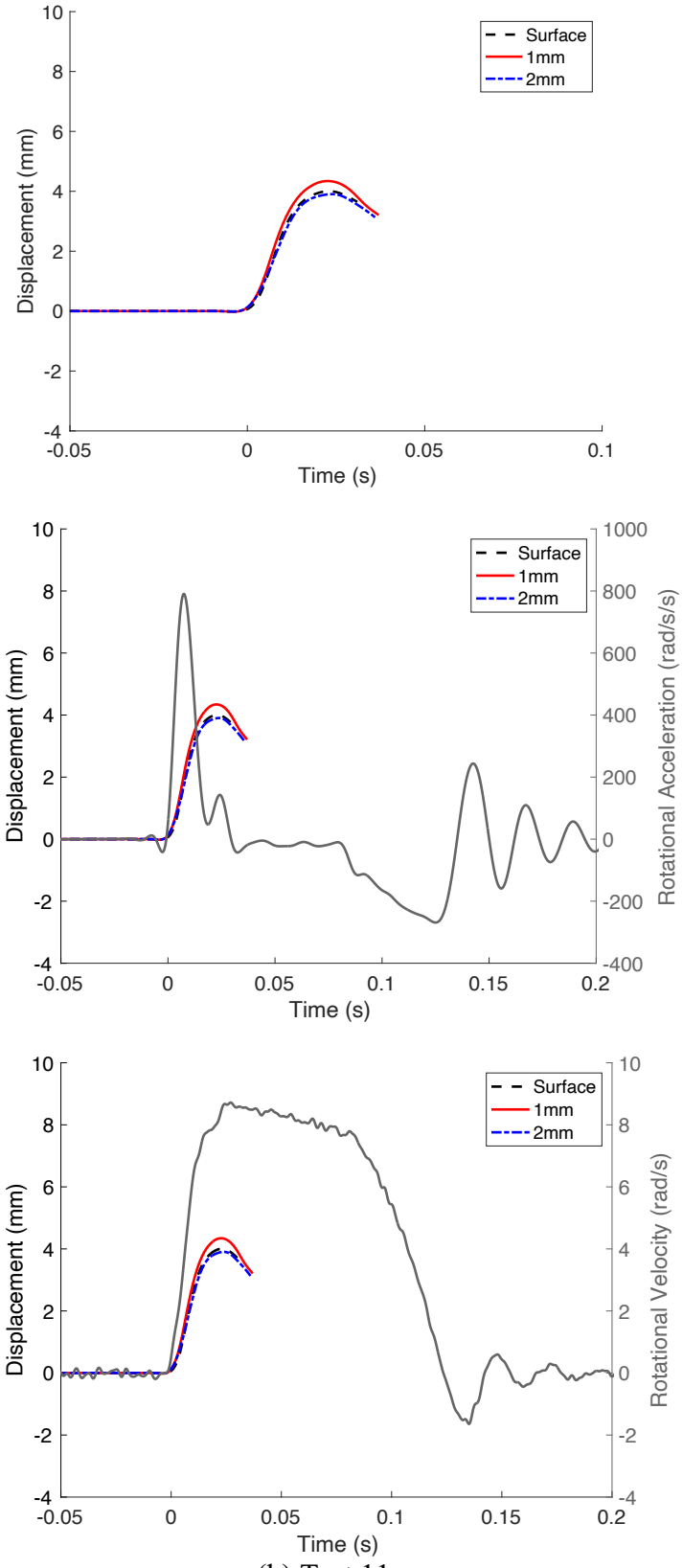

(k) Test 11

Figure 77 continued

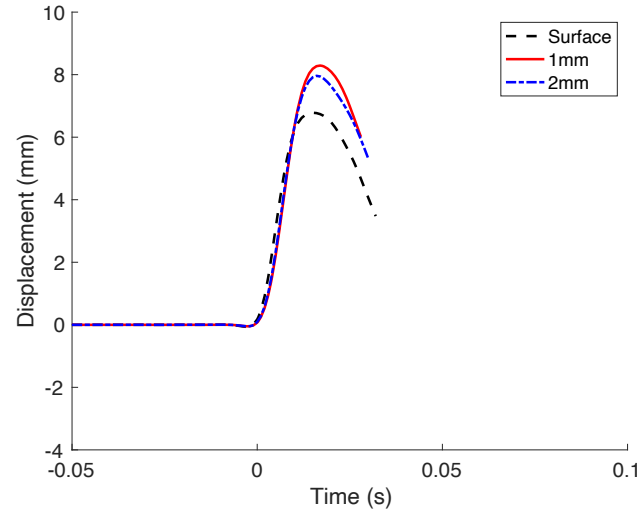

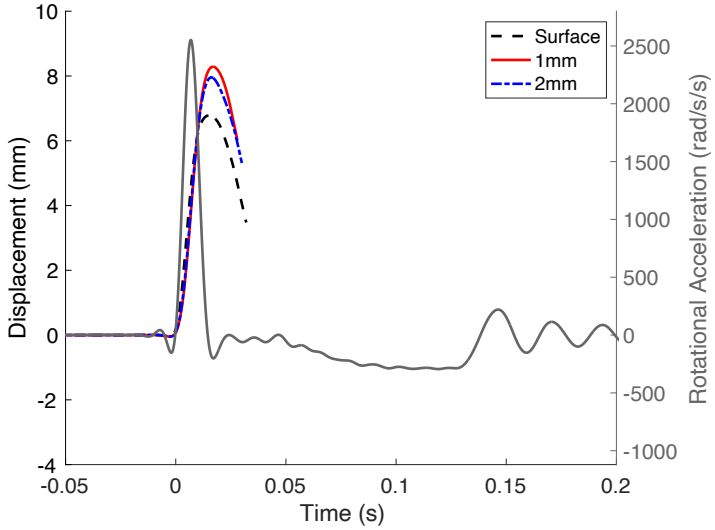

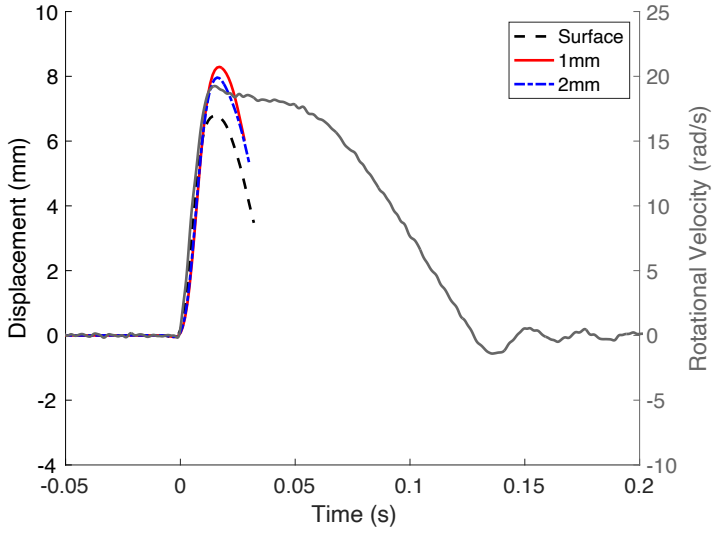

(l) Test 12

Figure 77 continued

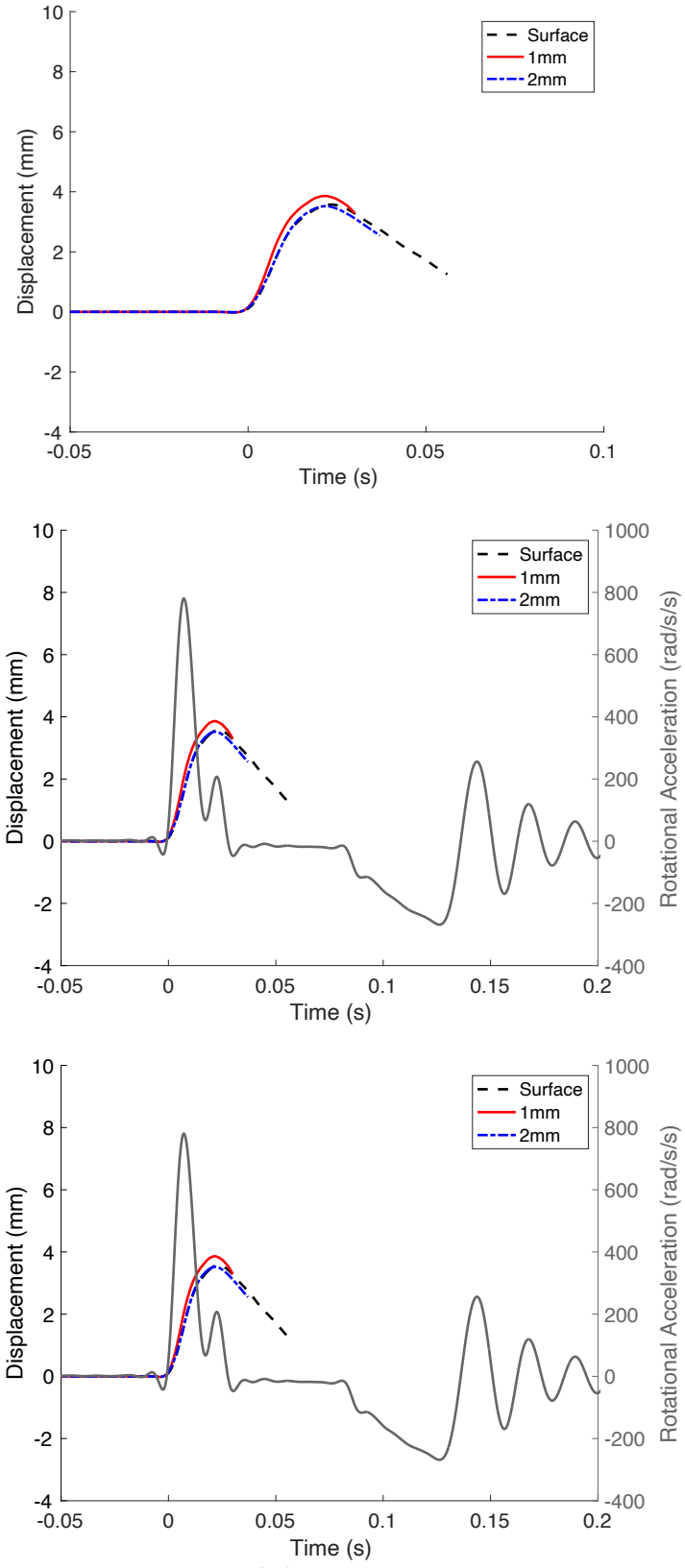

(m) Test 13

Figure 77 continued

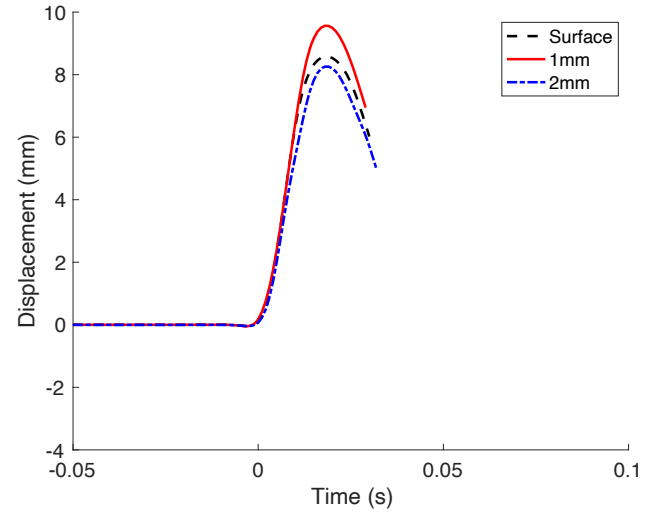

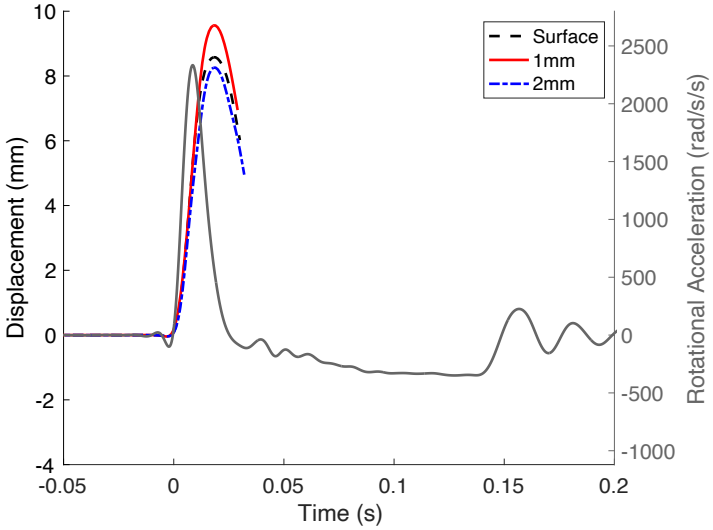

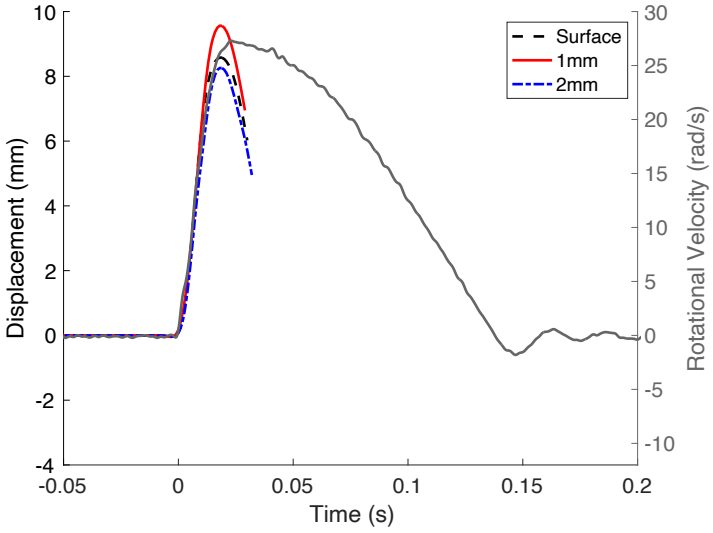

(n) Test 14

Figure 77 continued

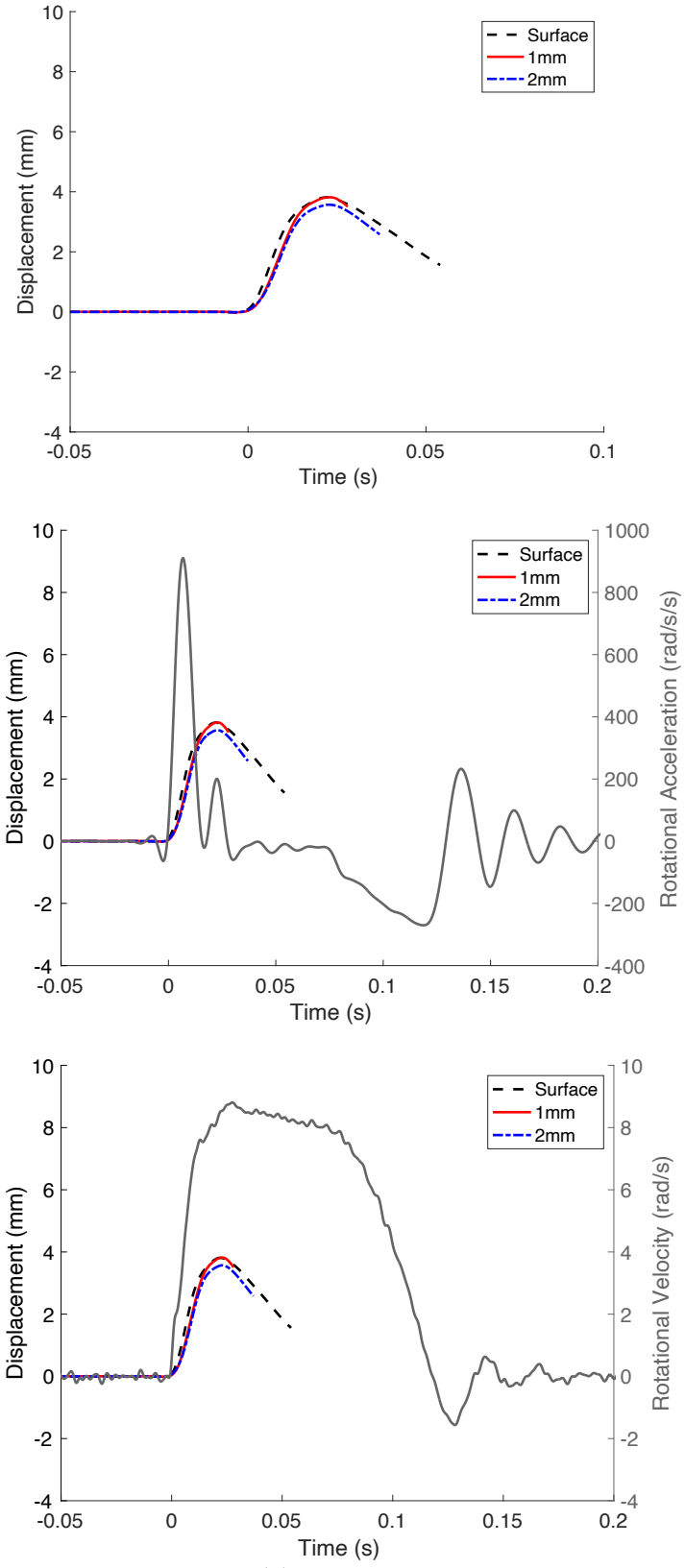

(o) Test 15

Figure 77 continued

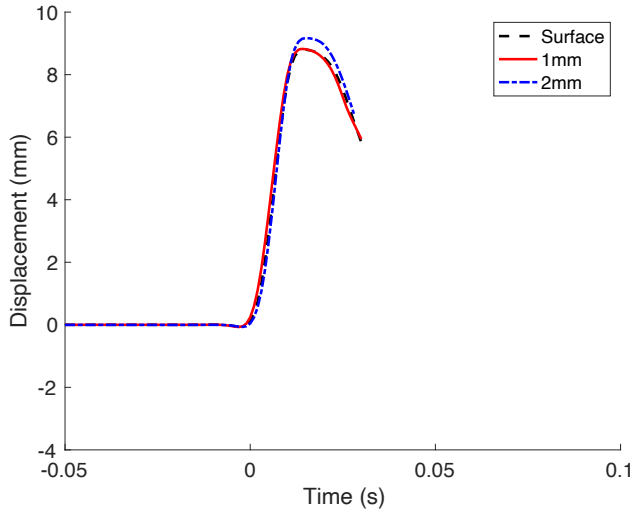

7

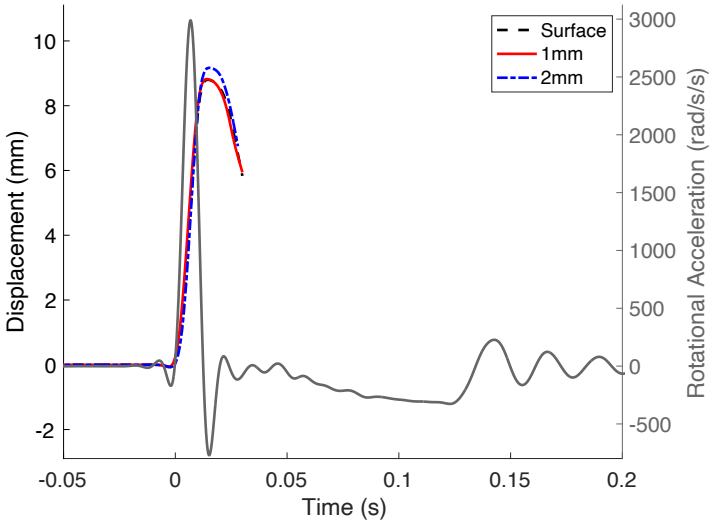

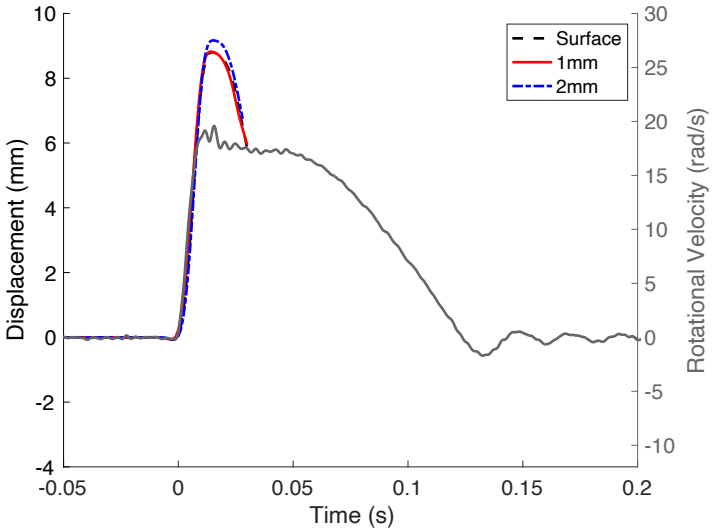

(p) Test 16

Figure 77 continued

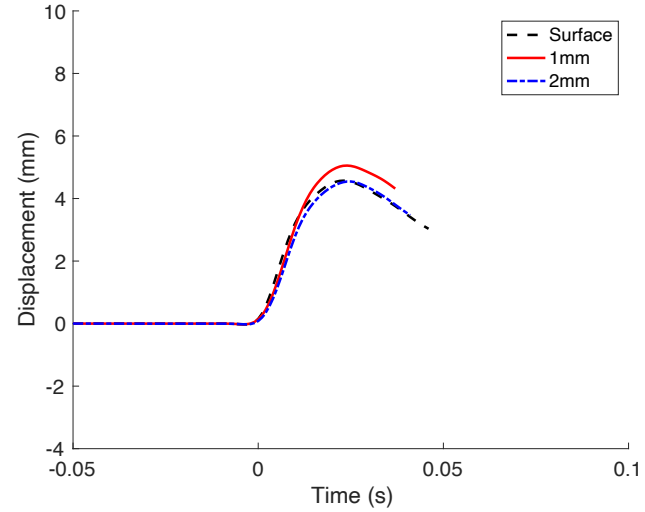

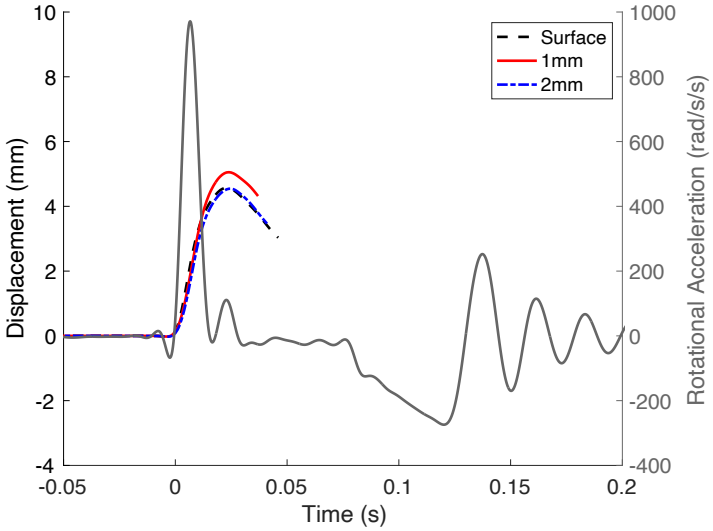

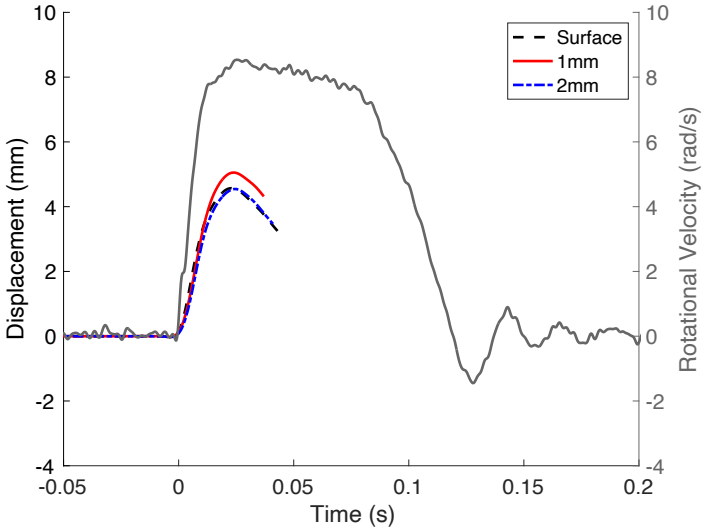

(q) Test 17

Figure 77 continued

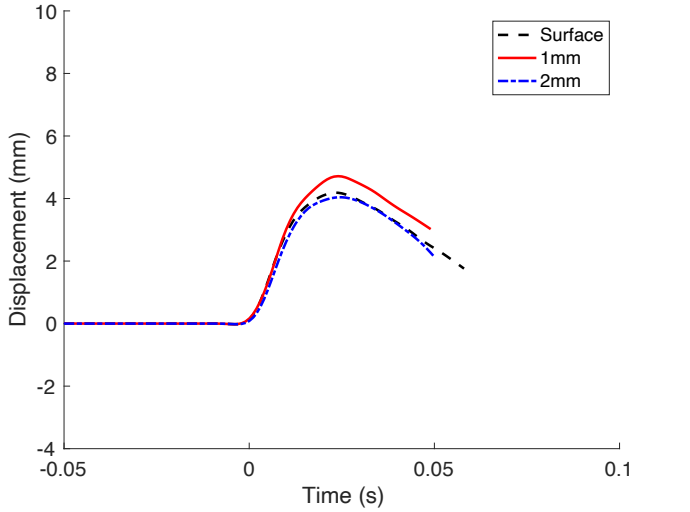

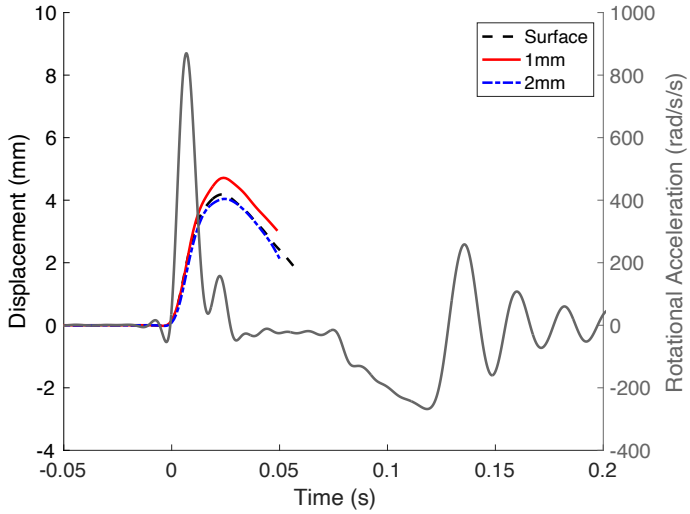

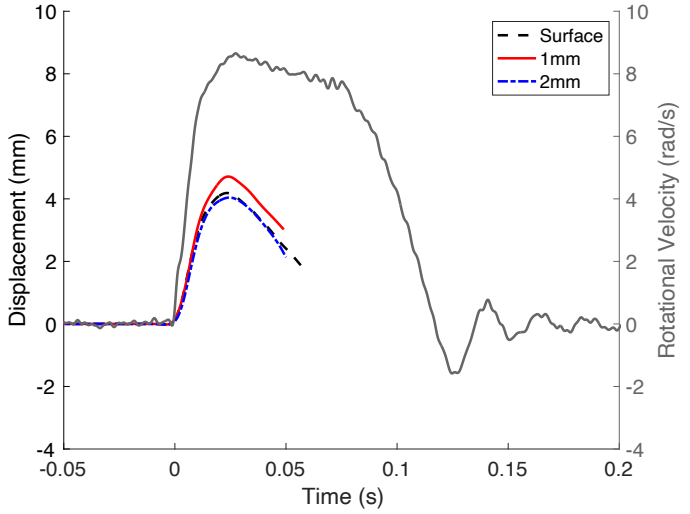

(s) Test 19

Appendix E: Subject 4 Results

Table 35: Main matrix results for subject 4

					Displacement (mm)		
Test #	Description	Postmortem time (hours)	Rotational Acceleration (rad/s^2)	Rotational Velocity (rad/s)	Cortex Surface	1mm deep	2mm deep
2104_01	Baseline	27.12	913	8.47	0.133	0.284	0.349
2104_02	Test 1	27.75	3187	21.1	1.017	1.326	1.553
2104_03	Baseline	28.15	852	8.49	0.099	0.265	0.330
2104_04	Test 2	29.03	3485	30.5	1.647	1.884	2.115
2104_05	Baseline	29.42	999	9.02	0.186	0.408	0.390
2104_06	Test 3	29.70	4541	26.4	1.371	1.710	1.876
2104_07	Baseline	30.05	821	8.40	0.177	0.298	0.350
2104_08	Test 4	30.45	4103	33.0	1.535	1.906	1.993
2104_09	Baseline	30.98	765	8.77	0.183	0.359	0.398

Table 36: Post-test matrix results for subject *4*

					Displacement (mm)		
Test #	Description	Postmortem time (hours)	Rotational Acceleration (rad/s^2)	Rotational Velocity (rad/s)	Cortex Surface	1mm deep	2mm deep
2104_10	Post-test 1	31.63	2290	19.3	0.523	0.825	0.843
2104_11	Baseline	31.80	896	8.38	0.216	0.381	0.365
2104_12	Post-test 2	31.98	2407	20.8	0.649	0.859	0.981
2104_13	Post-test 3	32.58	1100	22.5	0.452	0.761	0.809
2104_14	Baseline	32.77	2208	8.64	0.175	0.356	0.362
2104_15	Post-test 4	33.32	989	22.2	0.787	1.028	1.241
2104_16	Baseline	33.62	2793	8.61	0.187	0.267	0.436
2104_17	Post-test 5	33.88	1042	31.7	1.146	1.587	1.786
2104_18	Post-test 6	34.15	5173	32.0	1.715	1.858	2.041

Table 37: Comparison of baseline results for subject 4

					Displacement (mm)		
Test #	Description	Postmortem time (hours)	Rotational Acceleration (rad/s^2)	Rotational Velocity (rad/s)	Cortex Surface	1mm deep	2mm deep
2104_01	Baseline	27.12	913	8.47	0.133	0.284	0.349
2104_03	Baseline	28.15	852	8.49	0.099	0.265	0.330
2104_05	Baseline	29.42	999	9.02	0.186	0.408	0.390
2104_07	Baseline	30.05	821	8.40	0.177	0.298	0.350
2104_09	Baseline	30.98	765	8.77	0.183	0.359	0.398
2104_11	Baseline	31.80	896	8.38	0.216	0.381	0.365
2104_14	Baseline	32.77	1100	8.64	0.175	0.356	0.362
2104_16	Baseline	33.62	989	8.61	0.187	0.267	0.436
		Average	**917**	**2.60**	**0.170**	**0.327**	**0.373**
		Std. dev.	**108**	**0.22**	**0.036**	**0.055**	**0.034**
		% CV	**11.8**	**2.50**	**21.52**	**16.93**	**9.09**

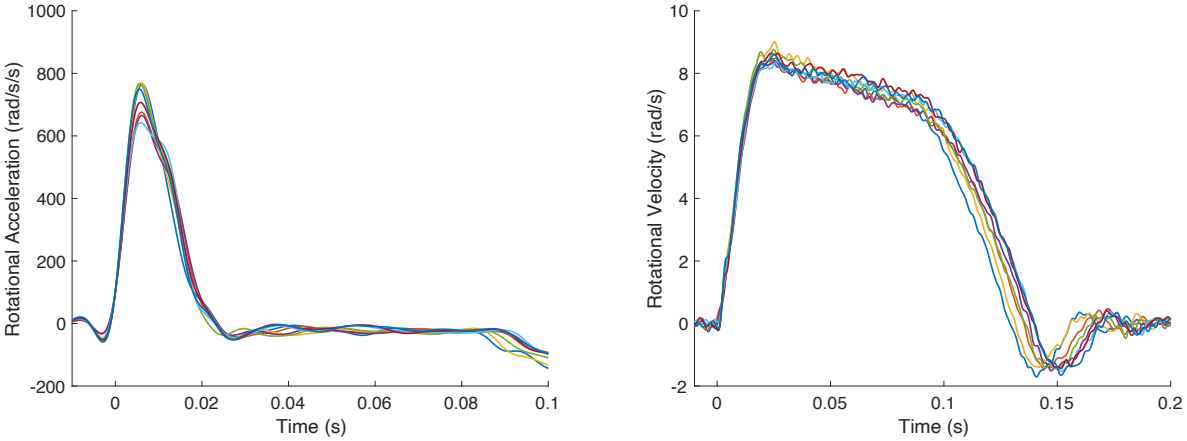

Figure 78: Comparison of baseline kinematics for subject 4

The spread of displacement values for the baselines tests at each tracked location is shown graphically in a boxplot in Figure 79. On average, peak displacements tracked at the cortex surface were the smallest, while peak displacement tracked 1mm deep in the cortex were the largest.

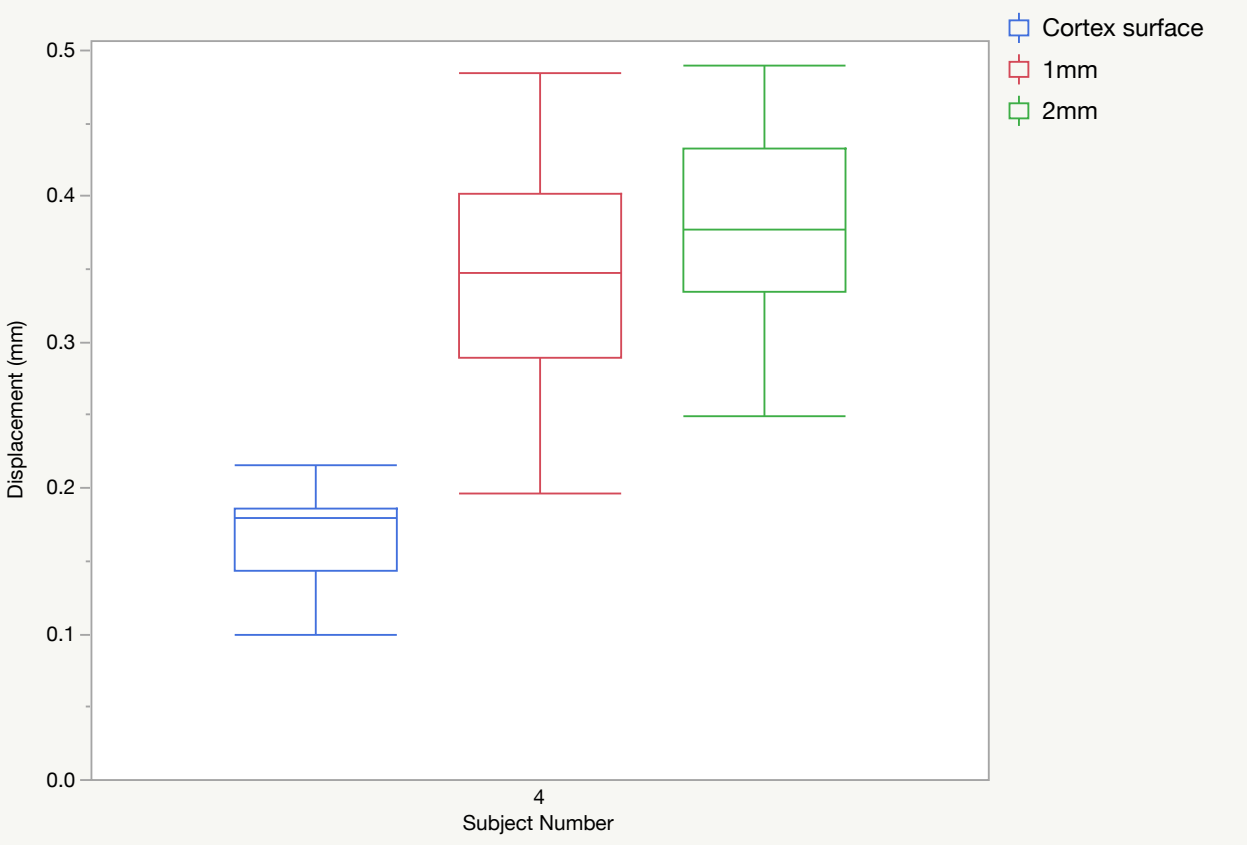

Figure 79: Boxplot of subject 4 baseline peak displacements at the three tracked locations

Table 38: Linear regression results for subject 4 displacements versus postmortem time, rotational velocity, and rotational acceleration

	Postmortem time	Rotational Velocity	Rotational Acceleration
	R^2		
Cortex surface	0.51*	0. 02	0.11
1 mm deep	0.39	0.21	0.21
2 mm deep	0.83*	0.15	0.30
*Indicates statistical significance ($p<0.05$)			

The linear regression results indicate that peak displacement is correlated with postmortem time. Rotational kinematics did not have a significant effect on the outcome of peak displacement at any tracked point location. Regressions with statistical significance are shown in Figure 80

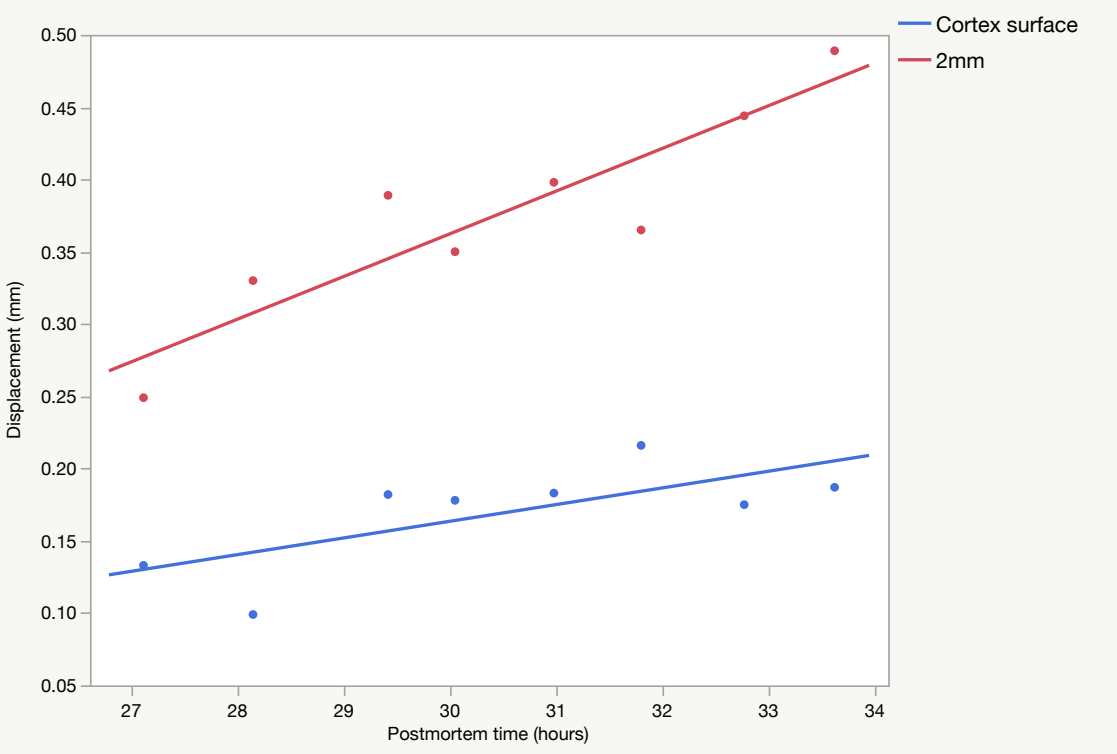

Figure 80: Statistically significant relationships for baseline data from subject 4

Additionally, the peak brain displacement for every test was utilized in a multiple linear regression to determine the dependence of brain deformation on postmortem time and angular head kinematics. The model fits had an R^2 ranging from 0.896-0.912. Coefficient values are presented in Table 40.

Table 39: Multiple regression summary statistics for subject 4

	Analysis of Variance		Summary of Fit		Parameter Estimates			
					intercept	Postmortem time (hours)	Rotational Velocity (rad/s)	Rotational Acceleration (rad/s/s)
	F-ratio	df	Adjusted R^2	RMSE	estimate (p-value)			
Cortex surface	<0.001*	17	0.907	0.177	1.207 (0.097)	-0.0485 (0.0423*)	0.0324 (0.0376*)	0.00017 (0.0728*)
1mm	<0.001*	17	0.912	0.201	0.836 (0.297)	-0.0359 (0.168)	0.0661 (0.001*)	1.705e-5 (0.0483*)
2mm	<0.001*	17	0.896	0.234	1.074 (0.252)	-0.0441 (0.148)	0.0745 (0.0014*)	-5.860e-6 (0.961)
*Indicates statistical significance ($p<0.05$)								

The multiple regression analysis was statistically significant for all three locations tracked as evidenced by the F-ratio value for each test. The regressions showed a dependence of peak brain displacement on angular velocity, and a weak but significant relationship with rotational acceleration at the cortex surface and 1 mm deep tracked locations.

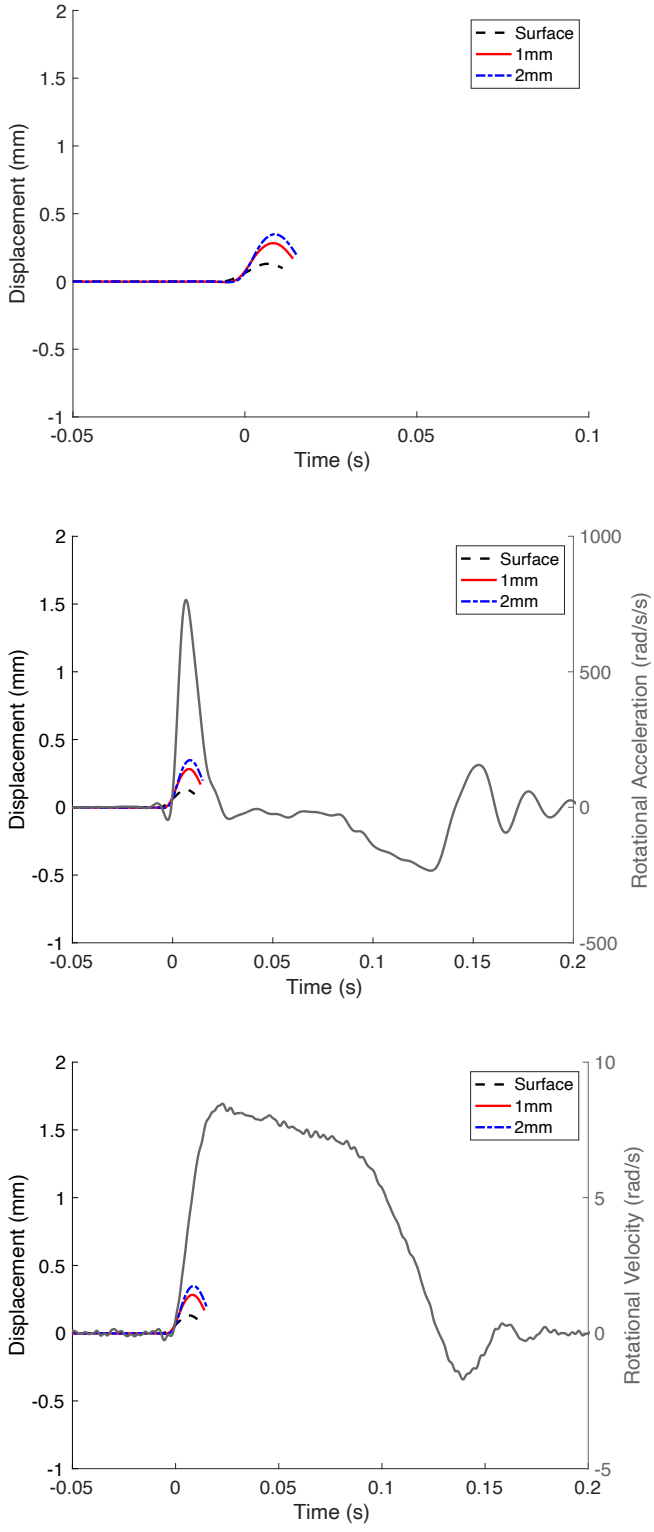

(a) Test 1

Figure 81: Time history of displacement (top), displacement compared to rotational acceleration (middle) and displacement compared to rotational velocity (bottom) for subject 4

Figure 81 continued

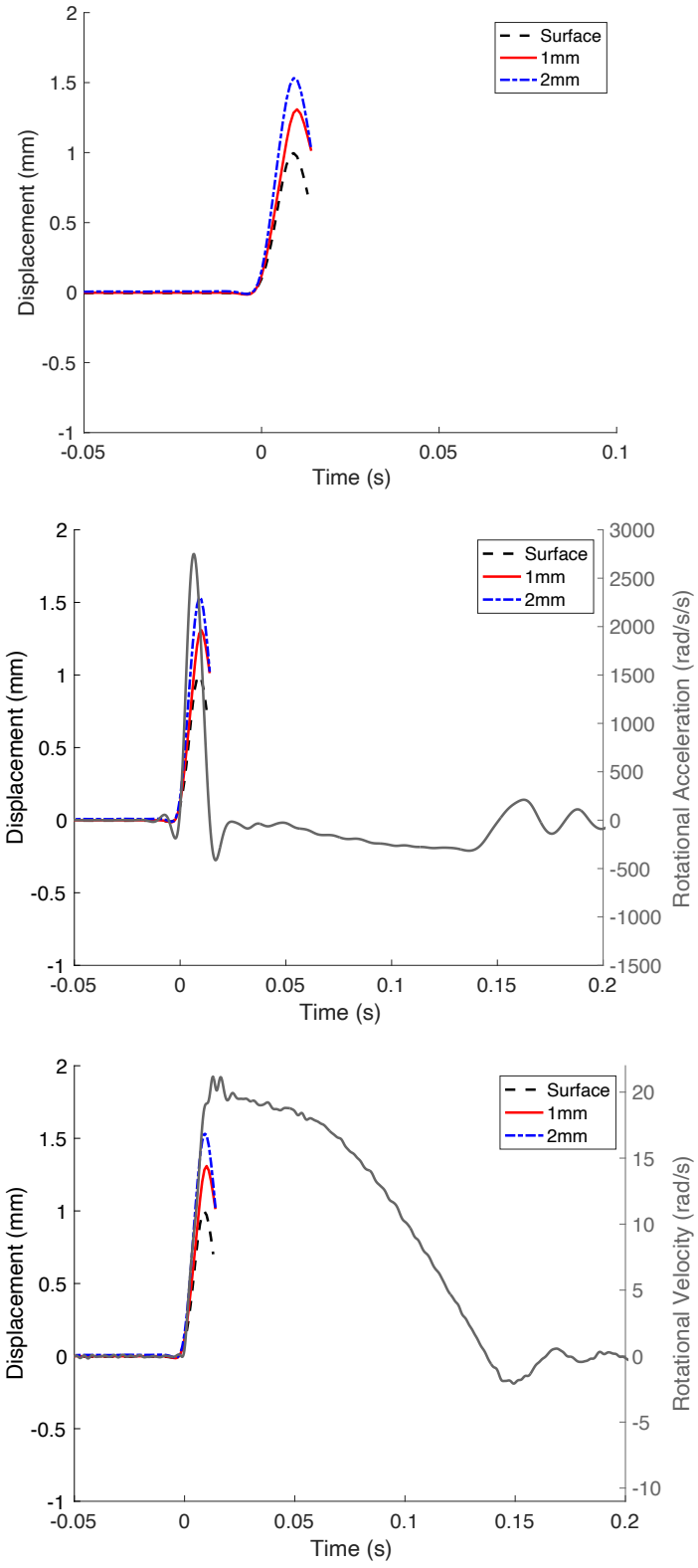

(b) Test 2

Figure 81 continued

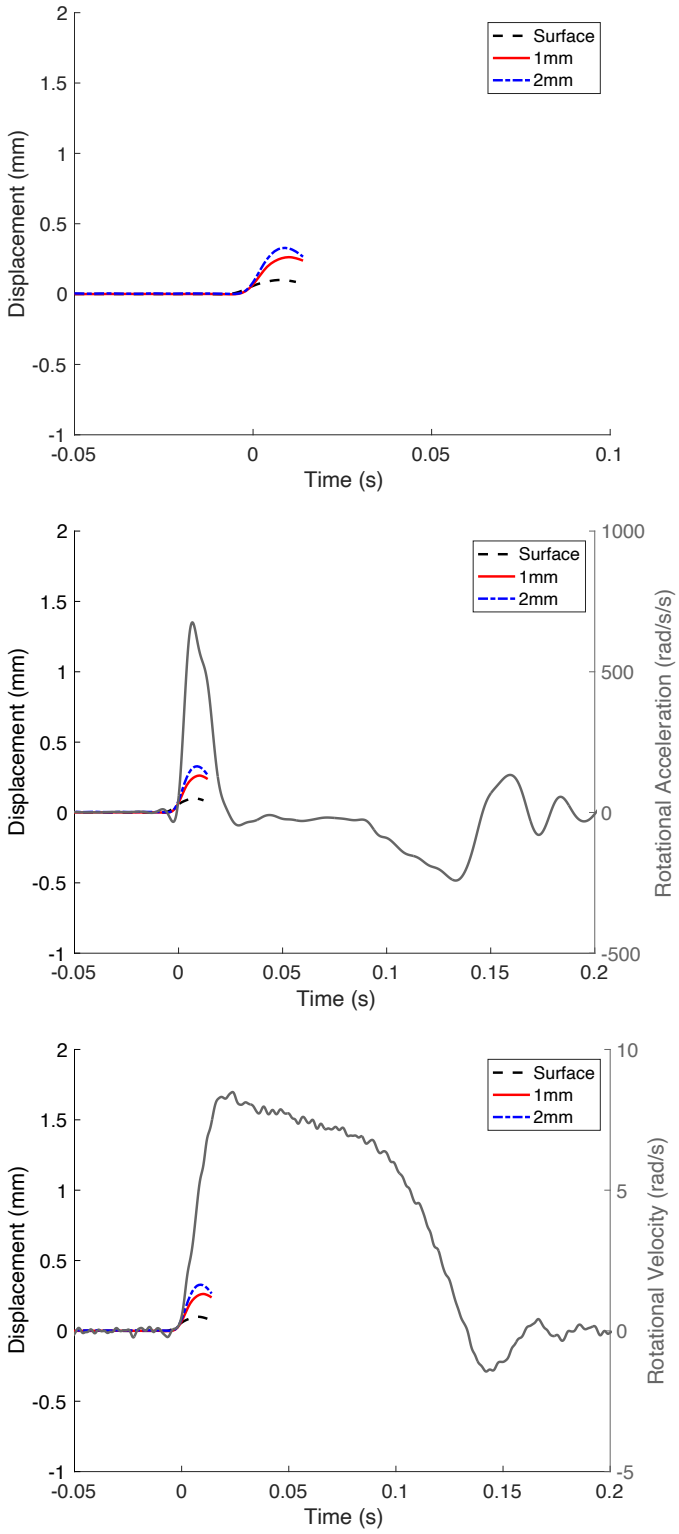

(c) Test 3

Figure 81 continued

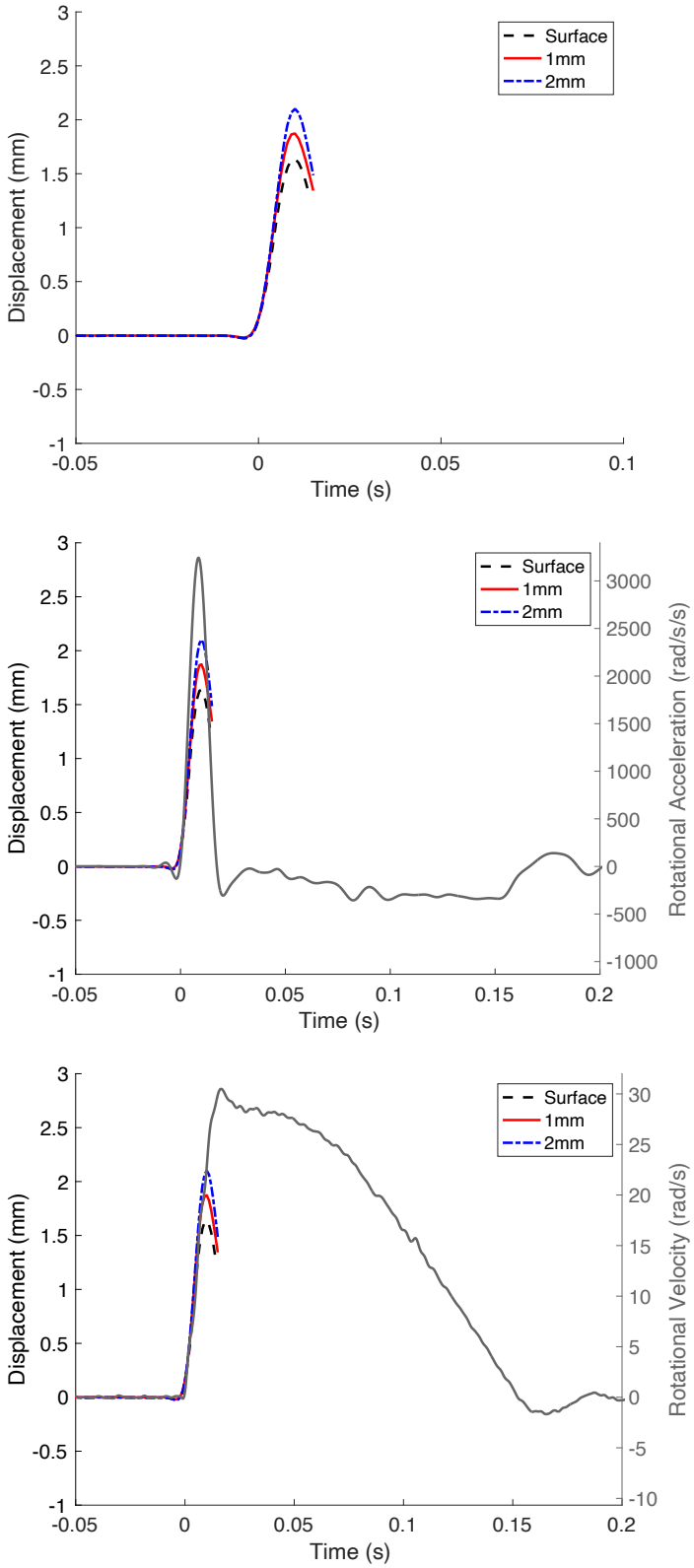

(d) Test 4

Figure 81 continued

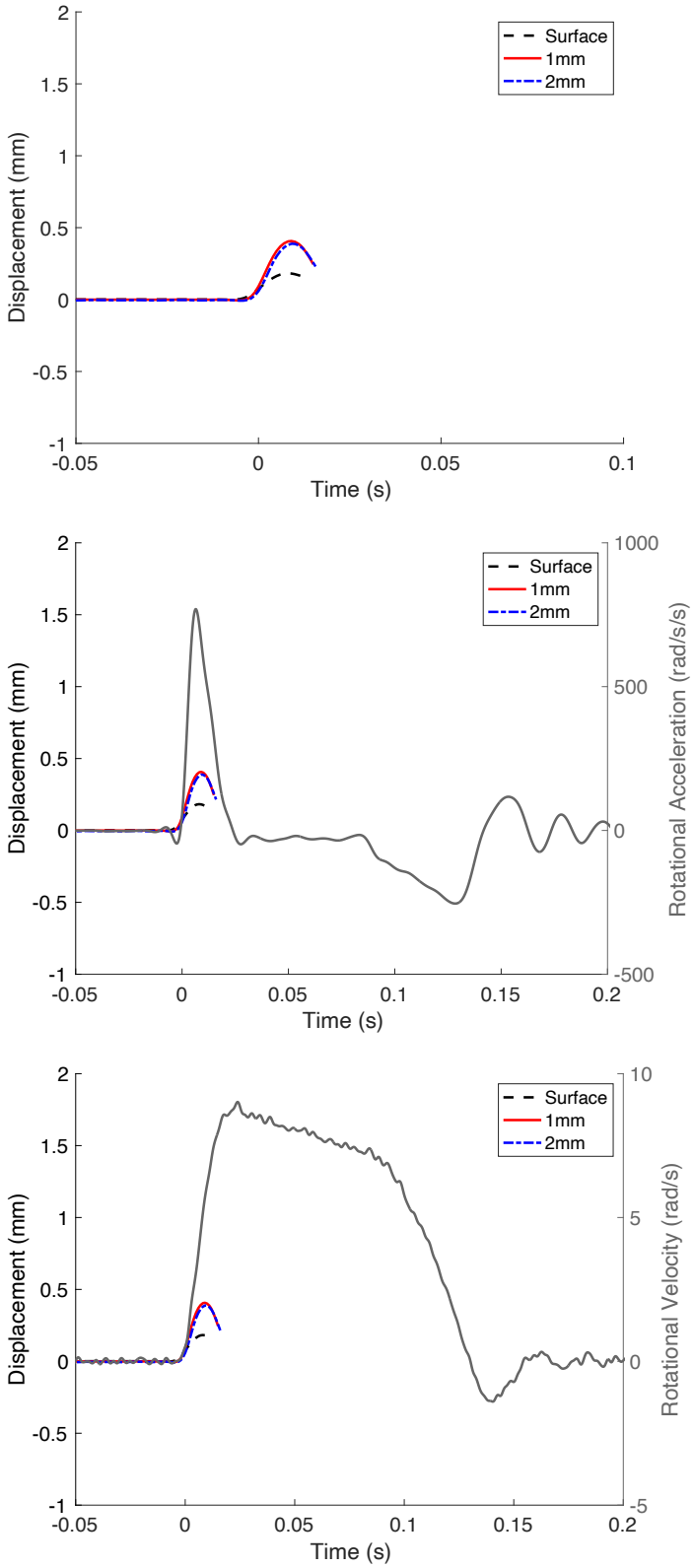

(e) Test 5

Figure 81 continued

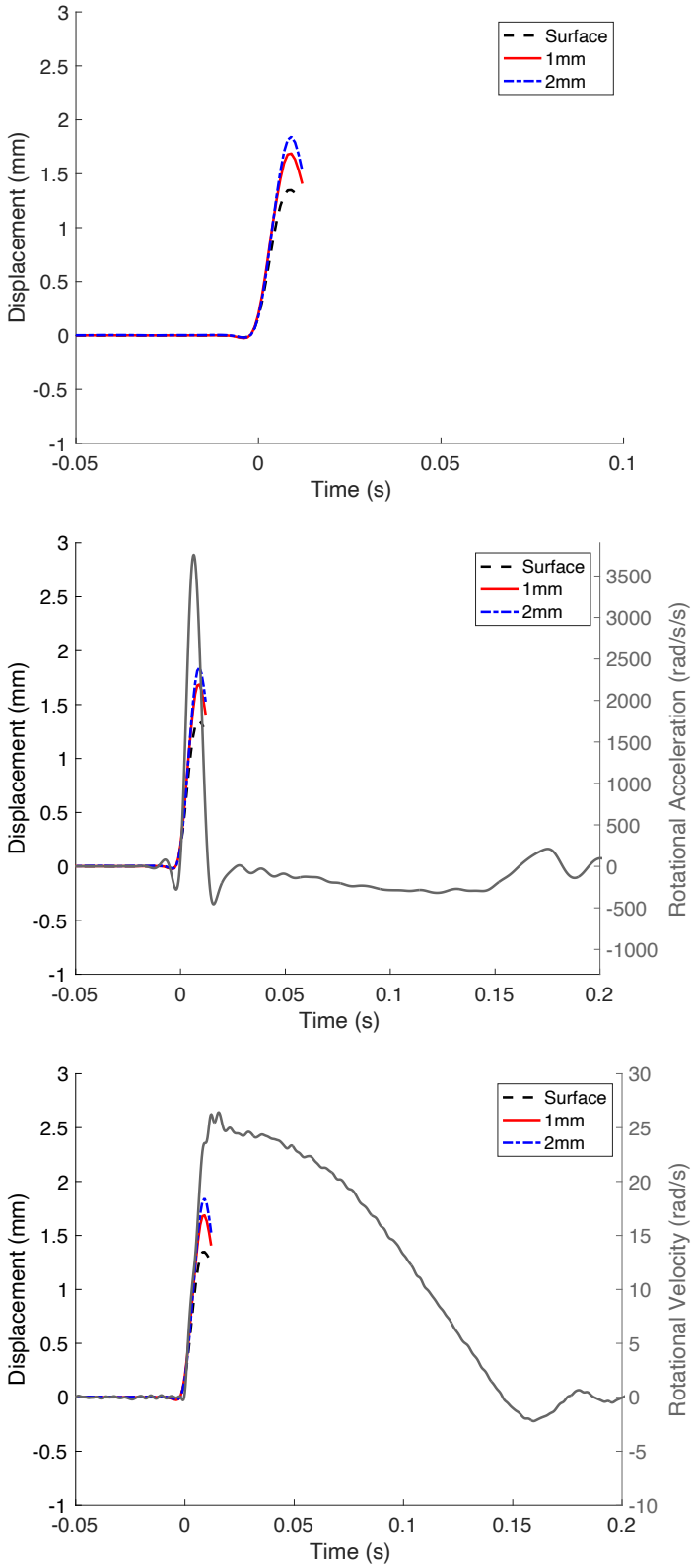

(f) Test 6

Figure 81 continued

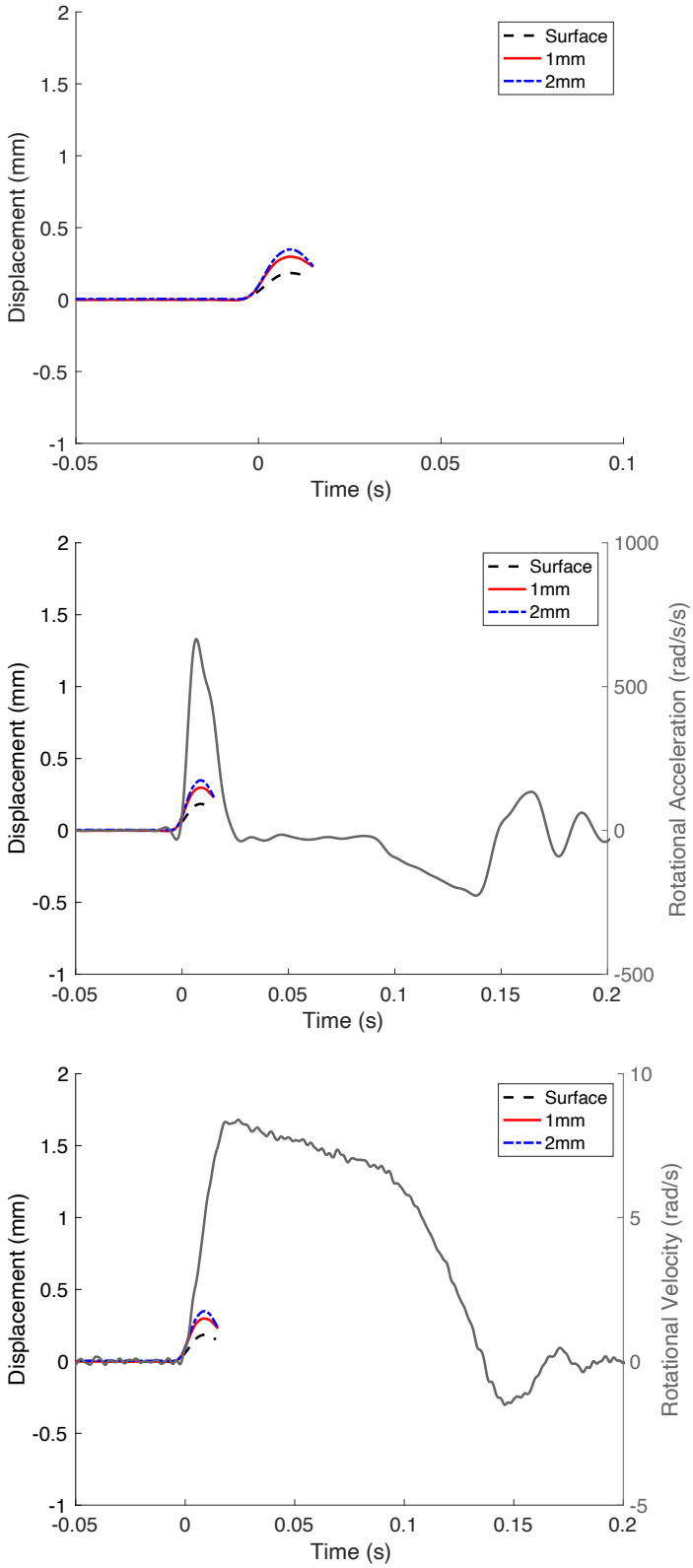

(g) Test 7

Figure 81 continued

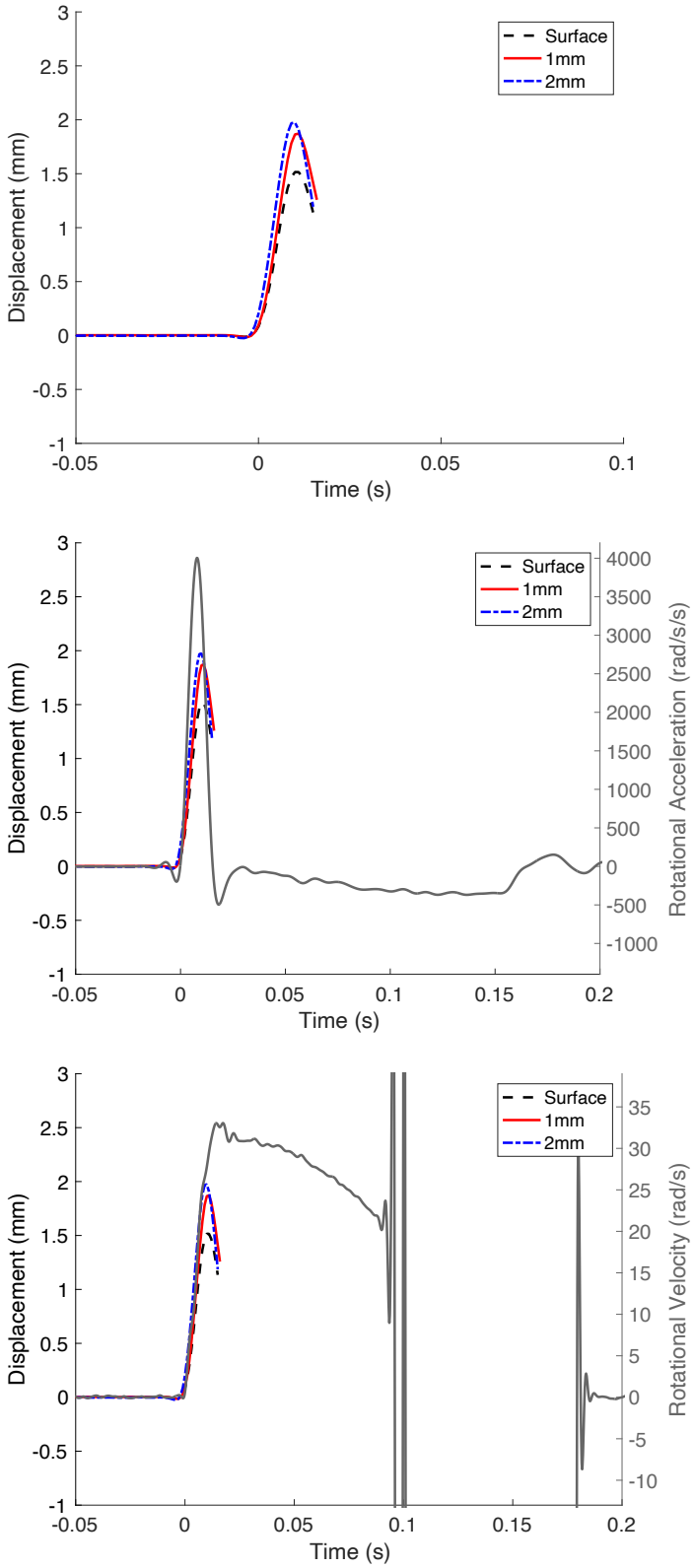

(h) Test 8

Figure 81 continued

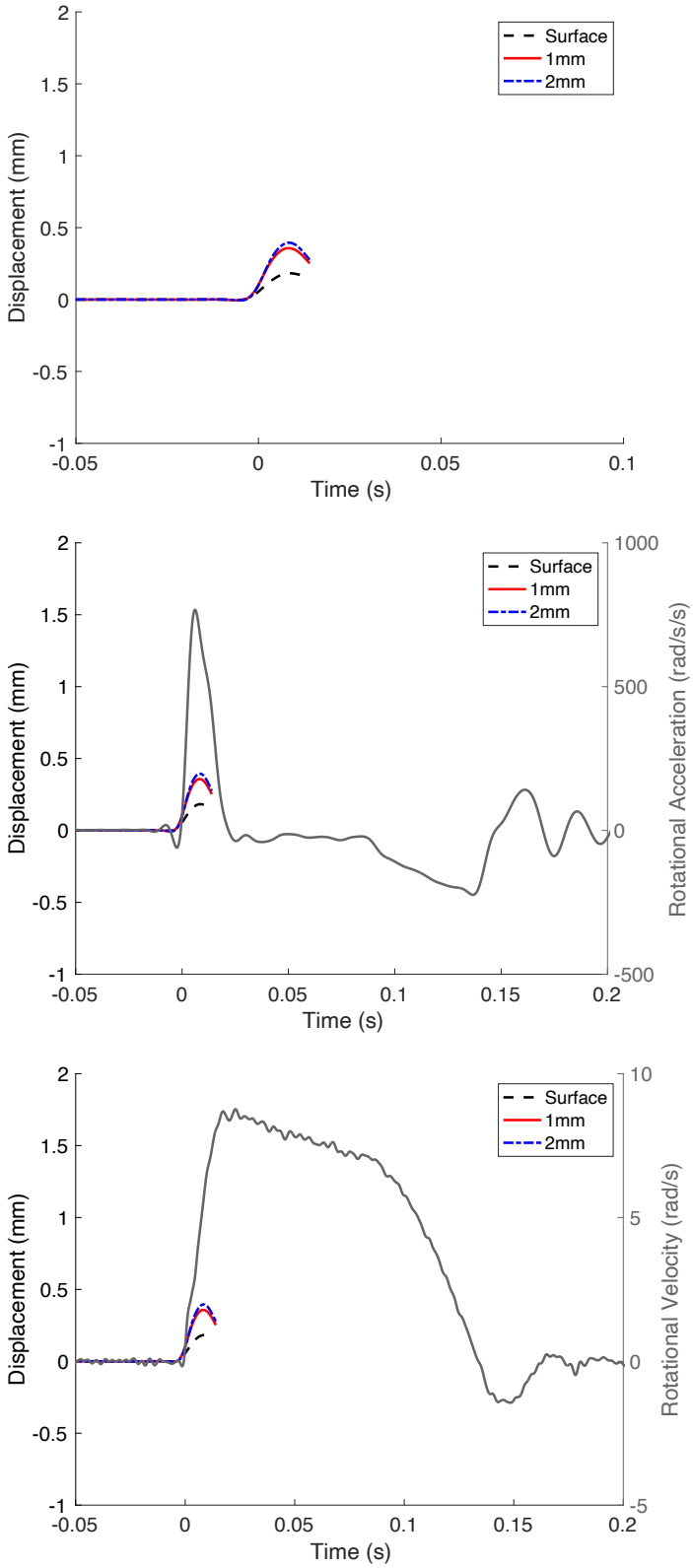

(i) Test 9

Figure 81 continued

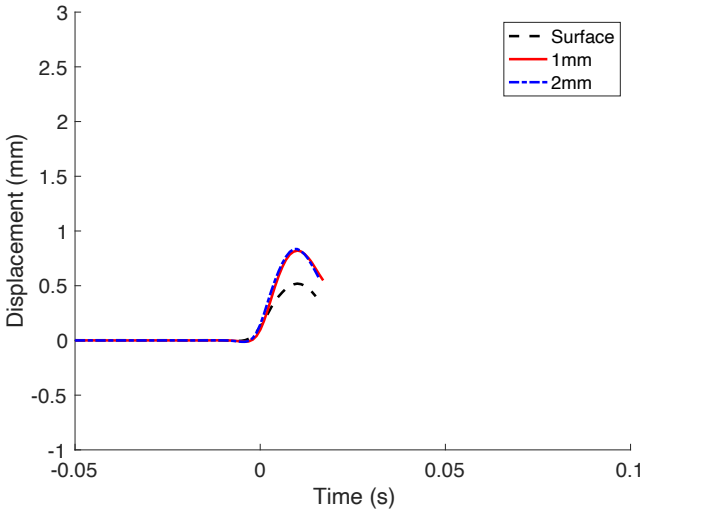

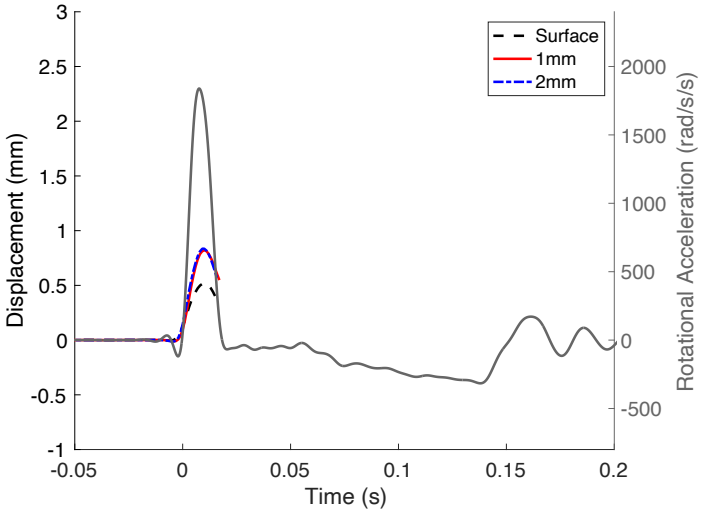

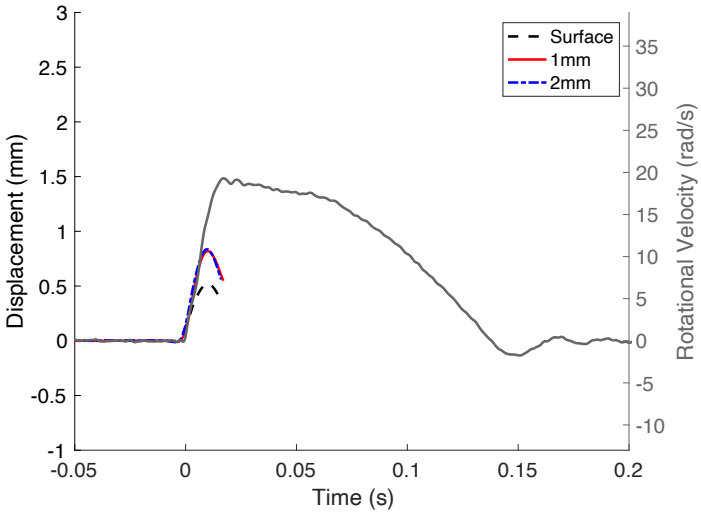

(j) Test 10

Figure 81 continued

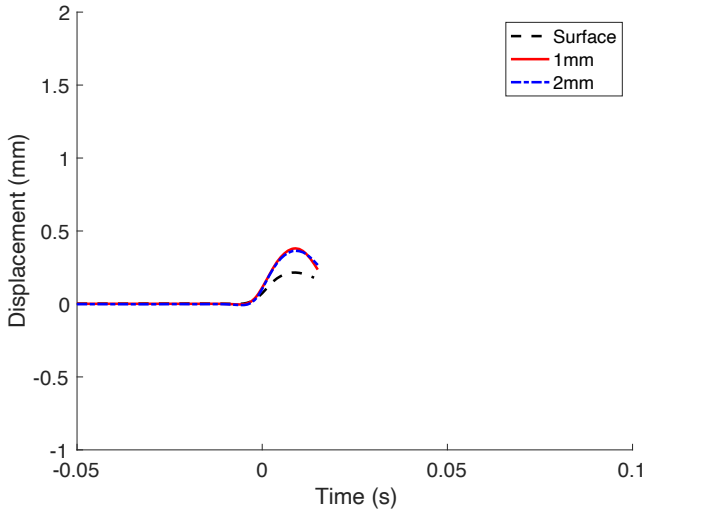

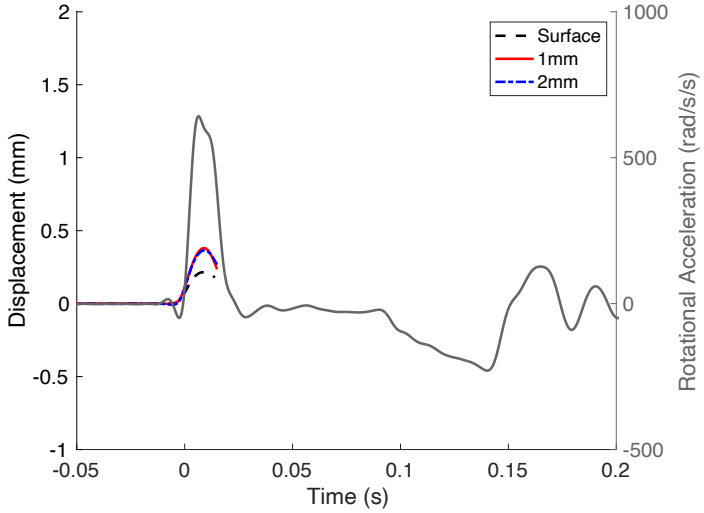

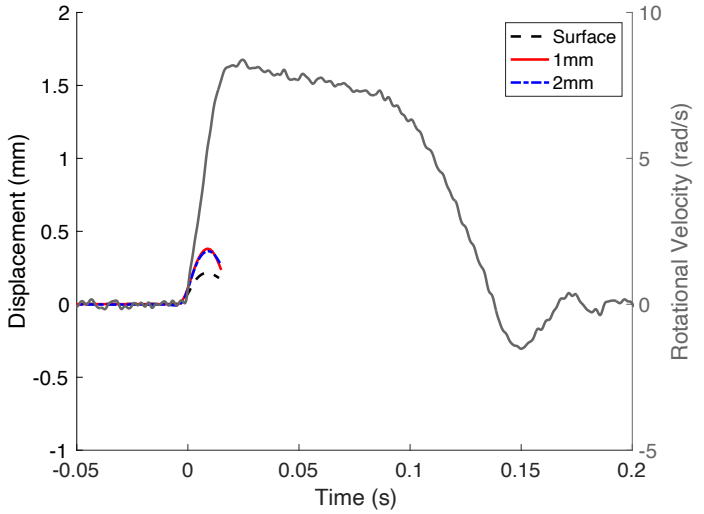

(k) Test 11

Figure 81 continued

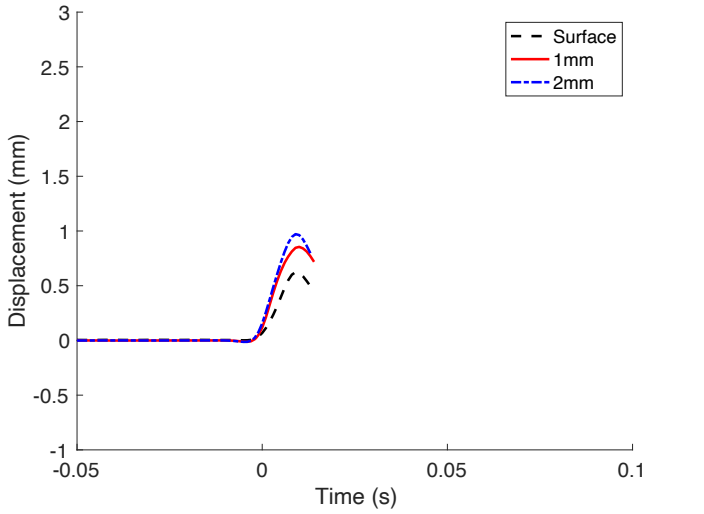

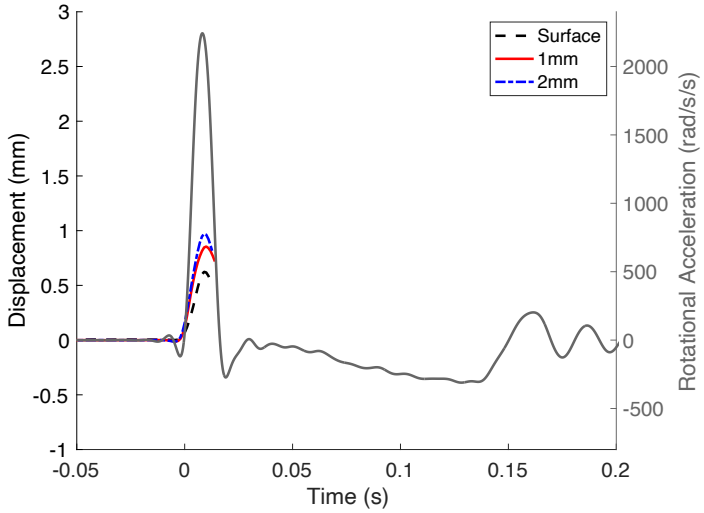

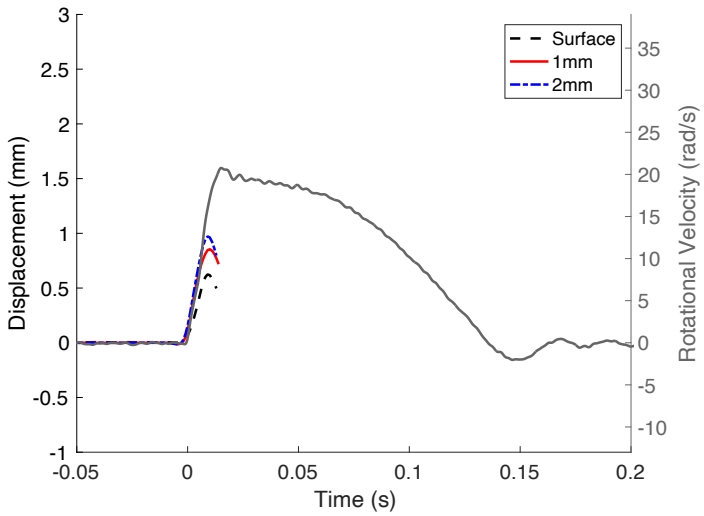

(l) Test 12

Figure 81 continued

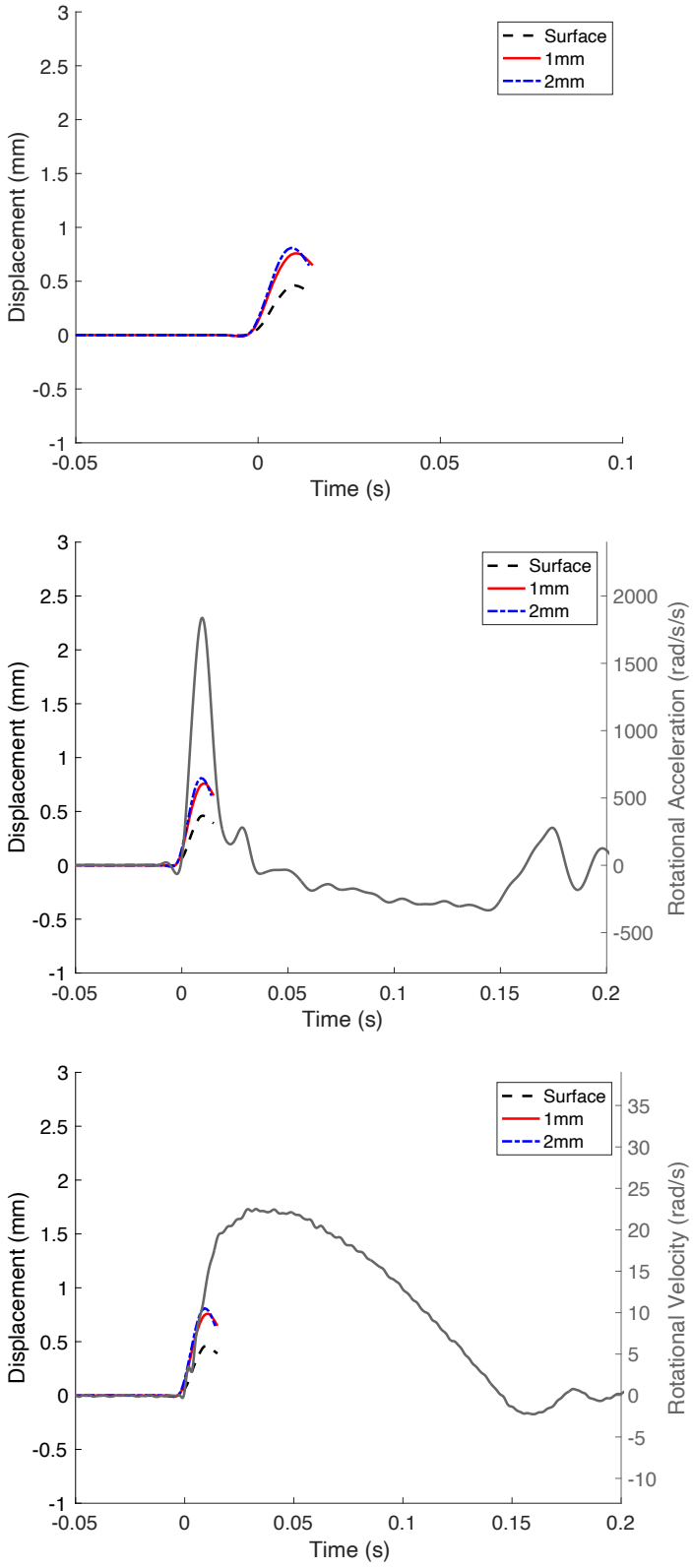

(m) Test 13

Figure 81 continued

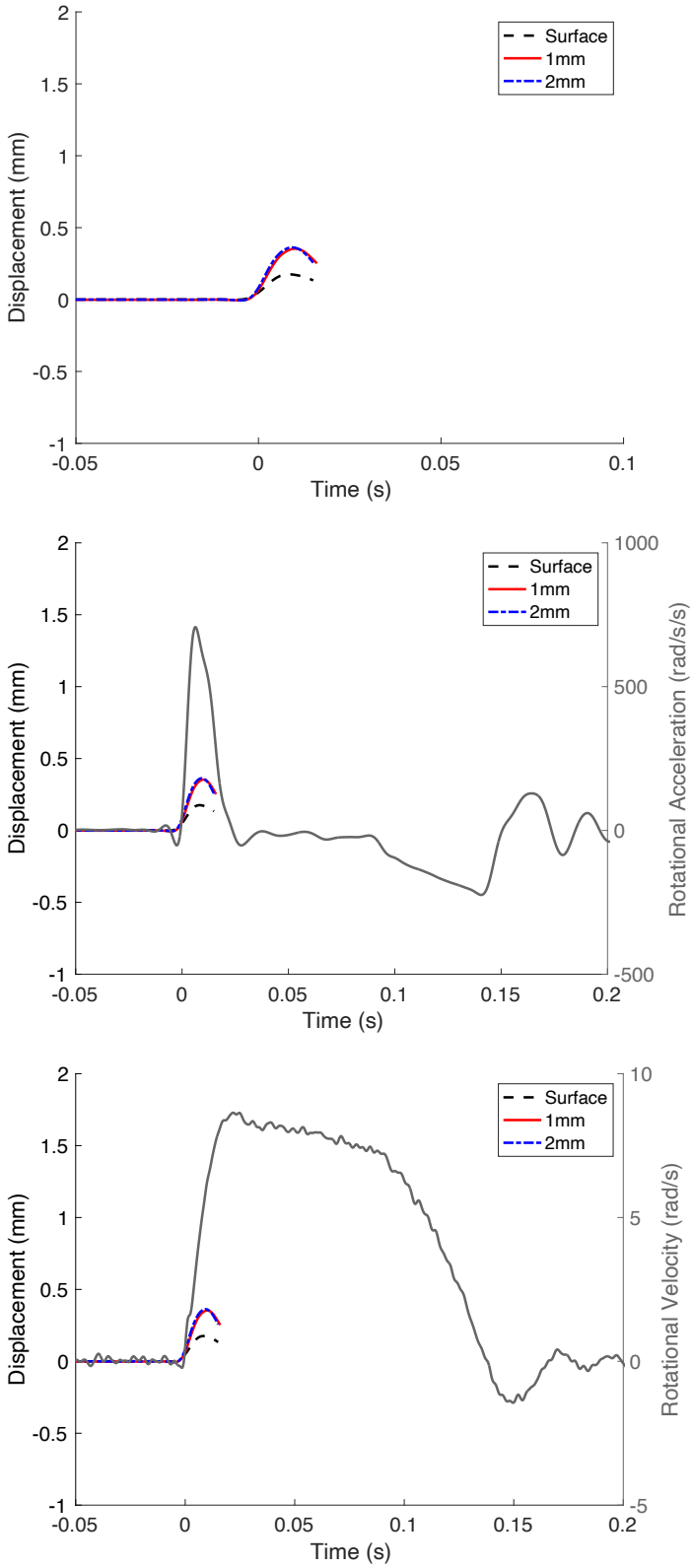

(n) Test 14

Figure 81 continued

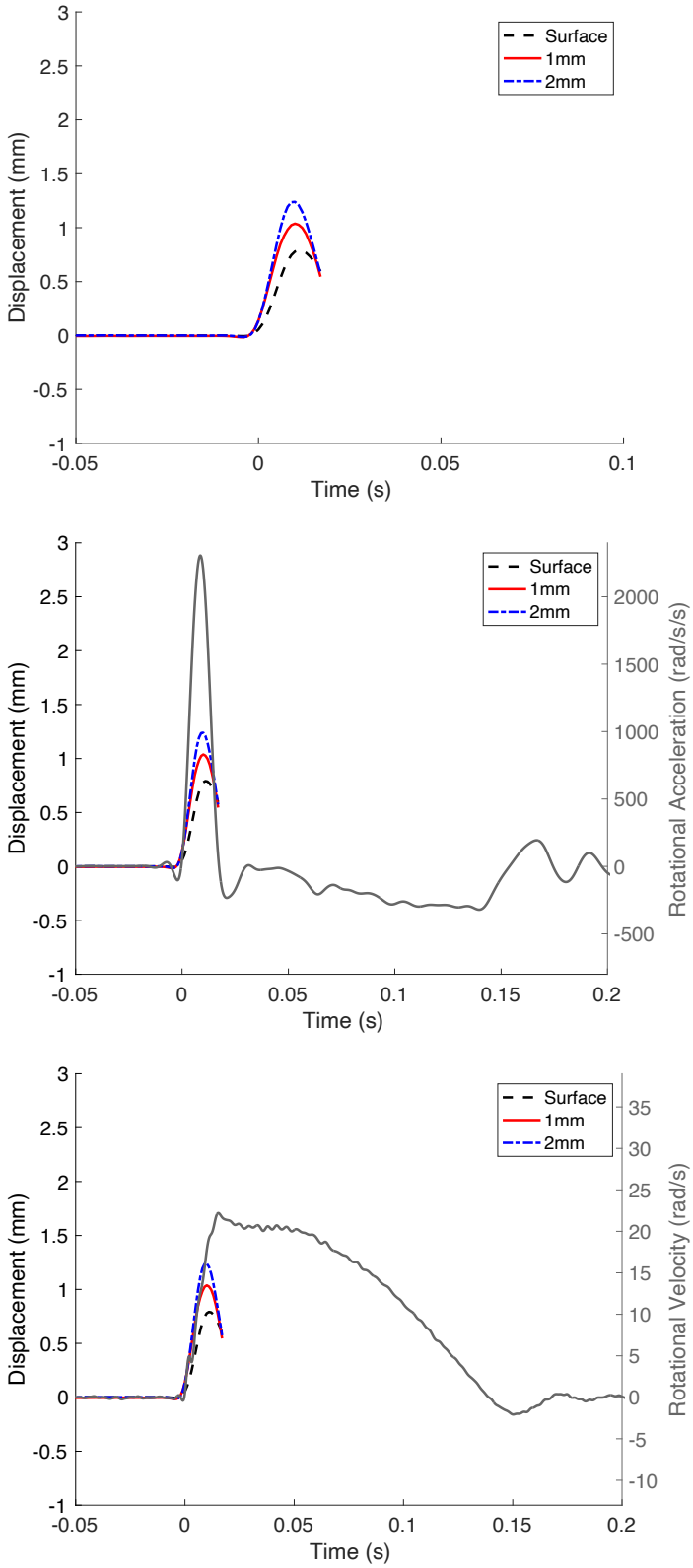

(o) Test 15

Figure 81 continued

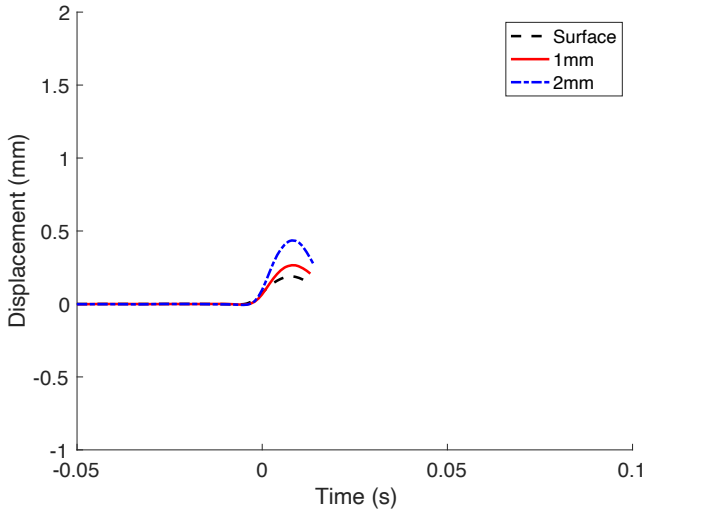

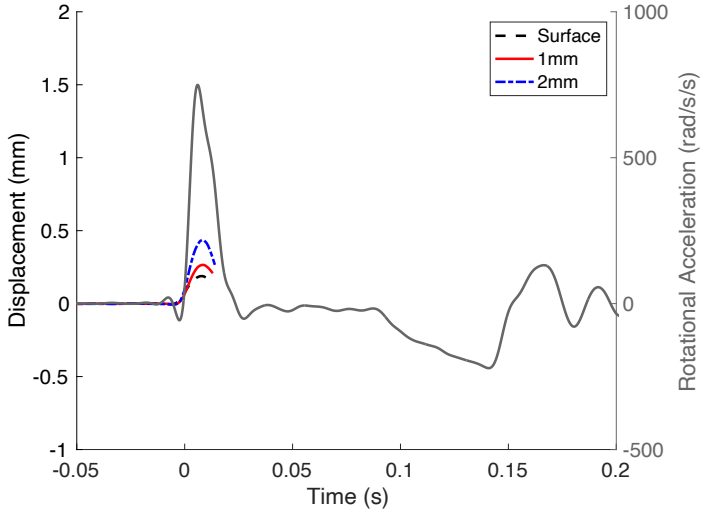

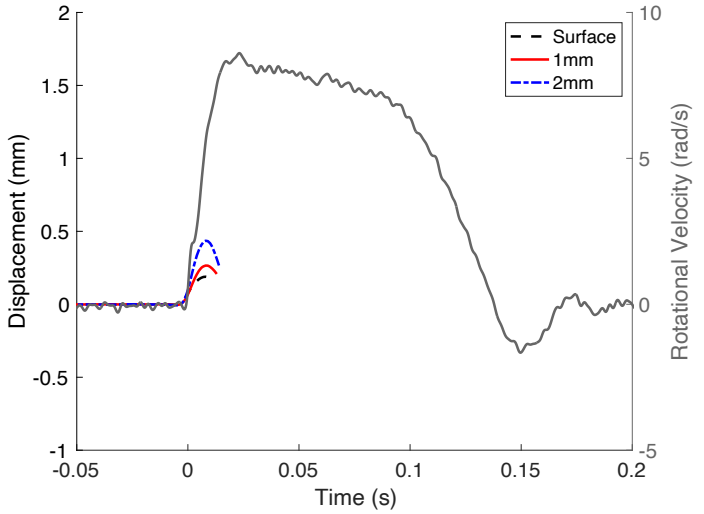

(p) Test 16

Figure 81 continued

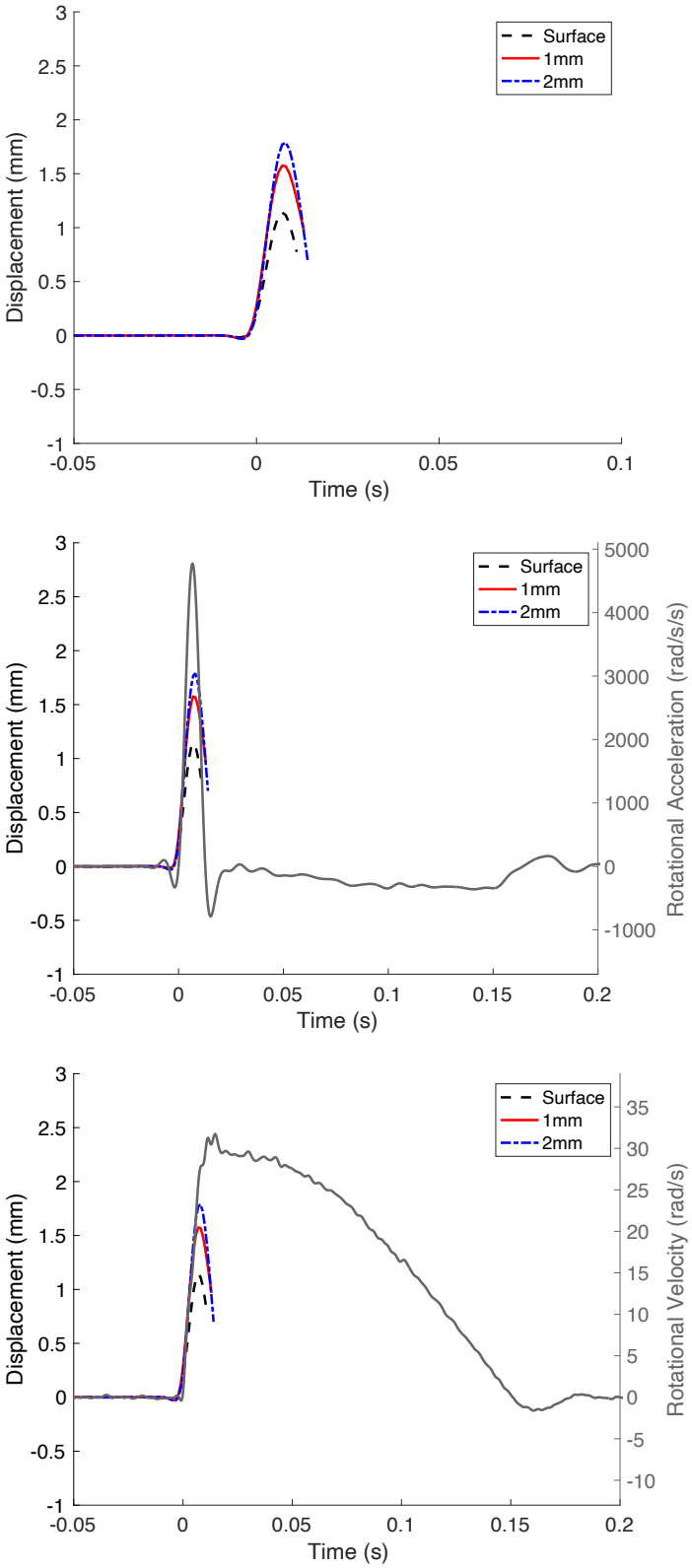

(q) Test 17

Figure 81 continued

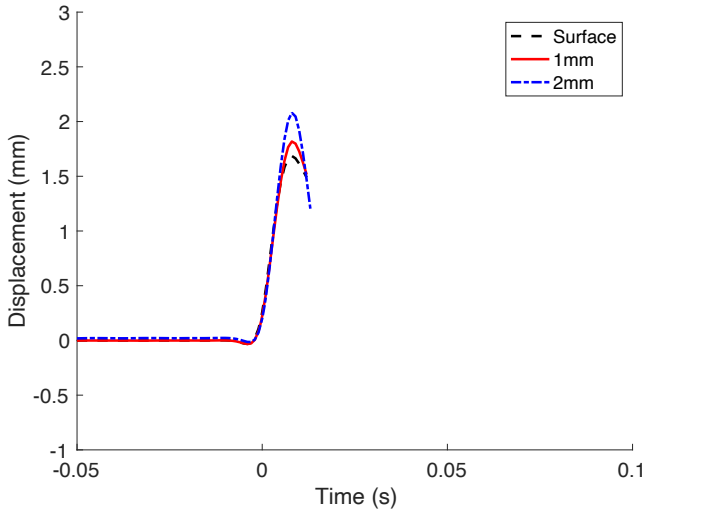

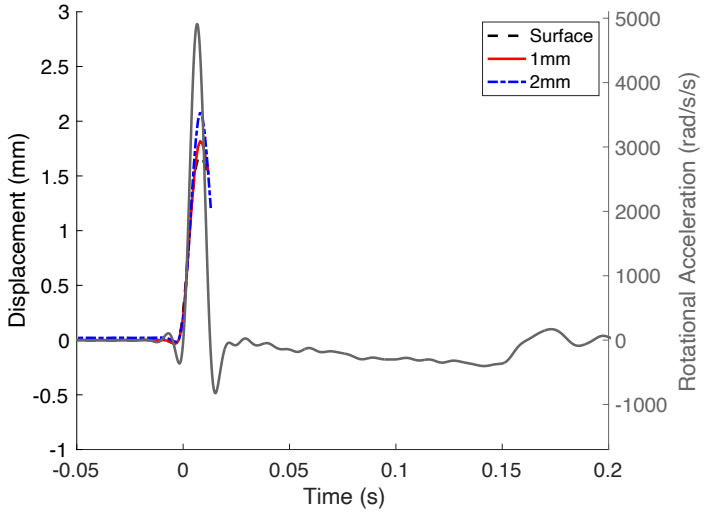

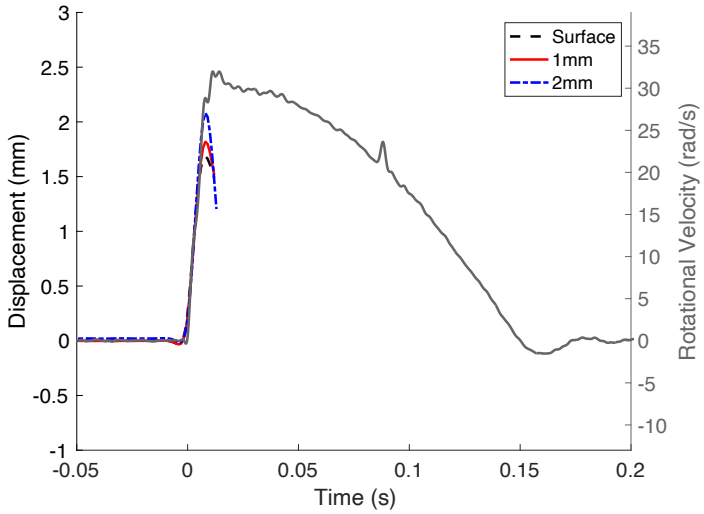

(r) Test 18

Appendix F: Subject 5 Results

Table 40: Main matrix results for subject 5

					Displacement (mm)		
Test #	Description	Postmortem time (hours)	Rotational Acceleration (rad/s/s)	Rotational Velocity (rad/s)	Cortex Surface	1mm deep	2mm deep
2205_01	Baseline	31.98	1069	8.89	0.429	0.830	1.11
2205_02	Test 1	32.33	2927	22.2	3.13	3.90	3.55
2205_03	Baseline	32.58	838	8.52	1.05	1.46	1.57
2205_04	Test 2	32.83	3257	31.0	6.07	6.87	5.81
2205_05	Baseline	33.08	921	8.74	3.16	4.06	3.79
2205_06	Test 3	33.48	4073	27.1	13.3	14.0	14.5
2205_07	Baseline	33.75	918	8.20	4.68	5.21	5.08
2205_08	Test 4	33.93	5021	42.3	18.3	18.9	19.1
2205_09	Baseline	34.13	942	9.06	4.44	4.91	4.98

Table 41: Post-test matrix results for subject 5

					Displacement (mm)		
Test #	Description	Postmortem time (hours)	Rotational Acceleration (rad/s^2)	Rotational Velocity (rad/s)	Cortex Surface	1mm deep	2mm deep
2205_10	Post-test 1	34.4	4077	22.4	11.6	11.2	11.9
2205_11	Baseline	34.6	839	8.98	4.99	5.13	5.37
2205_12	Post-test 2	34.78	1936	18.6	9.39	9.90	10.0
2205_13	Baseline	35.18	902	8.81	2.83	3.43	3.58
2205_14	Post-test 3	35.37	2174	21.4	8.55	9.24	9.75
2205_15	Baseline	35.52	775	8.84	2.95	3.74	3.73
2205_16	Post-test 4	35.82	3742	23.0	12.9	13.0	12.9
2205_17	Baseline	36.07	778	8.36	3.48	3.65	3.66
2205_18	Post-test 5	36.32	3933	21.9	8.90	9.26	10.1
2205_19	Baseline	37.2	901	8.85	1.14	1.77	1.93
2205_20	Post-test 5	37.43	3764	22.8	4.08	5.43	5.73
2205_21	Baseline	37.68	972	8.95	1.08	1.64	1.85

Table 42: Comparison of baseline results for subject 5

					Displacement (mm)		
Test #	Description	Postmortem time (hours)	Rotational Acceleration (rad/s^2)	Rotational Velocity (rad/s)	Cortex Surface	1mm deep	2mm deep
2205_01	Baseline	31.98	1069	8.89	0.429	0.830	1.11
2205_03	Baseline	32.58	838	8.52	1.05	1.46	1.57
2205_05	Baseline	33.08	921	8.74	3.16	4.06	3.79
2205_07	Baseline	33.75	918	8.20	4.68	5.21	5.08
2205_09	Baseline	34.13	942	9.06	4.44	4.91	4.98
2205_11	Baseline	34.60	839	8.98	4.99	5.12	5.37
2205_13	Baseline	35.18	902	8.81	2.83	3.43	3.58
2205_15	Baseline	35.52	775	8.84	2.95	3.74	3.73
2205_17	Baseline	36.07	778	8.36	3.48	3.65	3.66
2205_19	Baseline	37.20	901	8.85	1.14	1.77	1.93
2205_21	Baseline	37.68	972	8.95	1.08	1.64	1.85
		Average	**896**	**8.75**	**2.91**	**3.41**	**3.47**
		Std. Dev.	**86.0**	**0.272**	**1.60**	**1.58**	**1.51**
		% CV	**9.60**	**3.11**	**55.1**	**46.5**	**43.5**

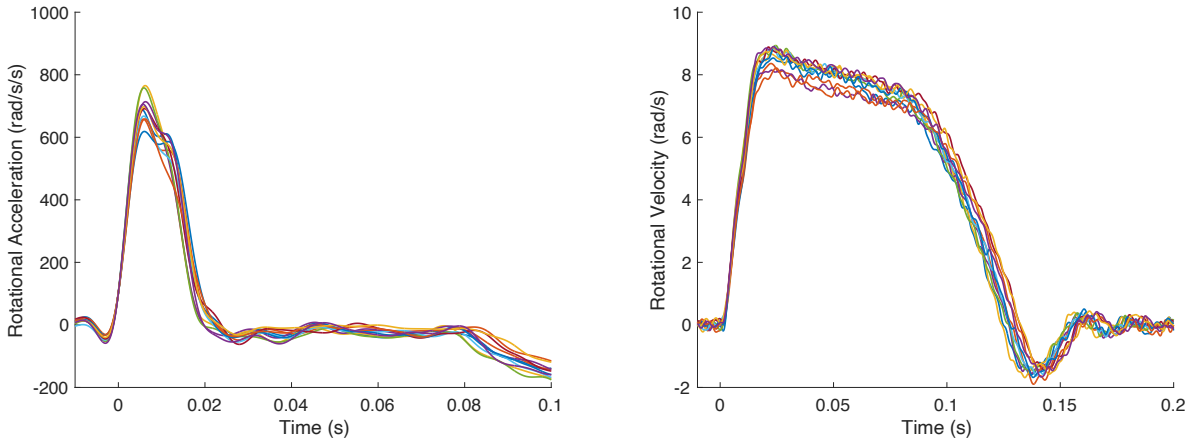

Figure 82: Comparison of baseline kinematics for subject 5

Test 1 was determined to be a damaging test (see 4.3. PMHS Testing Discussion *Evaluation of Damaged Tests*).

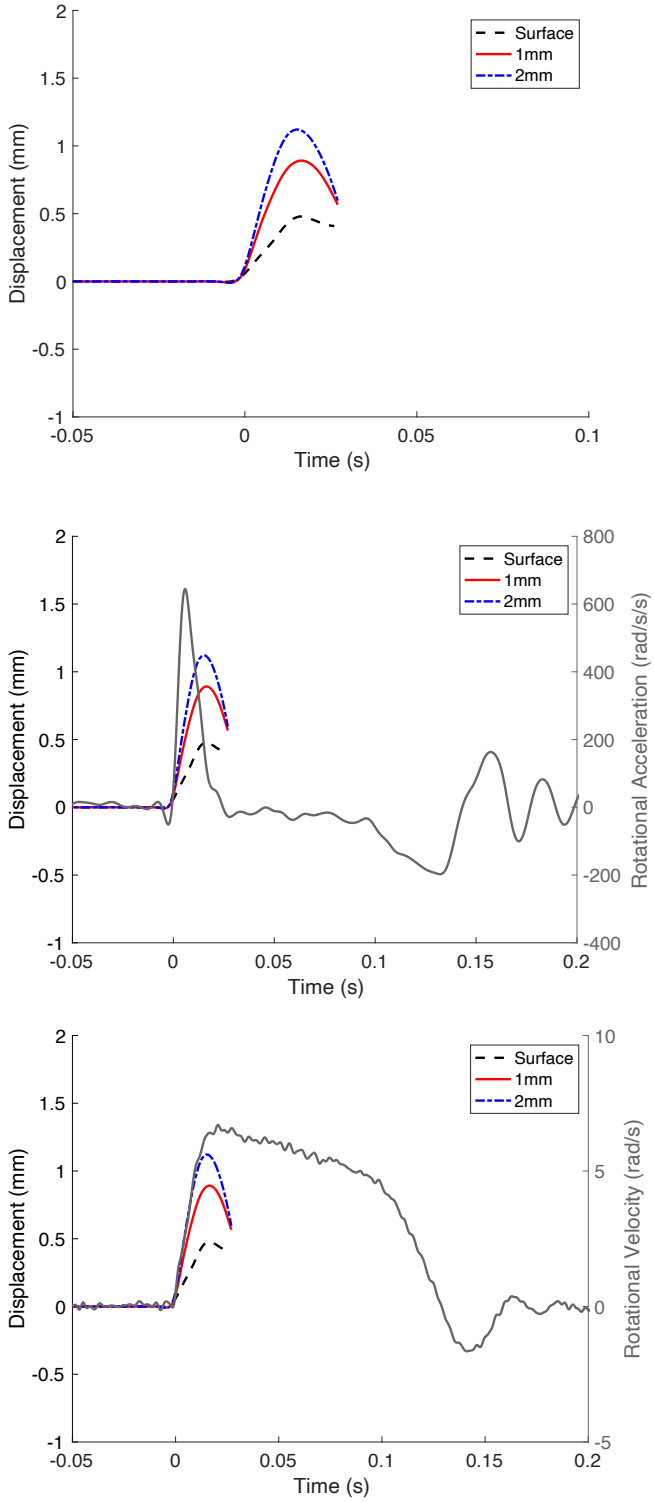

(a) Test 1

Figure 83: Time history of displacement (top), displacement compared to rotational acceleration (middle) and displacement compared to rotational velocity (bottom) for subject 5

Figure 83 continued

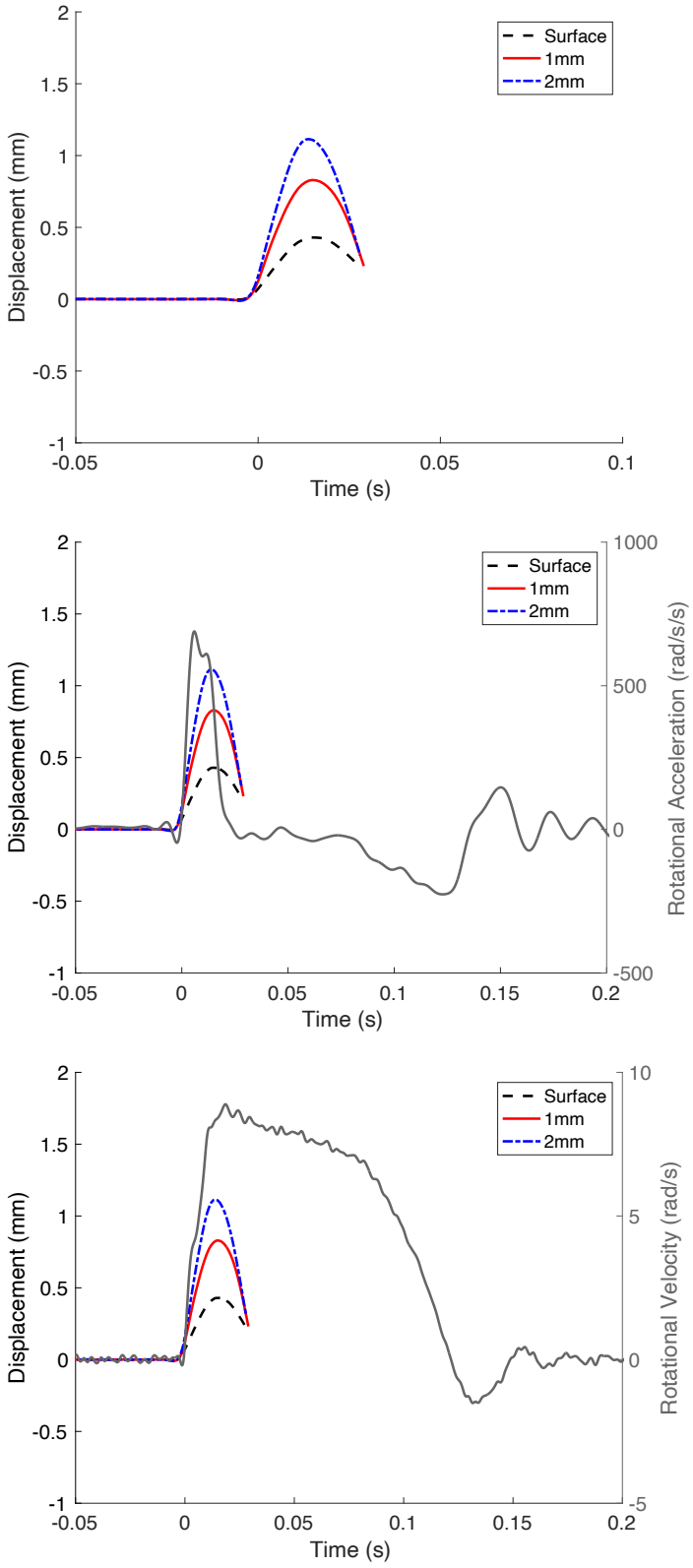

(b) Test 2

Figure 83 continued

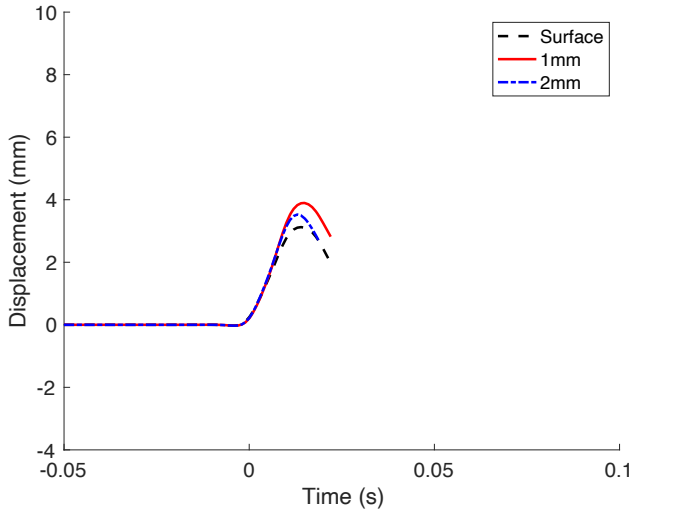

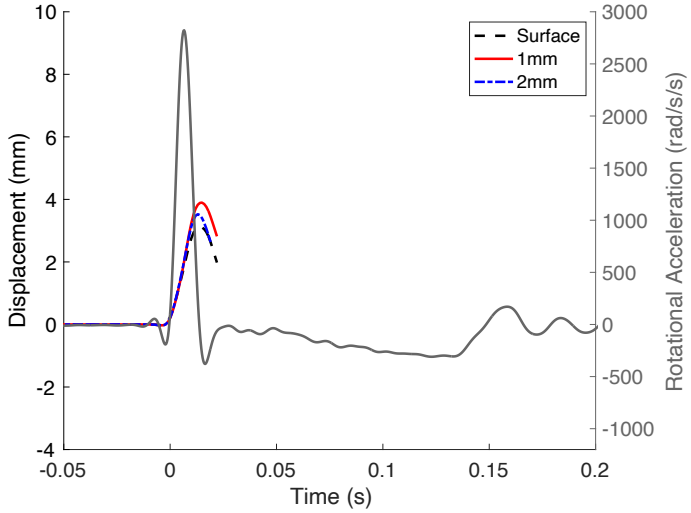

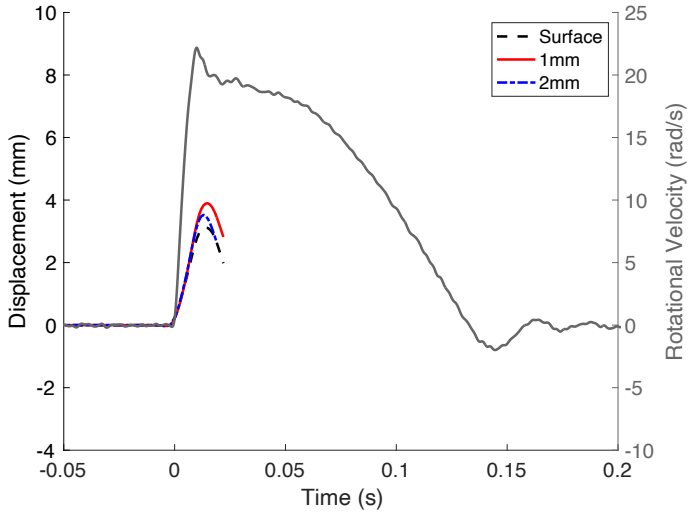

(c) Test 3

Figure 83 continued

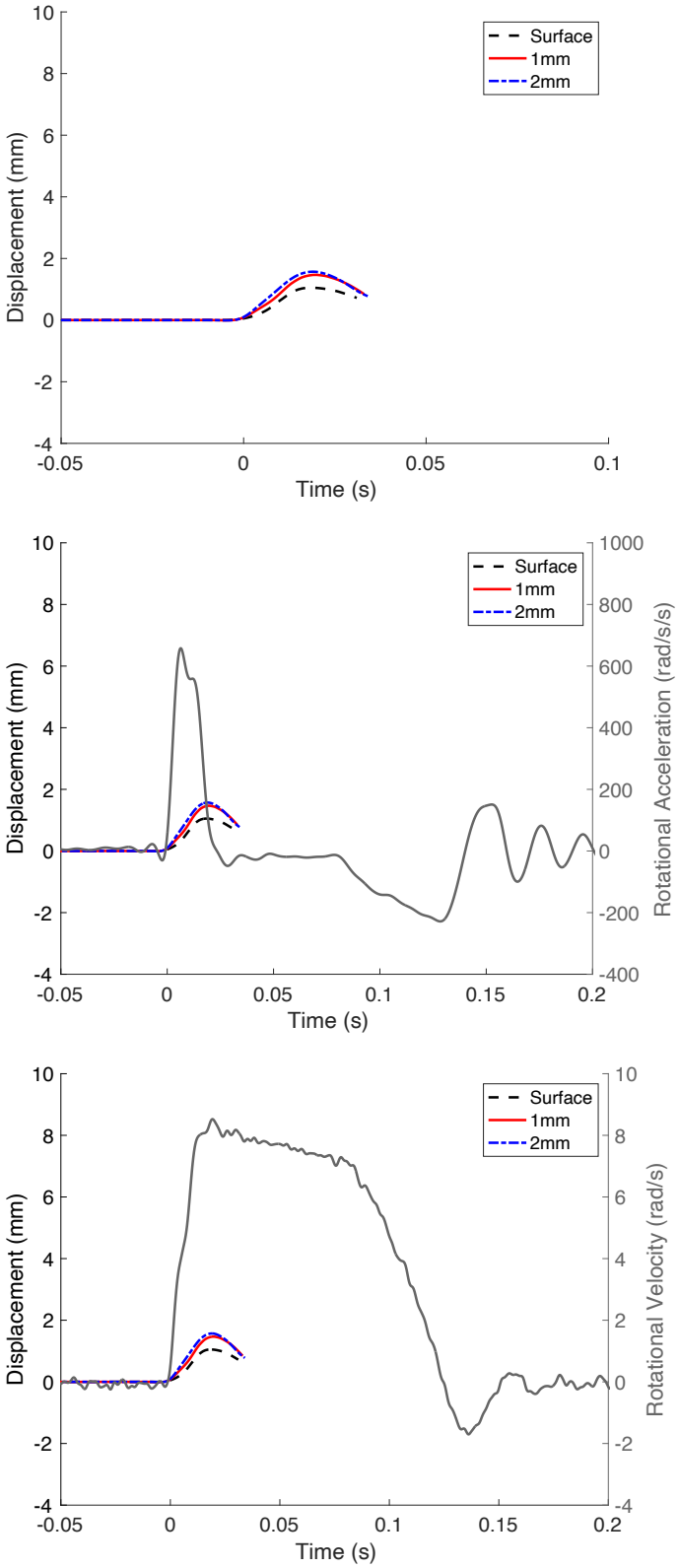

(d) Test 4

Figure 83 continued

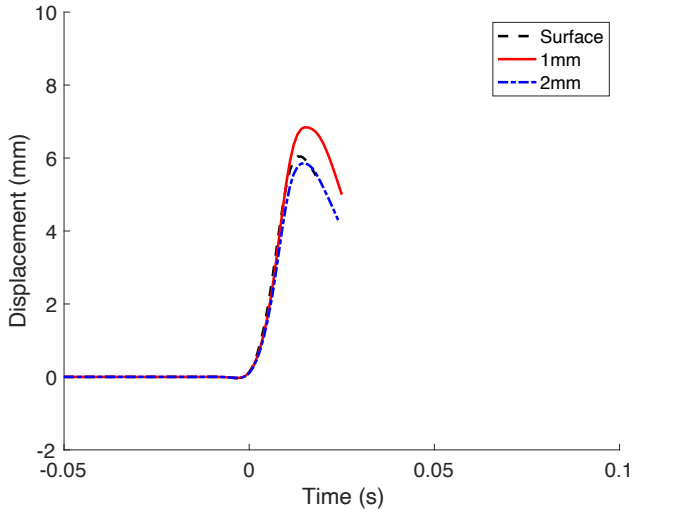

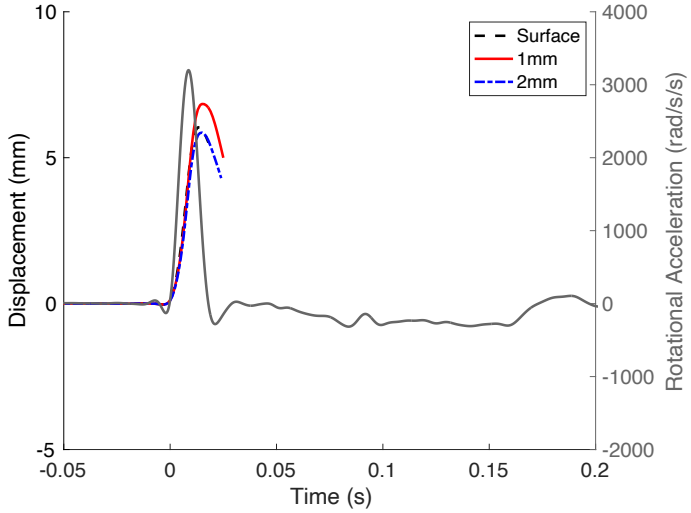

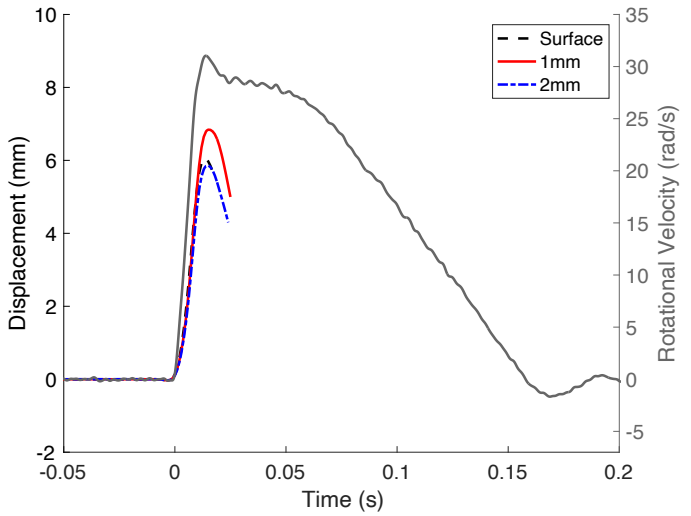

(e) Test 5

Figure 83 continued

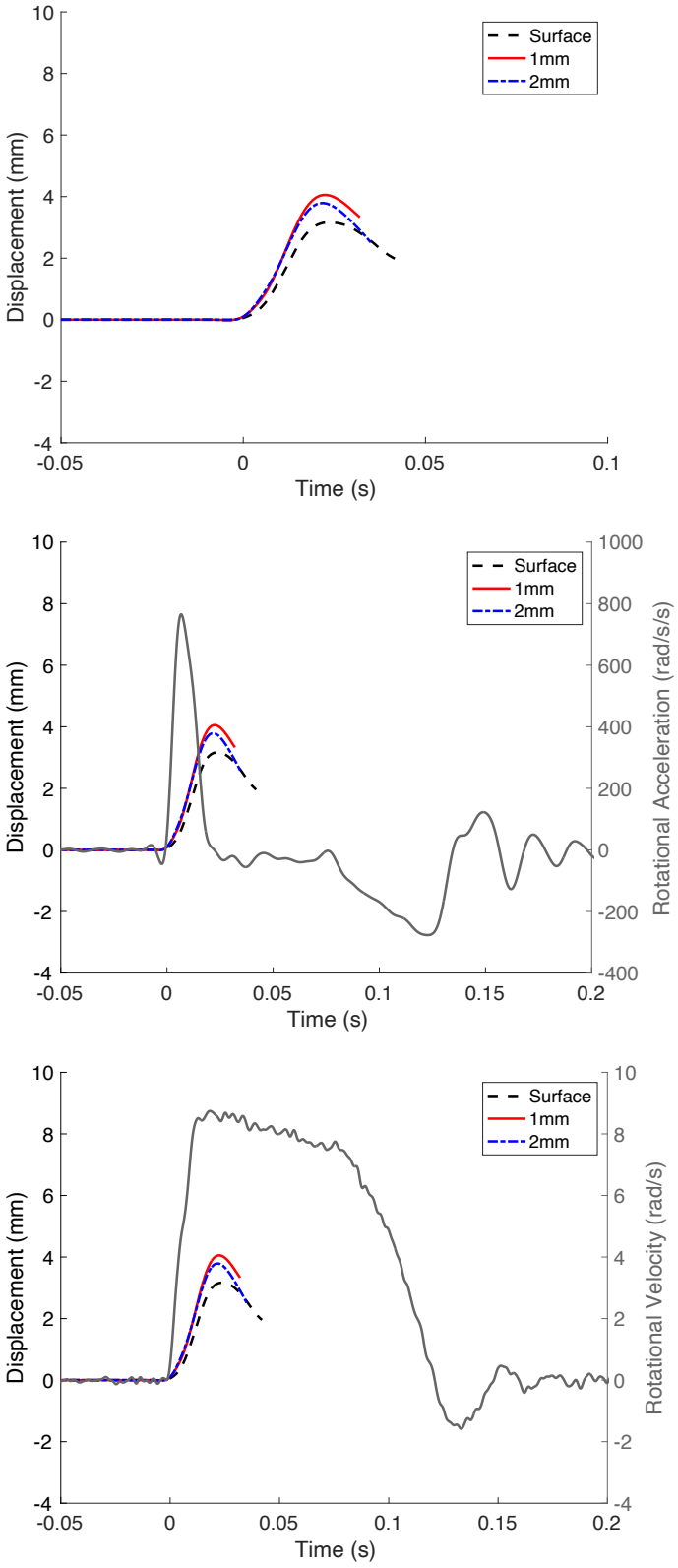

(f) Test 6

Figure 83 continued

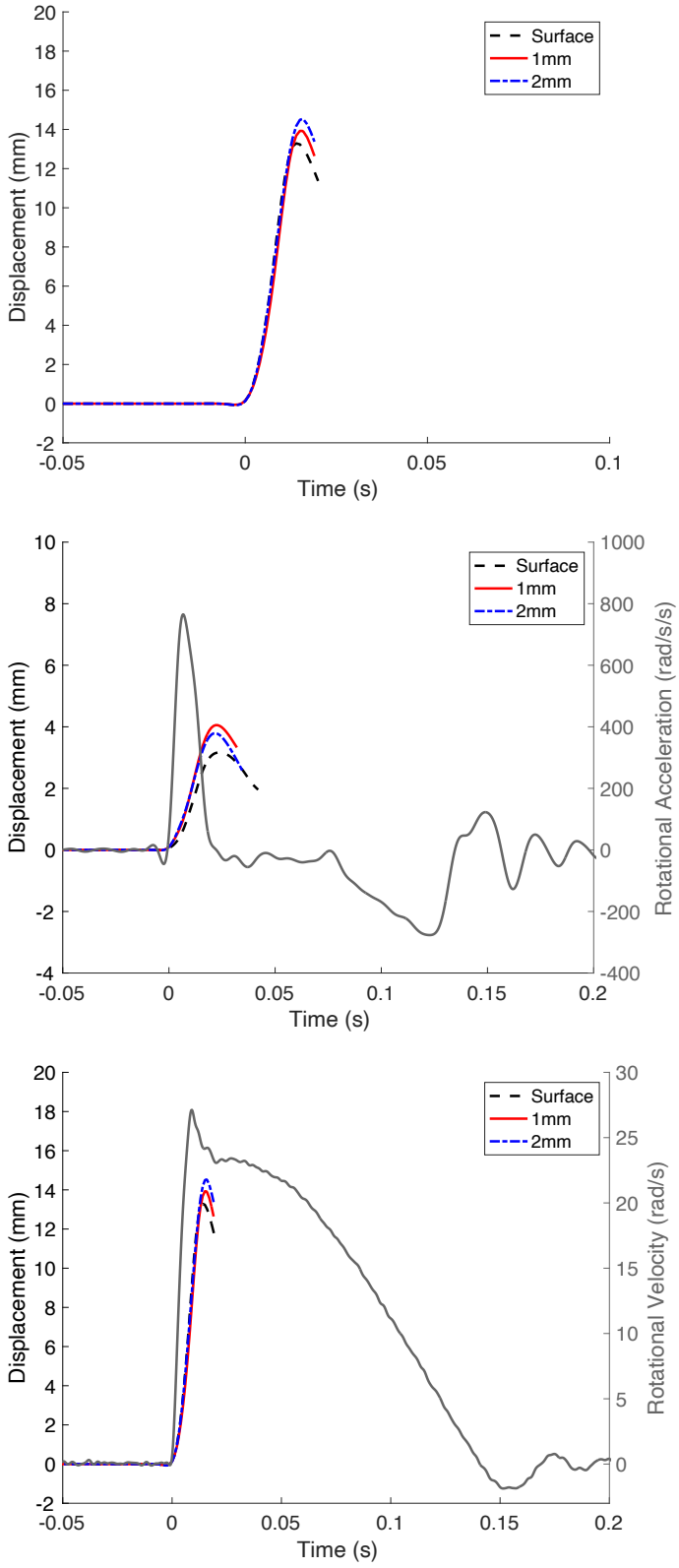

(g) Test 7

Figure 83 continued

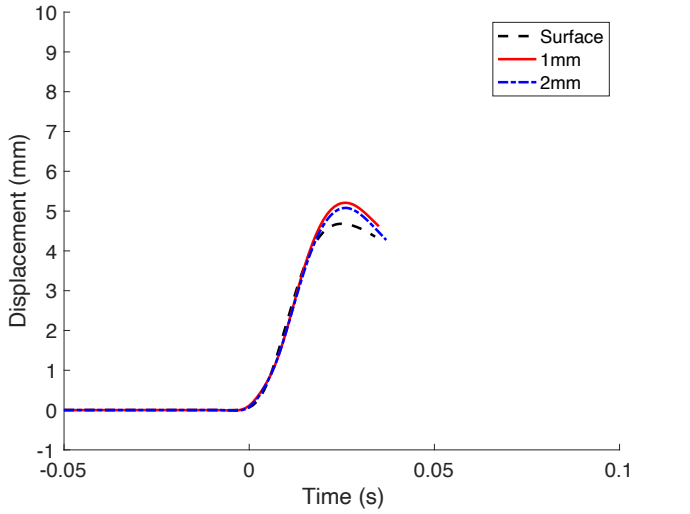

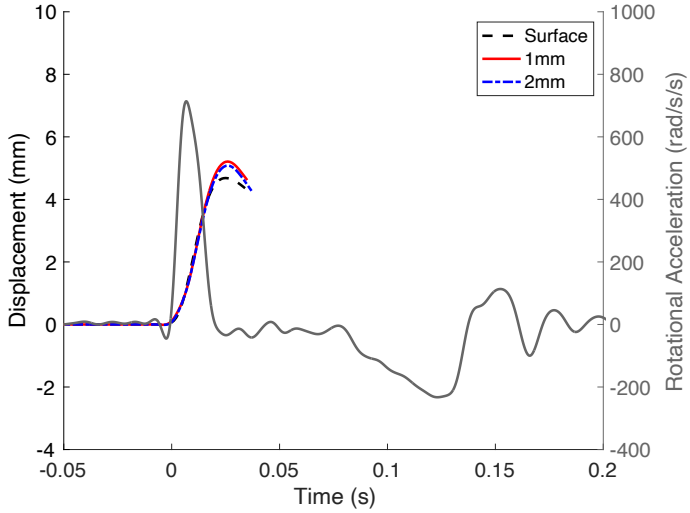

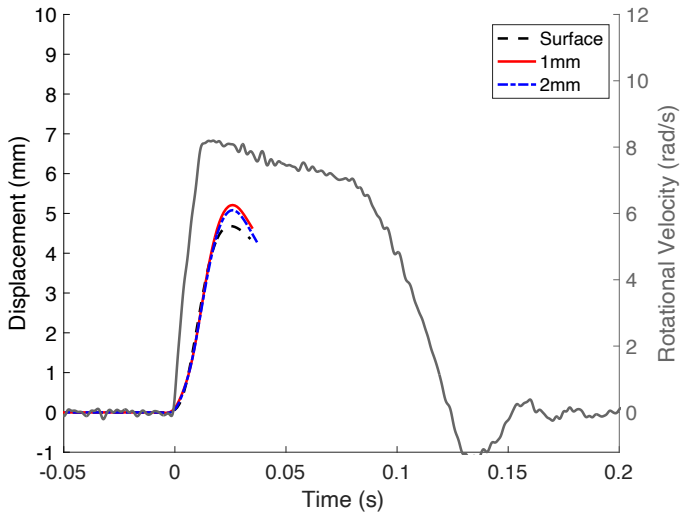

(h) Test 8

Figure 83 continued

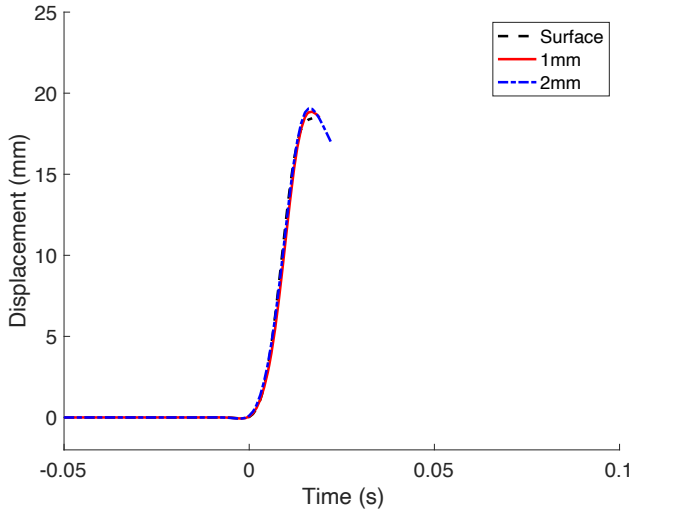

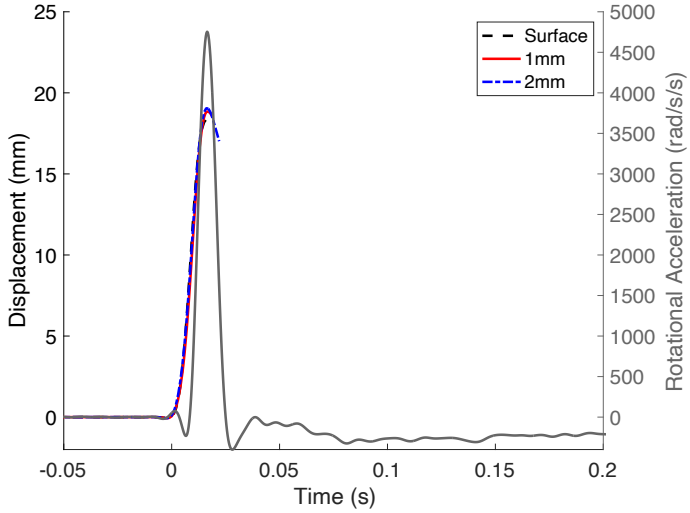

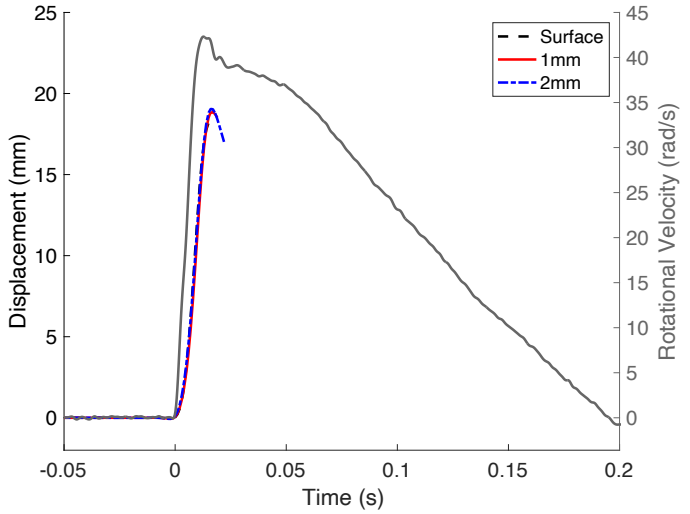

(i) Test 9

Figure 83 continued

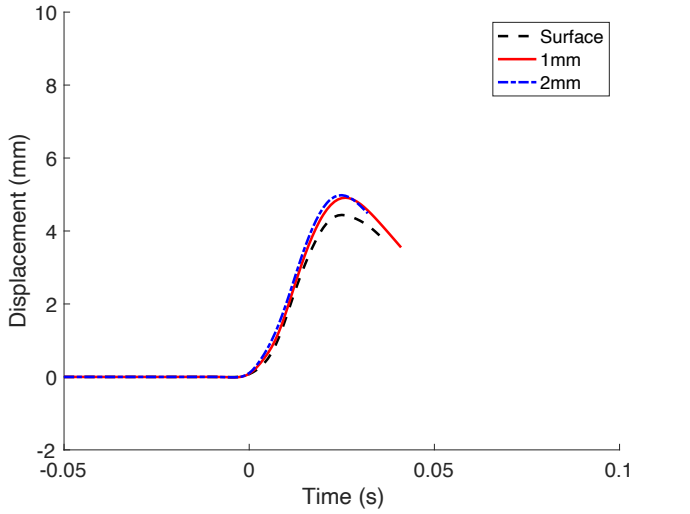

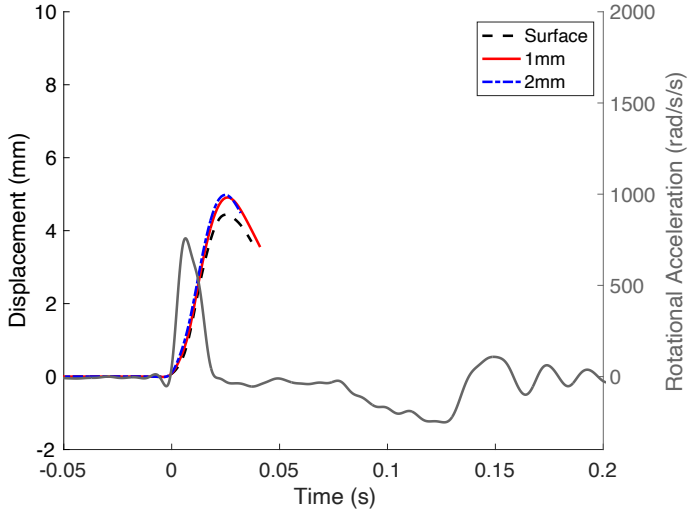

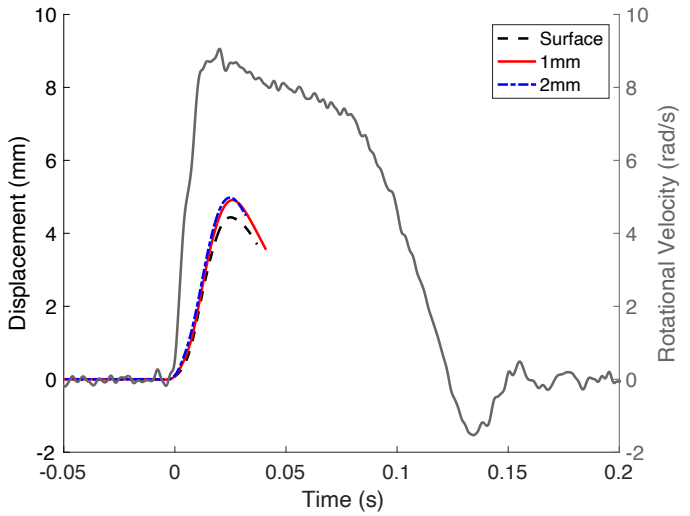

(j) Test 10

Figure 83 continued

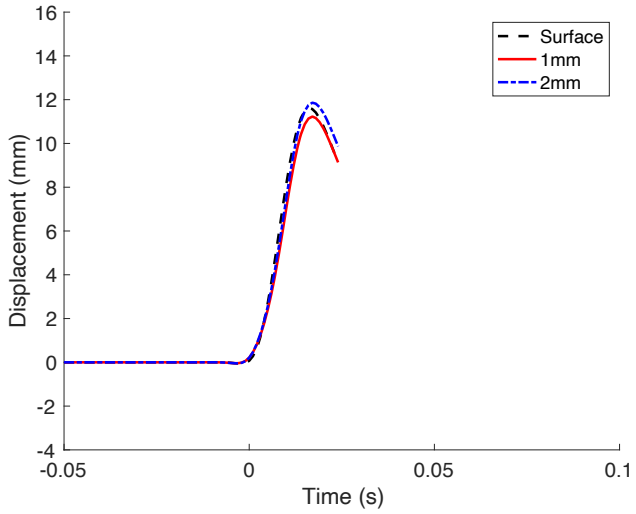

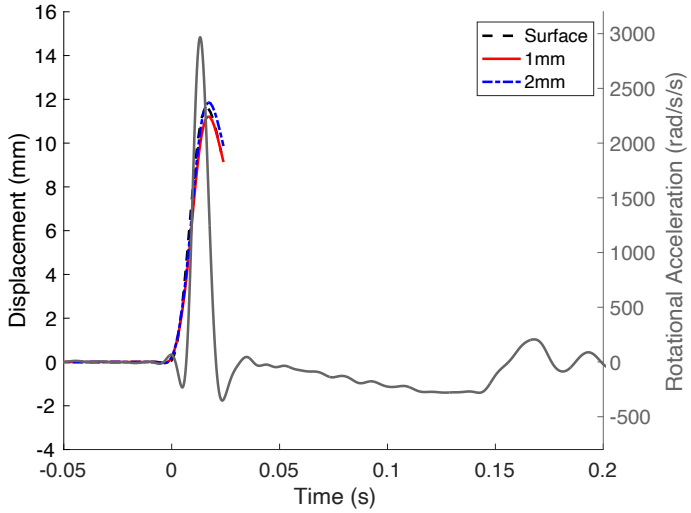

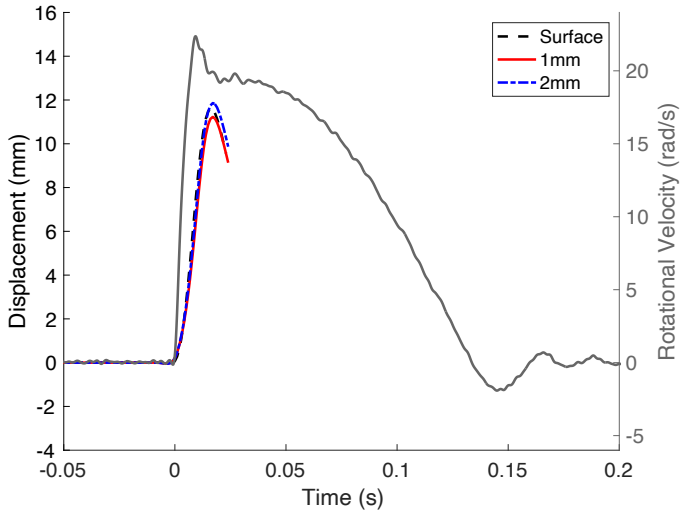

(k) Test 11

Figure 83 continued

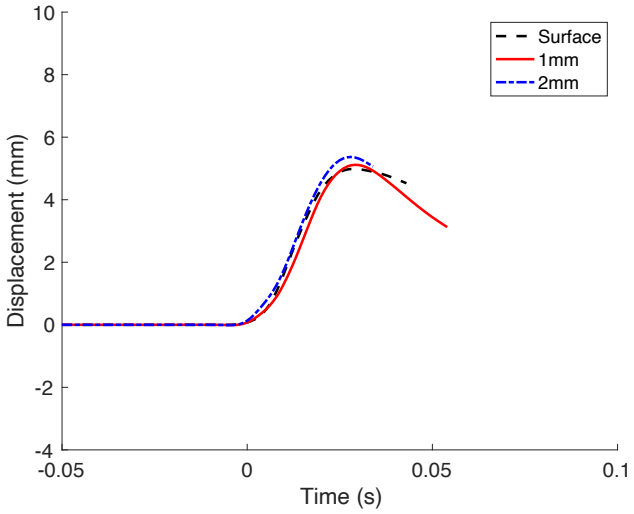

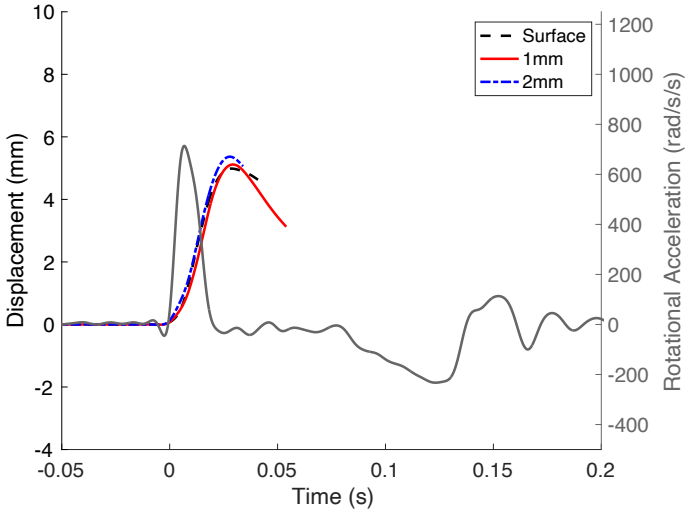

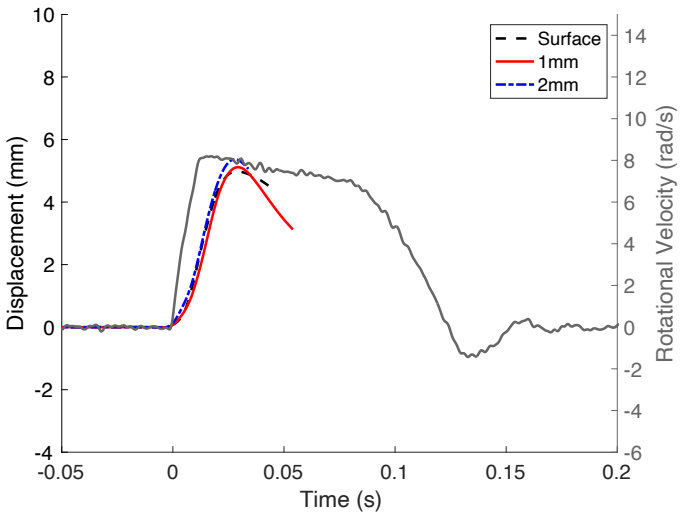

(l) Test 12

Figure 83 continued

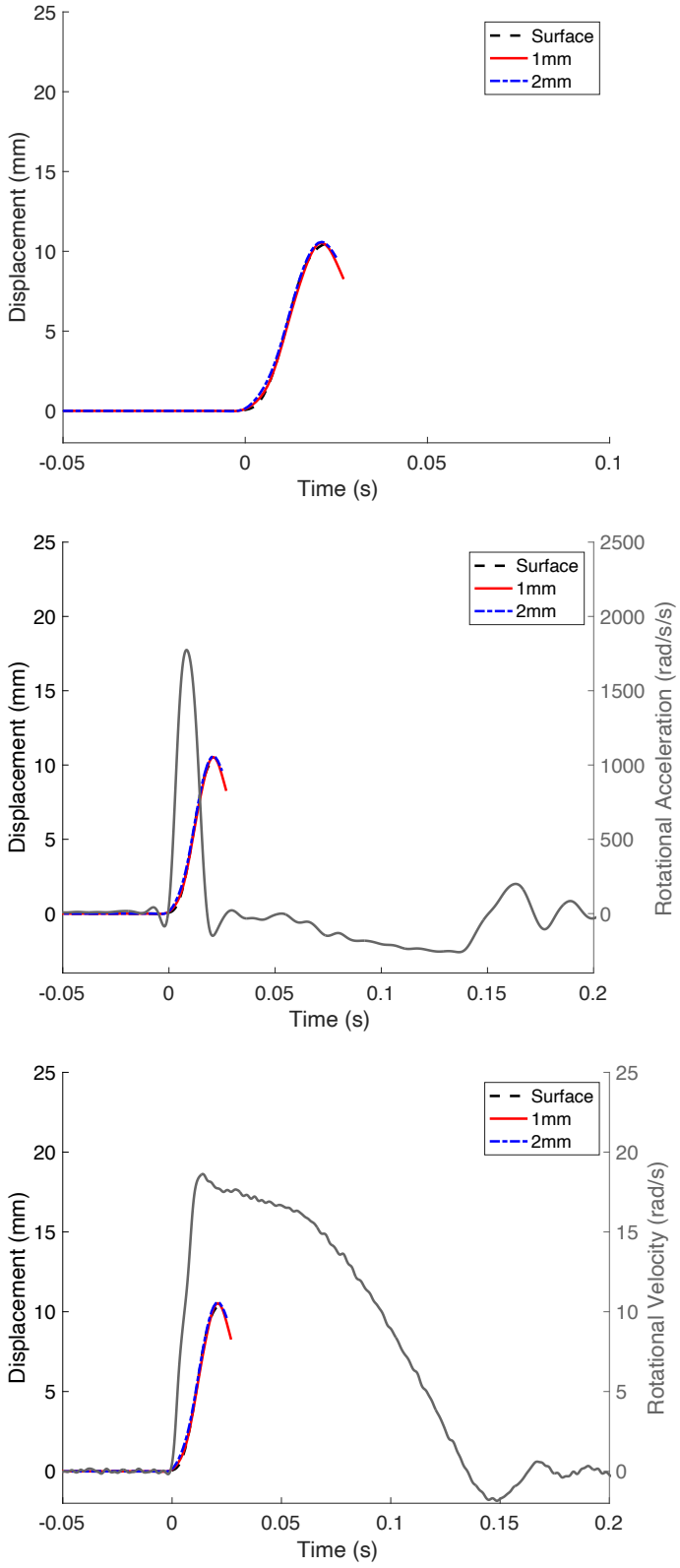

(m) Test 13

Figure 83 continued

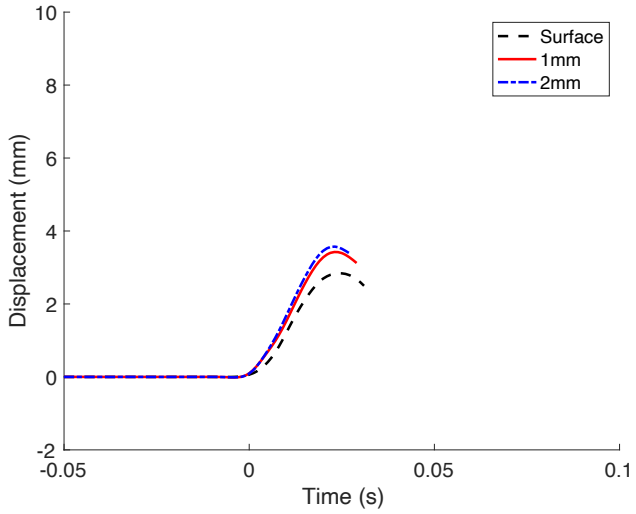

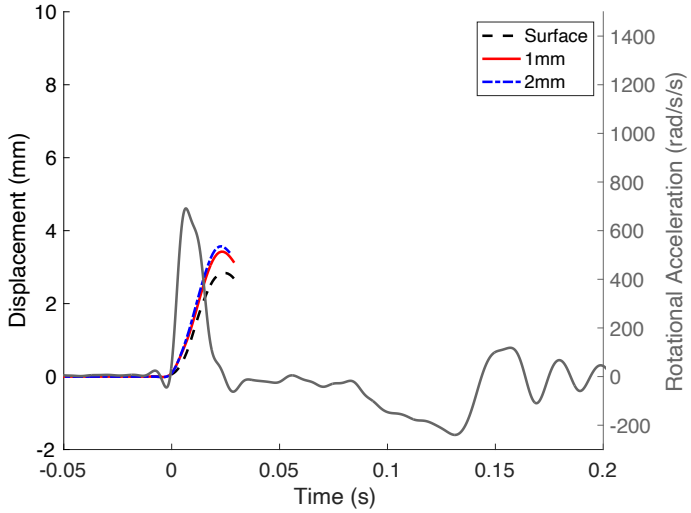

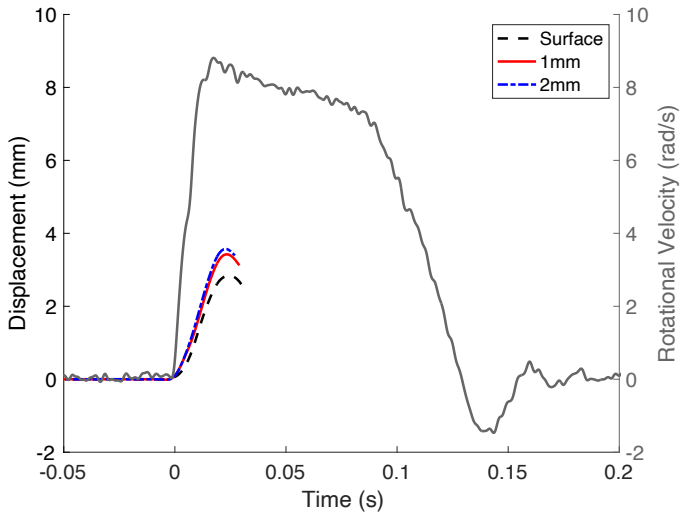

(n) Test 14

Figure 83 continued

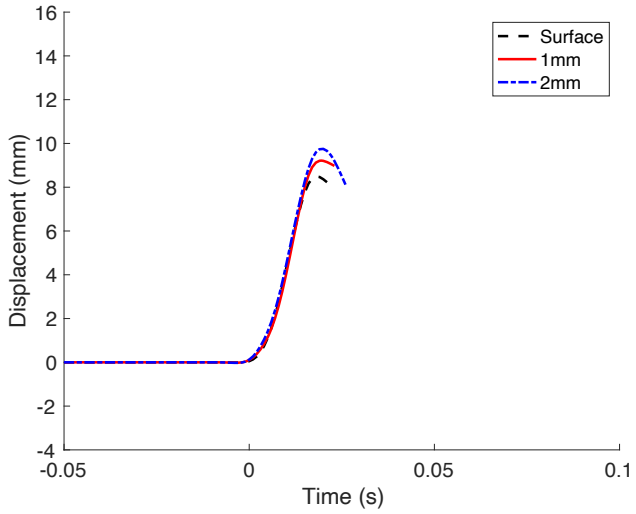

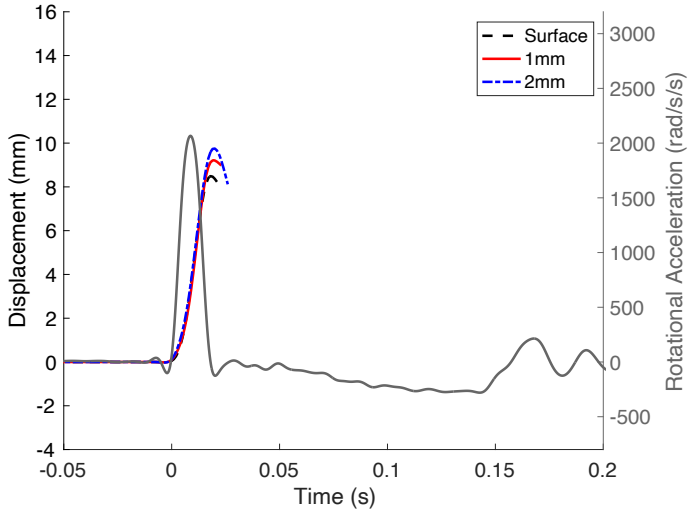

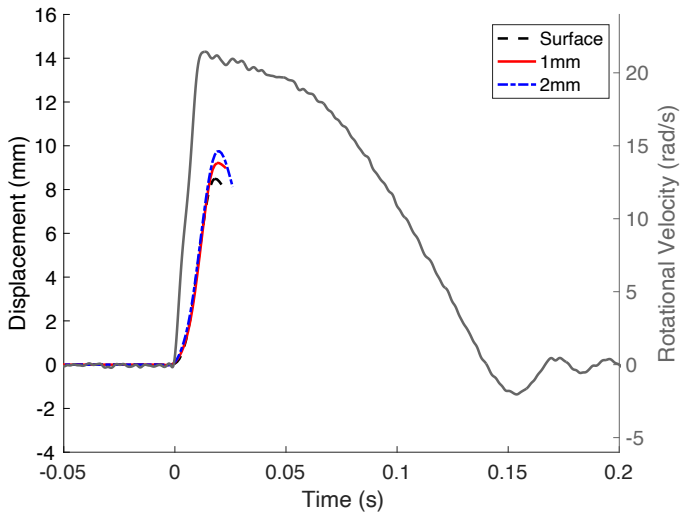

(o) Test 15

Figure 83 continued

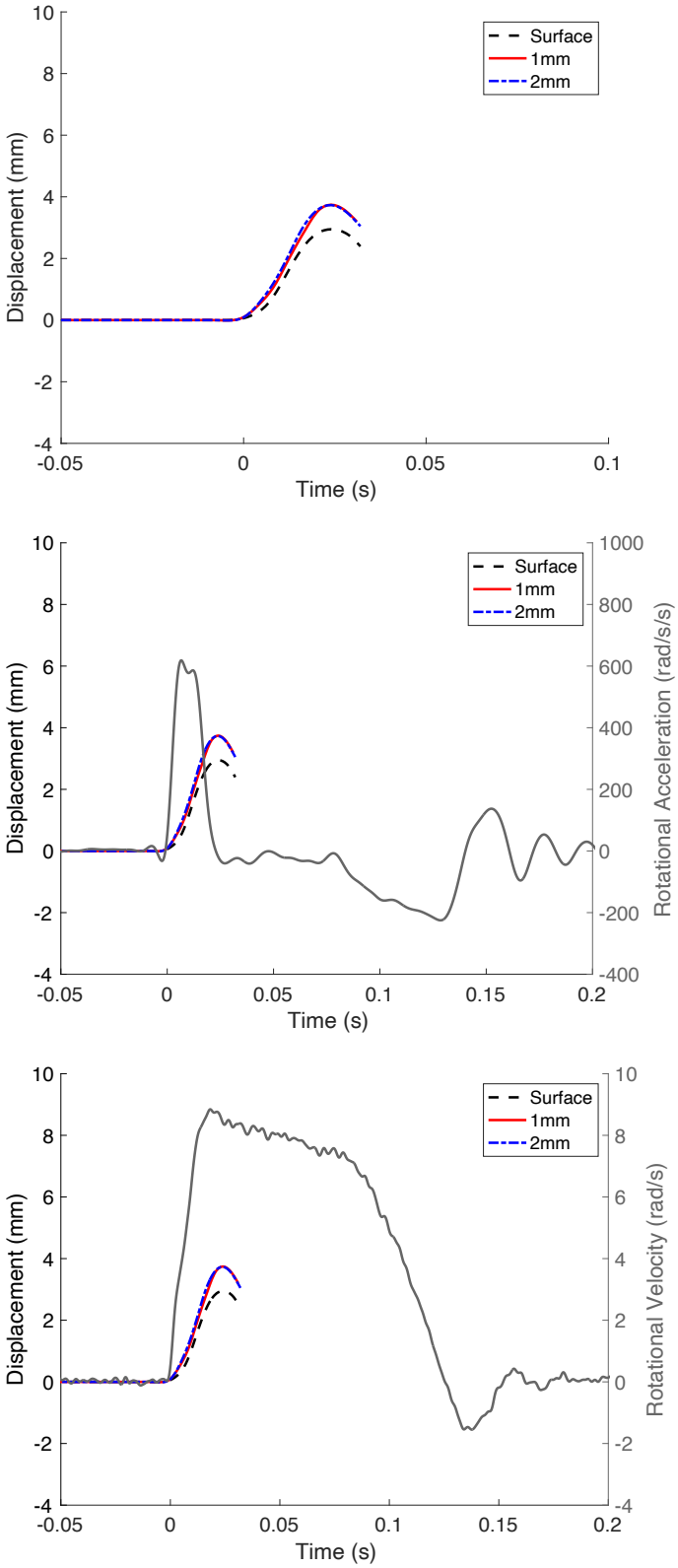

(p) Test 16

Figure 83 continued

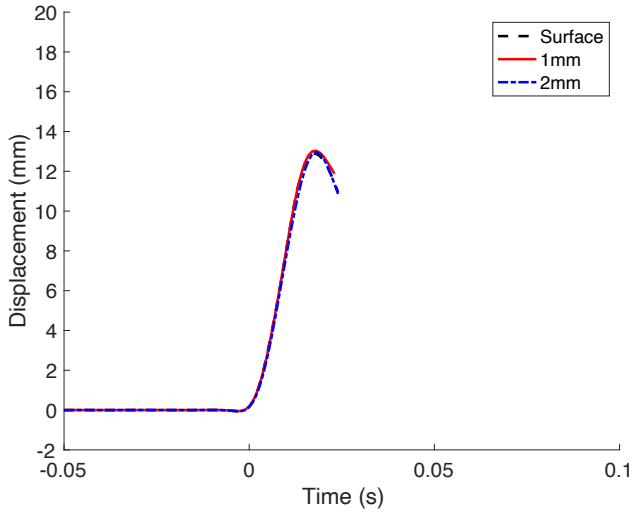

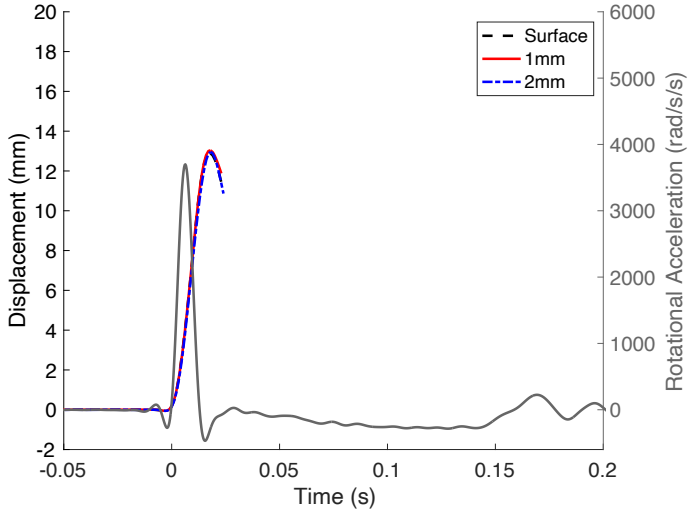

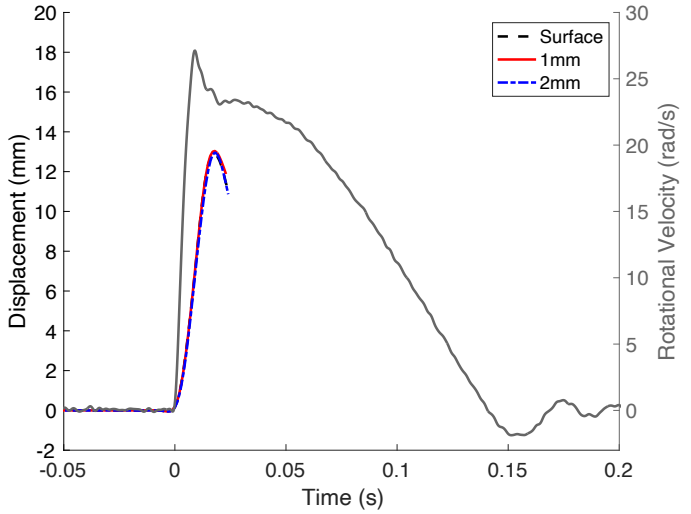

(q) Test 17

Figure 83 continued

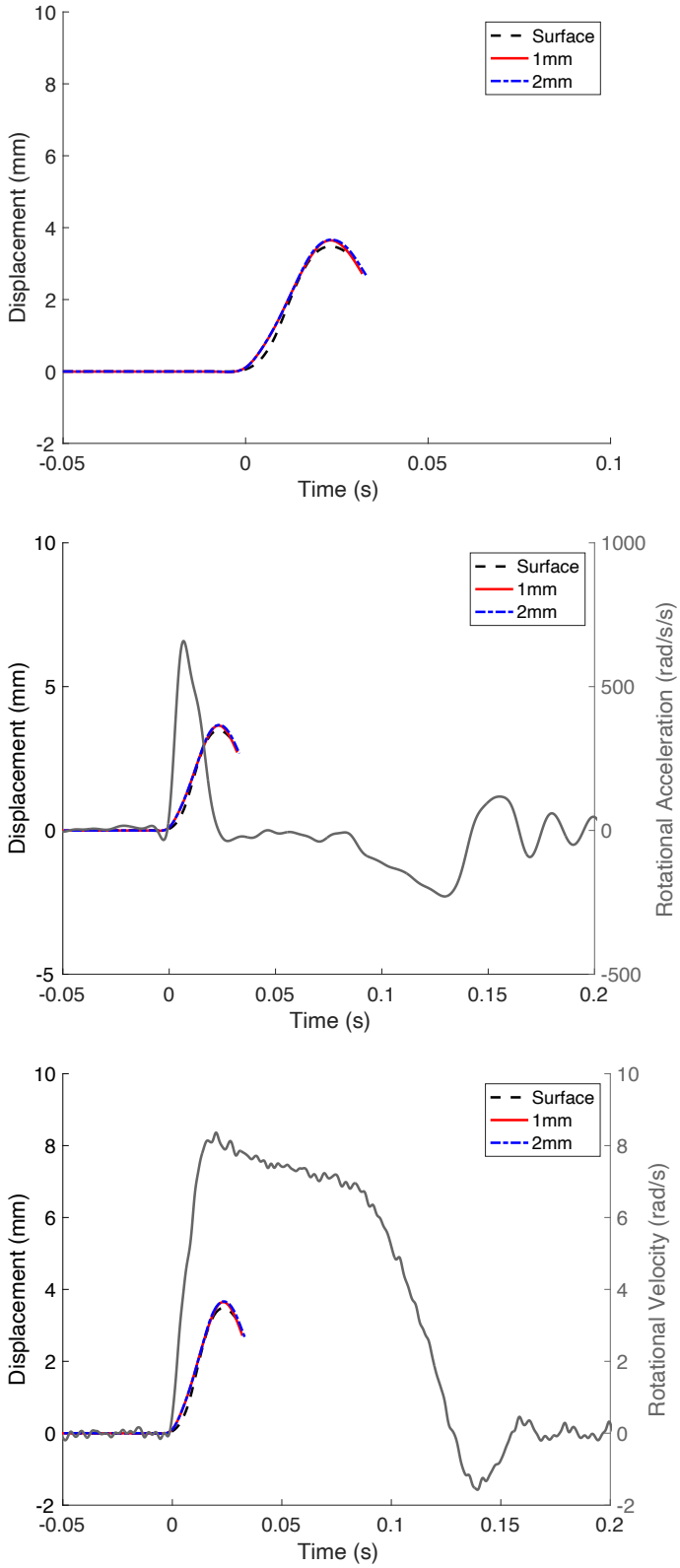

(r) Test 18

Figure 83 continued

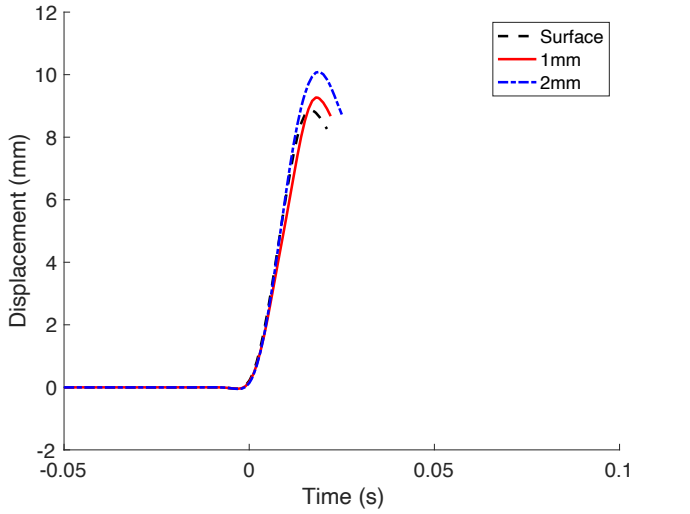

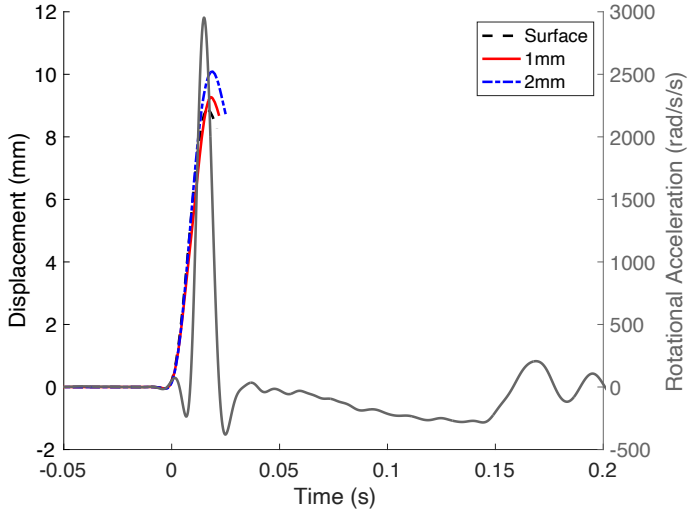

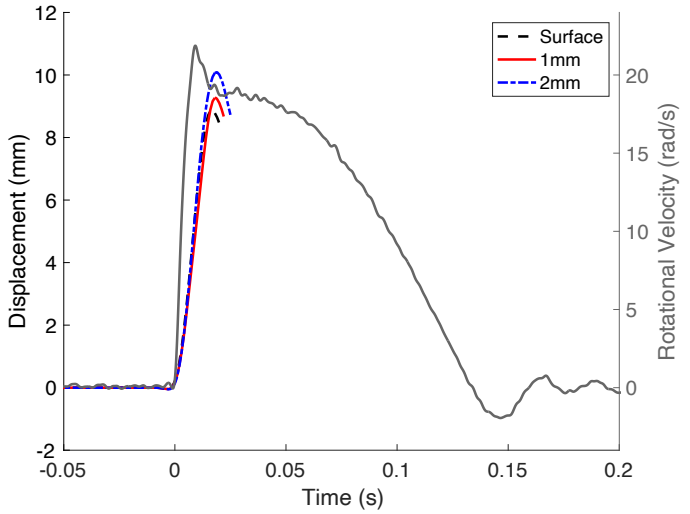

(s) Test 19

Figure 83 continued

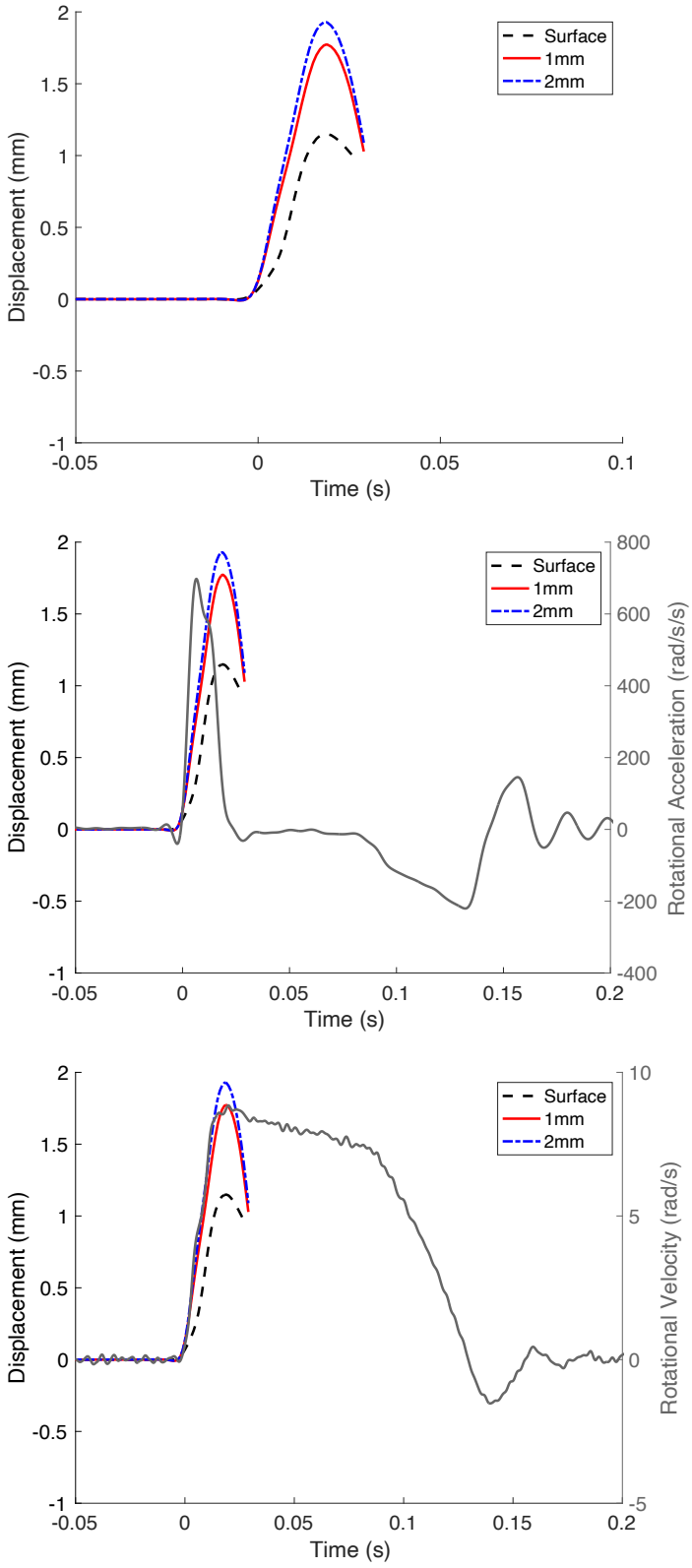

(t) Test 20

Figure 83 continued

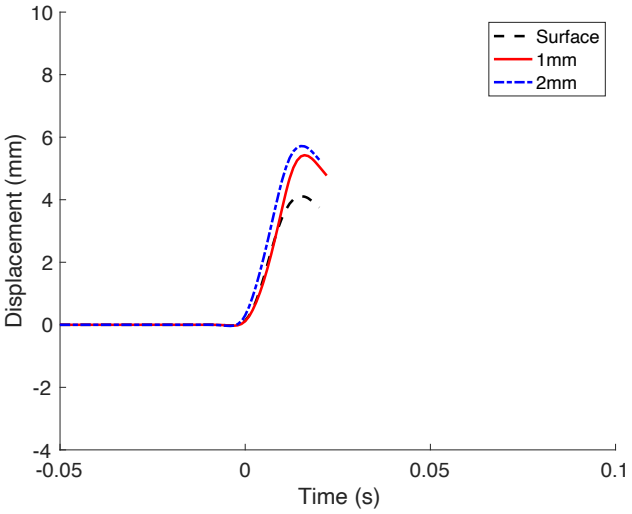

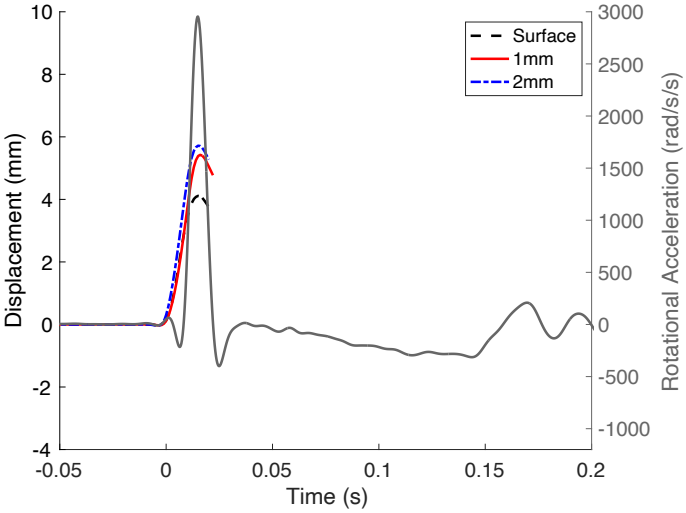

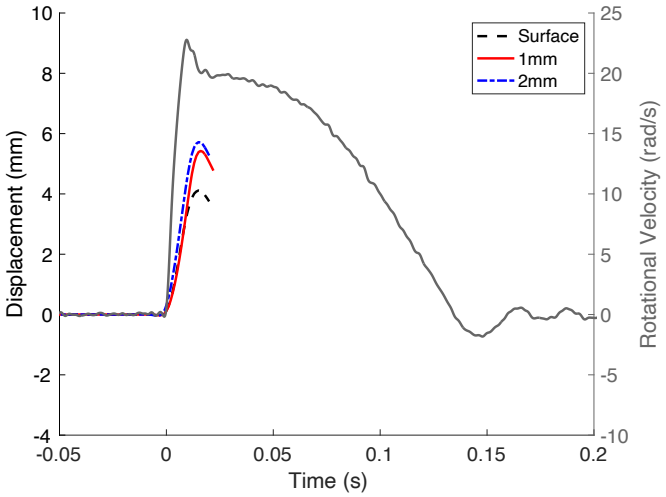

(u) Test 21